The PIP-II Conceptual Design Report

V1.00

September 2016

Primary authors:

M. Ball, B. Chase, A. Chakravarty, S. Dixon, J. Edelen, D. Johnson, S. Holmes, S. Kazakov, A. Klebaner, I. Kourbanis, T. Nicol, R. Pasquinelli, W. Pellico, L. Prost, I. Rakhno, A. Saini, A. Shemyakin, J. Steimel, V. Scarpine, A. Vivoli

Fermi National Accelerator Laboratory

P. Ostroumov

Argonne National Accelerator Laboratory

Edited by:

Valeri Lebedev / Fermi National Accelerator Laboratory

Contents

xxx

1. PIP-II Performance Goals and Summary

The Proton Improvement Plan-II (PIP-II) encompasses a set of upgrades and improvements to the Fermilab accelerator complex aimed at supporting a world-leading neutrino program over the next several two decades. PIP-II is an integral part of the strategic plan for U.S. High Energy Physics as described in the Particle Physics Project Prioritization Panel (P5) report of May 2014 [1] and formalized through the Mission Need Statement approved in November 2015. As an immediate goal PIP-II is focused on upgrades to the Fermilab accelerator complex capable of providing proton beam power in excess of 1 MW on target at the initiation of the Long Baseline Neutrino Facility/Deep Underground Neutrino Experiment (LBNF/DUNE) program [2], currently anticipated for the mid-2020s. PIP-II is a part of a longer-term goal of establishing a high-intensity proton facility that is unique within the world, ultimately leading to multi-MW capabilities at Fermilab.

PIP-II builds on three major recent developments at Fermilab: 1) the recently completed upgrades to the Recycler and Main Injector (MI) for the NOvA experiment, 2) the Proton Improvement Plan [3] currently nearing completion, and 3) the development of world-class capabilities in superconducting radio frequency (SRF) acceleration over the last decade. In parallel, the recently launched LBNF/DUNE project has created a compelling need for a revitalization of the Fermilab complex to support a vision of a research program based on very high intensity proton capabilities.

The NOvA project included the conversion of the Recycler Ring from an antiproton storage to a proton accumulation facility, while the PIP Proton Improvement Plan (PIP) consolidates a set of improvements to the existing Linac, Booster, and Main Injector (MI) aimed at supporting 15 Hz Booster beam operation. In combination, the NOvA upgrades and PIP create a capability of delivering 700 kW beam power from the Main Injector at 120 GeV and set the stage for PIP-II to deliver in excess of 1 MW at the start of the LBNF/DUNE experimental program.

This document describes the Conceptual Design for PIP-II. This concept balances the long-term vision of Fermilab's long baseline neutrino mission with the near- and mid-term goals endorsed by the P5 report and the Mission Need Statement.

1.1. Design Criteria

The P5 report and the Mission Need Statement call for a performance upgrade of the Fermilab accelerator complex to support a world-leading neutrino program, while maintaining high-reliability operations through the rejuvenation of aging systems within this complex and providing a platform for future enhancements. Based on these performance requirements pre-conceptual development for PIP-II has proceeded based on the following design criteria:

- Deliver 1.2 MW of proton beam power from the Fermilab Main Injector, over the energy range 60 – 120 GeV, at the start of operations of the LBNF/DUNE program;
- Sustain high reliability operations of the Fermilab accelerator complex throughout the initial phase of LBNF/DUNE operations;
- Support the currently operating and envisioned 8-GeV program at Fermilab including Mu2e, g-2, and the suite of short-baseline neutrino experiments;
- Provide a platform for eventual extension of beam power to LBNF/DUNE to >2 MW;
- Provide a flexible platform for long-range development of the Fermilab complex; in particular provide an upgrade path for a factor of ~10 increase in beam power to the Mu2e experiment, and for extension of accelerator capabilities to include flexible high-

bandwidth pulse formatting/high beam power operations.

The primary bottleneck limiting beam power to the LBNF target is the existing Linac/Booster. Performance following the completion of the PIP will be limited to about 4.2×10^{12} protons per Booster pulse by beam losses – primarily driven by space-charge forces at the 400 MeV Booster injection energy. The secondary bottleneck is slip-stacking of twelve Booster pulses in the Recycler – this performance is determined jointly by characteristics of the Recycler itself and by the characteristics of beam delivered from the Booster. Hence the primary need is to raise the injection energy into the Booster in order to support a roughly 50% increase in per-pulse beam intensity, while implementing modifications to the Booster, Recycler, and Main Injector to carry this increased beam intensity all the way to the LBNF target. A concept suggested in the PIP-II Reference Design [4] was further developed to satisfy these criteria. It is described in this Conceptual Design Report.

1.2. Alternatives Considered

A number of different approaches could be used to upgrade the Fermilab accelerator complex to achieve beam power in excess of 1 MW on the LBNF target. The challenge is to identify solutions that provide an appropriate balance between minimizing near-term costs and maintaining the flexibility to support longer-term physics goals. Following the release of the Mission Need Statement, four alternatives, including the Reference Design, were identified for analysis as mandated by DOE 413.3b. All alternatives were based on raising the injection energy of the Booster to provide a 50% increase in delivered protons per pulse. Paired with a modest decrease in the Main Injector cycle time (from 1.333 to 1.2 seconds) this provides 1.2 MW beam power at 120 GeV. Implementation was via either new or upgraded linacs, based on either superconducting or normal conducting technologies, and with pulsed vs continuous wave (CW) capabilities. The analysis of alternatives report found that all alternatives could meet the near-term needs of the neutrino program as identified within the Mission Need Statement, while the Reference Design (Alternative 1) provided significant long-term opportunities for the development of the Fermilab accelerator complex into a world-leading high intensity hadron facility. Furthermore, Alternative 1 was found to be realizable at a cost comparable to the other alternatives under the assumption that in-kind contributions from international partners are forthcoming as currently envisioned. The Acquisition Executive has received the Analysis of Alternatives Report and is currently considering the options. However, this Conceptual Design Report as written describes the Reference Design as all work undertaken to date aligns with this particular concept to be developed to the Conceptual Design level as described in this report. Because the development of Fermilab Accelerator Complex described in this report represents a natural continuation of the performance improvements being implemented within the PIP, it has therefore been named Proton Improvement Plan-II (PIP-II).

1.3. Overview of PIP-II

The goal of Proton Improvement Plan-II is to enhance the capabilities of the existing Fermilab accelerator complex to support the delivery of 1.2 MW beam power to the LBNF production target, while simultaneously providing a platform for subsequent upgrades of the accelerator complex to multi-MW capability. High-level goals, and supporting beam performance parameters, for PIP-II and their comparison to PIP parameters are given in Table 1-1. The central element of PIP-II is a new 800 MeV superconducting linac accelerating H^- ions and located in close proximity to the existing Booster as shown in Figure 1-1. This siting offers several advantages in terms of minimizing cost while retaining options for future development; in particular, the site affords direct access to significant electrical, water, and cryogenic infrastructure while providing a straightforward path for

eventual replacement of the Booster, which will be required to support beam powers in excess of 2 MW.

Table 1-1: PIP-II high-level performance goals

Performance Parameter	PIP	PIP-II	Unit
Linac Beam Energy	400	800	MeV
Linac Beam Current (chopped)	25	2	mA
Linac Pulse Length	0.03	0.54	ms
Linac Pulse Repetition Rate	15	20	Hz
Linac Upgrade Potential	N/A	CW	
Booster Protons per Pulse (extracted)	4.2	6.5	10^{12}
Booster Pulse Repetition Rate	15	20	Hz
Booster Beam Power @ 8 GeV	80	166	kW
8 GeV Beam Power to LBNF	N/A	83-142*	kW
Beam Power to 8 GeV Program	30	83-24*	kW
Main Injector Protons per Pulse (extracted)	4.9	7.5	10^{13}
Main Injector Cycle Time @ 120 GeV	1.33	1.2	sec
Main Injector Cycle Time @ 60 GeV	N/A	0.7	sec
Beam Power @ 60 GeV	N/A	1	MW
Beam Power @ 120 GeV	0.7	1.2	MW
Upgrade Potential @ 80-120 GeV	N/A	2.4	MW

* First number refers to Main Injector operations at 120 GeV; second number to 60 GeV.

The scope encompassed by the PIP-II as described in this document includes:

- An 800-MeV superconducting linac (SC Linac), constructed of CW-capable accelerating structures and cryomodules, operating with an average H^- beam current of 2 mA and a beam duty factor of 1.1%;
- Beam transport from the end of the SC Linac to the new Booster injection point, and to a new 800-MeV beam dump;
- Upgrades to the Booster to accommodate 800-MeV injection, and acceleration of 6.5×10^{12} protons per pulse;
- Upgrades to the Recycler to accommodate slip-stacking of 7.7×10^{13} protons delivered by twelve Booster batches;
- Upgrades to the Main Injector to accommodate acceleration of 7.5×10^{13} protons per pulse to 120 GeV with a 1.2 second cycle time, and to 60 GeV with a 0.7 second cycle time.
- Associated conventional facilities including enclosures, equipment galleries, and utilities. The linac enclosure will be constructed with a length to accommodate a future possible extension of the linac energy to 1.0 GeV

The SC Linac energy is selected to support a 50% increase in Booster beam intensity, accompanied by a 30% reduction in the space-charge tune shift as compared to the current operations. This choice is conservative and will ensure lower fractional beam loss required at the higher operating intensities and higher injection energy. The linac is constructed entirely of components

that are capable of operating in CW mode. The incremental cost to DOE in constructing the linac from CW compatible components is minimal[1].

The SC Linac is followed by a beam transport line to bring the H^- beam to the Booster. This line includes an arc bending the beam by about 210°. The bending radius of the arc is maintained above 23 m to prevent stripping of the beam prior to Booster injection. There is a provision for installation of an RF separator and septum at the SC Linac end which could be utilized to support the operation of multiple experiments following future linac upgrades.

The Booster repetition rate will be increased from 15 to 20 Hz. This is extremely helpful for reduction of beam losses during slip-stacking in the Recycler due to the larger momentum difference between the two streams of slip-stacked bunches. The repetition rate increase also increases overall particle flux through the Booster and yields higher power for the 8-GeV experimental program. The operation of Booster gradient magnets at 20 Hz was recently verified [5]. The transition to the higher rate will be achieved by decreasing the value of capacitors in the magnet resonance circuit. Although the acceleration rate increases proportionally to the repetition rate the peak RF voltage does not change from that being provided by the PIP due to the smaller slip-factor at the higher injection energy. However, doubling the RF power transferred to the beam, to support the increased beam intensity and more rapid acceleration rate, will require additional minor modifications to the present RF power amplifiers.

Protons will be injected into the Booster using multi-turn strip-injection similar to the injection method used in the SNS [6]. The number of injection turns is equal to about 300. Although the number of injection turns is much larger than what is presently used in the Booster, it is still about three times less than that used in the SNS. The large number of injection turns and small emittances of the SC Linac beam allow painting of transverse and longitudinal distributions resulting in a significant reduction of space-charge effects. In contrast to present operations, beam injection will proceed at non-zero RF voltage. This allows one to avoid adiabatic bunching, which is problematic because of the long bunching time[2]. To reduce beam losses during Booster injection the linac bunches arriving at the RF bucket boundaries are removed by a bunch-by-bunch chopper located in the Medium Energy Beam Transport (MEBT) of the linac. The same chopper creates a three-bunch long extraction gap. Slip-stacking in the Recycler and acceleration in the MI will be done in a manner similar to that presently used for NOvA [7].

Upgrades to a number of systems in the Booster, Recycler, and Main Injector will be required in order to support the higher Booster injection energy and higher beam intensities. These include upgrades to the Booster injection system, the RF systems in all rings, implementation of a γ_t-jump in the Main Injector, and various feedback systems. The upgrade to the Booster injection system is the most significant of these.

Modifications to the LBNF target facility to accept 1.2 MW protons are assumed to be undertaken by the LBNF project. However, the requirements for the beam delivery are described in this document. Note that the concept presented here is capable of delivering from 1 to 1.2 MW of beam power to LBNF for the energy range of 60 to 120 GeV. Although the LBNF operation is expected to take a major fraction of Booster intensity, considerable power will still be available at 8 GeV. In particular, it is expected to be 83 kW for 120 GeV operations and 24 kW for 60 GeV.

---

[1] The most expensive part of the accelerator making CW operation possible is a new cryo-plant capable to support CW operation. It is expected to be an in-kind contribution from the India Department of Atomic Energy.

[2] The long bunching time is related to the smaller value of the slip-factor at the higher injection energy. The higher Booster repetition rate additionally magnifies this problem.

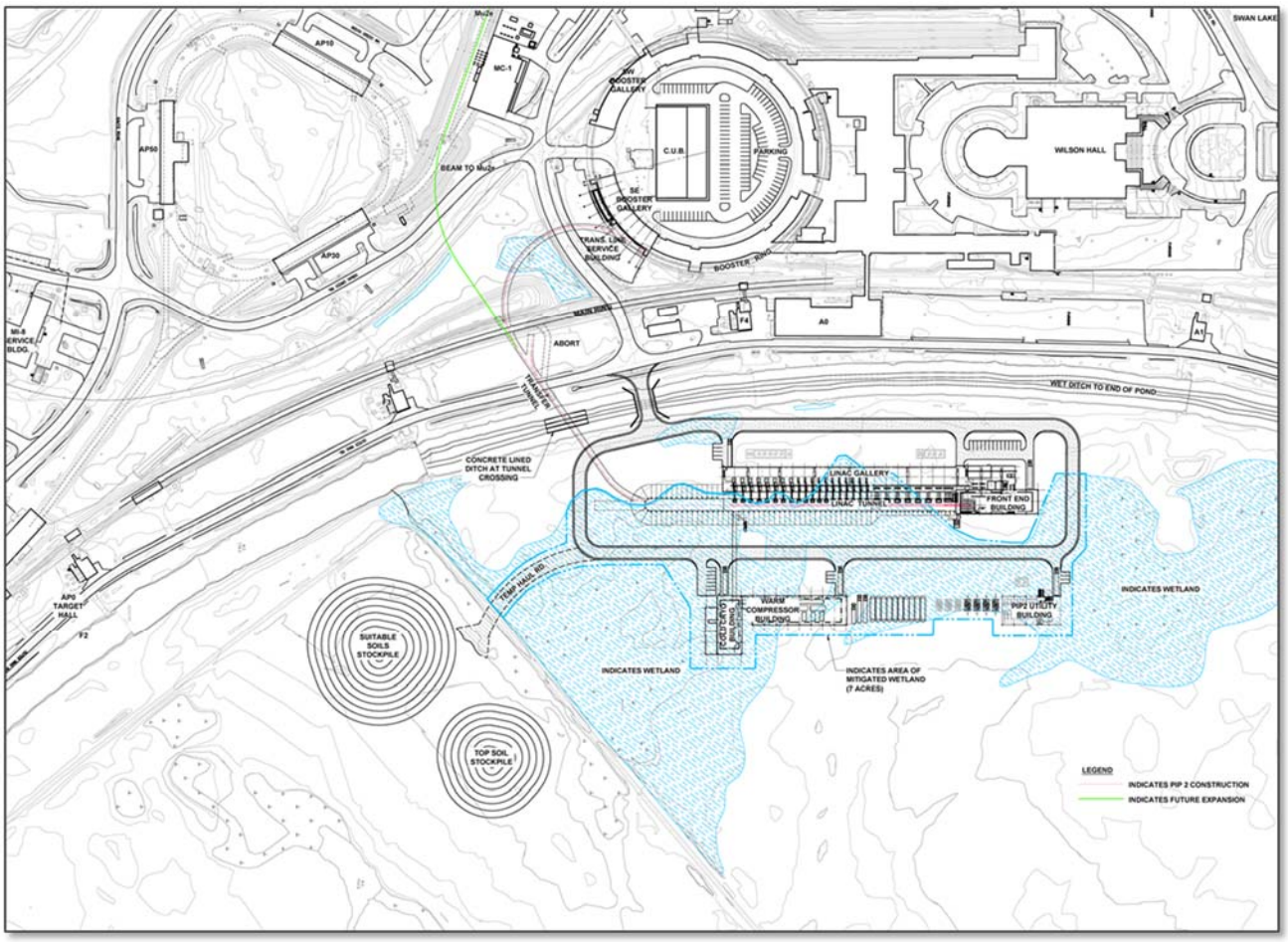

Figure 1-1: Site layout of PIP-II (north is to the right). New construction includes the linac enclosure, transfer line enclosure (including the beam abort area and a stub to facilitate future connection to the Muon Campus), linac gallery, utility building, and cryo/compressor building. The blue areas denote identified wetland areas.

PIP-II provides a variety of straightforward and cost effective upgrade paths. Delivery of more than 2 MW to the LBNF target will require replacement of the existing Booster. The most straight forward strategy would be to extend the 0.8 GeV linac to 1.5-2 GeV and to inject at this energy into a newly constructed 8-GeV rapid cycling synchrotron (RCS). Such a synchrotron could either be of a conventional sort, as currently deployed at the J-PARC facility in Japan, or could incorporate novel design features based on highly non-linear optical elements currently under study at Fermilab. In either case the siting shown in Figure 1.1 is compatible with siting of such a RCS to the south of the linac, providing capabilities for injecting beam into the Main Injector.

The estimated cost to DOE of PIP-II is ~$520M in 2020 dollars, including both development and construction costs, indirect costs, and 35% contingency. Offsets of roughly $200M from international in-kind contributions are included in this number. The upper end of the cost range is identified in the Mission Need Statement as $650M.

2. Accelerator Facility Design

It is envisioned that the PIP-II construction project will include the superconducting linac (SC Linac), the transfer line connecting the linac and the Booster, and corresponding upgrades to the Booster, Main Injector and Recycler rings. All constituents of the project are closely interconnected, and an achievement of successful operation for each of them represents a considerable challenge. Therefore, they are described below at the same level of detail.

2.1. 800 MeV Linac

2.1.1. Technical Requirements

The linac includes the following major elements:

- Ion source,
- Low Energy Beam Transport (LEBT),
- RFQ,
- Medium Energy Beam Transport (MEBT), including the bunch-by-bunch chopper and bunching cavities,
- One accelerating section composed of 162.5 MHz Half-Wave Resonators (HWR),
- two accelerating sections composed of 325 MHz Single-Spoke Resonators (SSR1 and SSR2),
- Two accelerating sections of 650 MHz elliptical cavities, one at low beta ($\beta_{opt} = 0.64$) and one at high beta ($\beta_{opt} = 0.97$) (LB650 and HB650).

Figure 2.1 shows the structure of the linac. A room temperature (RT) section accelerates the beam to 2.1 MeV and creates the desired bunch structure for injection into the SC Linac. The RFQ and the first SC section (HWR) operate in a CW mode. In the case when the beam is only delivered to the neutrino program, the rest of the linac is used in a pulsed regime to reduce the required cryogenic power. Otherwise, the entire linac operates in the CW regime. Operation with a peak current of up to 10 mA is supported by the ion source, LEBT and RFQ. The bunch-by-bunch chopper located in the MEBT removes undesired bunches leaving the beam current at up to 2 mA (averaged over a few μs) for further acceleration. There is also a "slow" chopper in the LEBT with rise and fall times of about 100 ns. It allows forming a macro-structure in the beam timing required for machine commissioning and allows one to avoid unnecessary beam loading in normal operations. Together the LEBT and MEBT choppers form the desired bunch structure.

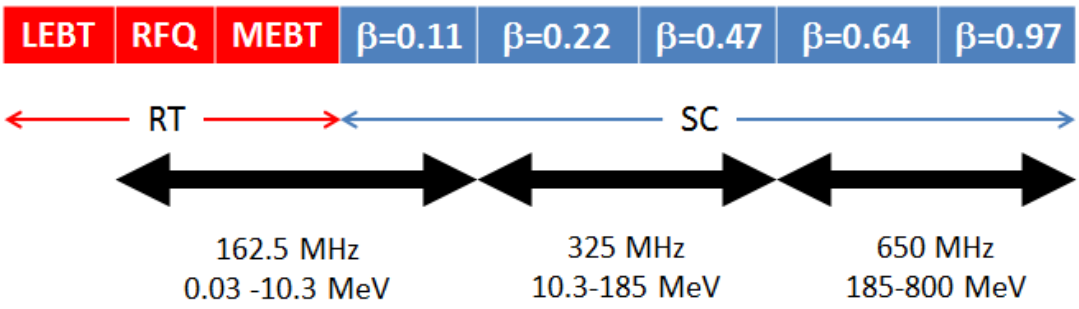

Figure 2.1: The linac technology map.

The energy stored in the SC cavities is quite large. Consequently, the accelerating voltage variations due to beam loading are below 10^{-3} if the bunch structure is repetitive with a period less than about 3 μs. The SC Linac accelerates up to 2 mA of beam current to 800 MeV with peak currents of up to 10 mA for periods of less than a few μs. The operational parameters for the SC Linac are given in Table 2.1.

Table 2.1: SC Linac Parameters

Parameter	Requirement	Units
Particle species	H^-	
Input beam energy (kinetic)	2.1	MeV
Output beam energy (kinetic)	0.8	GeV
Pulse repetition rate	162.5	MHz
RF pulse length	pulsed-to-CW	
Sequence of bunch pulses	Programmable	
Average beam current in SC Linac	2	mA
Final rms norm. transverse emittance, $\varepsilon_x = \varepsilon_y$	<0.3	mm-mrad
Final rms norm. longitudinal emittance	<0.35 (1.1)	mm-mrad (keV-ns)
Rms bunch length at the SC Linac end	4	ps

To support beam injection into the Booster, pulsed operation of the linac is sufficient. In this case the linac operates at 20 Hz with a beam pulse duration of 0.55 ms resulting in a 1.1% beam duty factor. The RF cavity filling requires a significantly longer time. The effective cryogenic duty factor is about 6.6% while the effective duty factor for high power RF is about 15%. To reduce the cryogenic power the phase of the RF amplifiers can be shifted by 180 deg. after a beam pulse to accelerate the voltage decay in cavities.

Maintaining sufficiently small emittances through the entire linear accelerator and the beam transport to the Booster is essential for minimizing the beam losses both in the linac and at injection into the Booster. The maximum allowed rms emittances along the accelerator are presented in Table 2.2 for an ion source beam current in the range of 2÷5 mA.

Table 2.2: Maximum allowed rms normalized emittances through the accelerator

	Normalized rms beam emittance (mm mrad)	
	Transverse	Longitudinal
Ion source	0.14	-
RFQ entrance	0.18	-
RFQ exit	0.20	0.28
MEBT exit	0.23	0.31
Exit of SC linac	0.3	0.35

2.1.2. Warm Frontend

The warm frontend of the PIP-II linac provides an H^- beam to the first superconducting module. The frontend beam current specifications go well beyond what is required to support operations of the Booster and Main Injector. While the nominal PIP-II peak current for Booster injection is about 4 mA, the nominal average current of the RFQ is 5 mA (10 mA maximum). A fast chopper providing bunch-by-bunch chopping is an important part of the frontend. It enables the removal of bunches that are too close to the RF bucket boundaries for in-bucket injection into the Booster. This capability will also be used in future multi-user operations.

The frontend consists of a 30 keV H^- ion source, a Low Energy Beam Transport (LEBT) delivering up to 10 mA DC beam to the entrance of a 2.1 MeV CW Radio Frequency Quadrupole (RFQ) accelerator, and a Medium Energy Beam Transport (MEBT). This is shown schematically by red boxes in Figure 2.1.

The choice for the LEBT energy of 30 keV is a compromise between considerations of beam space charge effects that may increase the transverse emittance at low energy and adiabatic bunching in the RFQ, where the longitudinal emittance is reduced with decreasing the injection energy. This choice balances the final warm frontend emittance among the three degrees of freedom.

The RFQ energy of 2.1 MeV is chosen because it is below the neutron production threshold for most materials, thereby simplifying the RFQ and MEBT maintenance. At the same time, this energy is sufficiently large to mitigate space charge effects in the MEBT with currents as high as 10 mA.

2.1.2.1. LEBT - Low Energy Beam Transport

The conceptual layout of the ion source and LEBT is shown in Figure 2.2. Two ion sources in a "Y"-configuration are installed with a slow switching dipole bending magnet to maximize beam availability. Vacuum valves isolate the ion sources from the rest of the LEBT. Thus, each source can be removed for repairs, reinstalled, and conditioned without interrupting the operation of the other source. The 3-solenoid LEBT (in each leg) transports the beam from the exit of the ion source to the entrance of the RFQ, matching the beam's optical functions to the ones required for low loss acceleration in the RFQ. In addition, a chopping system can form a beam with low duty factor required for commissioning and tuning of the downstream accelerator in a pulsed mode. At the same time, the chopping system interrupts the beam as part of the Machine Protection System (MPS), and prohibits beam to be accelerated in the RFQ accordingly to the safety system status. Ref. [8] presents the Functional Requirement Specifications (FRS) for the LEBT.

Achieving high reliability for the warm front-end and its components is a task of primary importance. With that in mind, a principal goal of the LEBT design is the requirement of maintaining good vacuum in the RFQ, as well as minimizing particle bombardment of the RFQ vanes in order to reduce the frequency of sparking. As a result, a fairly long LEBT (~2 m) is envisioned in order to isolate the inherently bad vacuum near the ion source exit from good vacuum required at the RFQ entrance. In addition, the bend between the first two solenoids ensures that there is no direct line of sight between the ion sources and the RFQ (as well as the superconducting elements further downstream). This greatly reduces the bombardment of the RFQ vanes by fast neutrals and should help the overall reliability of the RFQ. Good vacuum in the LEBT also reduces the stripping of H^- to protons with their subsequent acceleration in RFQ and uncontrolled losses in the accelerator downstream.

Similarly, the need for low duty factor operation mainly arises from the desire to limit the potential for failures during tuning of the SRF cryomodules, as well as to limit irradiation of the cavities.

However, because the neutralization process is not instantaneous, the optimal tune for a short pulse may noticeably differ from long pulse or DC operation. To minimize this effect, the PIP-II LEBT provides an atypical transport scheme in which the beam is not neutralized in the downstream part of the LEBT, independently of its time structure. Figure 2.3 illustrates the geometry of the transport scheme. The vacuum is quite poor near the ion source. It results in a relatively short neutralization time and nearly full beam space charge neutralization in the neutralized section.

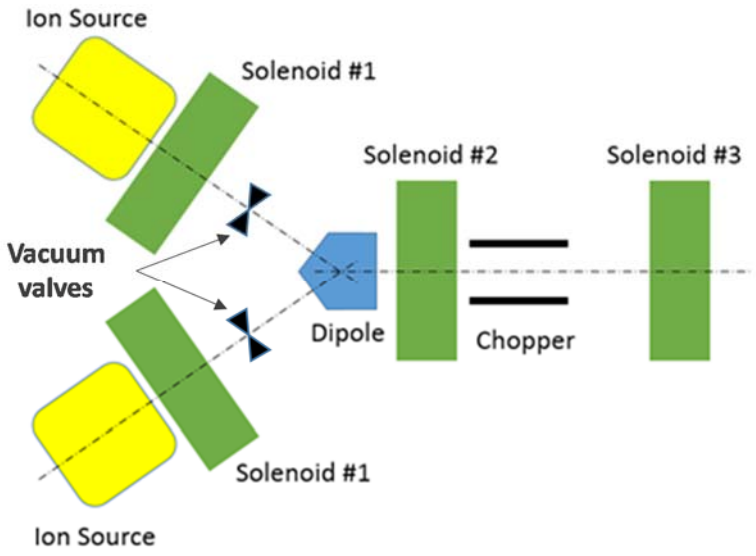

Figure 2.2: Conceptual schematic of the PIP-II LEBT with two ion sources.

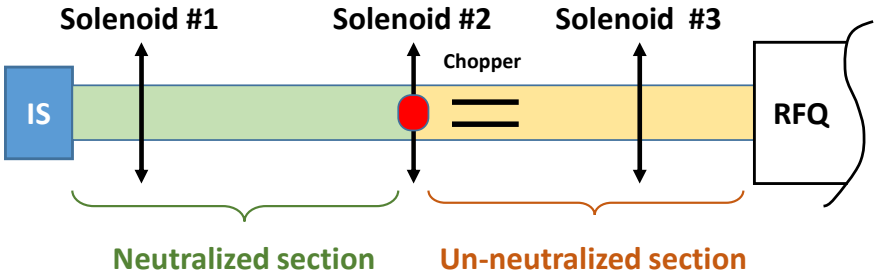

Figure 2.3: Transport scheme concept schematic.

The transition to un-neutralized transport is achieved by combining a potential barrier (red oval on Figure 2.3), which confines neutralized particles upstream, and a clearing electric field removing compensating ions downstream of the potential barrier. The clearing electric field is obtained by applying a DC voltage to one of the chopper electrodes, which sweeps ions out of the beam path. In addition, a low vacuum pressure is maintained between the potential barrier and the RFQ to limit the rate at which neutralized particles are created. The corresponding beam optics is shown in Figure 2.4. This optics has been implemented at the PIP-II Injector Test [9], where a low emittance beam ($\varepsilon_n \leq 0.18$ mm mrad, rms) with Twiss parameters adequate for injection into the RFQ was obtained at the end of LEBT. The initial distribution was derived from measurements of the ion source phase space carried out initially at LBNL [10] and later at the PIP-II Injector Test (PIP2IT).

The location of the chopper, between solenoids #2 and #3, hence relatively far from the RFQ entrance, conforms to the principles expressed previously for achieving high reliability (*i.e.* good

vacuum in the RFQ and low particle bombardment of the vanes). In addition, it leaves space for diagnostics both before and after solenoid #3, as well as provides room for a vacuum pump. Note that unlike many other LEBT designs, where a chopping system is located just upstream of the RFQ, the PIP-II LEBT layout provides sufficient room for a simple and robust chopper.

Finally, we would like to stress again that the design of the LEBT described above, beside the beam physics requirements, is driven by requirements of high reliability and efficiency in operation. They call for (1) good vacuum in the RFQ, (2) a simple and reliable chopper, (3) a beam transport scheme, which tuning is independent of the time structure, and (4) sufficient room for diagnostics.

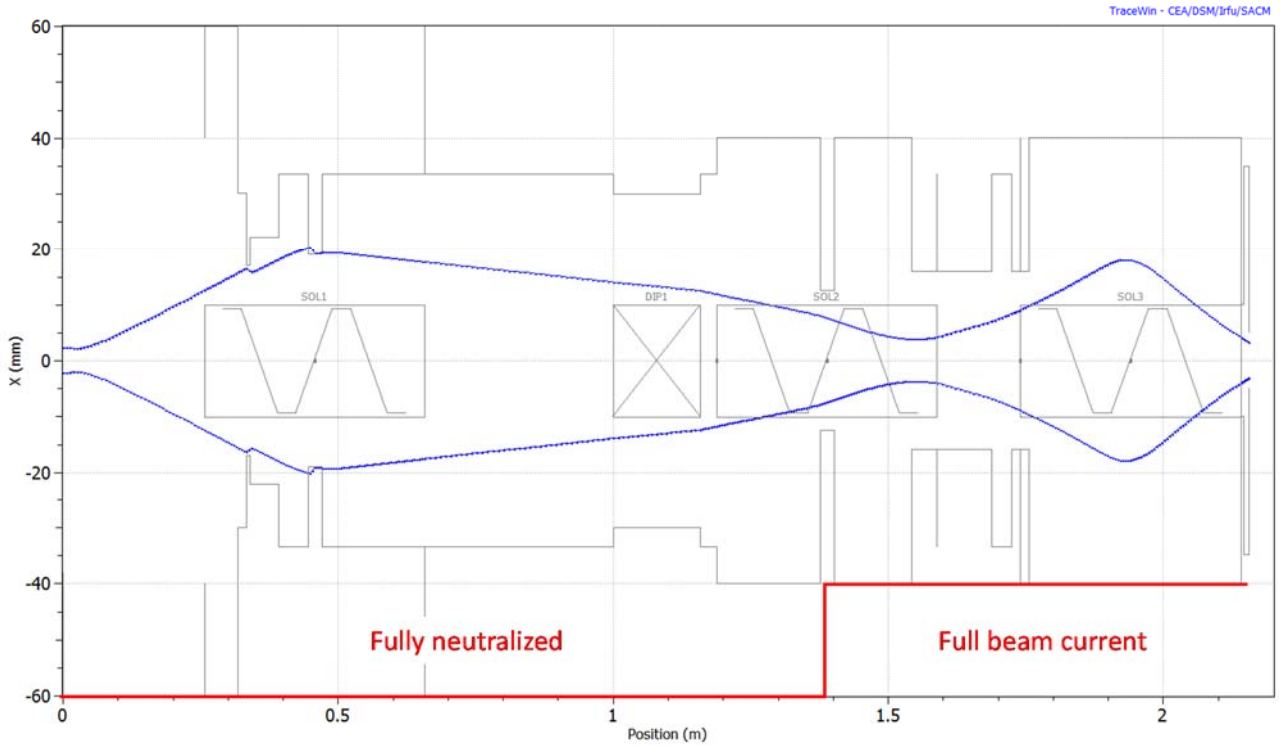

Figure 2.4: Beam horizontal envelope (2.5σ) for the partially un-neutralized LEBT optics solution simulated with TraceWin. The grey lines show aperture limitations. The red line indicates the level of neutralization (from fully neutralized to full beam current of 5 mA). Focusing is nearly symmetric which makes the vertical envelope quite close to the horizontal one.

2.1.2.2. RFQ - Radio Frequency Quadrupole Accelerator

The 162.5 MHz RFQ accelerates the 30 keV H^- ion beam to 2.1 MeV at beam currents of up to 10 mA CW. The design requirements are presented in Table 2.3.

The requirement of CW operation forced the design optimization to be aimed at the minimization of RF power loss in the structure since most of RF power is dissipated on the cavity walls creating considerable thermal load. The relatively low nominal vane tip-to-vane tip voltage of 60 kV was adopted to limit the overall RF power requirement, which in turn makes thermal management of the RFQ structure easier. The RF design is based on detailed simulations including 3D electro-magnetic simulations of the entire RFQ. The mode stabilization with pi-mode rods significantly reduces the structure sensitivity to manufacturing errors. The geometry of the vane-ends (vane – to - end-plate transition) was adjusted to achieve good field flatness [11]. It is also supported by 80 slug tuners compensating manufacturing errors and imperfections of simulations.

The beam dynamics design was simulated using PARMTEQ [12] and it either meets or exceeds all the requirements in terms of capture efficiency, transmission efficiency and emittance growth. Figure 2.5 shows a PARMTEQ simulation for a 5 mA beam, ideally matched into the RFQ. The transmission is 99.8% and output longitudinal emittance is 0.7 keV-ns. For an input emittance of 0.11 mm mrad, the output emittance is 0.15 mm mrad, a 35% increase but still well below the maximum specified. Additionally, error analysis (*e.g.* mismatch, centroid offsets, field errors…) was carried out and indicate that the design is very robust and error tolerant. Results of simulations of the transverse and longitudinal emittances as functions of the beam current (assuming a 0.11 mm-mrad rms normalized emittance at the RFQ entrance) are presented in Figure 2.6.

Table 2.3: Main parameters of the RFQ

Parameters	Value	Unit
Input energy	30	kV
Output Energy	2.1	MeV
Duty factor	100	%
Frequency	162.5	MHz
Beam current	5 (nominal); 1-10	mA
Transmission (1-10 mA)	> 95%	%
Output transverse Emittance (1-10 mA)	< 0.25	mm-mrad
Output longitudinal Emittance (1-10 mA)	0.8-1.0 (0.26-0.32)	keV-nsec (mm-mrad)

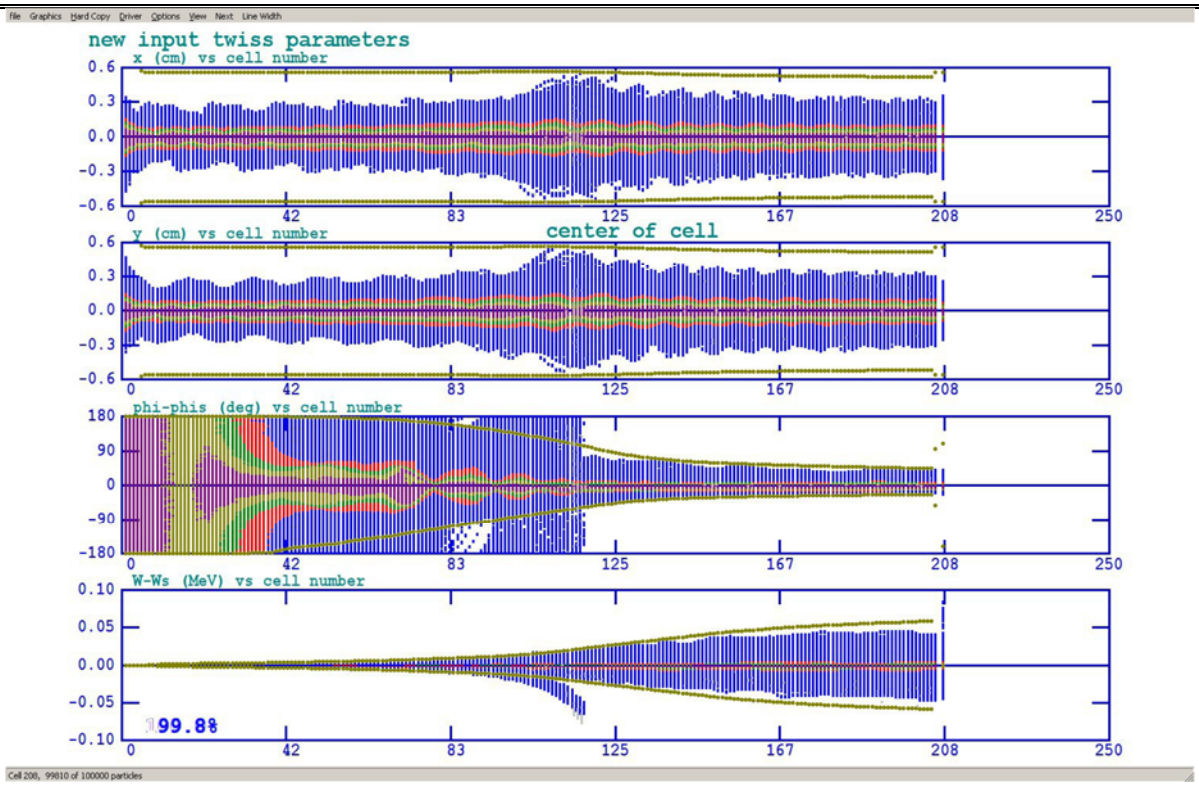

Figure 2.5: PARMTEQ simulation of a 5 mA beam using 100,000 macro-particles. The initial distribution was derived from the emittance measurements of the ion source performed during acceptance tests. The input Twiss parameters, however, are ideal.

Excessive longitudinal tails can result in beam losses in the course of acceleration and can limit the beam extinction of removed bunches[3]. The latter is an important requirement for future high duty factor experiments. Figure 2.7 presents the longitudinal distribution over the longitudinal Courant-Snyder invariant (single particle emittance), $\varepsilon_{s1} = s^2 / \beta_s + \beta_s (\Delta p / p)^2$, where β_s is the longitudinal beta-function, and s and $\Delta p/p$ are the deviations in the longitudinal coordinate and the momentum from the reference particle, respectively. Note that the boundary emittance is twice larger than the rms particle longitudinal emittance, which, by definition, should be averaged over particle longitudinal motion. One can see that the distribution has a non-Gaussian tail beyond ~4.6σ. This stresses the necessity of accounting for longitudinal tails in the computation of particle losses during further acceleration.

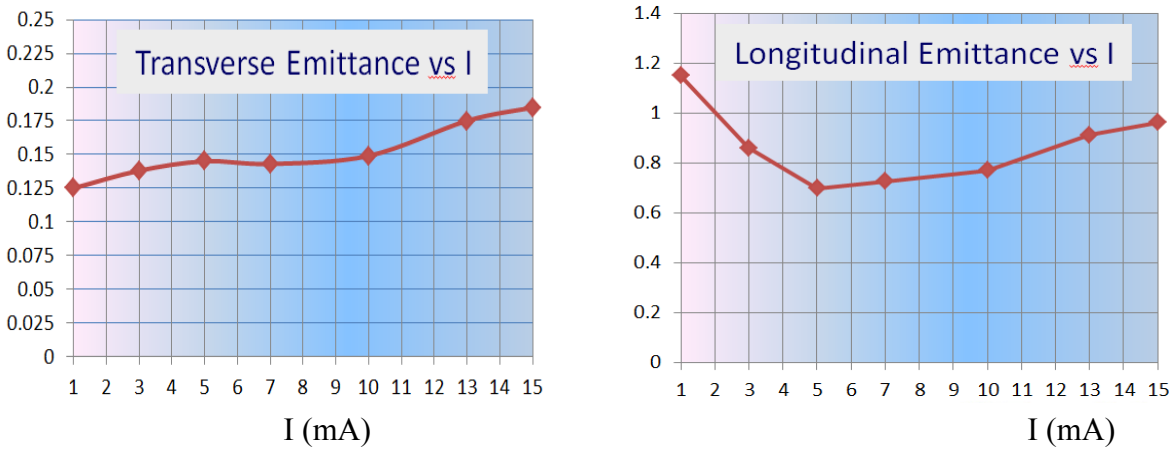

Figure 2.6: Dependence of the calculated transverse (left) and longitudinal (right) rms normalized emittances on the beam current; the transverse emittance is presented in mm·mrad and the longitudinal one in keV·ns (1 keV·ns ≈ 0.32 mm mrad).

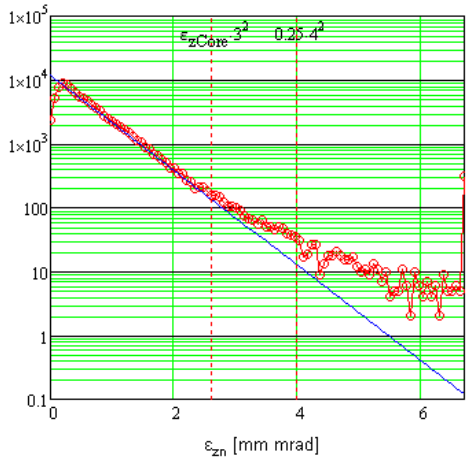

Figure 2.7: The particle longitudinal distribution at the end of the RFQ simulated for 5 mA beam current.

[3] A non-zero value for the beam extinction is associated with particles having large momentum deviation. In the course of their motion in the MEBT from the bunch-by-bunch kicker to the HWR cryomodule these particles, if their momentum deviations are sufficiently large, are not captured in the MEBT RF and can freely drift. This results in that some of these particles arrive to a nearby already emptied RF bucket and, then, be captured into HWR RF, which RF bucket height is significantly larger than the bucket height of the MEBT.

2.1.2.3. MEBT - Medium Energy Beam Transport

The Medium Energy Beam Transport (MEBT) transports the 2.1 MeV, 1-10 mA H^- beam between the RFQ and the HWR cryomodule with low emittance growth (< 10%) and low beam losses of the passing bunches.

Typically, the main functions of an MEBT are to provide optical matching between the RFQ and the main linac and to include tools for measuring the beam properties. The PIP-II MEBT is envisioned to have, in addition, several other distinctive features.

First, many of the PIP-II MEBT properties are determined by the bunch-by-bunch selection concept. The MEBT wideband chopping system directs unneeded bunches of the initial true-CW 162.5 MHz bunch sequence to an absorber according to a pre-selected pattern and transfers bunches chosen for further acceleration into the SC Linac with minimum distortions. This bunch separation is performed with two kickers separated by ~180º of betatron phase advance; the absorber is positioned at ~90º of phase advance downstream of the second kicker. Implementation of the chopping system requires significant elongation of the MEBT. On the one hand, the system itself requires ~5 m of the beam line. On the other hand, the high power density of the removed bunches on the MEBT beam absorber makes the absorber a critical and inherently risky device. To alleviate possible catastrophic effects on the SRF cavities in a case of an absorber vacuum failure, it is prudent to separate the absorber from the first cryomodule (HWR) by a beam line containing only more conservatively designed devices. The length of this region, determined by the time of closing a fast acting vacuum valve in front of the HWR and the speed of shock wave propagation, needs to be ≥5 m.

The second distinctive feature of this MEBT is a system of scrapers that protects from an errant beam both the SRF cavities and sensitive elements of the MEBT itself.

Finally, the MEBT allocates space for a wall protecting the low-energy part from radiation generated in the high-energy part. It should allow servicing the ion source with the PIP-II linac delivering the beam.

The complete list of the MEBT functional requirements is presented in Ref. [13].

The resulting MEBT design is 14 m long with transverse focusing provided mainly by equidistantly placed quadrupole triplets with the exception of the two doublets located immediately downstream of the RFQ. In this text, the spaces between neighboring triplets or doublets are referred to as MEBT sections. To keep the beam properly bunched, the MEBT includes four identical bunching cavities. The structure of the MEBT is presented schematically in Figure 2.8.

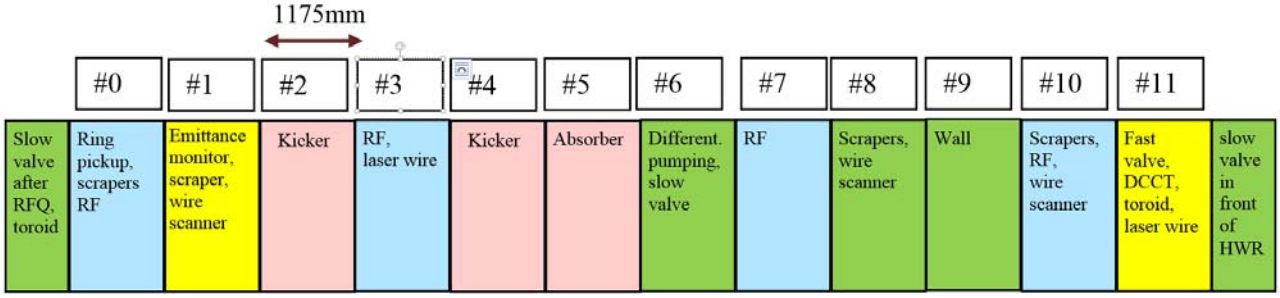

Figure 2.8: The MEBT structure. Sections are color-coded according to their main functions: green- vacuum, blue- RF, yellow- instrumentation, and pink – chopper.

The period in the regular part of the beam line is 1175 mm, which leaves a 650-mm long (flange-to-flange) space for various equipment. The first section labeled #0 in Figure 2.8 and located between doublets is shorter. It has available space of 480 mm.

2.1.3. SC Linac - Superconducting Linac

The SC Linac starts immediately downstream of the MEBT. It accelerates the beam from 2.1 MeV to 0.8 GeV and includes five types of superconducting (SC) cavities to cover the entire velocity range required for acceleration of H^- (or protons).

2.1.3.1. Accelerating Cavities

The cavity frequencies and cell configuration are selected to maximize the acceleration efficiency for each accelerating structure, to minimize the cost of the accelerator and its operation, and to minimize the beam loss.

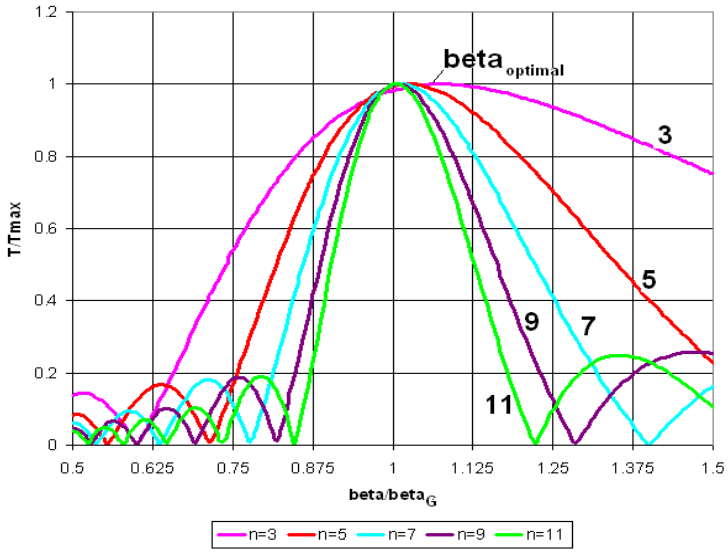

Figure 2.9: Transit-time factor versus the ratio of the beta to the geometric beta, β/β_G, for different number of cells in a cavity, n.

A primary efficiency factor for a RF cavity is the transit-time factor, $T(\beta)$. Its dependence on the beam velocity, β, is shown in Figure 2.9 for different numbers of cells in a cavity. The figure shows that the range in β over which the beam can be efficiently accelerated increases with a decreasing number of cells per cavity. On the other hand, a too small number of cells per cavity reduces the effective gradient and increases costs, due to end effects. The maximum acceleration is achieved for a velocity larger than the geometric-beta, β_G, determined by the cell periodicity. This velocity, where the maximum acceleration is achieved, is called the optimal beta, β_{opt}. For a periodic structure with a harmonic distribution of electric field along the axis,

$$E \propto \sin\left(\omega z / \beta_G c\right)\exp\left(i\omega t\right) , \qquad (2.1)$$

the transit-time factor for a cavity operating at the π-mode can be expressed by the following formula:

$$T(\beta) = \frac{T_0(\beta)}{T_0(\beta_{opt})}, \quad T_0(\beta) = \frac{2\beta}{\pi n}\left(\frac{\sin\left(\pi n(\beta-\beta_G)/(2\beta)\right)}{\beta-\beta_G} - (-1)^n \frac{\sin\left(\pi n(\beta+\beta_G)/(2\beta)\right)}{\beta+\beta_G}\right), \qquad (2.2)$$

where n is the number of cells in a cavity. Note that $T_0(\beta_G) = 1$, and $T_0(\beta)$ achieves its maximum at $\beta=\beta_{opt}$. That determines the normalization of $T(\beta)$ so that $T(\beta\text{opt}) = 1$. The above expression approximates well the transit-time factors obtained by numerical integration of the actual time dependent electric field of the PIP-II cavities. The geometric betas, β_G, presented in Table 2.4 were obtained by fitting Eq. (2.2) to the numerical integration results. Note that for typical multicell elliptic

resonators the value of β_G is slightly larger than the value obtained with other frequently used definition based on Eq. (2.1), where β_G is defined as the ratio of cavity period to the half-wavelength. The corresponding numbers are presented in the note to Table 2.4. For a large number of cells per cavity the geometric and optimal betas of Eq. (2.2) are related by the following approximate equation:

$$\beta_{opt} \approx \beta_G \left(1 + \frac{6}{\pi^2 n^2}\right). \qquad (2.3)$$

Recent developments in 1300 MHz ILC technology at Fermilab [14] and elsewhere have significantly improved SRF technology in general and have made it a preferable choice for the possible future extension of the PIP-II linac to higher energy. That forces the choice of accelerating frequencies to be subharmonics of the ILC frequency of 1300 MHz, and, consequently, yields 162.5, 325 and 650 MHz as frequencies for PIP-II. Such choice of frequencies results in a comparatively smooth frequency increase in the course of acceleration, accommodating bunch compression due to adiabatic damping.

Table 2.4 and Figure 2.10 present parameters of the cavities for the linac. The acceleration starts with half-wave resonators (HWR) operating at 162.5 MHz. They are followed by two types of single spoke resonators operating at 325 MHz (SSR1 and SSR2), and finally by two types of elliptical 5-cell cavities at 650 MHz (LB650 and HB650). Figure 2.11 presents the transit-time factors for the SC Linac. The accelerating voltage in each next cavity type is significantly larger than in the previous one. That determines that the transition happens earlier than the transit-time factors for two types become equal.

Table 2.4: Types of accelerating cavities for the SC Linac

Cavity name	β_G	β_{opt}	Freq. (MHz)	Cavity type	Energy gain at β_{opt} per cavity (MeV)	Energy range (MeV)
HWR	0.094	0.112	162.5	Half wave resonator	2	2.1-10.3
SSR1	0.186	0.222	325	Single-spoke resonator	2.05	10.3-35
SSR2	0.398	0.475	325	Single-spoke resonator	5	35-185
LB650	0.631*	0.647	650	Elliptic 5-cell cavity	11.9 (11.7♦)	185 – 500
HB650	0.947*	0.971	650	Elliptic 5-cell cavity	19.9 (19.6♦)	500 - 800

* Note that β_G for the elliptic cavities can be also defined as the ratio of regular cell length to half-wavelength. That yields β_G=0.61 for LB650 and β_G=0.92 for HB650.

♦ It represents a mean value among different field distributions with field flatness of 95%.

The choice of the RFQ frequency was determined by a requirement of bunch-by-bunch chopping. Chopping at 325 MHz is presently beyond the "state-of-the art". It leaves 162.5 MHz as the only

viable choice. The same frequency is also used for the first superconducting cryomodule (HWR), because, in comparison with 325 MHz, it results in reduced transverse defocusing and reduced longitudinal focusing from cavity fields, which would otherwise severely limit the accelerating gradient in the first SC cryomodule. The number of cavities, and the linac length, required to accelerate the beam to 11 MeV is reduced by more than a factor of 2, compared to cryomodules with 325 MHz cavities. Note that even this frequency choice does not enable a usage of nominal voltage for the first few HWR cavities. In particular, the first cavity uses about half of nominal voltage.

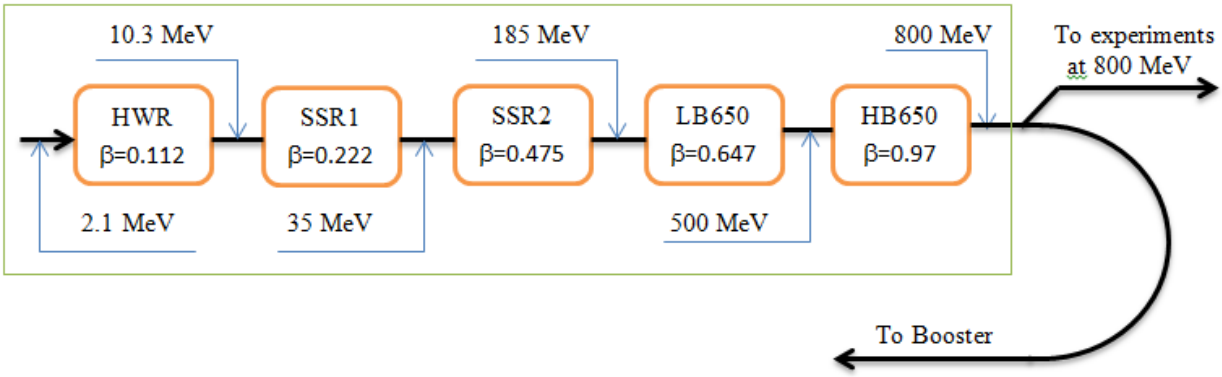

Figure 2.10: Technology map for SC part of PIP-II linac.

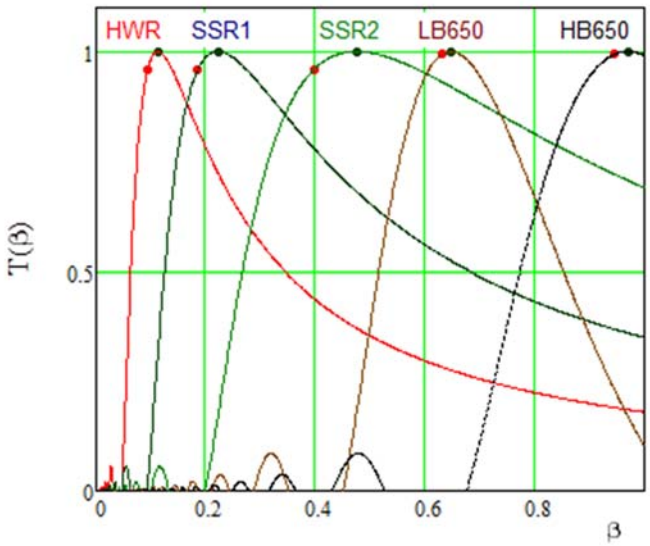

Figure 2.11: Transit-time factors for PIP-II SC cavities; red dots mark the position of β_G, and blue dots position of β_{opt} .

The cavity arrangement described above also yields:

- simplified longitudinal beam dynamics at each transition from one cavity type to another due to the limitation of frequency jumps to a factor of two, and
- an increased aperture at the beginning of the linac due to use of lower frequency sections.

The larger apertures reduce uncontrolled beam losses on low temperature surfaces to a tolerable level. We emphasize that the choice of cavities with lower frequencies reduces the effects of focusing/defocusing by accelerating cavities, and decreases the number of cells per cavity (for LB650 and HB650), consequently widening the dependences of transit-time factors on beta, which increases

the effective accelerating gradients and acceleration efficiency.

However, there are also some disadvantages related to the preference for lower frequencies:

- Microphonics is a more serious issue at lower frequencies.
- Lower frequency cavities are more expensive (more niobium), but that cost increase is compensated (within presently known accuracy) by the use of a smaller number of cavities and RF sources. The latter is mainly related to a smaller number of cells for the elliptic cavities (5 versus 9 for the ILC cavities), and, consequently, smaller variation of the transit-time factors.

There are few major factors, which limit the accelerating gradient. First, the operating gradient was chosen to provide a peak surface magnetic field that allows operation below the high-field Q-slope; see Figure 2.12 taken from Ref. [15] (see also [16]). For the frequency of 162.5 MHz we adopt a the maximum magnetic field of about 50 mT; while for the frequencies of 650 MHz it increases to about 75 mT. For all frequencies, the peak surface electric field is less than 45 MV/m [17] in order to avoid the risk of strong field emission (see details in Section 3). Another important limitation comes from increased difficulties to suppress microphonics and Lorentz Force (LFD) detuning with an increase of accelerating field. To be compatible with CW operation the PIP-II linac has comparatively small beam current. It results in high loaded Q-values, narrow bandwidths and susceptibility to microphonics and LFD (see details in Section 3).

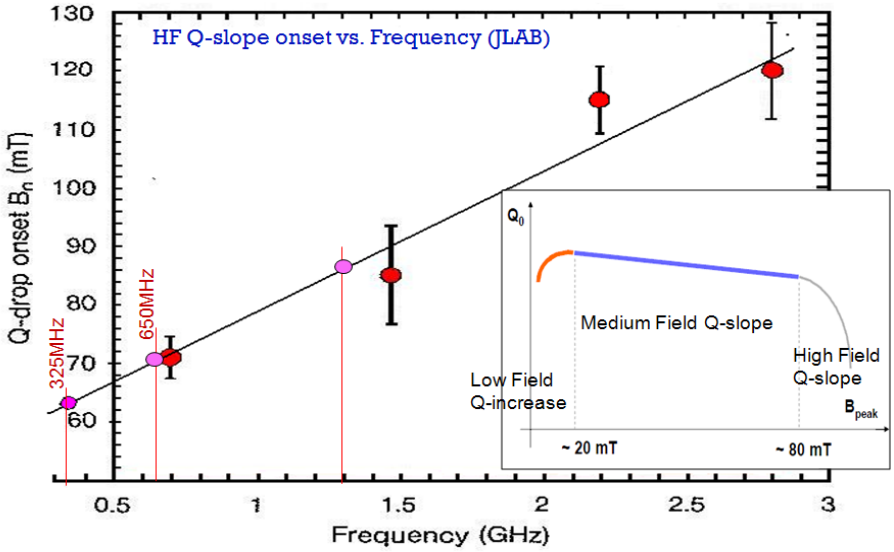

Figure 2.12: High field Q-slope versus frequency.

The transition from the 325 MHz single-spoke cavities to the 650 MHz elliptical cavities is chosen at the energy of about 185 MeV, because at lower energies elliptical cavities lose efficiency. It is inefficient to accelerate H^- ions from 170 MeV to 0.8 GeV using only one cavity type and, thus, two families of 650 MHz cavities are chosen. Table 2.5 presents the main electro-dynamical parameters of SC cavities. The effective length of a cavity is computed based on β_{opt} so that: $L_{eff} = n_{cell}\beta_{opt}c/(2f)$, where n_{cell} is the number of cells in a cavity (n_{cell} =2 for HWR, SSR1 and SSR2; n_{cell} =5 for LB650 and HB650). Consequently, the accelerating gradient is $\Delta E/L_{eff}$, where ΔE is the net energy gain at the optimal beta.

The transition energies between different types of cavities were optimized to minimize the total number of cavities. As an example of such optimization, Figure 2.13 displays the number of cavities

required as a function of geometric betas for LB650 and HB650. Here we additionally assume (1) a linear dependence of the field enhancement factors versus β_{opt} [18], (2) the initial synchronous phase is -30°, and (3) its modulus decreases inversely proportional to the square root of the energy to keep the desired RF bucket size. As one can see from the left pane of Figure 2.13 the number of cavities has a weak dependence on betas in the vicinity of the minimum. The optimal geometric betas for the two 650 MHz sections are 0.64 and 0.9 respectively (left), and the optimal transition energy is 466 MeV (right). More accurate simulations, taking into account realistic enhancement factors and other limitations discussed in Section 3, yield an optimal choice of betas at 0.61 and 0.92.

Table 2.5: Main electro-dynamical parameters of SC cavities

Cavity type	Aperture (diameter) (mm)	Effective length (cm)	Accelerating gradient * (MV/m)	E_{peak} * (MV/m)	B_{peak} * (mT)	$(R/Q)^4$ (Ω)	G (Ω)
HWR	33	20.7	9.7	44.9	48.3	275	48
SSR1	30	20.5	10	38.4	58.1	242	84
SSR2	40	43.8	11.4	40	64.5	297	115
LB650	83	74.6	15.9	39.7	75.4	377	191
HB650	118	112.0	17.8	38.3	73	610	260

* For energy gain per cavity presented in Table 2.4.

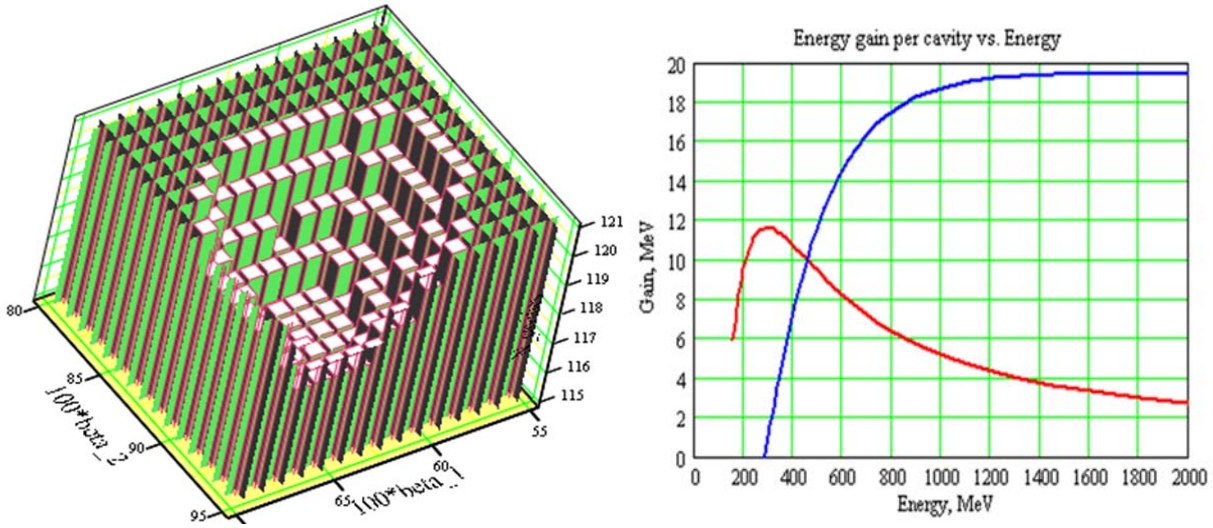

Figure 2.13: Number of cavities required for acceleration from 185 to 800 MeV versus cavity beta in the LB650 and HB650 sections (left) and the energy gain per cavity versus particle energy (right) for LB650 (red curve) and HB650 (blue curve) cavities.

[4] Throughout this document we define (R/Q) so that in the absence of cavity detuning and beam current, the RF power required to create the voltage amplitude U_0 is equal to: $P_g = (1+\beta_c^2)^2 U_0^2/(4\beta_c(R/Q)Q_0)$, where β_c is the coupling coefficient, and Q_0 is the cavity unloaded quality factor.

2.1.3.2. SC Cryomodules and Requirements to their Cryogenics

Cavities and focusing elements, as necessary, are grouped within cryomodules. In the 162.5 and 325 MHz sections transverse focusing is provided by superconducting solenoids, while in the 650 MHz sections by normal conducting quadrupole doublets located outside of the cryomodules. The main cryomodule parameters and the arrangement of focusing periods by cryomodule type are shown in Table 2.6. The periodicity of focusing elements is chosen to achieve sufficiently strong focusing required to reduce the effect of focusing variations due to variation of cavity transverse defocusing with longitudinal particle position inside the bunch. The distance between cavities in the HWR, SSR1 and SSR2 cryomodules is minimized to avoid longitudinal overfocusing representing severe limitation on the accelerating gradients at the beginning of each cryomodule type.

Table 2.6: General parameters of SC cryomodules

CM type	Cavities per CM	Number of CMs	CM configu-ration•	CM length (m)	Q_0 at 2K (10^{10})	Surface resis-tance, (nΩ)	Loaded Q (10^6)
HWR	8	1	8 × (sc)	5.93	0.5	9.6 (2.75♠)	2.7
SSR1	8	2	4 × (csc)	5.2	0.6	14 ($10^{\#}$)	3.7
SSR2	5	7	sccsccsc	6.5♦	0.8	14.4	5.8
LB650	3	11	ccc	3.9♦	2.15	8.9	11.3
HB650	6	4	cccccc	9.5♦	3	8.7	11.5

• Within the cryomodule (CM) configuration column "c" refers to an individual accelerating cavity, and "s" to a focusing solenoid.

♦ This number represents the present estimate of the cryomodule lengths. It will be finalized with advances in the cryomodule design.

♠ Measured value based on recent measurements of two HWR cavities at 2 MV accelerating voltage.

Based on recent measurements of SSR1 cavities made of CABOT niobium. We expect to get better results for the SSR2 cavities to be made of material, which satisfies Fermilab specifications [19].

Each magnet package (*i.e.* solenoid or quadrupole doublet) includes vertical and horizontal correctors and a 3-coordinate beam position monitor[5] (BPM) required for beam steering and optics measurements. All cryomodules are separated by warm sections. These warm sections are used for additional diagnostics (bunch transverse and longitudinal profile monitors, beam loss monitors, etc.) and for beam collimators required to avoid uncontrolled beam losses inside SC cryomodules. The composition of each of the warm insertions will be determined by requirements of safe and reliable operations, diagnostics, collimation, and cryogenic segmentation constraints. Details of the cryomodule designs are presented in Section 3.

The cavity Q_0's are based on an operating temperature of 2K and a conservative approach to the surface resistance based on values already obtained in operating cryomodules. As one can see the measured surface resistance values for the HWR and SSR1 cavities are considerably lower. Table 2.7 presents the cryogenic loads in SC cryomodules for operation in the CW regime. As one can see,

[5] The BPM has 4 plates and allows measurements of both transverse beam positions, as well as longitudinal bunch position measured by bunch arrival time.

the dynamic cryo-loads in the CW regime significantly exceed the static loads.

Table 2.7: Cryogenic loads in SC cryomodules for operation in the CW regime

CM type	Number of CMs	Static loads per CM, (W)			Dynamic loads per CM, (W)	Total load at 2 K per CM, (W)
		70 K *	5 K *	2 K	2 K	2 K
HWR	1	250	60	14	23.3	37.3
SSR1	2	194	71	12	23.1	35.1
SSR2	7	145	50	8.8	52.3	61.1
LB650	11	64	8.7	2.5	52.4	54.9
HB650	4	118	17.2	4.7	130	134.7
Total		2828	715	146	1532	1678

♦ Cryo-loads are computed with the nominal accelerating voltage for all cavities. The actual voltages required by the optics are smaller (see Figure 2.20) which yields somewhat smaller heating loads if all the cavities are operating at the design accelerating gradients.

* Static cryo-load includes heat flux from the couplers and current leads of magnets operating at their maximum currents.

A transition to pulsed linac operation (required to support Booster operation) allows one significant reduction of dynamic cryo-loads. In this case the duty factor of cryogenic operation is mainly determined by the time required to pump the energy into the cavity and then to discharge it. For this estimate, we assume that Q_0 does not depend on the field value. The duty factor for cryogenic operation is then equal to:

$$\eta_{cryo} = \frac{f_{rep}}{E_{\max}^{\ 2}} \int\limits_{\substack{\text{over} \\ \text{pulse}}} \left(E(t)\right)^2 dt \qquad (2.4)$$

where E_{max} is the accelerating voltage of a cavity, and f_{rep} is the repetition rate. Further, we assume that the cavity voltage changes as: $E(t) = 2E_{\max}\left(1-e^{-t/2\tau}\right), 0 < t < 2\tau \ln 2$ at cavity charging, and as $E(t) = E_{\max} e^{-t/2\tau}, t > 0$ at cavity discharging, where $\tau = Q_L / 2\pi f$ is the time constant for energy decay. The accelerating voltage stays constant during the beam pulse of 0.55 ms. Table 2.8 presents the cryo-duty factors and the dynamic cryo-loads assuming all cavities operate at the nominal voltages presented in Table 2.4. The static losses are the same as for CW operation and are presented in Table 2.7. As one can see for the normal cavity discharge described above the cryo-duty factor is almost an order of magnitude larger than the beam duty factor of 1.1%. The cavity discharge can be accelerated by pumping RF power with phase shifted by 180 deg. relative to the cavity field starting at the end of beam pulse and ending when the cavity voltage is zero. The corresponding dependence of electric field on time is: $E(t) = E_{\max}\left(e^{-t/2\tau} - 2\left(1-e^{-t/2\tau}\right)\right), 0 < t/\tau < 0.8109...$. Such arrangement reduces the dynamic cryo-loads by almost factor of two but requires a larger duty factor for RF amplifiers. It also greatly increases the peak power seen by the RF coupler after the phase shift. The

couplers are designed to withstand the resulting four-time increase in RF power if this mode of operation will be used in the future. Note that the HWR cavities are designed so that they cannot be used in a pulsed regime and therefore are excluded from Table 2.8.

Table 2.8: Cavity parameters for operation in the pulsed regime

CM type	Time constant τ, (ms)	Normal cavity discharge		Accelerated cavity discharge	
		Cryo-duty factor, %	Dynamic cryo-loads per CM (W)	Cryo-duty factor, %	Dynamic cryo-loads per CM (W)
SSR1	1.8	6.8	1.6	3.8	0.89
SSR2	2.9	9.9	5.2	5.3	2.8
LB650	2.8	9.7	5.1	5.2	2.7
HB650	2.8	9.8	12.7	5.2	6.8
Total*			170		102

* This value includes contribution of HWR cryomodule operating in CW mode.

The projected cooling power of a cryo-plant is presented in Table 3.15. It allows CW operation. To minimize the cost of cryogenic system operation, the PIP-II linac will initially operate in a pulsed mode with a capability to be moved to CW operations at later time. Details of the technical implementation of the cryo-plant are presented in Section 3.

Assuming pulsed operation one obtains the total dynamic cryo-loads at 2 K for all cryomodules to be 170 W for normal cavity discharge and 102 W for accelerated cavity discharge. Adding the static cryo-loads yields the total cryo-load at 2 K to be 315 and 247 W, respectively. As shown in Table 3.15 the cooling power of the cryo-plant at 2 K is 1900 W. Therefore, to be efficient for operation in the pulsed regime, the cryo-plant should have corresponding provisions (see Section 3 for details). Note, that the total cryogenic heat load at 2K is almost equally distributed between the static load and dynamic loads and is less than 16% of the cryogenic load for CW operation. The margin for cryo-plant cooling powers for the 5K and 70K circuits is large as can be seen from comparison of the total static loads of Table 2.7 with the cryo-plant powers presented in Table 3.15. Note that the Q_0 values presented in in Table 2.6 are well above what is routinely achieved at large superconducting accelerators, and their achievement is a challenging problem. The present status and expectations for achievable high Q_0 value are described in Section 3.

Table 2.9: Maximum allowed heat loads per cryomodule

CM type	70 K	5 K	2 K
HWR	250 W	80 W	50 W
SSR1	250 W	80 W	50 W
SSR2	250 W	80 W	75 W
LB650	100 W	15 W	100 W
HB650	300 W	25 W	220 W

In conclusion, we note that the Functional Requirements Specifications (FRS) on the designs of the cryomodules determine the requirements to the maximum cryo-loads, which each cryomodule has to withstand. These values determine mechanical designs of cryostats (sizes of piping *etc*.). They were chosen so that there would be sufficiently large margins between the expected cryo-loads and actual abilities for cryomodules to remove heat. Table 2.9 summarizes these FRS requirements.

2.1.3.3. RF Power and Suppression of Microphonics

The RF system has to support 2 mA beam operation in both CW and pulsed (0.55 ms, 20 Hz) regimes. The system is based on a single RF source driving each RF cavity, for a total of 113 separate RF sources for SC cavities. It is anticipated that all RF amplifiers will be solid state.

For operation in the pulsed regime, the average RF power delivered to the cavities has two contributions: 1) the energy transferred to the beam, and 2) the energy required to fill and discharge the accelerating cavities. The second contribution is about ten times larger than the first one. The average power associated with this contribution is determined by the accelerating gradient and does not depend on the peak RF power. For a fixed average power the RF cost increases with peak power and therefore the RF cost minimum is achieved with RF power equal to that required to accelerate the beam. Adopting this strategy yields a duty factor for the RF power amplifiers of about 9% for operation with the normal cavity discharge and about 13% for operation with the accelerated cavity discharge. One consequence of this strategy is that the cost savings associated with the pulsed power amplifiers in going from CW to low duty factor is modest and therefore CW capable RF amplifiers are planned. The RF requirements are summarized in Table 2.10. To estimate the peak RF power we assume that the maximum cavity detuning due to microphonics and Lorentz Force Detuning, δf, is equal to 20 Hz for all cryomodules [20]. That sets the optimal coupling,

$$\beta_c = \sqrt{\left(1+\frac{I_b \cos\phi_a \left(R/Q\right)Q_0}{U_0}\right)^2 + \left(\frac{2\delta f\, Q_0}{f_0}\right)^2} \ , \tag{2.5}$$

the corresponding cavity bandwidth,

$$\Delta f = \frac{f_0}{Q_0}\left(1+\beta_c\right) \ , \tag{2.6}$$

and the peak RF power,

$$P_{\max} = \frac{{U_0}^2\left(1+\beta_c\right)^2}{4\beta_c \left(R/Q\right)Q_0}\left(\left(1+\frac{I_b \cos\phi_a \left(R/Q\right)Q_0}{U_0\left(1+\beta_c\right)}\right)^2 + \left(\frac{2\delta f\, Q_0}{f_0\left(1+\beta_c\right)}\right)^2\right) . \tag{2.7}$$

Here I_b is the beam current, U_0 is the cavity voltage amplitude, and ϕ_a is the accelerating phase assumed to be equal to zero in these estimates.

The peak RF power presented in the last column of Table 2.10 sets the requirements on the power of the RF power sources. It accounts for power loss in transmission (implying cable for 325 MHz and wave-guide for 650 MHz) and the power margin required for effective operation of voltage control system (low-level RF).

The large values of accelerating gradient and the comparatively small beam current determine a small cavity bandwidth and, consequently, high sensitivity of cavity detuning to microphonics and LFD. The major sources of cavity detuning are:

- Variations in the pressure of the surrounding helium bath,
- Mechanical vibrations driven by external sources, and
- Radiation pressure on the walls from the electromagnetic field inside the cavity due to Lorentz force (LFD).

Table 2.10: Requirements for RF power*

CM type	Power transferred to beam per cav. (kW)	Microphonics amplitude (Hz)	Cavity half-bandwidth, $f/2Q_L$, (Hz)	Power transfer efficiency	Power margin	Peak RF power per cavity (kW)
HWR	4	20	33	90%	80%	6.5
SSR1	4.1	20	43	90%	80%	6.1
SSR2	10	20	28	90%	80%	17
LB 650	23.8	20	29	94%	80%	38
HB 650	39.8	20	29	94%	80%	64

* Powers are computed for a beam current of 2 mA. Allowances for transmission loss and microphonics suppression are included in the peak RF power.

♦ Microphonics amplitude represents a target value for maximum cavity detuning due to microphonics.

As can be seen from Eq. (2.7) the power required to maintain a constant accelerating gradient in a detuned cavity rises rapidly as the cavity detunes. Providing sufficient reserve power to drive detuned cavities increases both the capital and the operating costs of an accelerator. If sufficient reserve is not available, the beam may be lost. Thus, all measures minimizing cavity detuning need to be taken to keep RF power at a reasonable level. The measures can be separated into two broad categories: passive compensation and active compensation.

Passive compensation involves designing the machine and its components to minimize cavity detuning. In particular, the following design objectives are aimed:

- Minimization of the sensitivity of the cavity resonance frequency to variations in the helium bath pressure;
- The cryogenic system design has to minimize pressure variations in the 2K helium bath; the target value is below 0.1 mbar for rms fluctuations and 1 mbar for maximum pressure deviation;
- The cryomodule design has to minimize transmission of external vibrations to the cavities;
- The civil engineering has to minimize vibrations in the tunnel and the transfer of these vibrations to cryomodules. In particular, large compressors have to be well isolated from ground and be located far enough from the linac tunnel.

Active compensation involves sensing cavity detuning and using feed-forward and feedback to drive a piezo-actuator to compensate detuning in real-time. The detuning of each cavity can be determined from the base-band forward, reflected, and probe RF signals and used to drive a piezo actuator in a combination of adaptive feed-forward and feedback loops.

Table 2.11 presents requirements to cavity detuning due to helium pressure variations [20], estimates for Lorentz force detuning and recently measured values for the HWR and SSR1 cavities. Measurements for SSR1 were done with a dummy tuner installed. As one can see the LFD detuning exceeds the cavity bandwidth by about one order of magnitude. That determines that operation in the

pulsed regime is impossible without active frequency control with fast piezo-based tuners. Note that the HWR has no piezo tuner, and thus, cannot be used in a pulsed regime. As was already stated, the cryo-load in the HWR cryo-module is negligible compared to the total cryo-load and the HWR will always operate with CW RF.

Table 2.11: Functional requirement specifications on cavity detuning due to helium pressure variations and Lorentz force detuning (LFD)

	HWR	SSR1	SSR2	LB650	HB650
Sensitivity to He pressure (FRS), df/dP , Hz/Torr	<25	<25	<25	<25	<25
… (measurements), df/dP , Hz/Torr	13	4.0	-	-	-
Estimated LFD sensitivity, df/dE^2, Hz/(MV/m)^2	-	-5.0	-	-0.8	-0.5
… (measurements), df/dE^2, Hz/(MV/m)^2	-1.5*	-4.4	-	-	-
Estimated LFD at nominal voltage (FRS), Hz	-	-500	-	-192	-136
… (measurements) at nominal voltage, Hz	-122.4	-440	-	-	-

* Two cavities were measured in a test stand. The results are: -1.82 and -1.3 Hz/(MV/m)^2.

2.1.4. Beam Dynamics in the SC Linac

High efficiency multi-turn injection to the Booster requires small transverse emittances of the injected beam. This determines quite strict requirements to the beam emittance. The rms normalized beam emittance budget for the SC Linac has been established at 0.15 mm-mrad at the ion source and 0.3 mm-mrad at the linac exit linac. The lattice design and the beam dynamics optimization are obtained using the TRACK, TraceWin and GenLinWin codes, which accurately account for the effects of beam space charge making profound influence on the particle motion. A considerable effort was carried out to benchmark the codes and ensure that they produce reliable calculations.

Figure 2.14 shows the structure of one period inside the HWR, SSR1 and SSR2 cryomodules; and Figure 2.15 shows the structure of one period for the low- and high-beta sections of the SC linac (LB and HB sections). Other details of the beam optics can be found in Ref. [21]. Transverse focusing in HWR, SSR1 and SSR2 sections is provided using superconducting solenoids, while normal conducting quadrupole doublets are utilized in the LB and HB sections. The period in the HWR cryomodule starts from the SC solenoid to minimize gas penetration from the MEBT to the first SC cavity. It is supported by cryo-pumping of the vacuum chamber inside solenoid. The sequence of elements in the SSR1 and SSR2 cryomodules is chosen to minimize optics perturbations at the cryomodule-to-cryomodule transitions.

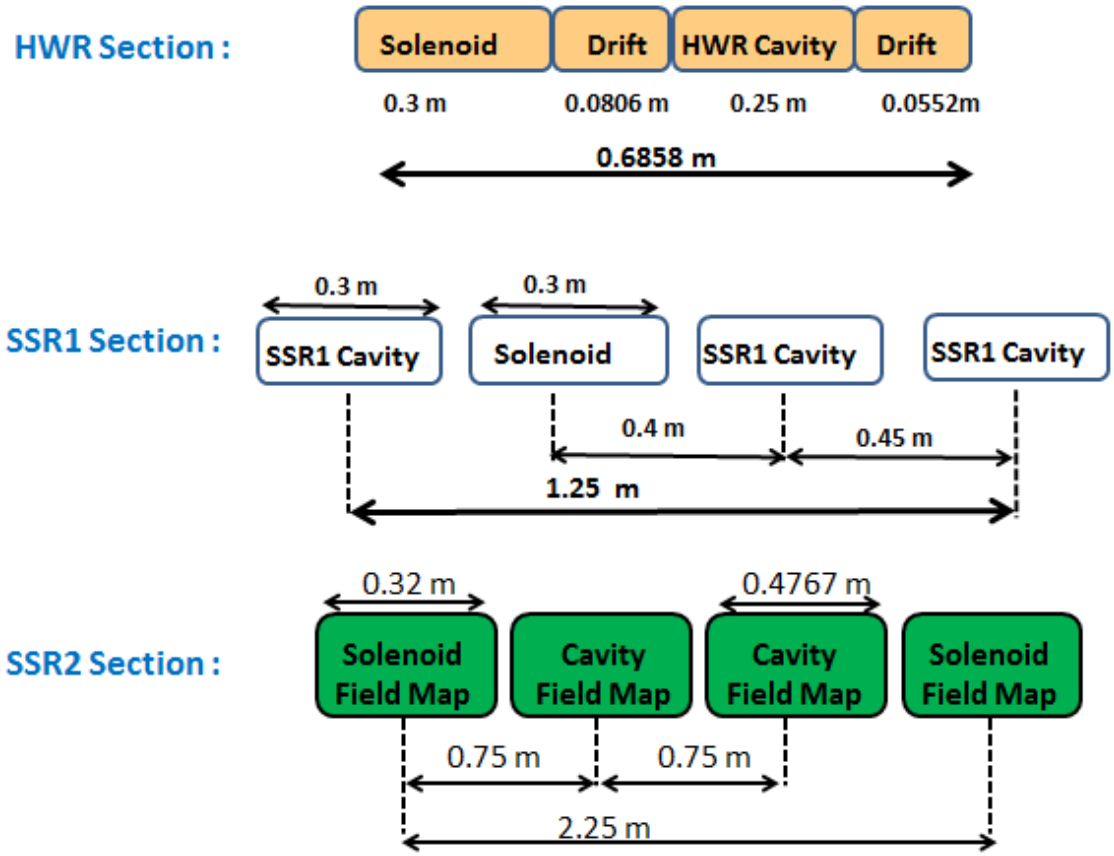

Figure 2.14: Element-to-element distances and element lengths in HWR (top), SSR1 (center) and SSR2 (bottom) sections of the PIP-II SC linac. The structures of cryomodules are: (sc)×8 for HWR, (csc)×4 for SSR2, and (sccsccsc) for SSR2; where c and s denotes cavities and solenoids, respectively.

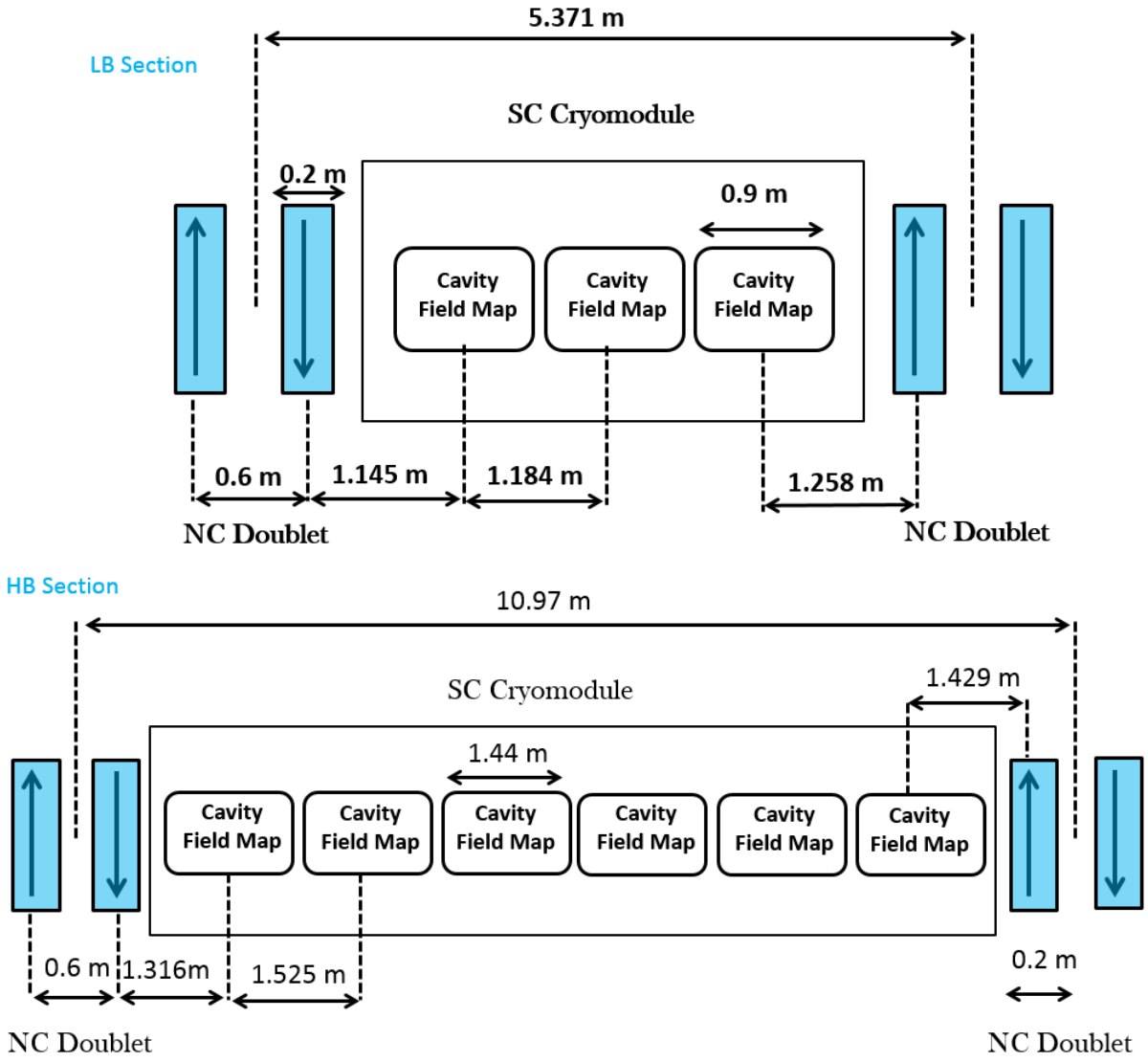

Figure 2.15: Focusing period in the LB (top) and HB (bottom) sections of PIP-II SC linac.

Figures 2.16 and 2.17 present the evolution of 1σ beam envelopes and the corresponding rms longitudinal and transverse normalized emittances through the entire SC Linac. As one can see there is an emittance growth at the linac beginning where the space charge effects are large. Their effect diminishes with energy. Simulations show considerable margin for the final value of transverse emittance, which is critically important for multi-turn strip injection into Booster. Figure 2.18 presents the phase space density of a bunch at the linac end. As one can see, there are no significant distortions in the bunch phase space. Simulations show that there are no particles beyond ~6σ. That result is supported by measurements performed at the SNS, which has a bunch brightness similar to what is expected in the PIP-II. As in the SNS, intrabeam stripping [22, 23] is expected to be the major source of particle loss. Figure 2.19 shows the power density of beam losses due to intrabeam stripping. As one can see, the losses due to this mechanism are below 0.1 W/m everywhere even for CW operation. Figures 2.20 – 2.23 show the strengths of focusing elements, the accelerating voltage and its phase. Finally, Figure 2.24 presents the beam energy along the linac, and Figure 2.25 presents the beta-functions obtained from the rms beam sizes and emittances, and hence describes the beam transport with the beam space charge forces included.

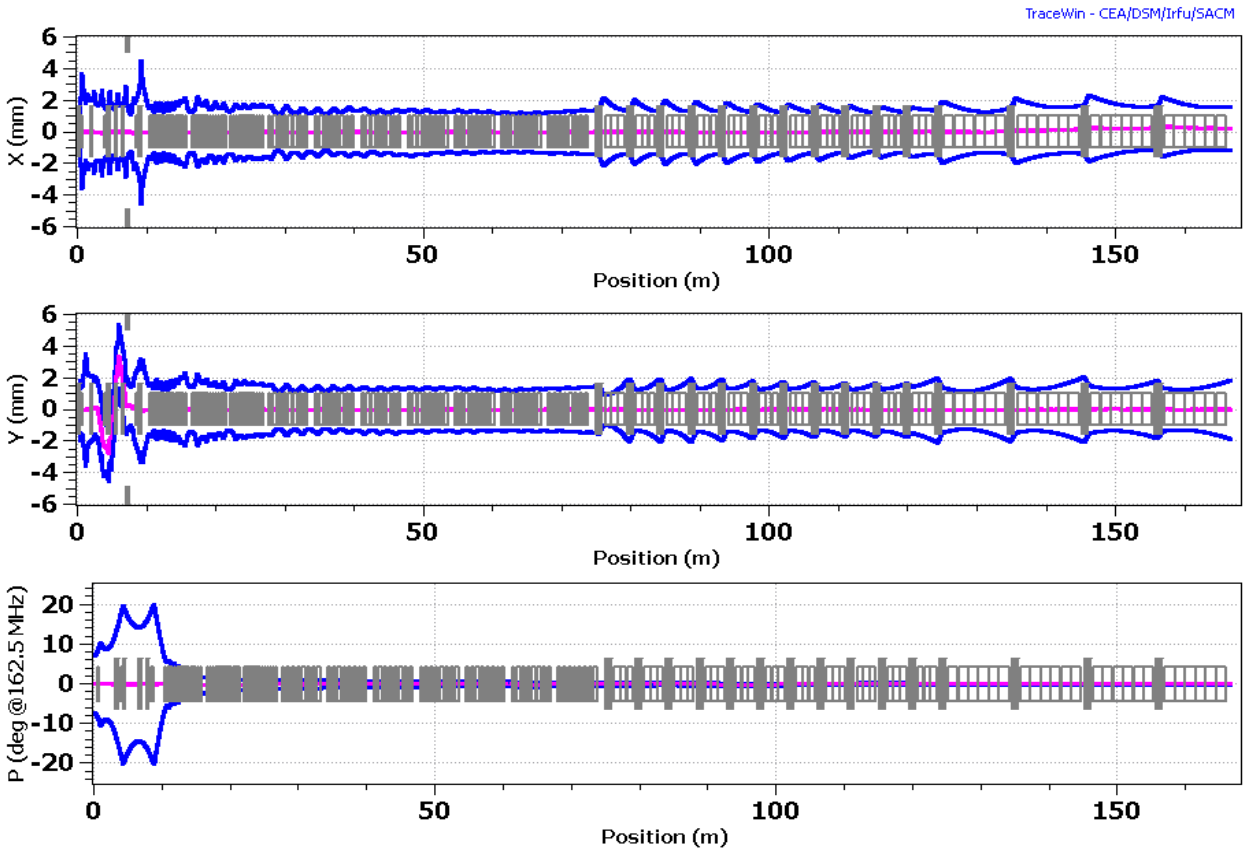

Figure 2.16: Horizontal (top) and vertical (center)) rms bunch envelopes and rms bunch length (bottom) along entire linac (from beginning of MEBT to the end of 0.8 GeV linac); bunch population corresponds to the RFQ beam current of 5 mA. Magenta lines show displacements of the bunch centroid.

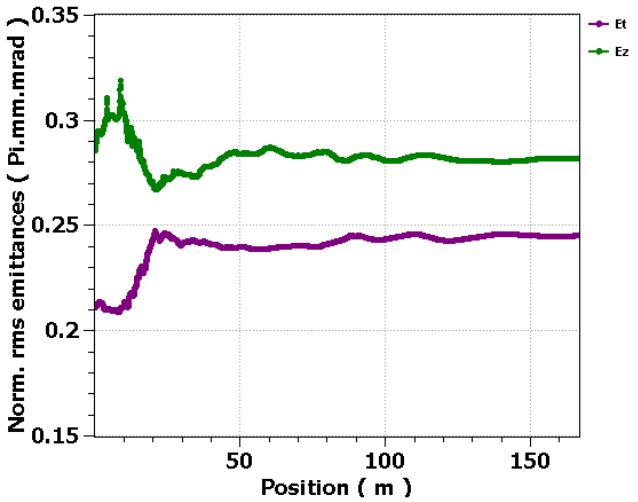

Figure 2.17: Rms normalized transverse (magenta, $\varepsilon_x=\varepsilon_y$) and longitudinal (green) emittances along the linac (from the RFQ exit to the linac end); the beam optics is the same as for Figure 2.16.

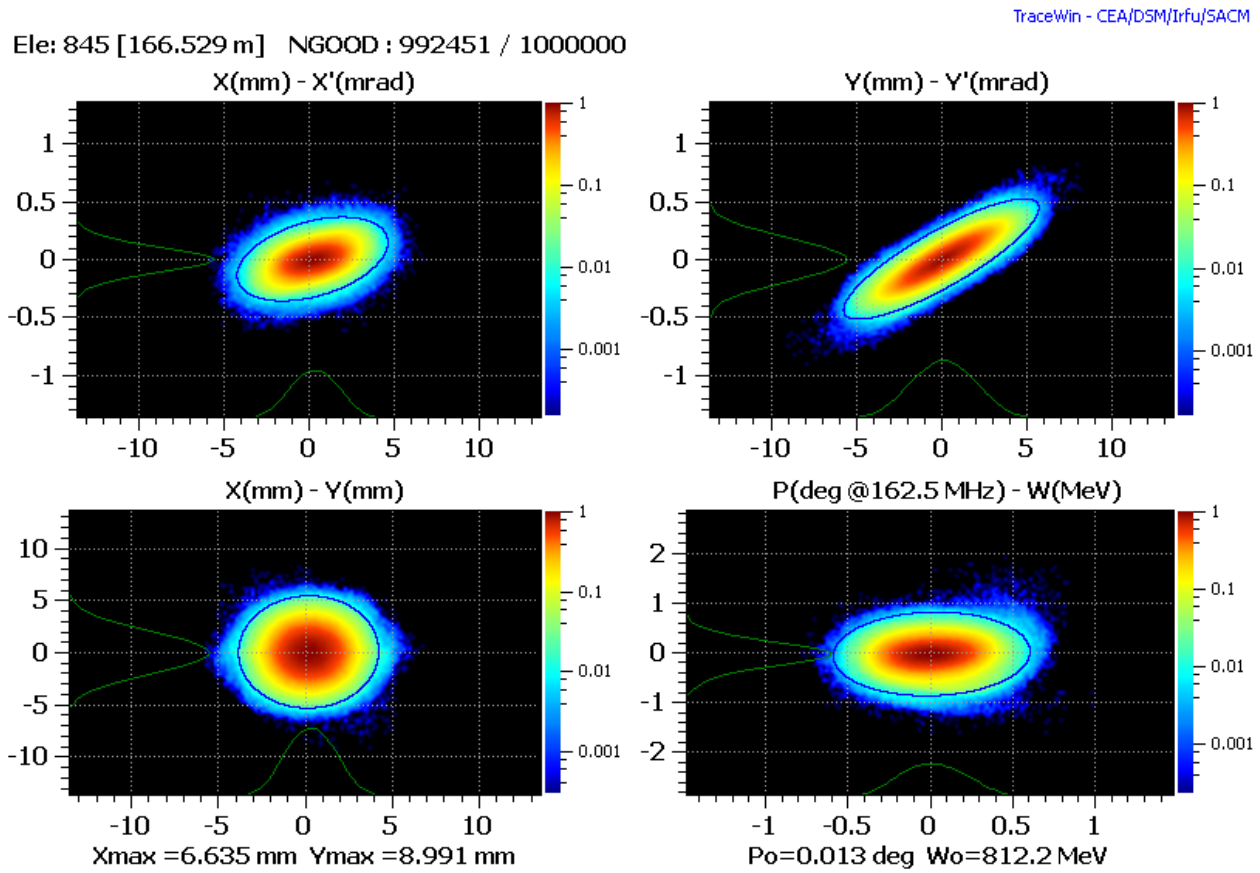

Figure 2.18: Phase space density of a bunch at the linac end; the beam optics is the same as for Figure 2.16.

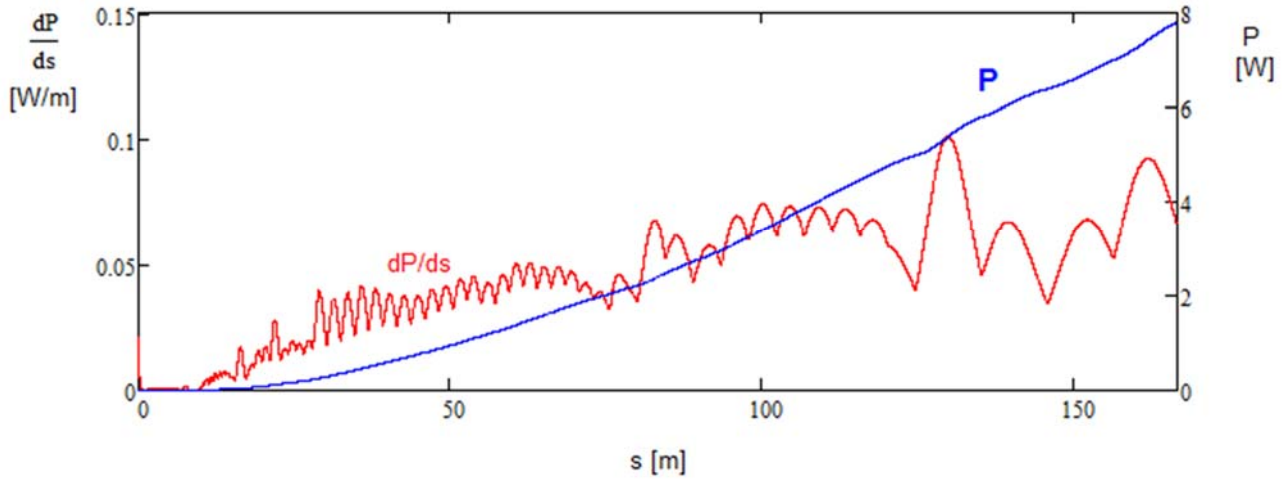

Figure 2.19: The beam power loss per unit length caused by intrabeam stripping (red) and its value integrated along the linac (blue); RFQ beam current 5 mA, CW beam of 2 mA in the SC Linac (60% of bunches RFQ bunches are chopped off).

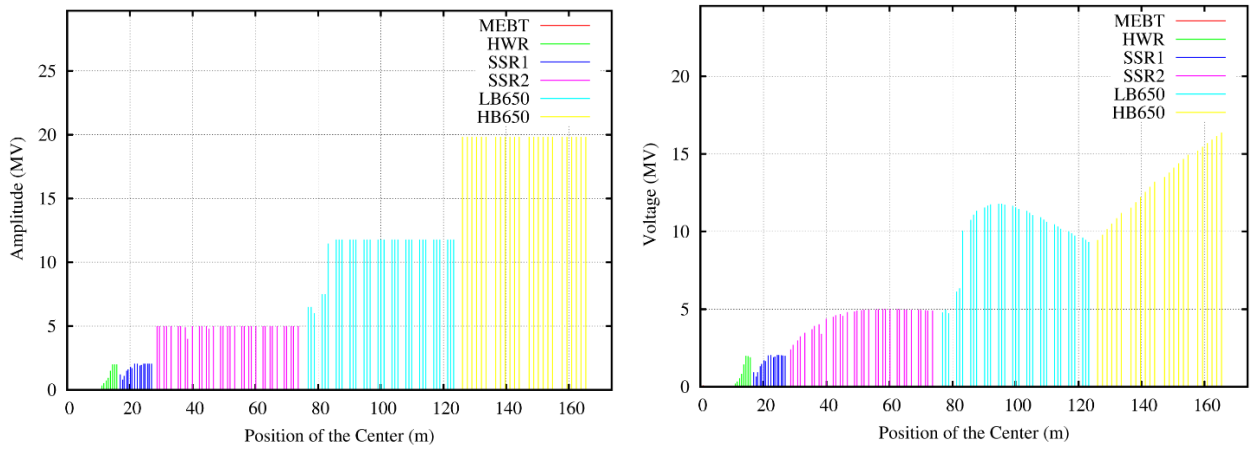

Figure 2.20: Accelerating voltage per cavity along the SC Linac corresponding to the beam optics used for Figure 2.16; left – the voltage amplitude at the optimal beta, right – the voltage amplitude with the transit-time factors accounted.

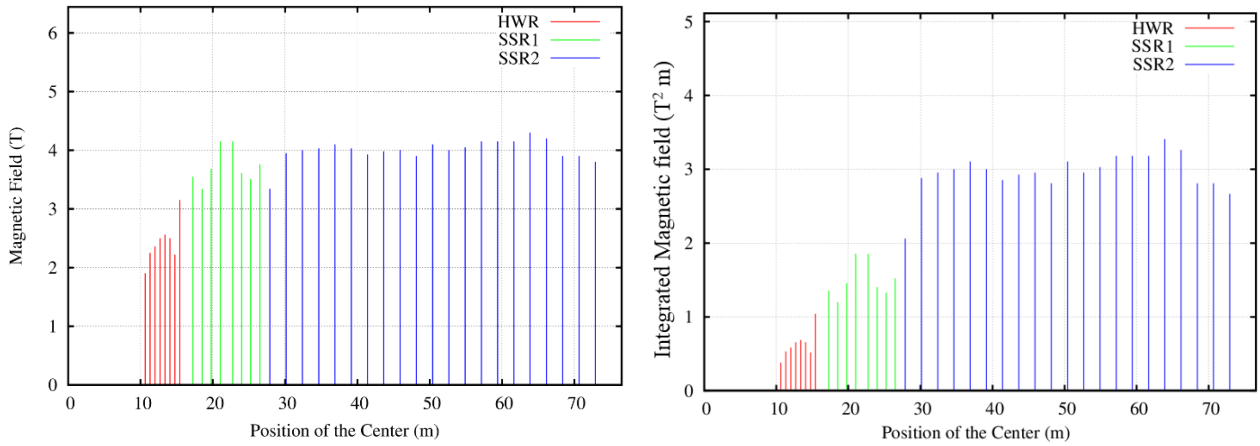

Figure 2.21: Magnetic field of focusing solenoids (left) and their integral strength (right) along the linac corresponding to the beam optics used for Figure 2.16.

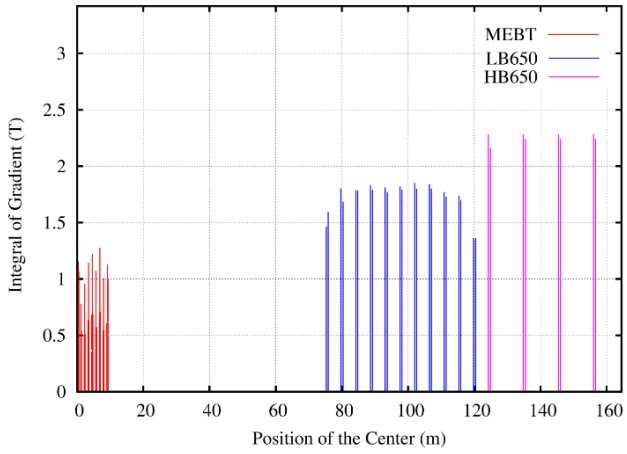

Figure 2.22: Integral strength of quadrupoles along the linac corresponding to the beam optics used for Figure 2.16.

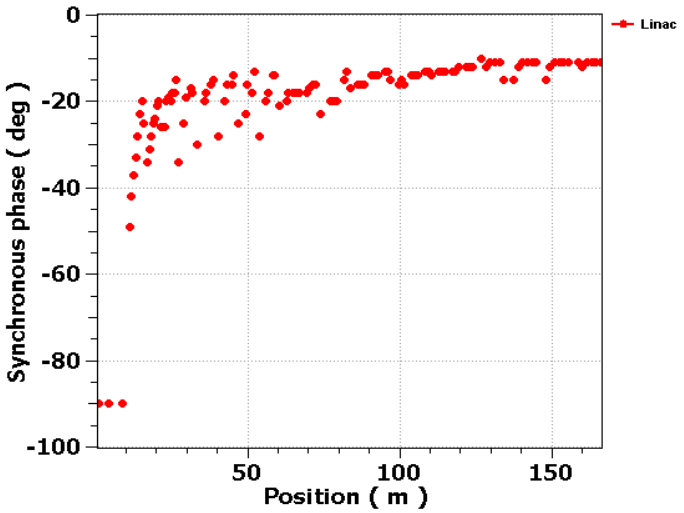

Figure 2.23: Accelerating phase along the linac corresponding to the beam optics used for Figure 2.16. The first three dots belong to the MEBT bunching cavities, which do not produce acceleration.

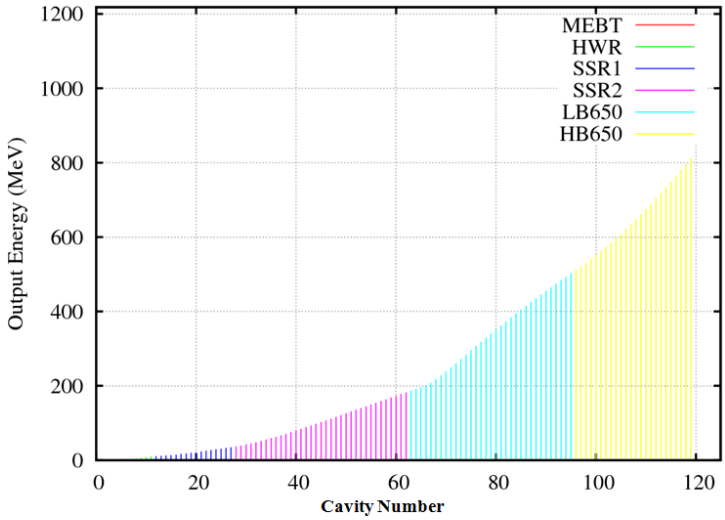

Figure 2.24: The beam energy along the linac.

As one can see from Figure 2.16 the transverse rms beam sizes change comparatively little along the linac, and their values do not exceed 3 mm; *i.e.* the beam size reduction due to adiabatic damping with beam acceleration is compensated by corresponding increase in the beta-functions. Figure 2.26 presents the beam density projection to the *x*-plane and the aperture limitations along the linac. For the HWR, SSR1, and SSR2 cryomodules, the aperture is limited by apertures in the SC cavities of 33, 30 and 40 mm, respectively. For the LB650 and HB650 cryomodules, the cavity apertures are 83 and 118 mm, correspondingly. They are sufficiently large and the aperture limitations are determined by the aperture of the vacuum pipe in the quadrupoles of 46 mm (standard 2" pipe). As stated above, in the case of a well-tuned machine the intrabeam stripping represents the main source of beam loss. To avoid the beam losses to cryogenic surfaces fixed aperture beam collimators are installed between each cryomodule for HWR, SSR1, and SSR2. Apertures in the collimators are chosen to be 5 mm smaller than the apertures of the downstream cryomodules. Their thickness increases with energy, reaching 4 cm of steel at the end of SSR2 section. There are no dedicated collimators in the LB650 and HB650 sections. As in the SNS, the vacuum chambers in the quadrupoles will perform this role.

Taking into account the comparatively small beam losses it appears unnecessary to have additional radiation shielding around the collimators which otherwise would require quite a large amount of shielding material.

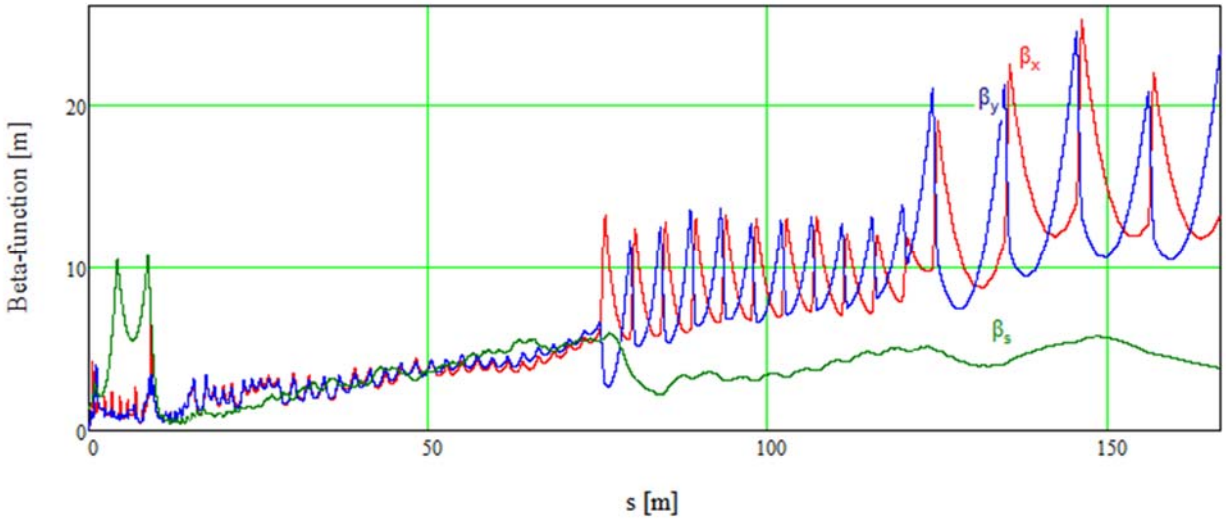

Figure 2.25: The beta-functions for x,y and s planes. The values were computed from rms beam sizes and emittances obtained by beam tracking with TraceWin for 5 mA RFQ current.

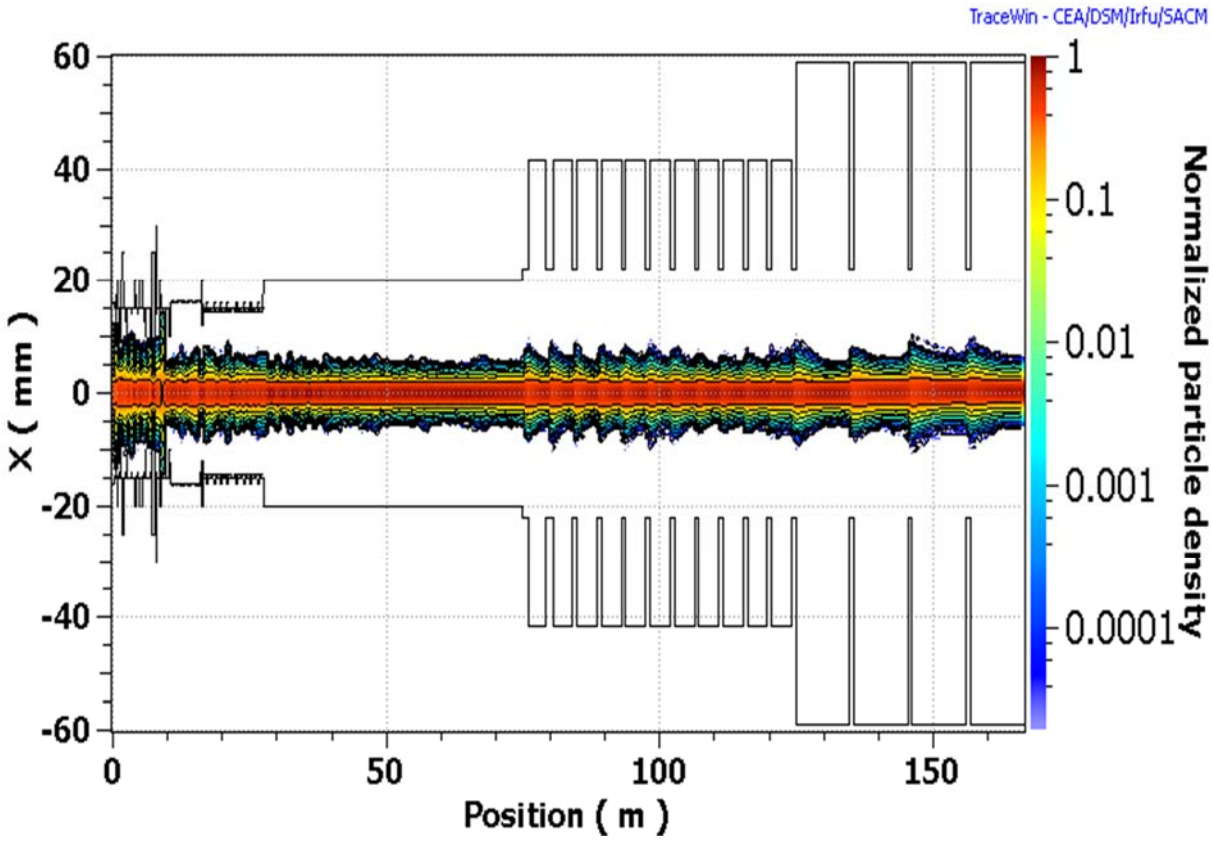

Figure 2.26: Beam density projection to the *x*-plane and aperture limitations along the linac from RFQ exit to the linac end.

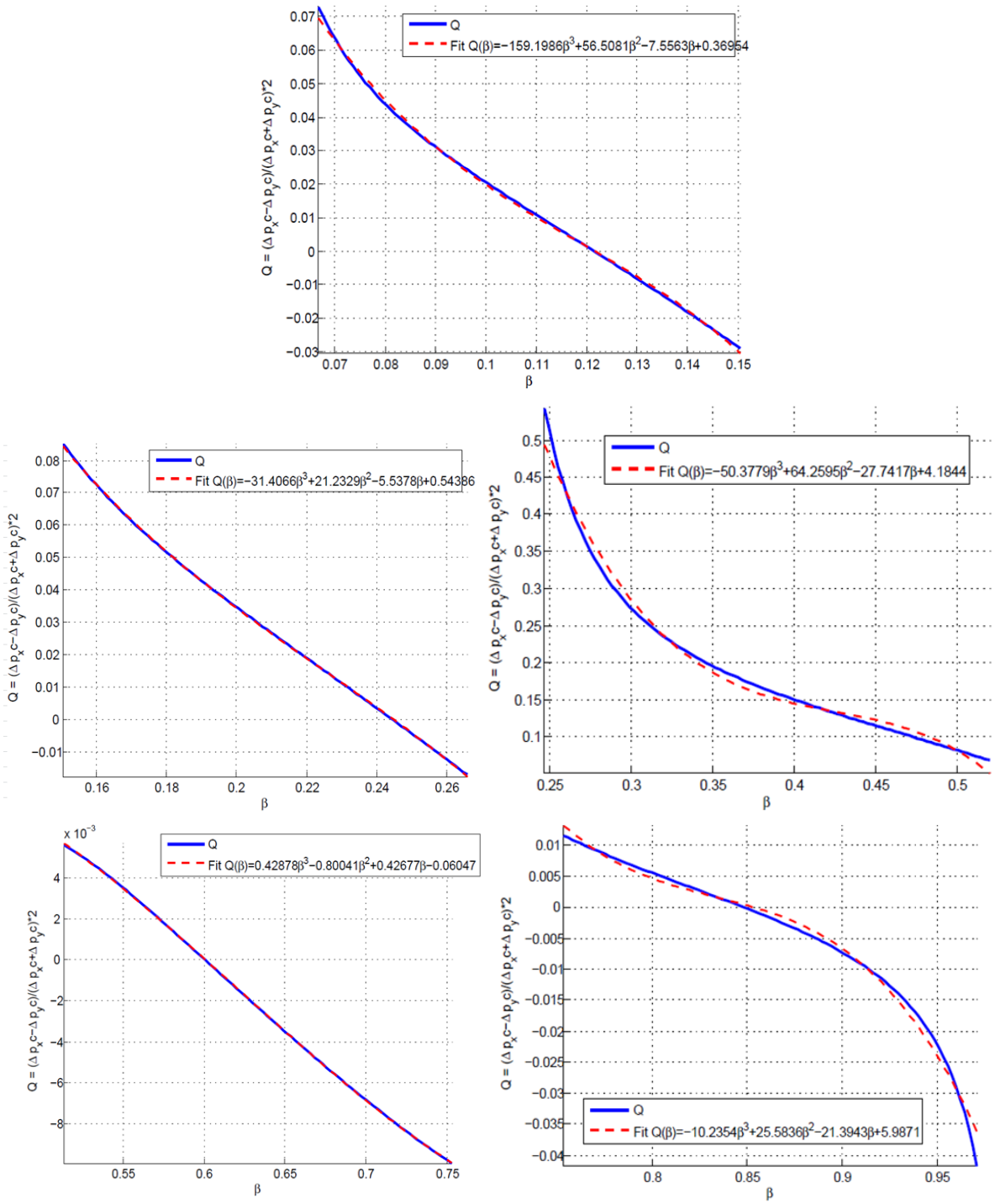

Figure 2.27. Ratio of quadrupole focusing to axial symmetric focusing for HWR (top), SSR1 (middle-left), SSR2 (middle-right), LB650 (bottom-left) and HB650 (bottom-right) versus the particle velocity β in the operating domain; blue and red lines present simulation results and a polinomial fit, respectively.

The HWR, SSR1 and SSR2 cavities are not axially symmetric. Therefore, their quadrupole components cannot be compensated over the entire range of cavity operation. Figure 2.27 presents the dependence of the quadrupole effect on the beam velocity. Numerical simulations verified that in the range of PIP-II parameters the strength of quadrupole field is proportional to the strength of

axially symmetric cavity defocusing and, consequently, is proportional to the sine of accelerating phase. That determines the definition of parameter Q presented in Figure 2.27. The stem in the HWR cavity is located in the horizontal plane and therefore this quadrupole field represents a normal quadrupole. Due to engineering limitations, mainly related to the RF couplers, the SSR1 and SSR2 cavities are rolled by 45°. Consequently, their quadrupole fields are also rolled and are equivalent to a skew-quadrupole field. The cavity quadrupole and skew-quadrupole fields have comparatively small effect on the beam dynamics. To compensate these fields the SSR1 and SSR2 cryomodules will have skew-quadrupole correction coils located inside the focusing solenoids. The skew-quadrupole field will be created by a imbalance in the currents of independently powered coils of x- and y-dipole correctors. Note that the focusing solenoids located in the HWR, SSR1 and SSR2 cryomodules rotate the plane of betatron motion. That allows one to improve quality of compensation by choice of appropriate signs of the magnetic fields in solenoids. The HWR cryomodule has eight cavities, which introduce sufficiently small coupling between x- and y-planes. Therefore, the HWR cryomodule does not have coupling correction.

The quadrupole fields in the LB650 and HB650 cavities are related to the RF couplers. Compared to the HWR, SSR1 and SSR2 they are significantly smaller as can be seen in the bottom row of Figure 2.27. These quadrupole fields will be corrected by the main focusing quadrupoles located between cryomodules. The RF couplers of LB650 and HB650 cavities also create dipole fields resulting in dipole kicks which values are also dependent on the beam velocity. The peak values of the kick, $\Delta p_{\perp} c$, are about 3.6 keV for LB650 and 2.6 keV for HB650 cavities. These values are small and are not expected to produce any visible effect on the beam motion in the linac. The final coupling accumulated in the linac is corrected by four skew-quadrupoles located at the linac end near the first two doublets immediately following the last cryomodule and nearby doublet.

2.1.5. Fault Scenarios in SC Linac

An essential characteristic of a successful accelerator is its ability to deliver a high quality beam with high beam availability. The SC linac includes numerous elements and their continuous operation represents a great challenge. There are non-zero probability of their temporary or permanent failures. In this section we consider ways to mitigate such failures.

Failure of the beam transport elements like cavity, solenoid or quadrupole alters the periodicity of beam focusing, resulting in a mismatch of beam transport with downstream sections. This, in turn, may degrade beam quality and, in the worst case, may cause beam losses. Implications of failures on the overall machine performance depend on failure locations. In some cases, a faulted element results in significant beam losses, and, if the machine cannot be retuned to an acceptable state, it becomes necessary to replace this element to continue nominal operation. In a superconducting linac, a cryomodule replacement can be required to fully recover its performance. It is a long process requiring a cryomodule warmup to the room temperature with subsequent cooldown after repair. In order to improve reliability, optics design should be capable to deal with at least one major fault in each section. An extensive study has been performed to address this problem for the PIP-II SC linac. Below we discuss failure of beamline elements at critical locations and demonstrate that the optics design of the PIP-II SC linac is sufficiently robust to compensate for failure of a cavity or cryomodule by retuning nearby elements.

Failure of Beamline Elements

Failures of beamline elements can be placed in two categories, temporary failures and permanent failures. As the name suggests the temporary failures are recoverable after applying appropriate

mitigation measures. Quenching of a SC cavity and vacuum breakdown represent typical temporary failures. Normally such failures do not require linac retuning and can be resolved comparatively quickly. A permanent failure results in that one or more elements become malfunctioning and have to be withdrawn from operations. In this case, retuning of the machine, if possible, can be the most efficient way to maximize machine availability. Such action implies that repairs will be done later when conditions allow. The most probable permanent failures are expected to be:

- Failure of a cavity tuner resulting inability to keep this cavity in the resonance and making this cavity unavailable for beam acceleration;
- Malfunctioning of the power-coupler resulting in loss of accelerating gradient or inability to use this cavity;
- Failure of a RF power supply requiring its repair;
- Degradation of Q_0 can result in reduced voltage;
- Failure of a focusing magnet due to a problem with its coil (electrical insulation, quenching, non-functioning power supply, *etc.*).

In the following sub-sections we discuss permanent failures of accelerating cavities and focusing magnets at critical locations in the PIP-II SC linac.

Local Compensation of Failed Elements

As will be seen in the following sections, a failure of a beamline element excites longitudinal and transverse mismatches leading to emittance growth and beam losses in the downstream part of the linac. In order to restore the beam quality, a local compensation is used. That involves adjustments for settings in nearby elements. The procedure is aimed at minimization of excessive oscillations of the bunch sizes. Separate powering for each cavity and solenoid is greatly helpful for achieving this objective. The constraints and assumptions used for local compensation are summarized below:

- Accelerating field in cavity: fields are varied to recover the beam energy but the corresponding surface peak magnetic and electric fields in a cavity should not exceed their design limits.
- Integral fields in quadrupoles and solenoids should not exceed their design limits.
- Synchronous phases of cavities are varied in such a way that the ratio of synchronous phase to longitudinal rms beam size should be greater than 3. It is required to achieve sufficiently large longitudinal acceptance to accommodate 3σ beam.
- A minimum number of retuned elements should be used in order to expedite retuning and to minimize overall effort.
- 100% beam transmission and minimal emittance growth at the linac end has to be achieved.

Failure of the First HWR Accelerating Cavity and its Local Compensation

The HWR is the first SC section in the PIP-II linac. It accelerates and focuses the beam coming out of the MEBT. Each focusing period in the HWR section includes a solenoid and a HWR cavity. A failure of the first cavity in the HWR section is considered to be the most serious due to large transverse and longitudinal beam sizes at this location. The beam is non-relativistic with initial energy of 2.1 MeV, and therefore a failure of the first HWR cavity, if uncompensated, results in phase and energy mismatches propagating downstream and growing in amplitude along the linac. Furthermore, the space charge forces are quite large resulting in an amplification of beam losses. Figure 2.28 shows the rms longitudinal and transverse beam sizes along the linac after failure of the first HWR cavity. Abrupt changes in the longitudinal beam profile indicate a location of beam losses

mainly located at transitions between cryomodules. The total beam losses below 0.01 % are observed in the SC linac after failure of the first HWR cavity. The momentum mismatch results in a perturbation of transverse motion. However, as can be seen from Figure 2.28, the transverse beam sizes have comparatively small perturbations. It is related to the small energy gain in the first HWR cavity. This cavity operates at half of nominal voltage and has a large accelerating phase offset from on-crest acceleration in order to capture the beam with large longitudinal emittance.

Figure 2.29 shows normalized rms transverse and longitudinal emittances along the linac. The abrupt change in the longitudinal emittance is related to the beam losses at beginning of the LB650 section. The longitudinal emittance decreases swiftly after beam losses. Conversely, there is no significant transverse emittance growth along the linac.

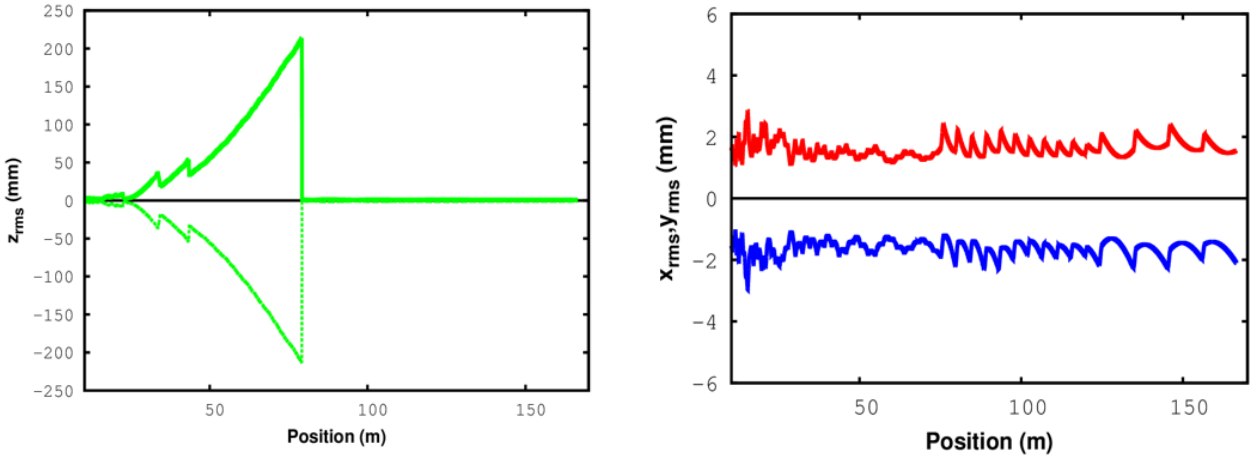

Figure 2.28: Longitudinal (left) and transverse (right) rms beam sizes along the linac (starting at the MEBT end) after failure of the first HWR cavity (horizontal – red, negative vertical - blue).

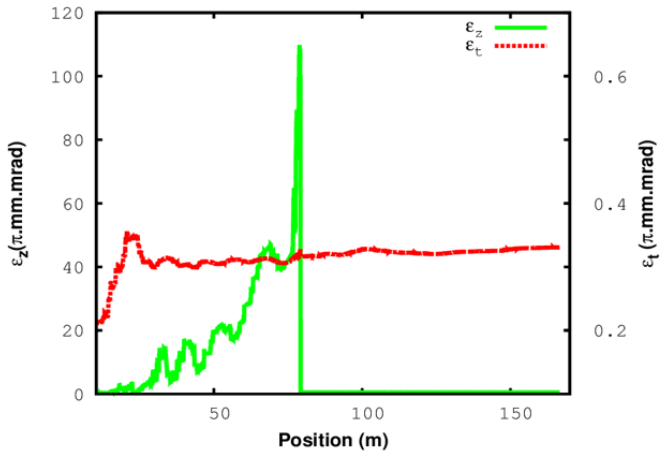

Figure 2.29: Normalized rms longitudinal (green, left scale) and transverse (red, right scale) emittances along the linac after failure of the first HWR cavity.

Figure 2.30 presents results of an application of local compensation used to restore the beam quality. The figure shows the rms bunch sizes and the elements used in the retuning: the last bunching cavity at MEBT and the three HWR cavities downstream of the failed cavity. Additionally, the two subsequent HWR cavities are retuned to recover the beam energy. This prevents excessive bunch size oscillations in the downstream linac without its retuning.

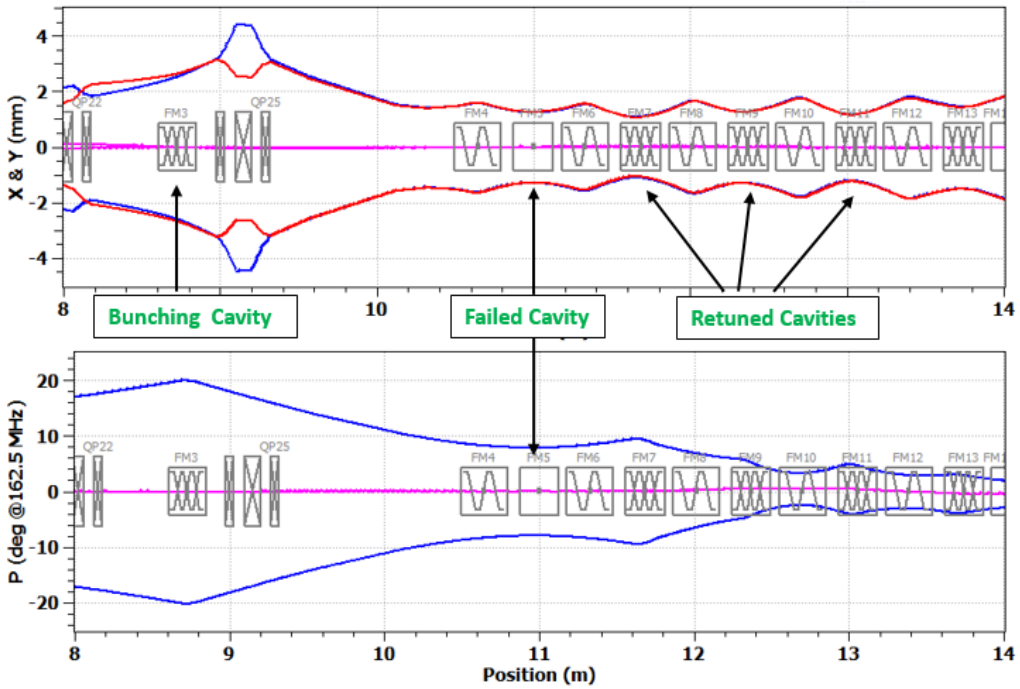

Figure 2.30: Enlarged view of beam profile in the transverse (top) and longitudinal (bottom) planes after applying local compensation of a first HWR cavity failure. Elements used for retuning are pointed out by arrows.

Figure 2.31 presents the bunch envelopes for the entire linac with and without compensation. As can be seen, both the transverse and longitudinal envelopes are completely recovered, and there is no beam losses. Figure 2.32 shows the synchronous phases and the longitudinal beam size. As one can see the longitudinal acceptance is large enough to accommodate 6σ beam. The left pane in Figure 2.33 shows the normalized rms longitudinal emittances before and after compensation. Note that the emittance after compensation is plotted for the secondary *y*-axis. The compensation resulted in smaller emittances; and there is no significant emittance growth in all planes after applying the local compensation. Table 2.12 presents a comparison of beam emittances at the linac end for different cases.

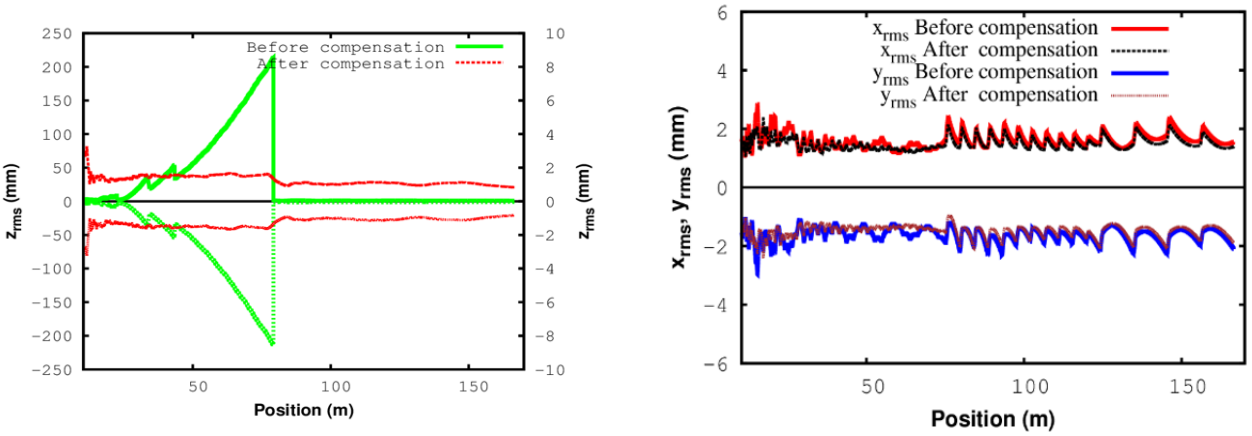

Figure 2.31: Longitudinal (left) and transverse (right) beam sizes along the linac before and after applying local compensation for a failure of the first HWR cavity.

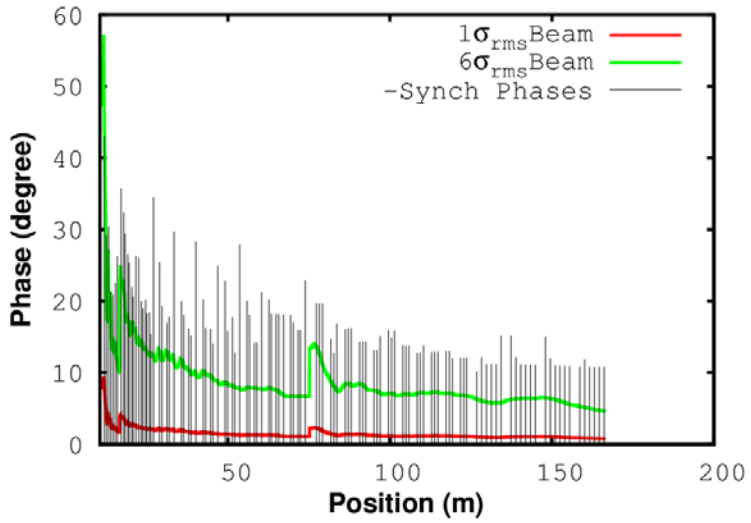

Figure 2.32: Synchronous phases with longitudinal beam size along the PIP-II SC linac.

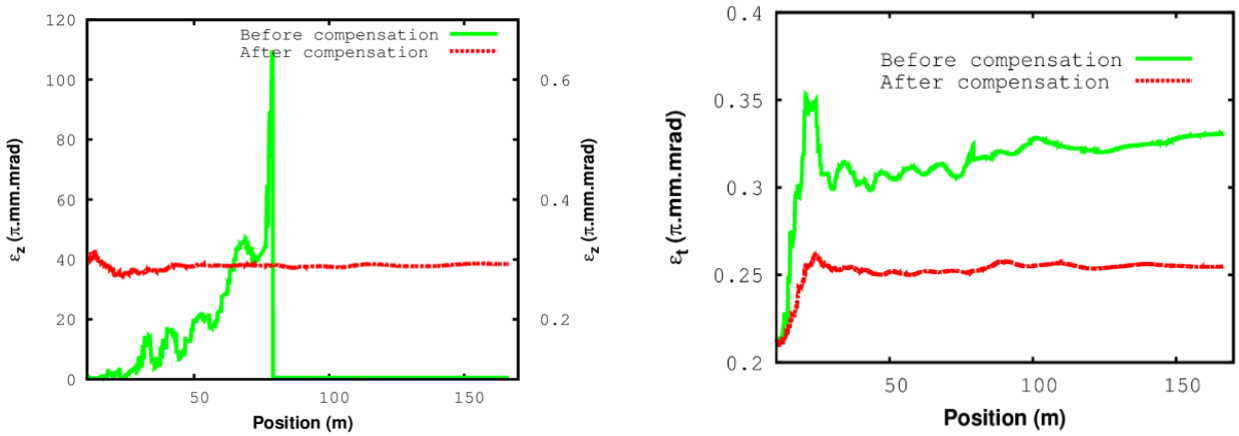

Figure 2.33: Normalized rms longitudinal (left) and transverse (right) emittances along the linac in the presence of first failed HWR cavity. The picture on the left has different scales for the emitances with and whithout compensation.

Table 2.12: Final normalized rms beam emittances

Parameters	Unit	Nominal	Failure of first HWR cavity	
			No Comp.	After Comp.
ε_z	mm mrad	0.28	0.52	0.29
ε_t	mm mrad	0.25	0.33	0.25

Failure of the First Solenoid in the HWR Section and its Local Compensation

At the beginning of the linac the transverse beam size is relatively large and the beam barely fits in the physical aperture. Thus, a failure of the first solenoid in the HWR section is as critical as a failure of the first HWR cavity. It results in transverse beam size oscillations with large amplitude leading to emittance growth and beam losses. Local compensation is applied by using the same approach as discussed above - the neighboring elements are retuned to achieve a smooth beam profile along the linac. Figure 2.34 shows beam envelopes before and after applying the local compensation.

The figure demonstrates that the transverse beam oscillations are minimized and the transverse beam profiles are restored. Figure 2.35 shows the corresponding normalized rms emittances before and after applying this compensation.

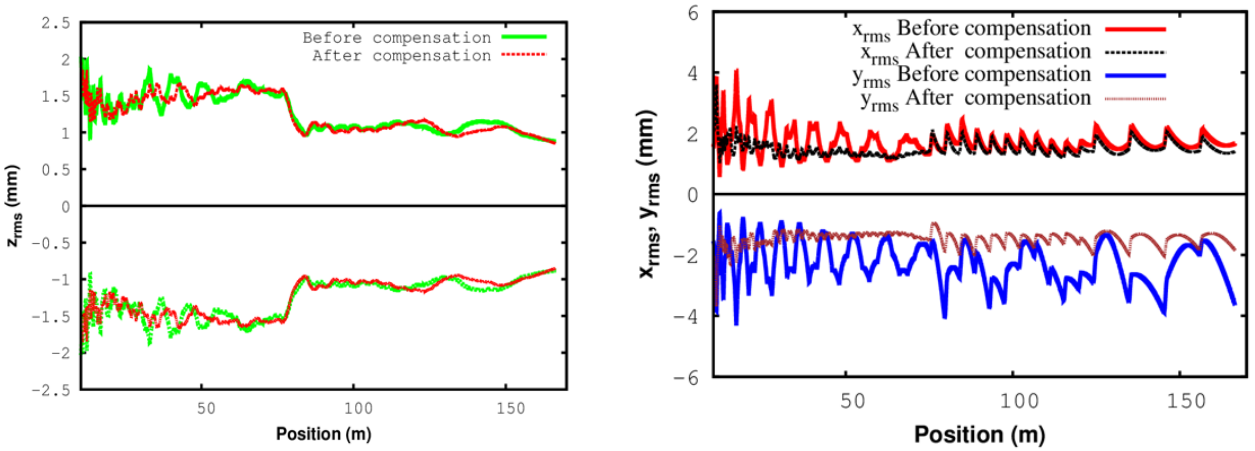

Figure 2.34: Longitudinal (left) and transverse (right) beam sizes along the linac before and after applying a local compensation to a failure of the first solenoid in the HWR section.

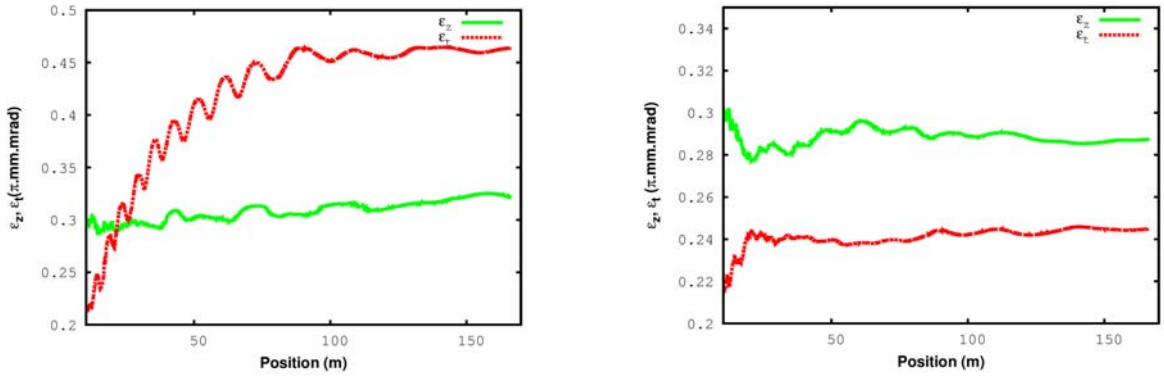

Figure 2.35: Beam emittance growth along the linac before (left) and after (right) applying the local compensation to a failure of the first solenoid in the HWR section.

Failure of the Last Cavity in the HWR section and its Local Compensation

The HWR section is followed by the SSR1 section. There is a short warm section separating the HWR and SSR1 cryomodules. Beam matching is performed using nearby elements of each cryomodule to achieve a smooth beam profile around the transition. Accelerating gradients and synchronous phases in cavities are used to adjust the longitudinal beam profile, while focusing strengths of solenoids are changed to achieve matching conditions in the transverse planes. The left pane in Figure 2.36 shows rms longitudinal beam envelope along the linac after failure of the last HWR cavity. Beam oscillations are observed after the failed cavity. However, a smooth beam profile is obtained after applying the local compensation scheme. It can also be noticed from the right pane in Figure 2.36 that longitudinal emittance is restored after applying the local compensation.

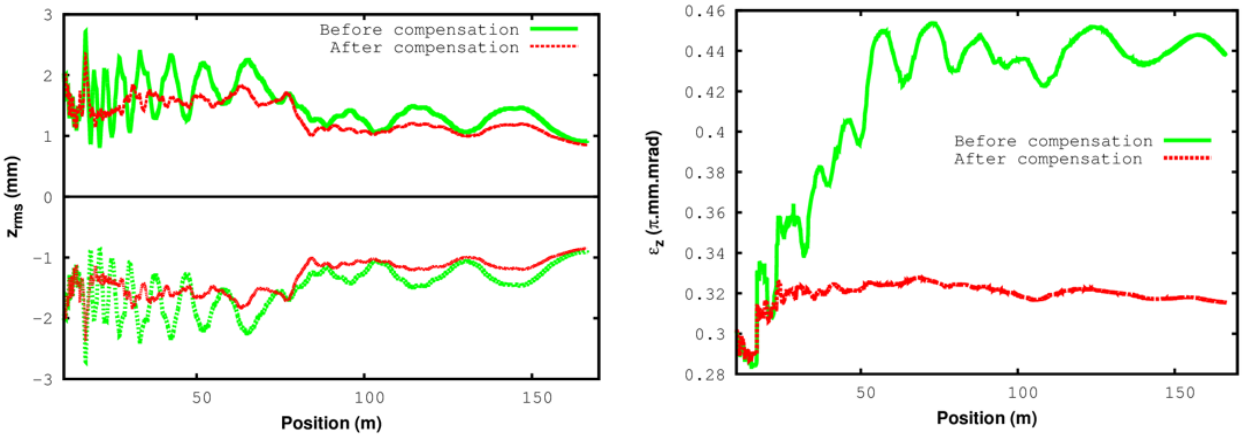

Figure 2.36: Longitudinal rms beam envelopes (left) and normalized rms emiitances (right) along the linac before and after applying the local compensation to the failure of the last HWR cavity.

Failure of the Last Solenoid in the HWR section and its Local Compensation

It was found that a failure of the last Solenoid in the HWR section represents one of the most dangerous situations with ~13% beam losses immediately downstream. The center-to-center distance between the last solenoid in the HWR section and the first solenoid in the SSR1 section is about ~1.82 m. A failure of the last HWR-solenoid increases the length of beam transverse focusing cell to 2.51m. This change in the length and the resulting mismatch due to the absence of focusing lead to a beam envelope instability. However, local compensation allows one to restore the beam quality. Figure 2.37 shows the rms beam envelopes and transverse emittance before and after applying the local compensation.

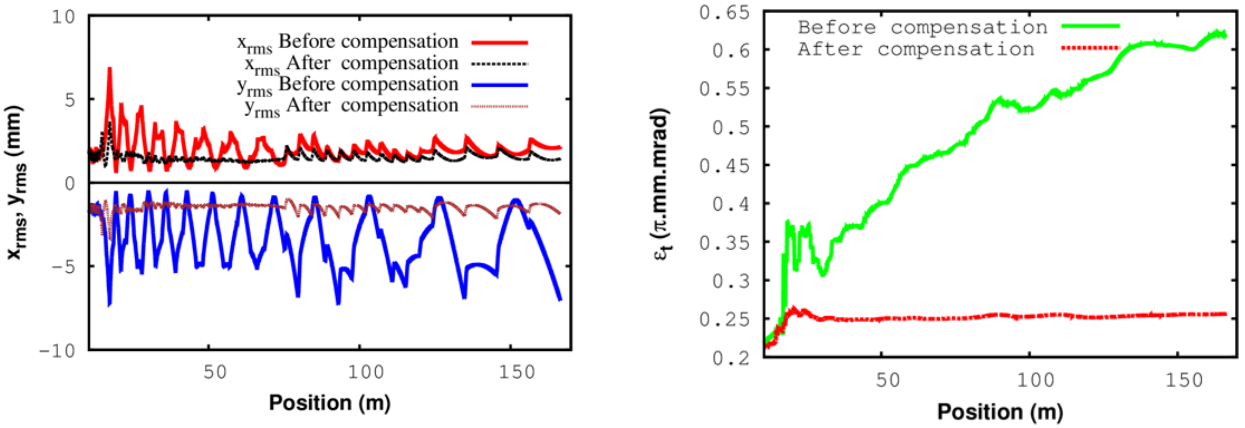

Figure 2.37: Rms transverse beam sizes (left) and normalized rms beam emittances (right) before and after applying the local compensation to failure of the last solenoids in HWR section.

Failures at other Critical Locations

As the beam energy increases, the machine performance becomes more immune against a single element fault. Higher beam energy reduces the impact of non-linear space charge forces as well as a focusing effect of a single element. The amplitude of synchrotron oscillations also decreases with increase in the beam energy. That reduces the possibility of phase slippage. A study was performed to analyze the performance of the linac in the presence of failed elements at higher energy but in critical locations. The transition from SSR2 to LB650 section is considered to be a vulnerable

location in the linac because of two major reasons:

- Solenoidal focusing in SSR2 is replaced by focusing with quadrupole doublets in the LB section.
- A frequency jump from 325 to 650 MHz occurs at this transition.

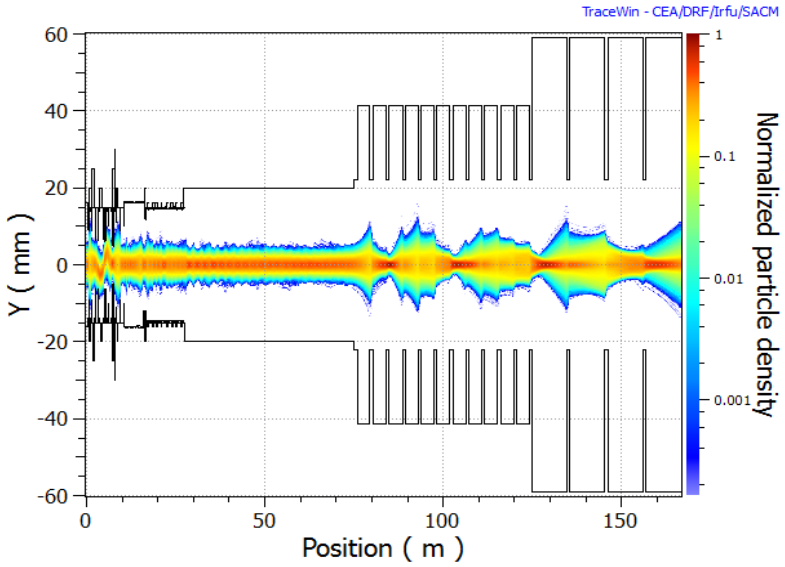

Figure 2.38: Normalized vertical particle density along the linac after a falure of the first quadrupole doublet at the SSR2 to LB650 transition.

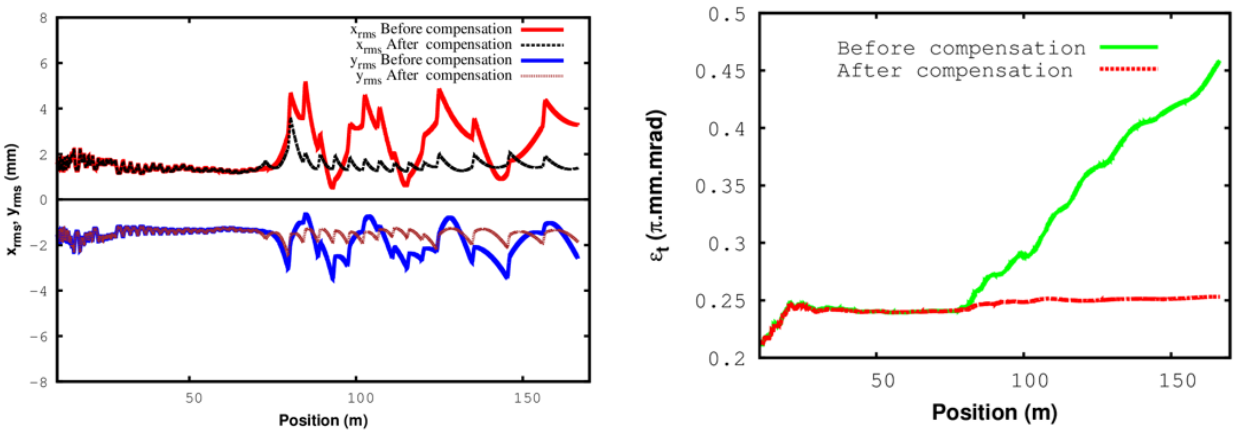

Figure 2.39: Beam transverse sizes (left) and normalized rms transverse emittances (right) before and applying local compensation for a fault of the first quadrupole doublet at the SSR2 to LB650 transition.

Although a replacement of a failed normal conducting quadrupole is much simpler and faster than for a SC solenoid, a study was performed to evaluate performance of the linac in the presence of a failed quadrupole. In this study, we assumed that after failure of one quadrupole in a doublet, the remaining quadrupole is also turned off. Figure 2.38 shows the normalized beam density in the vertical plane along the linac for the case when the first quadrupole doublet in the LB section has failed. One can observe mismatch in the beam profile. However, the physical aperture in the downstream sections is sufficiently large to accommodate the oversized beam. One can see that there is still significant margin (ratio of beam aperture to maximum beam size) even for 6σ beam. Local compensation is applied to restore the beam quality. Figure 2.39 shows the beam transverse

envelopes and the normalized rms emittances.

A study performed to evaluate implications of cavity failure in the LB section shows no beam losses even after failure of the first complete LB 650 cryomodule. However, the beam energy is reduced to 786.5 MeV and the final normalized rms longitudinal emittance is increased to 0.38 mm mrad.

2.2. Linac-to-Booster Beam Transport

2.2.1. Particle Loss and Limitations on Beam Transport Parameters

A low loss beam transport is critical in the operation of a MW class facility. The H^- transport should have sufficiently small losses to minimize residual radiation in the tunnel. It is highly desirable to keep the residual radiation level below 15 mrem/hr at 30 cm from component surface. Many facilities use the metric of 1 W/m as a limit for "hands on" maintenance; however, at energies about or above 1 GeV, a 1 W/m loss rate produces a peak contact residual dose rate of ~150 mrem/hr at 30 cm on a bare beam pipe [24]. Although magnets shield the radiation and significantly reduce the residual activation on their external surfaces, the radiation of unshielded pieces including magnet interfaces and instrumentation locations has to be sufficiently small. That sets the maximum acceptable loss rate. Setting a desirable activation level to 15 mrem/hr at 30 cm results in a loss goal of ~0.1 W/m at energies about or above 1 GeV. Initial Linac operation will be in a pulsed regime where the total beam power is about 18 kW. Consequently, a fractional loss rate of 5×10^{-6} m^{-1} is required. Future CW operation will require a fractional loss rate limit of about 5×10^{-8} m^{-1}.

The primary loss mechanisms for 0.8 GeV transport are the H^- intrabeam stripping, Lorentz stripping, inelastic beam-gas scattering, and scraping of beam halo on the apertures. Stripping due to black-body radiation inside the room temperature beam pipe is negligible at this energy.

As shown in Figure 2.19, the intrabeam stripping in the Linac results in an acceptable loss rate even in the case of CW beam. The strength of transverse focusing in the beam line is similar to the focusing strength at the Linac end. Consequently, the beam loss at the transfer line beginning is close to the beam loss at the linac end. The particle momentum spread leads to natural debunching in the course of beam transport from Linac to Booster. It results in a bunch length increase by more than an order of magnitude (from 1.1 mm to about 14 mm), and, consequently, a reduction of intrabeam stripping inversely proportionally to the bunch length resulting in a negligible intrabeam stripping loss of about 100 μW/m at the transport line end for 1% duty factor. Note that this 1% duty factor is used for the beam injection to the Booster and the major part of the line sees this beam only; while the initial part of this line is also planned to be used for beam transport to an upgrade of the Mu2e experiment requiring 100 kW beam (see Appendix A). Consequently, a maximum beam loss of up to 5 mW/m is expected.

Beam motion in a magnetic field excites an electric field in the beam frame. If this electric field is sufficiently strong, it can detach a weakly bound outer electron (Lorentz stripping) from the H^- ion. The results of experimental measurements for H^- lifetime are presented in Ref. [25] and can be approximated by the following equation:

$$\tau_E(E) = \frac{A_\tau}{E} e^{B_\tau/E} \ , \qquad (2.8)$$

where the constants are A_τ=2.47·10^{-8} s V/cm, B_τ=44.94·10^6 V/cm. Figure 2.40 shows the corresponding loss rates per meter for a 0.8 and 1 GeV H^- beams as a function of magnetic field. The magnetic field in the dipoles of the transfer line is chosen so that the loss rate would not exceed 10^{-8} m^{-1} for a beam of 1 GeV energy. This corresponds to a limit of 2.77 kG equivalent to a bending radius of 20.431 m. Keeping the same radius of curvature for the 0.8 GeV beam one obtains a limit for the magnetic field in the dipoles of 2.39 kG with a loss rate of $3\cdot10^{-13}$.

The loss rate due to H^- scattering on residual gas molecules is proportional to their density and their ionization cross sections. The cross sections decrease proportionally to β^{-2} and therefore are weakly dependent on the beam energy for energies about or above 1 GeV. The cross section of H^-

stripping for 0.8 GeV beam on residual gas is about 10^{-19} cm^2 for atomic hydrogen and $7 \cdot 10^{-19}$ cm^2 for atomic oxygen and nitrogen and grows somewhat slower than proportional to Z for heavier atoms [26, 27]. The requirement of less than 10^{-8} m^{-1} for the partial loss rate yields a vacuum requirement of 10^{-8} Torr or better for H_2 and about an order of magnitude better for heavy molecules (hydrocarbons, water, etc.). Consequently, an application of vacuum practices developed at Fermilab for not-baked vacuum systems, which routinely achieve low 10^{-8} Torr, should be sufficient.

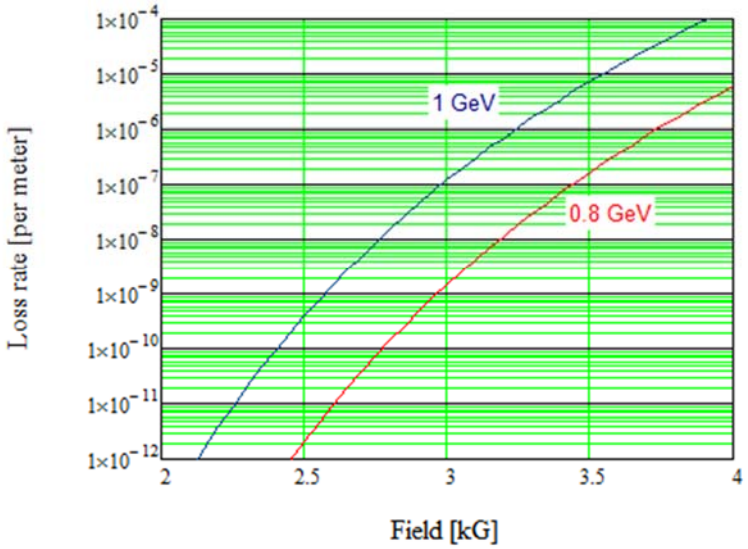

Figure 2.40: Fractional loss due to Lorentz stripping for 0.8 and 1 GeV H$^-$ beams traveling in a dipole field.

2.2.2. Linac-to-Booster Transfer Line

The Linac-to-Booster Transfer Line transports the beam from the exit of the SC Linac to the injection girder of the Booster. Figure 2.41 presents the transport line layout. The transport line has two arcs and the straight section connecting them. In this straight section the Booster line splits into two additional lines. One goes to the linac beam dump and the other one goes to the Mu2e experiment which future upgrade is expected to receive 800 MeV beam from the SC linac.

As can be seen in Figure 2.41 the second arc crosses the Tevatron tunnel. In the vicinity of this crossing, the line has a local vertical bump bringing the line close to the Tevatron tunnel ceiling. It is done to allow a free passage for people and equipment along the Tevatron tunnel, which contains the operating 120 GeV transfer line. This line brings beams extracted from the Main Injector to the Fermilab Test Beam Facility and is scheduled to be still in use at the time of PIP-II operations.

The SC Linac beam is at the same elevation as the Booster beam; that is 726.48 ft. (221.431 m) above sea level. The Linac beam is at 1.300 m above the Linac floor. That yields the floor elevation of 722.215 ft. (220.131 m) above the sea level. The tunnel floors for the SC linac, Transfer Line, and Tevatron are at the same elevation. The injection into the Booster will be vertical with a C-dipole. At its entrance, the beam orbit is located 33.6 cm (13.23") above the Booster orbit. The angle difference in the horizontal plane between the linac direction and the Booster injection straight is around -210 deg. This bending angle is produced by 32 identical 2.45 m long dipoles with 2.406 kG field. All these dipoles are connected serially and powered by a single power supply.

The first section of the Transfer Line is located in the extension of the Linac tunnel. This is reserved for a possible future energy upgrade and includes four periods with doublet focusing and

the same period length as in the HB section of the Linac. Such choice enables the installation of up to four additional HB650 cryomodules in the future, so that the Linac energy could be upgraded to about 1.2 GeV.

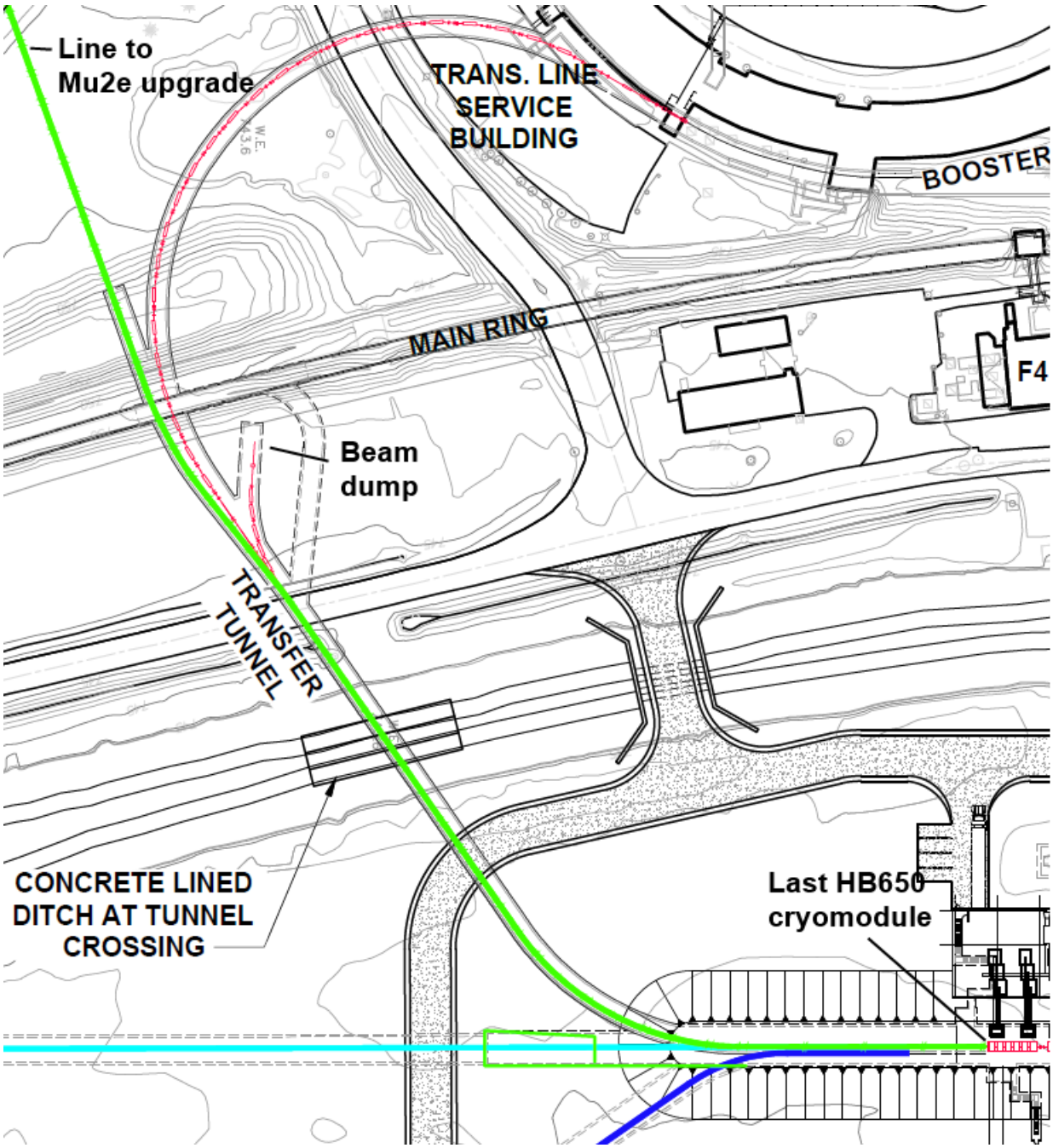

Figure 2.41. Layout of the beam transport line from the SC Linac to Booster. The linac beam dump and future transport line to the Mu2e upgrade are also shown.

The momentum spread of the Linac beam is sufficiently small. Therefore RF debunching is not planned and, consequently, no debunching RF cavities are presently anticipated, although there is sufficient space for debunching cavities if their installation will be required in the future. A FODO lattice is used for the rest of beam transport. Its period is chosen to keep the dispersion and beta-functions comparable to their values in the SC Linac and Booster. Geometrical constraints set the

cell length to about 11.8 m.

The FODO cells have 90 and 111 deg. horizontal and vertical phase advances, respectively, in order to have cancellation of horizontal and vertical dispersions at the end of the arcs. The cells of the straight section and of the arcs are identical except that in the arc cells the dipoles are inserted between the quadrupoles. Such choice automatically ensures that arcs and straight sections are matched to each other, and allows one to connect all focusing (defocusing) quads serially and power them from two power supplies: one for focusing and one for defocusing quads. The two arcs are composed of 4 and 12 cells and are both achromatic. The straight section connecting them consists of 8 cells. Low power adjustable collimators are installed at the beginning and at the center of the first arc. Two collimators at the arc beginning (each collimating on both sides for both the vertical and horizontal planes) separated by one cell remove particles having large betatron oscillations. Another collimator installed in the arc center, where the maximum dispersion is achieved, is used for momentum collimation. The length allocated for each collimator is about 1 m. Since each arc cell includes two dipoles, the packing factor of the arcs is 42%. This choice leaves sufficient space for horizontal and vertical correctors after each focusing and defocusing quadrupole respectively, as well as for ion pumps, BPMs and other instrumentation. It also foresees space for a possible installation of debunching RF cavities and additional collimators if needed in the future. The integrated strengths of the quadrupoles are set by the constraints on the phase advances per cell and are about 0.25 m^{-1} and -0.28 m^{-1} for focusing and defocusing quads, respectively (L=20 cm, G=0.61 and -0.69 kG/cm at E_{kin} = 800 MeV).

The second arc of the Transfer Line crosses the Tevatron tunnel. To create the mentioned above vertical bump the first few dipoles of the second arc are rolled around their longitudinal axis in order to increase the beam elevation from 1.3 m to about 2.4 m at the location of crossing. A roll of few other dipoles before and after crossing returns the beam to the Linac elevation. This vertical bump creates the vertical dispersion and perturbs the horizontal dispersion. Therefore, in addition to bringing the line to the linac level, rolls of these dipoles are adjusted to cancel both dispersions. Note that the choice of the phase advances was also driven by a necessity of dispersion cancelation. Note also that the dipoles have sufficiently small focusing, and therefore their rolls do not produce measurable *x-y* coupling.

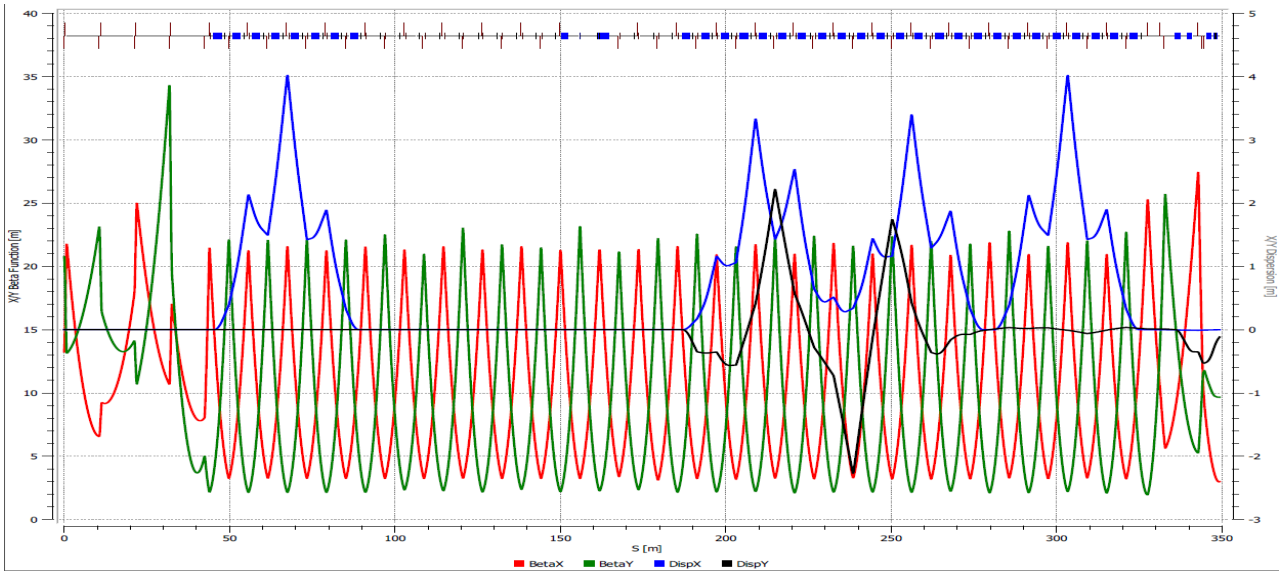

Figure 2.42: Optics of the Transfer Line from the SC linac end to the stripping target.

The aperture in the first part of the line located in the extension of linac tunnel is the same as in

the HB section *i.e.* Ø46 mm (2" stainless steel pipe with 2 mm wall thickness). Starting from the beginning of the first arc the line aperture is reduced to 17 mm (1.5" stainless steel pipe with 2 mm wall thickness). The optical functions of the entire Transfer Line are presented in Figure 2.42 [see optics details in Ref. [21]). The maximum horizontal dispersion in the arcs is about 4 m and the maximum beta-function is about 23 m. With 5 mm allowance for orbit distortions, they yield ±13.6σ momentum aperture and 5.7σ aperture for betatron motion of each transverse plane. Here we assumed the nominal rms momentum spread at the Linac end of $\sigma_p = 2.2 \cdot 10^{-4}$ and the transverse normalized rms emittances of 0.3 mm mrad.

The last straight section of the Transfer Line is downstream of the second arc and is aligned with the Booster injection straight. At its beginning, this line has the same elevation as the Booster and SC Linac. The Booster injection is in the vertical plane with a C-Dipole bending the beam downward into the Booster as shown in Figure 2.43. To bring the beam to the elevation of the C-Dipole a vertical dogleg is created. It uses two bending dipoles with length of 1.8 m and magnetic field of 2.5 kG. A triplet is placed after the second vertical dipole to match the line Twiss parameters to the values required for efficient injection into the Booster. The C-Dipole is 1.8 m long with 3.26 kG magnetic field.

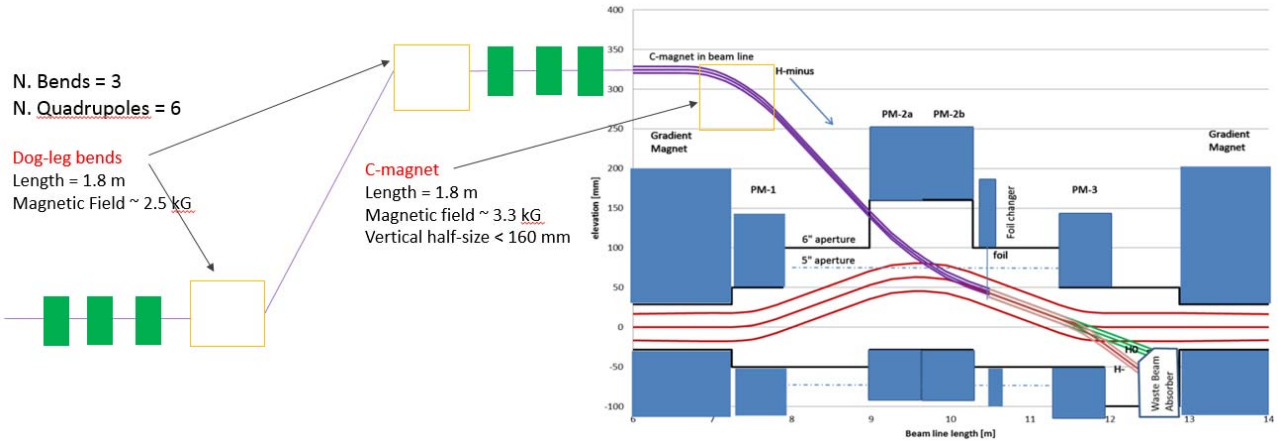

Figure 2.43: Schematic layout of the injection beam line.

A beam switching system is installed in the sixth and seventh cells of the straight section (located between the arcs). The system can switch the beam from the Booster line to the Dump Line or to the line going to the future upgrade of the Mu2e experiment. The Dump Line consists of five dipole magnets of the same design as used in the arcs. It deflects the beam horizontally to the beam dump placed so that there would not be any other beam lines at distances smaller than 10 m. Beam focusing is provided by alternate focusing and defocusing quadrupoles of the same design as used in the arcs, for a total of four. Dipoles and quadrupoles of the Dump Line are powered in series with the corresponding families of the transfer line. A sweeping magnet in the long drift before the dump helps to reduce the power density on the dump entrance. The beam dump is rated for 50 kW of 800 MeV beam. Twiss functions of the entire line from the end of the SC Linac to the dump entrance are shown in Figure 2.44. It assumes that the switching system is on and directs the beam to the dump.

Details of the beam transport for the Mu2e upgrade are presented in Appendix A.

The beam switch consists of a fast corrector (located right after the focusing quadrupole of the sixth cell) and a Lambertson septum with 3 apertures (located after the focusing quadrupole of the seventh cell). When the field in the fast corrector is on the beam is deflected from the central orbit and passes through two large aperture quadrupoles before it comes to the septum. When the beam

reaches the septum, it enters into one of two side apertures which magnetic field deflects the beam to the Dump Line or the Mu2e line. If the fast corrector is off, the beam remains at the vacuum chamber axis and arrives the septum central aperture. There is no magnetic field in this aperture and the beam is directed to the Booster line. The layout of the switching system is shown in Figure 2.45 where 10σ envelopes of the deflected and undeflected beams are presented.

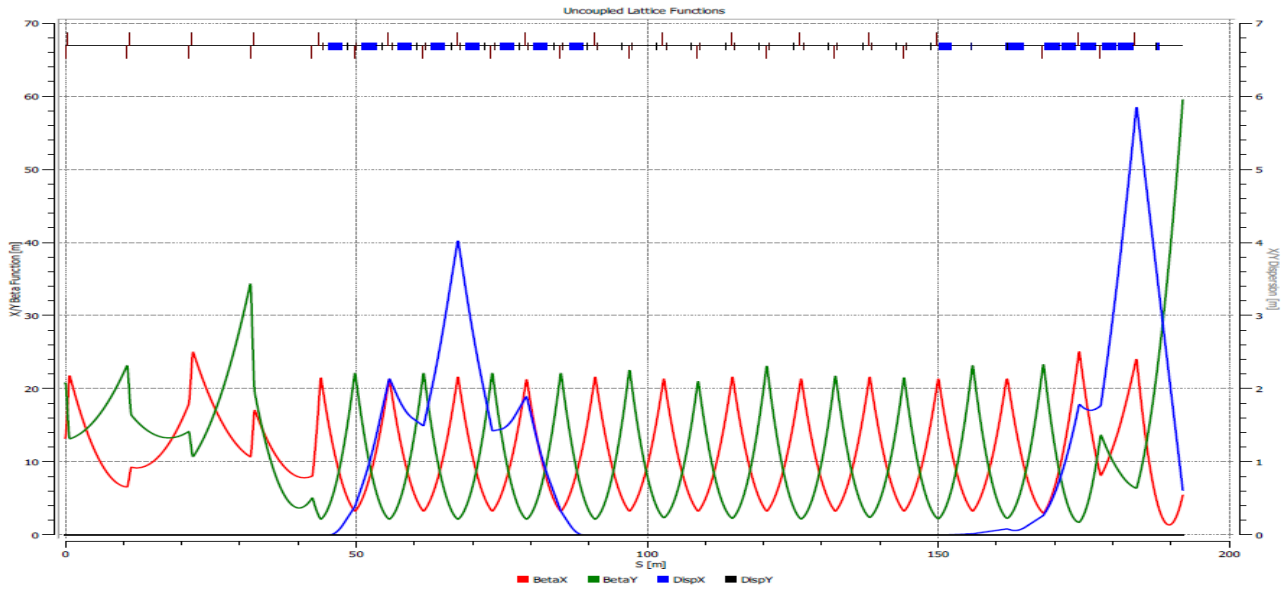

Figure 2.44: Optics of the Transfer Line from the SC Linac end to the dump.

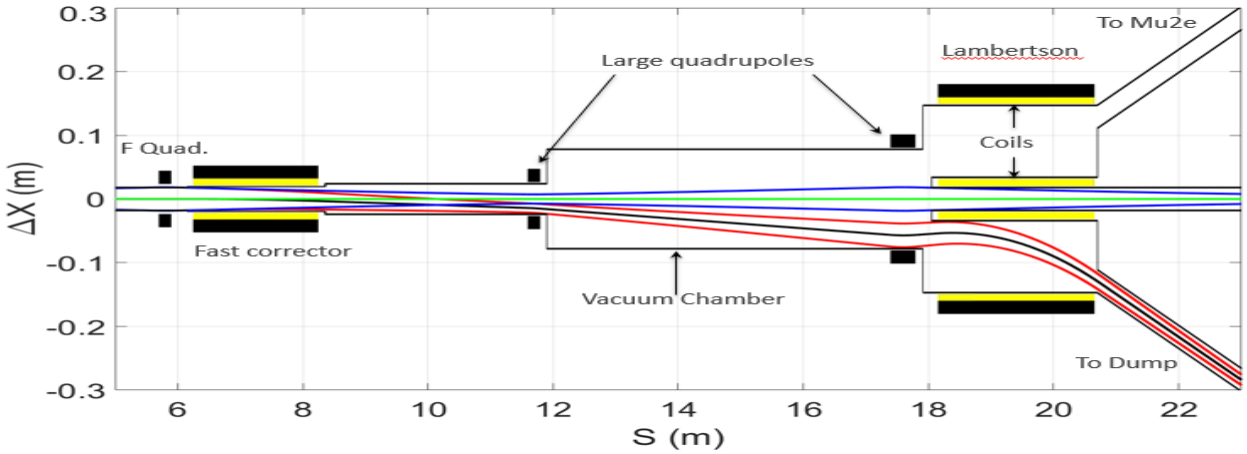

Figure 2.45: Horizontal 10σ envelopes of the beam directed to the Booster (blue) and to the dump (red). An inversion of field polarity for the fast corrector directs the beam to a symmetric trajectory leading to the Mu2e upgrade.

The beam based energy stabilization discussed below requires that the fast corrector must be able to switch the beam from one aperture to another nearby aperture in ~20 μs. The corrector is powered by a special power supply capable to create sufficiently large voltage required for fast switching. The usage of a ceramic vacuum chamber inside the corrector avoids eddy currents, which even for a thin stainless steel chamber would increase the field rise-time to an unacceptably large value. The Lambertson septum, like the other magnets, is powered by DC. The strengths of fast corrector and septum are 0.15 and 3.6 kG·m, respectively.

2.2.3. Beam Based Linac Energy Stabilization

As shown below, high quality injection into the Booster requires relative energy stability better than 10^{-4} rms. The present experience does not guarantee that such energy stability can be achieved if the beam energy is stabilized only by internal feedbacks separately stabilizing each cavity voltage. In this case, the beam based energy stabilization is the only possibility to address the problem. A similar approach is used in the present Fermilab linac. The energy correction is applied to the cavities of the last SC cryomodule where the synchrotron motion is greatly slowed down and voltage variation will have little effect on the beam dynamics. It is expected that such a system will improve the energy stability from ~10^{-3} level achieved with local feedbacks to the desired value of better than 10^{-4}.

To avoid unnecessary beam loss in the Booster while the beam energy is still not stabilized to the required level the beam is initially directed to the beam dump located after the first arc of the transport line (see Figure 2.41). After the energy is stabilized to the required level (~100 μs is required) the beam is switched to the transport line and delivered to the Booster. The switching requires the beam being off and therefore it has to be done sufficiently fast (~20 μs) to avoid changes of accelerating voltage during switching time.

The beam energy is measured by BPMs located in the first arc of the transport line. The accuracy of the system is determined by the BPM accuracy and is expected to be ~10^{-5} with ~1 μs sampling time. A time-of-flight system placed in the slots reserved for the energy upgrade of the Linac can also be used. Although it hardly can achieve the accuracy of the BPM based system. This energy measurement will be used to support operation of the beam-based energy stabilization system. A high accuracy absolute energy measurement is not required.

2.3. Booster Modifications

2.3.1. Technical Requirements and Scope

The performance requirements of the Booster are summarized in Table 2.13. The 800 MeV injection energy is selected to provide an increase in beam intensity of about 50% beyond current operations, accompanied by a 30% decrease in the space-charge (Laslett) tune shift at injection. This choice is made to provide more efficient beam capture and acceleration, in order to minimize losses at the higher beam intensity required in PIP-II. The requirement on the longitudinal beam emittance is set by slip-stacking in the Recycler.

Table 2.13: Performance requirements for the Booster

Performance Parameter	Requirement
Particle Species	Protons
Input (H^-) Beam Energy (Kinetic)	800 MeV
Output Beam Energy (Kinetic)	8.0 GeV
Protons per Pulse (injected)	6.7×10^{12}
Acceleration efficiency	97%
Protons per Pulse (extracted)	6.5×10^{12}
Beam Pulse Repetition Rate	20 Hz
RF Frequency (injection)	44.7 MHz
RF Frequency (extraction)	52.8 MHz
Total RF voltage	1.2 MV
Injection Efficiency	98%
Injection Time	0.55 ms
Injection Turns	292
Beam Emittance (95%, normalized; $\varepsilon_x = \varepsilon_y$)	16 μm
Maximum Laslett Tune Shift (space charge)	-0.17
Delivered Longitudinal Emittance (97%)	0.1 eV·s
Delivered Momentum Spread (97% full height)	12.2 MeV
Delivered Bunch Length (97% full length)	8.2 ns

The primary areas that need to be addressed in order to reach the performance goals listed above are given in Table 2.14. Among them the injection and the beam quality are expected to present the primary challenges.

This section will describe concepts and approaches in the areas listed in Table 2.14. This description assumes successful completion of the PIP tasks currently underway. However, this discussion is preliminary and may change after more extensive investigations are completed. It is required that Booster beam losses be maintained at less-than-or-equal-to present levels. The current operating loss limit is 525 W ring-wide, augmented by independently set beam loss monitor (BLM) trip points in each long and short straight section.

Table 2.14: Booster areas requiring consideration as part of PIP-II

Topic	Associated Items
Injection	Injection girder and loss control
Capture	RF capture, timing and emittance control
Acceleration and Transition	Loss control, RF requirements and transition control
Extraction	Loss control, timing and beam manipulations
Beam Quality	MI/Recycler requirements
Operations	Shielding, Booster Hardware

2.3.2. Booster Injection

2.3.2.1. Present Booster Injection

The Booster lattice contains 24 periods and can be described as a FDooDFo lattice utilizing combined function dipoles with long straight sections (~5.7 m) between the defocusing (D) dipoles and a short straight section (~0.9 m) between the focusing (F) dipoles. The horizontal beta-function varies from about 6 meters in the long straight to 33 m in the short straights while the vertical beta function varies from 20 m in the long straights to ~5.3 m in the short straights. The horizontal dispersion varies between approximately 1.2 (in the long straights) and 2.2 meters (in the short straights). The optical functions for one period are shown in Figure 2.46. It should be noted that the optical functions for all periods are almost equal. Some differences appear due to optics errors and the focusing effect of the extraction dogleg. The latter is quickly reduced with acceleration and has a negligible effect on the beam optics above 1.5 GeV energy.

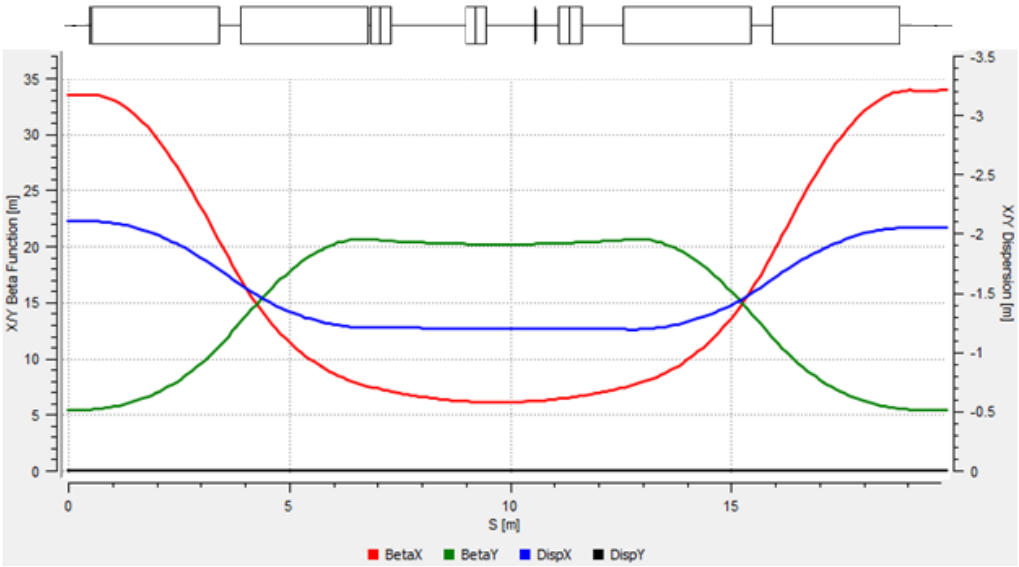

Figure 2.46: Optical functions for one Booster period. The presented period includes the Booster Long 1 straight section where the beam injection is happening. A schematic of the present injection straight is shown at the top of the plot. The locations of pulsed injection dipoles (ORBUMP dipoles) are shown by double rectangles. The vertical line in the center marks position of stripping foil.

The top part of Figure 2.46 also shows the magnet configuration for the present injection straight

section which is considered to be the ring beginning and therefore is named Long 1. The schematic of the line is shown at the top of the figure. It includes the combined function dipoles, pulsed injection dipoles (ORBUMP magnets) and correctors. The layout of injection area is shown in Figure 2.47. It is based on the three bump system installed in 2006 [28, 29]. The center dipole of this insert is used to merge the incoming H^- ions with the proton beam circulating in the ring. The orbit bump is produced by the three pulsed dipoles which displace the closed orbit by ~44 mm to the stripping carbon foil for the duration of injection (~35 μs). The center dipole runs at twice the field of the outer dipoles. The injection foil is located immediately after the middle ORBUMP magnet. The field in the ORBUMP dipoles does not change during the injection, and there is no phase space painting in any degree of freedom. All three dipoles are powered by a single power supply. The angle produced by the center dipole is approximately ~44 mrad which corresponds to an integrated field of 1.4 kG-m. The separation of the ORBUMP magnets is approximately 1.75m. Lorentz stripping in these magnets is not an issue at 400 MeV.

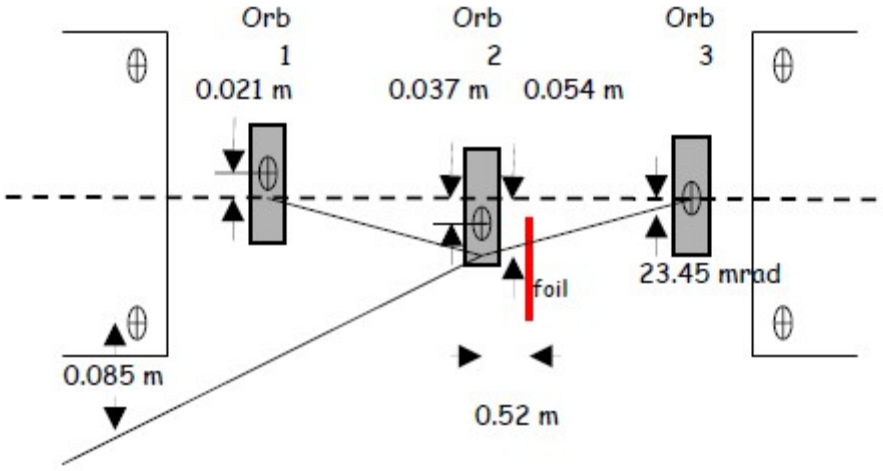

Figure 2.47: The current 400 MeV horizontal injection insert showing the layout of the three chicane dipoles, foil and injection beam line.

The existing ORBUMP magnets cannot be utilized for 800 MeV injection. Their use would require a magnetic field in the center dipole of ~4.5 kG, resulting in unacceptably large Lorentz stripping. There is also insufficient space for the beam dump. Addressing these problems requires a complete redesign of the injection straight.

2.3.2.2. Conceptual Design of Booster Injection at 800 MeV

The injection into the Booster during the PIP-II era will be moved from “Long 1” to ”Long 11” straight section to facilitate injection from the SC Linac located in the Tevatron infield (Figure 2.48). As already noted, all long straight sections have the same geometry and optics. The flange-to-flange length available for the injection insert is 5.6804 m.

The beam current of the SC Linac (2 mA) is more than an order of magnitude smaller than that of the present 400 MeV linac. It will require much longer injection time (~300 turns over ~500 us) which together with much smaller linac emittance ($\varepsilon_{n\_95\%} \approx$ 1.5 mm-mrad versus 16 mm-mrad specified for the Booster beam) allows us to perform transverse phase space painting. It is expected to be a very efficient cure for suppression of the harmful effects of beam space charge and improvement of the longitudinal beam stability. During the phase space painting process, the Booster

closed orbit in each plane will be moved by ~2σ of the final Booster accumulated phase space (see details below). The vertical displacement will be performed by pulsed magnets of the injection 3-bump, the horizontal displacement by regular Booster dipole correctors.

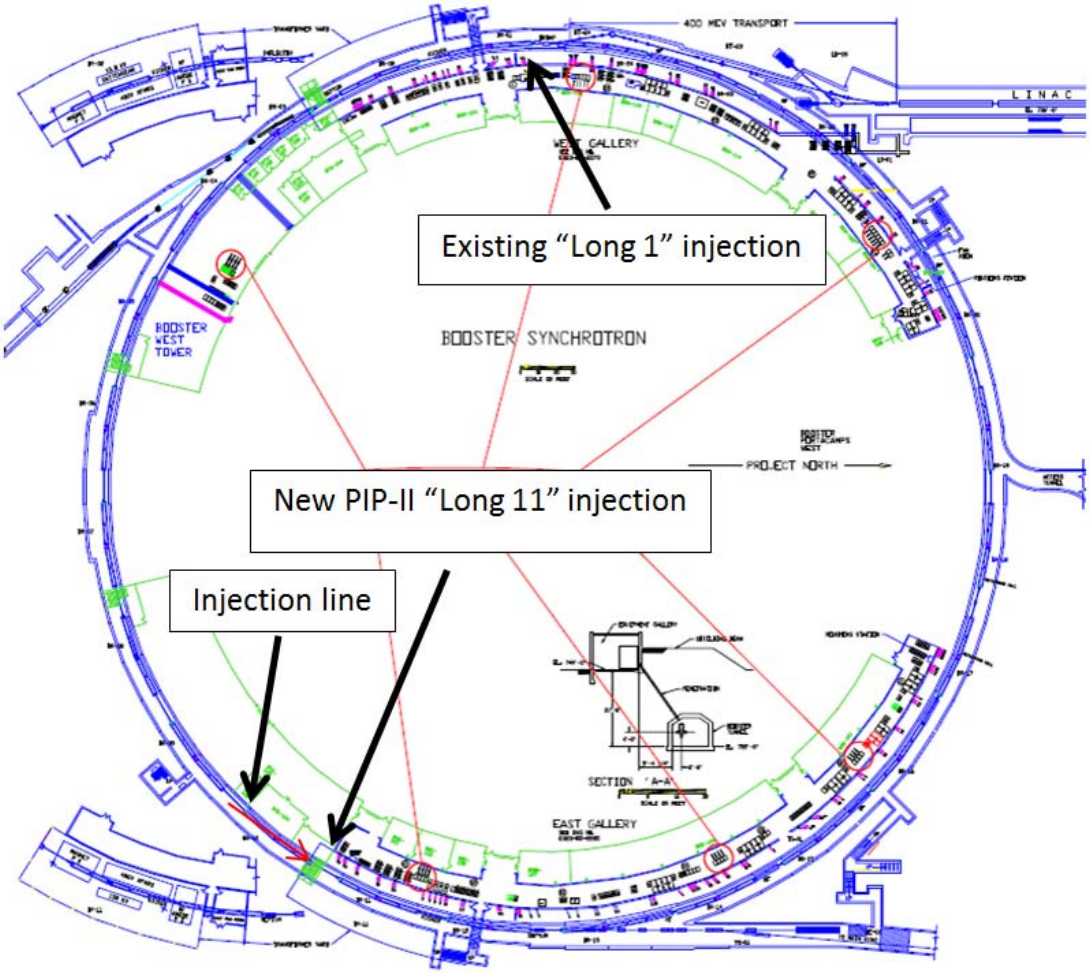

Figure 2.48: Plan view of Booster showing the location of existing and new PIP-II injection insert.

The conceptual design for the straight section is patterned after the present 400 MeV injection three-bump design by adding a second dipole to the middle bend center. The layout of the injection concept, beam envelopes, and apertures are shown in Figure 2.49. The vertical dimensions of the chicane dipoles and foil changer are represented by the blue boxes and are not to scale. The horizontal dimensions of these devices are roughly to scale. The physical aperture is represented by the black line and the absorber is labeled in the open box. The aperture in the D dipoles is set by the pole tip separation on the central orbit of 2.25" (+/- 28.6 mm). The aperture in the central chicane magnets, PM-2a and PM-2b, is determined by the injected beam trajectory.

The chicane dipoles move the Booster closed orbit to 45 mm at the foil location. During the injection process this closed orbit is collapsed by ~2σ of the final vertical rms beam size or ~17 mm down to ~28 mm. After the end of injection, the chicane dipoles return the closed orbit back to zero. The closed orbit displacement in the center of the two central dipoles is approximately 68 mm. The H^- injected beam at the foil position is 45 mm with a vertical angle of -40 mrad.

Incompletely stripped H^- ions (mostly excited states of H^0) and H^- ions which miss the foil will be

intercepted by the beam absorber. It is located downstream of the last chicane dipole and upstream of the Booster combined function dipole. For 800 MeV the required space for the dump is 0.5 m at minimum. There are also other equipments (*i.e.* correction element package, 0.6 m; vacuum bypass and valve, 0.45 m; ion pumps, 0.2 m; horizontal painting dipole, ~0.2 m, and diagnostics/ instrumentation, ~0.25 m) which are located in the space between the dipoles.

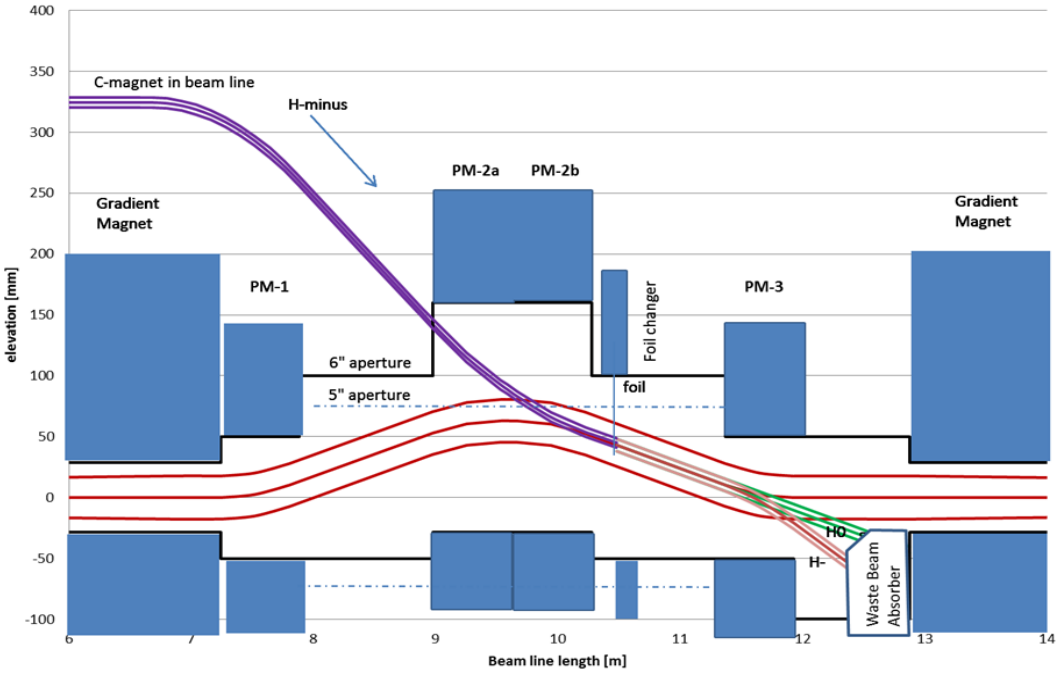

Figure 2.49: Conceptual design for 800 MeV injection using a three-bump chicane within the Booster long straight section.

Table 2.15: Parameters of elements located in the injection straight

#	Name	Accumulated Length (m)	Flange-Flange or Drift Length (m)	Magnetic Length (m)	Magnetic Field (kG)
1	Drift 1	.07067	0.07067		
2	ORBUMP 1	0.7624	0.69171	0.5585	3.496
3	Drift 2	1.7724	1.01		
4	ORBUMP2a	2.4641	0.69171	0.5585	3.496
5	ORBUMP2b	3.1558	0.69171	0.5585	3.496
6	Drift 3	3.2570	0.1012		
7	Foil changer	3.5617	0.3047		
8	Drift 4	4.1667	0.6050		
9	ORBUMP 3	4.8584	0.69171	0.5585	3.496
10	Drift 5	5.1584	0.3		
11	Absorber	5.6584	.05		
12	Drift	5.6804	0.02202		

The current placement of the C-dipole in the transport beam line is just over the upstream Booster dipole with a beam elevation of ~0.15 m above the top of steel of the Booster dipole. The bend angle of the C-dipole is 3 times the angle of the chicane dipoles or approximately 120 mrad. To obtain acceptable Lorentz stripping of the incoming H^- ions the design of this magnet has to be driven by a requirement of minimization of the peak dipole field. A value less than 4 kG has to be achieved. Table 2.15 present lengths allocated for different elements and their parameters. The accumulated length is between the flanges of the gradient magnets at either end of the straight section and is given at the end of each element. In addition to the elements in the Booster ring, the last magnet in the transfer line (C-dipole) ends 0.505 meters upstream of the ORBUMP2 magnet. It has a magnetic length of 1.8 meters with an angle of -120 mrad and field of 3.26 kG.

2.3.2.3. Phase Space Painting

Small values of beam emittances of the linac beam allow us to perform phase space painting in all degrees of freedom. It reduces the harmful effects of beam space charge on the transverse particle motion due to a reduction of the space charge incoherent tune shifts, and it is expected to be helpful in achieving longitudinal stability (see below).

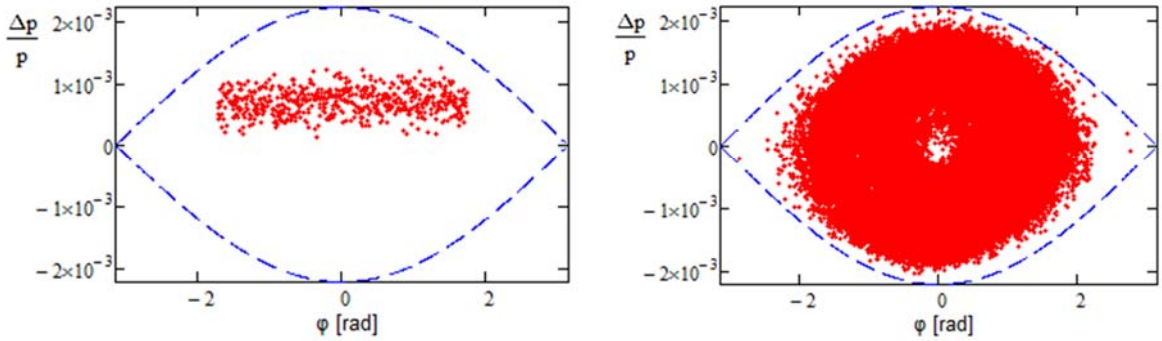

Figure 2.50: The longitudinal phase space of particles incoming to the Booster (left) and the phase space at the end of injection process (right).

The rms momentum spread of linac beam of $2.2 \cdot 10^{-4}$ is an order of magnitude smaller than the RF bucket height in the Booster ($2.2 \cdot 10^{-3}$). Together with the long duration of the injection process corresponding to 7 synchrotron periods it enables static longitudinal painting, which greatly simplifies the procedure. In this case the linac energy is offset relative to the Booster reference energy and the synchrotron motion mixes particles in the longitudinal phase space in the course of injection. Linac bunches that would be outside of RF buckets are removed by the bunch-by-bunch chopper in the MEBT. Figure 2.50 presents the longitudinal phase spaces of injected beam and the Booster beam at the injection end. The value of the momentum offset ($7 \cdot 10^{-4}$) and the duration of the injection window (55%) were optimized to minimize the bunching factor. Figure 2.51 presents the longitudinal density along a Booster bunch. The corresponding bunching factor is 2.5. In average each Booster RF bucket receives two linac bunches per injection turn. The linac bunch frequency of 162.5 MHz and the Booster RF frequency of 44.705 MHz are not related as integers and therefore the injection process is asynchronous. It results in a variation in the number of linac bunches injected to one Booster bunch in the range of ±0.34% (±2 bunches out of 588 bunches injected into an RF bucket per injection cycle). The rms bunch lengthening in the course of beam transport from linac to Booster is about 14 mm. This value is much smaller that the RF bucket length of 5.65 m and can be neglected in most practical considerations.

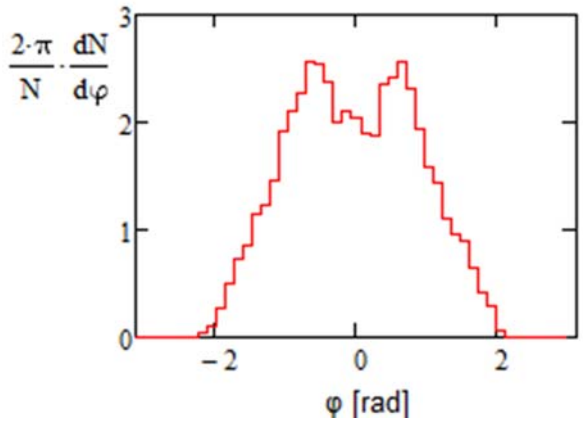

Figure 2.51: The longitudinal density of an injected bunch after injection.

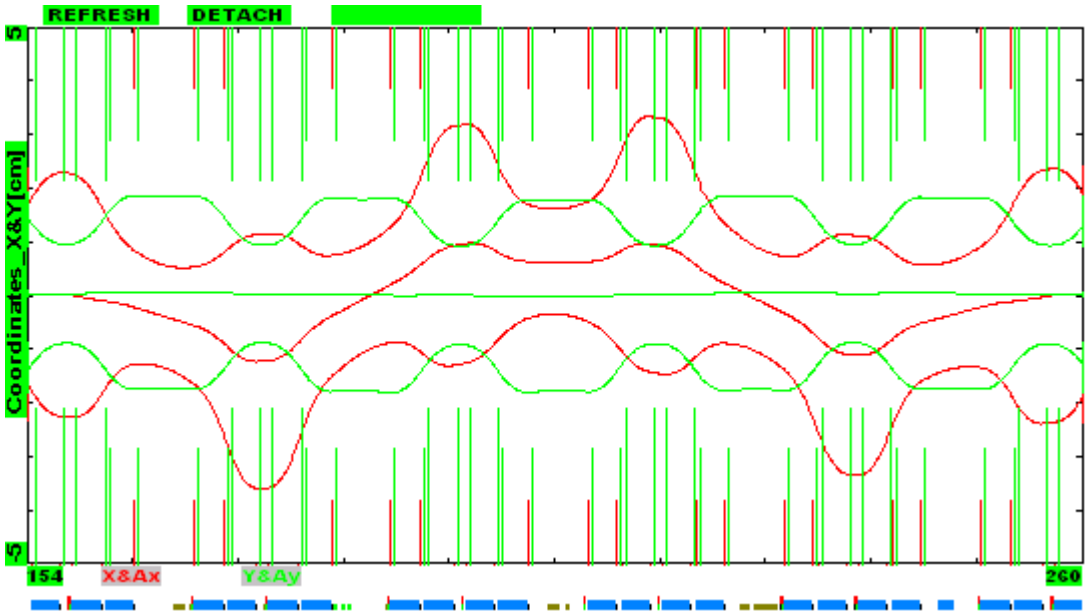

Figure 2.52: The horizontal orbit bump for beam painting at the maximum horizontal (red) and zero vertical (green) displacements. Beam envelopes for the normalized acceptances of 25 mm mrad are also shown. The injection straight (Long 11) is in the center of the plot ($s \in [204.3 – 210.3]$ m). Vertical lines show aperture limitations in the dipoles (horizontal – red, vertical green).

As mentioned above, phase space painting in the vertical plane is performed by the dipoles of the injection chicane. Phase space painting in the horizontal plane will be performed by regular Booster correctors located outside of the injection straight. The correctors should create a closed orbit bump with maximum beam displacement on the foil of 6.1 mm. The shortest orbit bump could be implemented using only the correctors closest to the injection straight (HL10, HS10, HS11, HL12). Such choice requires considerable corrector strength of 6.3 kG·cm. Although the strength of the present horizontal correctors of 9 kG·cm is sufficient, their slew rate of 3.24 kG·cm/ms is about 5 times less than the slew rate required for painting. Therefore, a longer bump using correctors from nearby short straights was chosen. Table 2.16 presents the corrector strengths and Figure 2.52 shows the corresponding beam displacements together with the beam envelopes in the vicinity of the injection straight. The envelopes are plotted for the normalized emittance of 25 mm·mrad, which includes almost 100% of the particles (see below). The horizontal beta-function in the short straights

is about 5 times smaller than in the long ones. This enables a reduction of corrector strengths by ~3.4 times. The required slew rate of 4.5 kG·cm/ms still exceeds the slew rate for the present correctors by about 1.4 times. This problem can be addressed by an upgrade of corrector power supplies or by usage of a longer orbit bump.

Table 2.16: Corrector strengths required to create horizontal injection orbit bump

Name	HS08	HS09	HS011	HS12	HS13
BdL [kG·cm]	-1.867	0.72	0.192	0.72	-1.723

The stripping foil and the injected H^- beam do not move during injection (see Figure 2.53). Similar to the beam injection in the SNS the rectangular foil is hanged in the vacuum chamber and the linac beam hits it near a corner to minimize number of secondary foil hits by particles of already injected beam. Both betatron and synchrotron oscillations in average push particles out of the foil.

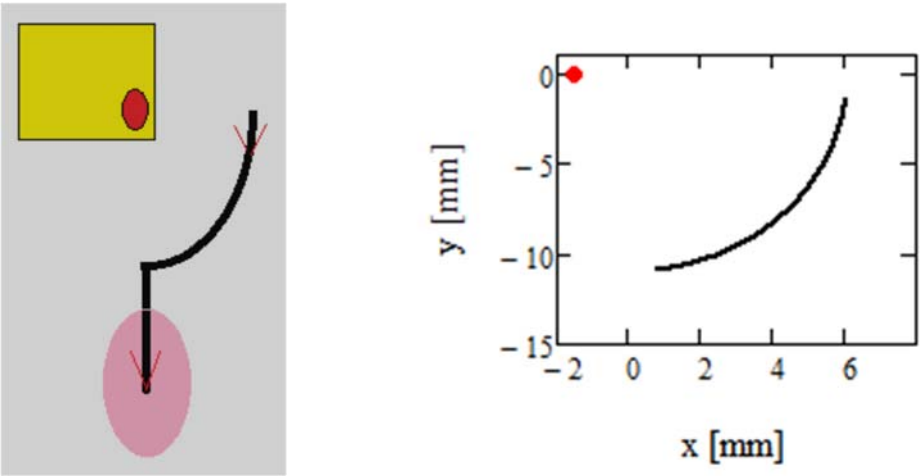

Figure 2.53: Left pane - schematic of injection painting: square (yellow) – stripping foil, small ellipse (red) – linac beam hitting the foil, large ellipse (pink) – circulating beam after the end of injection process, black line – trajectory of closed orbit displacements in the course of beam painting. Right pane - plot of closed orbit displacements in the course of beam painting relative to the linac beam center (shown by the red dot). The reference orbit of Booster beam is located at zero *x*-coordinate. The linac beam is displaced outward by 1.5 mm to account for the energy offset ($\Delta p/p=7\cdot10^{-4}$) required for the longitudinal painting. Positive values of beam displacement in the horizontal and vertical planes correspond to inward and upward displacements, respectively (consequence of the right-hand coordinate frame chosen for description of ring orbit and optics).

The horizontal and vertical displacements of the closed orbit are correlated and follow the ellipse as shown in Figure 2.53. The ellipse semi-axes are 6.1 and 11 mm for horizontal and vertical amplitudes, respectively. To reduce the number of foil secondary hits and improve the uniformity of the distribution the painting curve covers only 84% of the ellipse quarter as shown in the right pane of Figure 2.53. That results in the actual beam displacements of 5.3 and 9.5 mm for horizontal and vertical planes, respectively. After painting the closed orbit and, consequently, the beam are moved vertically down to the nominal (central) orbit. As can be seen in Figure 2.53 the center of linac beam is additionally displaced outward by 1.5 mm to account for the energy offset required for the longitudinal painting. It also reduces the number of foil hits because the synchrotron motion keeps the center of accumulated beam at zero horizontal coordinate.

The limited space available for beam injection and the small vertical aperture of Booster dipoles force us to obtain vertical painting by changing the magnetic field of the chicane. Unfortunately, it also affects the vertical position of the linac beam on the foil. This displacement is induced by changing the magnetic field of the central chicane dipole (see Figure 2.49) as the linac beam passes through it. This beam position change is corrected by fast dipole correctors located at the end of transport line (just upstream of injection aria).

To minimize the number of passages through the foil the beta- and alpha-functions of the linac beam are scaled from the corresponding values of the Booster by factor of 0.483 so that the linac phase space would be inscribed into the *x* and *y* machine acceptances as shown in Figure 2.54. The offsets of linac beam relative to the Booster beam presented in Figure 2.54 are equal to the painting offsets discussed above. Table 2.17 presents Twiss parameters for the linac and Booster beams on the stripping foil. To minimize displacements of linac beam position on the stripping foil we require that the dispersions and their derivatives are equal to zero at the foil. The emittance increase for the injected beam related to the dispersion mismatch to the linac dispersion is negligible. The number of secondary foil hits increases quickly with distance between the linac beam center and the foil edges, *i.e.* if the foil is moved closer to the circulating beam. To minimize foil hits we assume that one percent of the linac beam can miss the foil. For a Gaussian beam it determines that the distances to the foil edges has to be 2.58 times of the corresponding rms beam sizes or 1.95 mm and 3.51 mm for the horizontal and vertical planes, respectively.

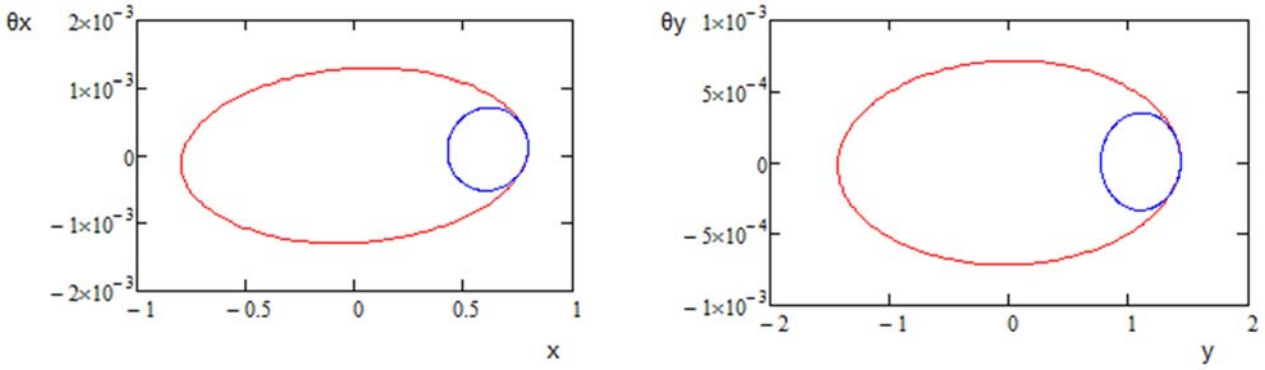

Figure 2.54: Phase space boundaries of the linac (blue) and RCS (red) beams. The linac beam boundaries correspond to the normalized boundary emittance of 1.8 mm·mrad (95% normalized linac emittance) the RCS beam boundaries correspond to the normalized emittances of 16 mm mrad.

Table 2.17: Twiss parameters for the Booster and linac beams at the stripping foil

	β_x (m)	α_x	β_y (m)	α_y	D_x (m)	D'_x
Booster	6.17	-0.095	20.03	-0.028	2.18	0
Linac	2.98	-0.046	9.67	-0.014	0	0

Figure 2.55 presents results of experimental measurements of H^- stripping by a carbon foil at 800 MeV, as presented in Ref. [30], with their extrapolation for a thicker foil. The extrapolation assumes the following cross-sections for transitions: $\sigma_{H^-\to H0}=67.6\cdot10^{-16}$ cm^{-2}, $\sigma_{H^-\to H^+}=1.2\cdot10^{-16}$ cm^{-2} and $\sigma_{H0\to H^+}=26.4\cdot10^{-16}$ cm^{-2} [31]. It also assumes that there are no transitions with electron capture *i.e.* $H^0\to H^-$, $H^+\to H^-$ and $H^+\to H^0$. This assumption is well justified for 800 MeV energy. The thickness

of stripping foil was chosen to be 600 μg/cm^2. This is thick enough to strip the major fraction of H$^-$ to protons leaving less than 0.1% particles as H^0 and a negligible fraction as H$^-$. As shown below, this thickness does not cause problems with particle scattering in the foil and foil overheating but should support longer foil operation than a thinner foil. Spattering resulting in foil evaporation is expected to be a major mechanism limiting the foil lifetime. As shown in Figure 2.55, operation with foil thickness as thin as 400 μg/cm^2 is still possible.

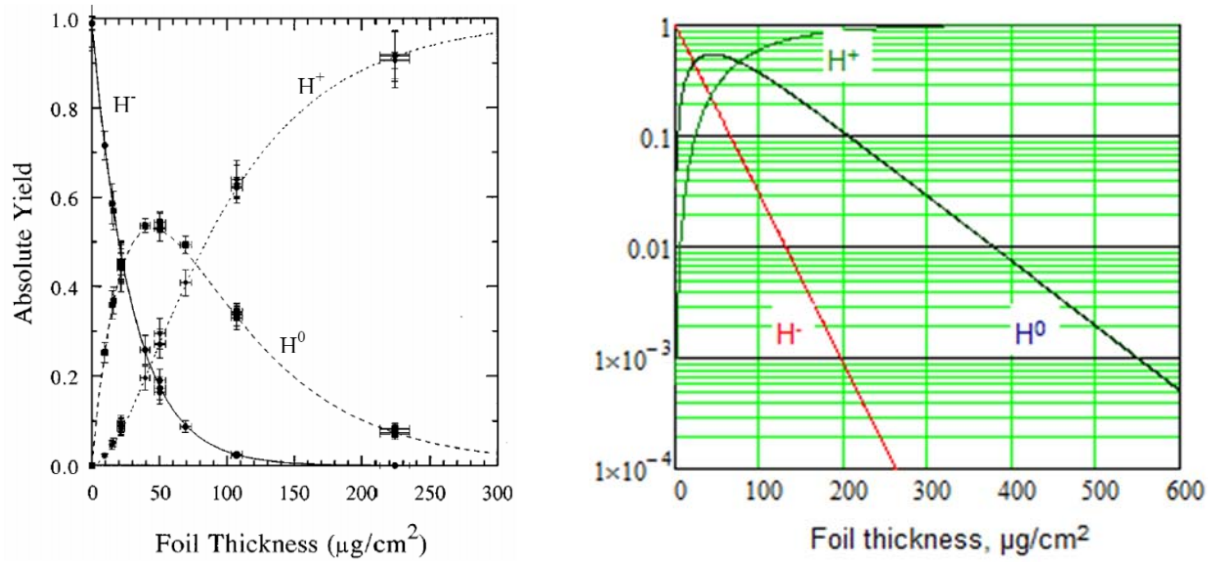

Figure 2.55: Measurement of 800 MeV H⁻ stripping by carbon foil presented in Ref. [30] (left pane) and their extrapolation for a thicker foil (right pane).

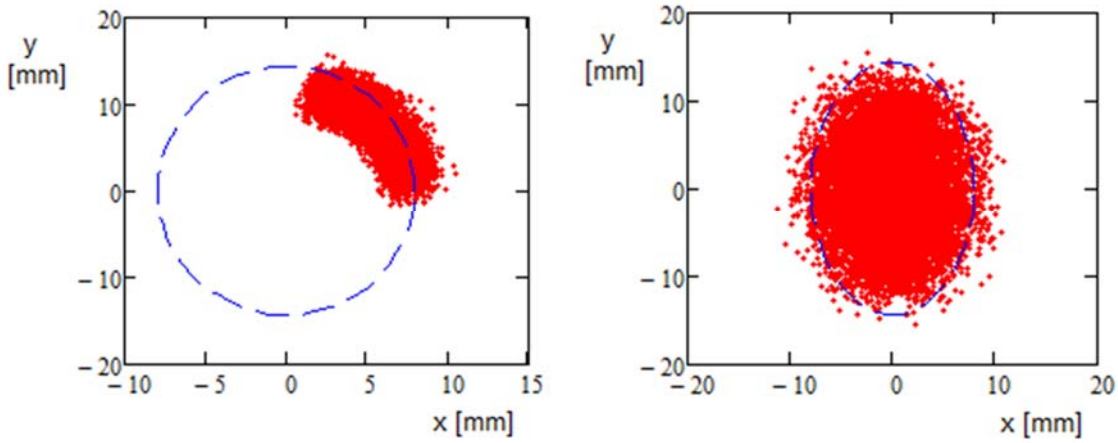

Figure 2.56: X and Y coordinates of all injected (in simulation) particles relative to the current orbit position for particles incoming to the Booster (left) and at the end of injection process (right).

Figure 2.56-2.59 present results of numerical simulation of the strip-injection. The simulation includes multiple scattering in the foil, synchrotron and betatron motions and the details of the painting process described above. The beam space charge effects are not taken into account and betatron motion is linear and without *x*-*y* coupling. The simulation showed that that the betatron tunes have to be different by more than 0.01 for uniform painting. The results were obtained for the following tunes: Q_x=6.8 and Q_y=6.81. Tune values have little effect on the result as long as they are

different. The left pane in Figure 2.56 presents *x* and *y* coordinates of all particles relative to the orbit position at particle injection time. The right pane presents particle coordinates at the end of the injection process. The left pane in Figure 2.57 shows the particle distribution in Courant-Snyder invariants (single particle emittances). One can see that the distribution is somewhere between the Gaussian and K-V distributions. The latter would be represented by the δ-function, $\delta\left(\varepsilon_{4Dn}-\varepsilon_{bn}\right)$, in the 4-dimensional phase space, where $\varepsilon_{4Dn}=\varepsilon_{xn}+\varepsilon_{yn}$, and ε_{bn} is the normalized boundary emittance of KV-distribution. The right pane in Figure 2.57 shows the integrals of the particle distributions presented in the left pane normalized to 1. One can see that 95% of particles are within 17 mm mrad and almost 100% within 23 mm mrad. Similarly, Figure 2.58 presents the longitudinal distribution and its integral. As one can see, 100% of particles are within 0.06 eV·s.

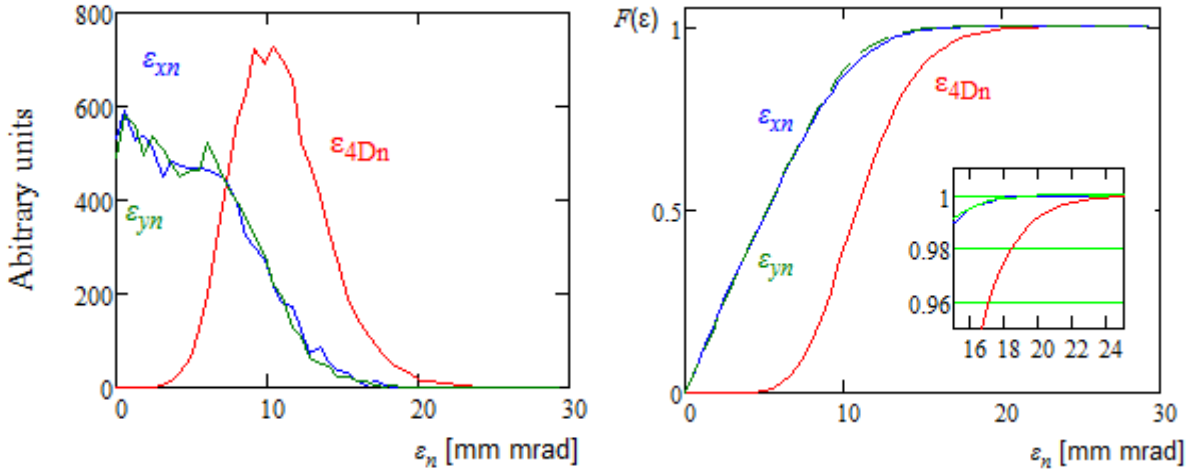

Figure 2.57: Left pane - the particle distribution over particle normalized Courant-Snyder invariants: $\varepsilon_{xn}=\beta\gamma\left(x^2/\beta_x+2\alpha_x x\theta_x+(1+\alpha_x{}^2)\theta_x{}^2/\beta_x\right)$, (and similarly for *y* plane); blue – horizontal plane, green – vertical plane, red – the distribution over sum of invariants, $\varepsilon_{4D}=\varepsilon_x+\varepsilon_y$. Right pane – the integrals of particle distributions (normalized to unity) presented in the left pane. The insert shows detail near the top of the picture.

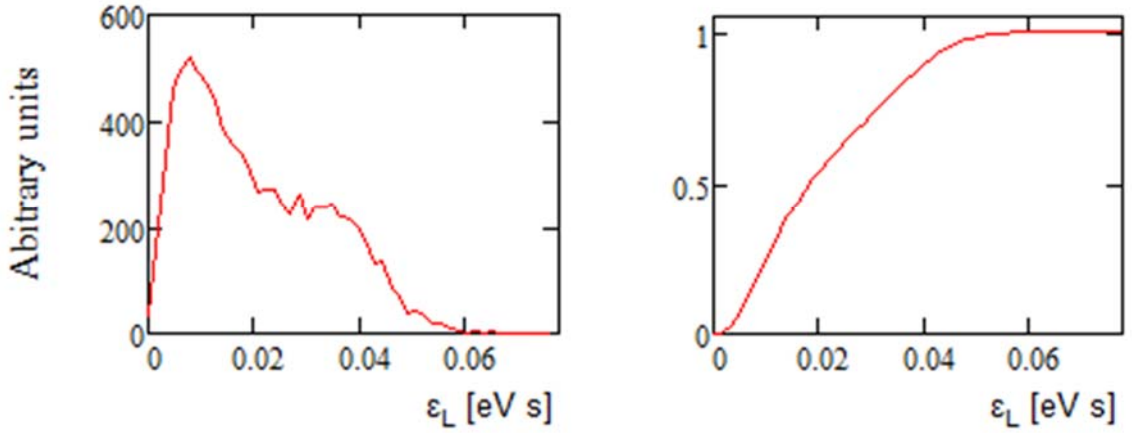

Figure 2.58: Left pane - the particle distribution over particle longitudinal emittance (phase space area subtended by particle trajectory). Right pane – the integral of particle distribution presented in the left pane (normalized to 1). The horizontal axis ends at the bucket boundary.

Figure 2.59 presents the distribution of secondary and primary hits of the surface of stripping foil. The peak of secondary hits is located at the foil corner and is equal to 63 hits per particle per cm^2. The average number of secondary foil hits is 6.1 per injected particle. The distribution of primary hits is peaked at the center of incoming linac beam and is about 4 times smaller (15.4 hits per particle per cm^2). As can be seen from the right pane in Figure 2.59 the peak of the total (summed for primary and secondary hits) hit distribution is determined by secondary hits.

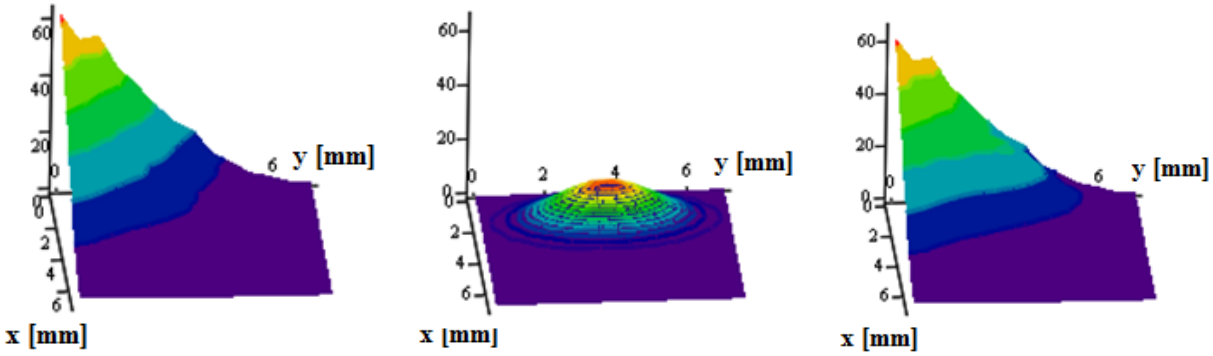

Figure 2.59: The distribution of particle hits on the stripping foil (hits per injected particle per cm^2): left – secondary hits, center – primary hits of the incoming linac beam, right – sum of primary and secondary hits.

The beam passing through the foil results in its heating. Although the total deposited power of 33 mW is small, the power density is still considerable due to small size of the injected beam. At its peak in the foil corner the power density is about 2 W/cm^2. The major cooling mechanism for the foil is the black body radiation. Conservatively assuming the foil emissivity of 50% one obtains the peak temperature of 640 C^o at the foil corner. This temperature is sufficiently small to guarantee a long lifetime for the foil. Figure 2.60 presents a dependence of the hottest spot temperature on time after initiation of beam operation. The temperature reaches its peak after the fourth pulse. An estimate shows that accounting for the foil thermal conductivity yields a quite small correction and it was neglected in the above calculation.

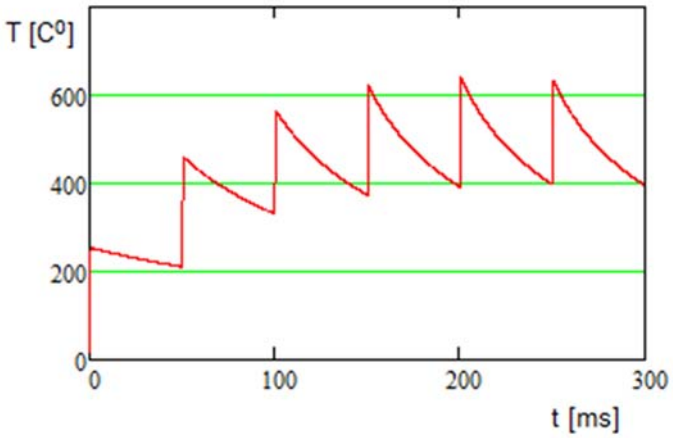

Figure 2.60: The dependence of temperature on time for the hottest place on the foil; t = 0 corresponds to the first injection pulse.

The total power of the injected beam is about 18 kW. About 1.2% of these particles are expected to be lost during injection: ~1% miss the foil, 0.1% are not completely stripped in the foil, and 0.1%

are lost due to single scattering in the foil (direct and secondary hits are accounted). In normal operating conditions, the resulting heat load on the injection beam dump is about 200 W with 20 W of uncontrolled beam loss mostly intercepted in the first two dipoles.

Stripping of H^- also yields two 400 keV electrons for each stripped H^-. These electrons carry a power of about 18 W that needs to be intercepted by the electron beam dump. After leaving the foil the electrons are reflected from the downstream dipole where they are bent by its magnetic field. It results in their bending by 180 deg. and a displacement by a few centimeters in the vertical plane. The design of the electron dump must prevent heating of the foil by these electrons, their accumulation and interaction with the circulating beam.

The injection to the Recycler, and, subsequently, to the Main Injector requires injection gaps of 3 buckets in the bunch structure of the Booster beam. Removal of these bunches will be performed by the bunch-by-bunch chopper located in the linac MEBT.

2.3.3. Beam Acceleration in the Booster

The longitudinal emittance of the Booster beam is limited by the RF bucket size in the Recycler. Although the RF bucket size in the Recycler will be larger by 33% due to an increase of Booster repetition rate from 15 to 20 Hz (see details below) the longitudinal rms emittance of the Booster beam is required to be about the same. A larger ratio of bucket size to the beam emittance should enable a reduction of beam loss by factor more than 2, tentatively from 5% to 2%. Thus, the RF bucket size in the Booster is expected to be close to the PIP value.

An increase of the Booster ramp rate increases the magnetic field ramping rate and the RF voltage required for acceleration. However, for a small intensity beam an increase of the peak RF voltage is not required if the RF bucket area stays the same. Actually, to keep a desirable size of RF bucket during acceleration in the present Booster the maximum RF voltage is required at the cycle beginning (~5 ms after injection) when the accelerating rate is still comparatively small. The decrease of the slip-factor with higher injection energy used in the PIP-II reduces the RF voltage required for the longitudinal beam focusing, thus resulting in about the same requirements for the peak RF voltage for 20 Hz ramping rate. Figure 2.61 presents the time dependences of beam and RF system parameters in the course of low intensity beam acceleration. The RF waveform was tuned to keep a fixed value of the bucket size before transition and ~1.5 times larger value after it. The dependencies presented in the top two rows of the figure were computed assuming adiabatic longitudinal motion in the course of acceleration. The latter is not true in the close vicinity of transition and therefore the divergences for the bucket area and the bucket height do not describe actual beam behavior. The plots in the bottom row were computed by turn-by-turn particle tracking and therefore they describe the transition crossing accurately if the beam intensity is sufficiently small.

As will be seen, the PIP-II intensity requires significantly larger RF voltage. Results of simulations presented below satisfy the PIP-II requirements. They use the peak RF voltage of 1.18 MV. Reliable operations require that the Booster should be capable to operate without one cavity yielding the installed RF voltage of ~1.25 MV. It will be supported by 22 RF cavities (stations). This goal will be achieved as part of the PIP program. The present RF cavities and power amplifiers are adequate for the beam acceleration although minor modifications to the power amplifiers will be required due to 1.5 times larger beam power. Detailed simulations of transition crossing are presented in the following subsections.

Compared to the present Booster operation, the injection energy increase combined with the beam painting results in a significant decrease of the incoherent tune spread due to beam space charge. This effect is usually characterized by the space charge tune shift for particles with small betatron

and synchrotron amplitudes, which, for a Gaussian bunch, is equal to:

$$\delta\nu_{SC_{x,y}} = -\frac{r_p q N_b B}{2\pi\beta^2\gamma^3}\left\langle \frac{\beta_{x,y}}{\sigma_{x,y}\left(\sigma_x+\sigma_x\right)}\right\rangle_s . \qquad (2.9)$$

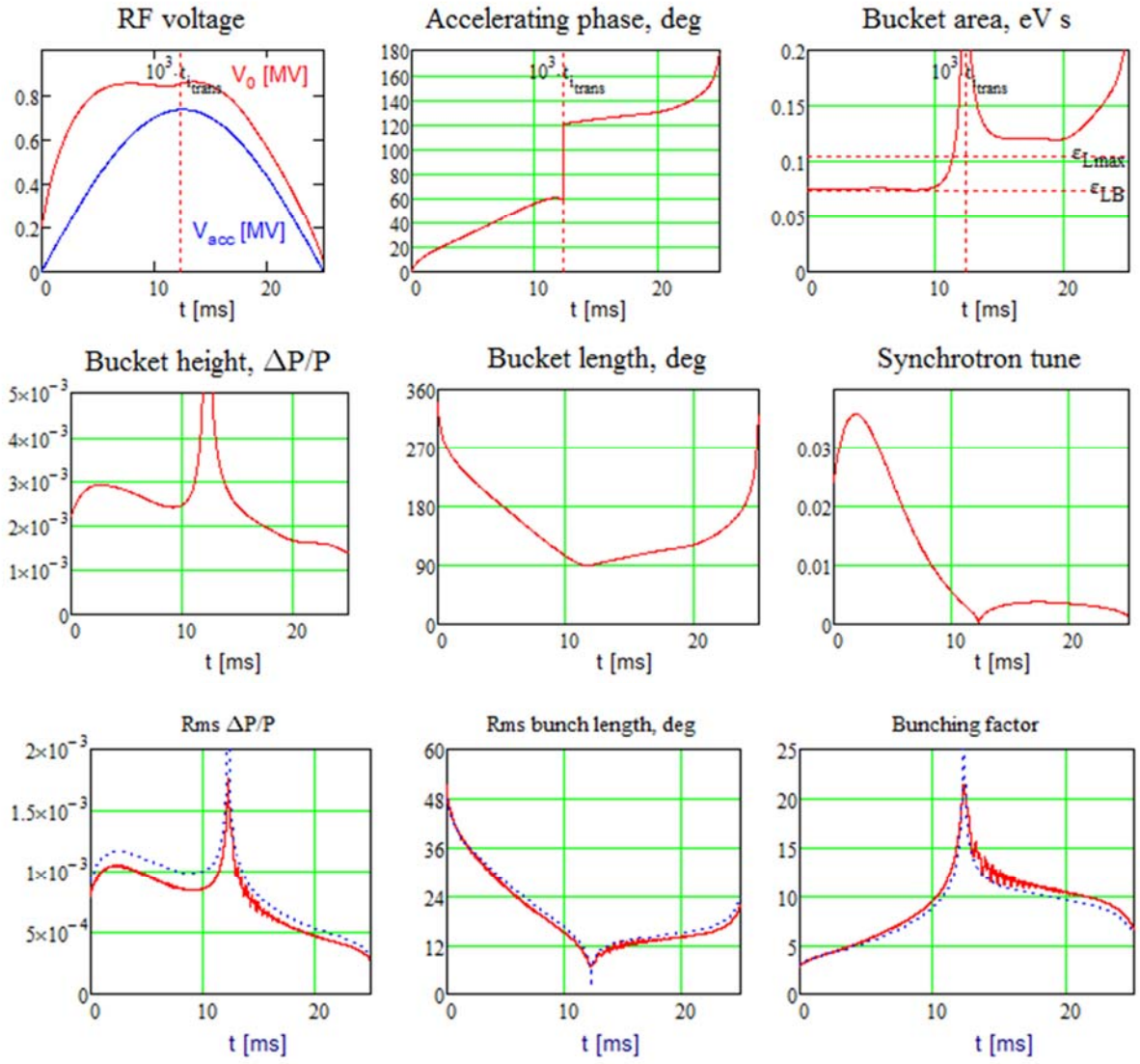

Figure 2.61: Beam and RF system parameters for acceleration of small intensity beam. The initial RF bucket size is 0.075 eV·s, and the 100% initial longitudinal emittance is equal to 0.06 eV·s. The red lines in the bottom row present the tracking results for a small intensity bunch, and the blue lines the results of adiabatic approximation.

Here N_b is the number of particles per bunch, β and γ are relativistic factors, $\sigma_x = \sqrt{\varepsilon_x\beta_x + D_x{}^2\sigma_p{}^2}$ and $\sigma_y = \sqrt{\varepsilon_y\beta_y}$ are the rms beam sizes, β_x and β_y are the beta-functions, D_x is the ring dispersion, ε_x and ε_y are the rms emittances, σ_p is the rms relative momentum spread, $< >_s$ denotes averaging along the ring circumference, and B is the bunching factor defined as: $B = \left(dN/ds\right)\big|_{\max} / \left(N_b q / C\right)$ with C being the ring circumference and q the harmonic number. The painting simulations discussed above result in a particle density in the bunch center which coincides with the particle density of

Gaussian beam with horizontal and vertical normalized rms emittances equal to 5 mm mrad. Note that the 95% emittance corresponding to the rms emittance of 5 mm mrad is equal to ~30 mm mrad, while the 95% emittance of the painted beam is 16 mm mrad. Thus, the transverse painting decreases the space charge tune shifts by about two times. Figure 2.62 presents the dependence of the space charge tune shifts on time within accelerating cycle. As one can see the space charge tune shifts do not exceed 0.2.

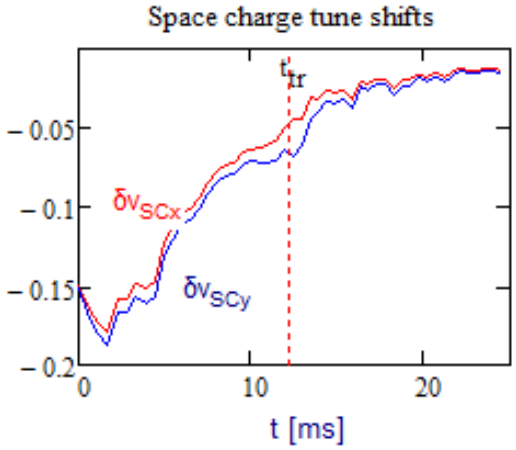

Figure 2.62: The betatron tune shifts due to beam space charge for horizontal and vertical planes within accelerating cycle. The reduction of tune shifts due to non-Gaussian shape of the particle distribution (see details of painting in Section 2.3.2.3) is taken into account. Bunching factor and momentum spread are taken from simulations of full intensity beam acceleration described in Section 2.3.5. Vertical line marks transition crossing.

For the present RF system the beam-induced voltage significantly exceeds the RF system voltage required for beam acceleration and capture. Figure 2.63 and 2.64 present the measured shunt impedance of the present Booster cavities, the beam induced voltage and the beam and cavity powers. As one can see, even at the maximum RF voltage, the beam-induced voltage (at resonance) exceeds the required RF voltage by almost 2 times. This ratio achieves its maximum of about 30 at the end of the accelerating cycle.

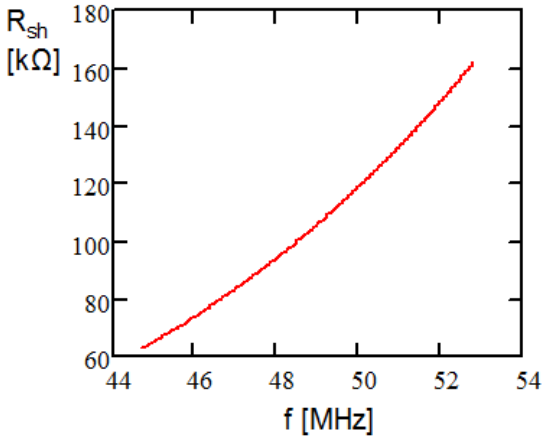

Figure 2.63: The shunt impedance of the Booster RF cavity in the frequency range required for PIP-II operation.

Note that the power loss in the cavity walls presented in Figure 2.64 assumes equal voltage distribution in all cavities and their perfect phasing. A practical way of obtaining small RF voltage

in the presence of large beam current is paraphasing of two groups of cavities. This technique is presently used in the Booster and will be used in the future for PIP-II. In this case, a small voltage is achieved by operating two groups of cavities with comparatively large and equal voltages with an RF phase difference close to 180 deg. That implies that power loss in the cavity walls will be significantly larger at the cycle beginning and the cycle end (where the RF voltage is small) than the value presented in Figure 2.64.

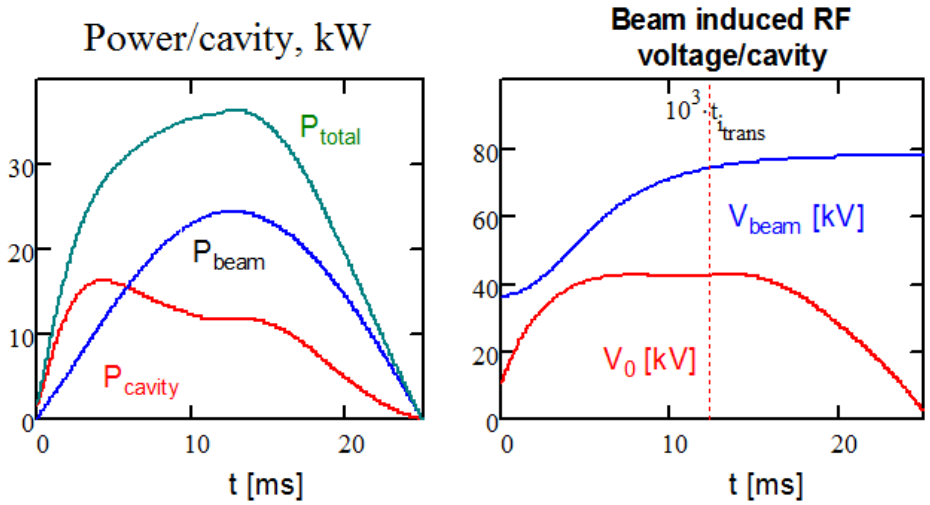

Figure 2.64: Left pane: dependences on time within accelerating cycle for the power loss in the cavity walls (red, $P_{cavity}=V_0^2/R_{sh}$), the beam power transferred to the beam (blue) and the total RF power to a cavity (green). Right pane: dependences on time within accelerating cycle for the total RF voltage per cavity (red) and the beam induced voltage. 22 accelerating cavities are implied. The presented cavity voltage is used in the simulations of full intensity beam acceleration described in Section 2.3.5.

An additional reduction of the space charge betatron tune shifts can be achieved with a double harmonic RF system. In this case the voltages of the fundamental (first harmonic) RF system and an additional RF system operating at the second harmonic can create a longitudinal potential well with a flat bottom resulting in a reduction of the bunching factor. The installation of the second harmonic RF system is planned for the presently proceeding Proton Improvement Plan (PIP). Note that relative misphasing of the first and second harmonic RF systems deteriorates the flat bottom of the potential well. That can result in an increase of longitudinal density and, subsequently, can lead to a particle loss. The required accuracy of relative phasing is about 5 deg. of the first harmonic frequency. Addressing the voltage stability and relative phasing will require a sophisticated low level RF.

2.3.4. Booster Longitudinal Impedance

To avoid the eddy currents that would be excited in a vacuum chamber by fast changing magnetic field the Booster does not have a vacuum chamber in the usual sense of this word, rather its beam aperture is formed by poles of laminated combined function dipoles. That greatly amplifies its longitudinal and transverse impedances.

To estimate the longitudinal impedance of such a "laminated" beam aperture we use the model presented in Ref. [32], where the longitudinal impedance of a flat laminated dipole with constant gap between poles is derived. The chamber geometry is presented in Figure 2.65. The results of Ref. [32] (see Eqs. (5.12) and (5.19) in there) can be rewritten in the following form, presenting the longitudinal impedance per unit length as a function of frequency:

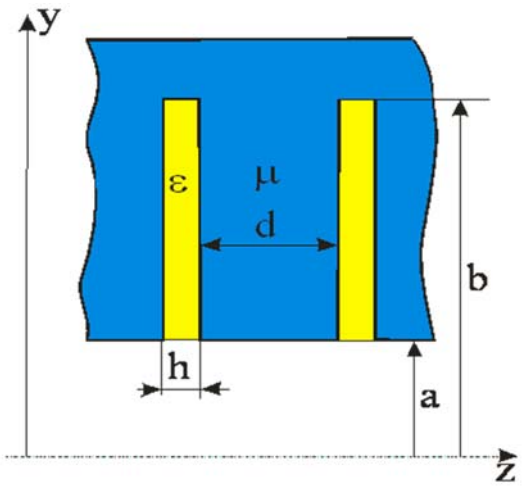

Figure 2.65: Geometry of the laminated beam aperture (or "vacuum chamber"). The beam moves in the z-direction. The chamber is infinite in x-direction (normal to the picture plane). The scale along z-axis is magnified for clarity.

$$Z_{\parallel_{LM}}(\omega) = iZ_0 \frac{\omega}{2\pi c} \int_0^\infty \frac{F_L(\xi)}{1 + F_L(\xi)\tanh\xi} \frac{d\xi}{\xi \cosh^2 \xi} \ , \tag{2.10}$$

where

$$\begin{aligned} F_L(\xi) &= \frac{h}{d+h} \frac{\xi}{k_y(\xi)} \left(1 + (1-i)\frac{\mu\delta_S}{h}\right) \tan\left(k_y(\xi)\left(\frac{b}{a} - 1\right)\right), \\ k_y(\xi) &= \sqrt{\frac{\varepsilon\omega^2 a^2}{c^2}\left(1 + (1-i)\frac{\mu\delta_S}{h}\right) - \xi^2} \ , \end{aligned} \tag{2.11}$$

$Z_0 = 4\pi/c \approx 377\ \Omega$, c is the light velocity, a is the half-gap between dipole poles, $(b - a)$ is the depth of laminations, ε is the effective dielectric constant of the filling (epoxy plus an insulating oxide layer), h is the distance between laminations[6], $\delta_S = c/\sqrt{2\pi\sigma_R\omega\mu}$ is the skin depth, σ_R is the steel conductivity, and μ is the steel permeability. At frequencies of interest the skin depth in soft steel is smaller than, or about the same as, the magnetic domain size, which greatly reduces the magnetic permeability and makes its imaginary part being non-zero. In the below estimate, we use the measured magnetic permeability of soft steel presented in Ref. [33]. The measurements for intermediate values of magnetic field were fitted to the following expression,

$$\mu(\omega) = \frac{26}{1 + i\omega/\omega_1} + \frac{9}{(1 + i\omega/(2\omega_2))(1 + 2i\omega/\omega_2)}, \quad \begin{aligned} \omega_1 &= 2\pi \cdot 7 \cdot 10^7 \ \mathrm{s}^{-1}, \\ \omega_2 &= 2\pi \cdot 3 \cdot 10^9 \ \mathrm{s}^{-1}, \end{aligned} \tag{2.12}$$

which plot is presented in Figure 2.66. Other parameters used in Eq. (2.10) are presented in Table 2.18. The steel conductivity was taken from Ref. [33]. Results of the numerical integration of Eq. (2.10) are presented in Figure 2.67. We assume here that the distance between laminations is constant, while in reality it is changing within each gap and from gap to gap in some uncontrolled way. Consequently, Eq. (2.10) has a quite limited accuracy and direct measurements of the dipole impedance are highly desirable. As shown in Ref. [33] the magnetic permeability at high frequency,

[6] The distance between laminations, h, was initially estimated from the known packing factor and then was adjusted to match observed and predicted shifts of accelerating phase with beam intensity.

the same as for DC case, depends on the magnetic field in a dipole. That results in a dependence of the dipole impedance on its magnetic field. The fitting of Eq. (2.12) was performed for high magnetic field so that it would represent the value of μ near transition crossing where an accurate estimate of impedance is critical for simulations.

Table 2.18: Parameters of laminations used for the impedance estimates of the Booster laminated dipoles

Dipole type	F	D	
Dipole length	2.89		m
Number of dipoles	48	48	cm
Half-gap, a	2.1	2.9	cm
Lamina half-height, b	15.2		cm
Lamina thickness, d	0.64		mm
Dielectric crack width, h	45		μm
Conductivity, σ	$2.07 \cdot 10^{16}$ ($2.3 \cdot 10^{6}$ Ω^{-1} m^{-1})		s^{-1}
Dielectric permittivity, ε	2.5		

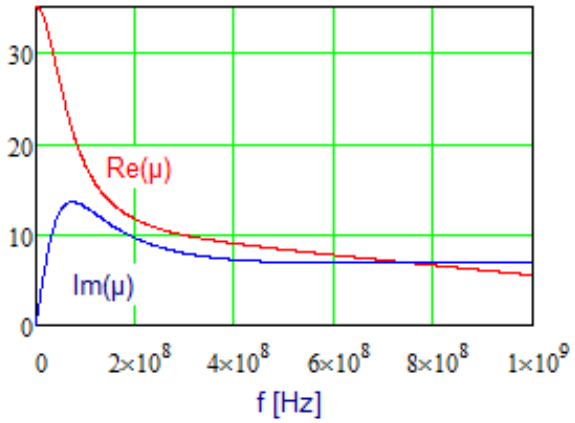

Figure 2.66: The dependence of magnetic permeability on frequency used for computation of the Booster longitudinal impedance.

Two types of impedance measurements were used. The first method is based on stretched wire measurements [34] of a single dipole impedance, and the second one is based on the shift of accelerating phase with beam intensity. The first method yields a dependence of single dipole impedance on the frequency, while the second one allows one to measure only the effective impedance but for the entire Booster.

Figure 2.68 presents results of the longitudinal impedance measurements for two spare Booster dipoles [34] performed with the stretched wire. As on can see from comparison of Figures 2.67 and 2.68 the measurements and the calculations are in a reasonable agreement for D-dipole. However, the agreement is much worse for the F-dipole. It is important to note that the measured impedance of the D-dipole is larger than that of the F dipole while theory predicts the opposite - the dipole with larger aperture should have smaller impedance. Most probably, it is related to a difference in details of lamination packing in these two dipoles. Therefore, we expect that each dipole has a unique impedance. Consequently, a beam-based measurement is the only reliable way to measure the

Booster impedance with required accuracy. Unfortunately, the measurements with bunched beam do not measure the dependence of impedance on frequency, and measurements with continuous beam at the energy of transition crossing cannot be done. Therefore, taking into account that the frequency dependencies presented in Figures 2.67 and 2.68 are sufficiently close, we use the theoretical prediction of Eq. (2.10) where we adjust the gap between plates to match the measured and observed shifts of accelerating phase with intensity.

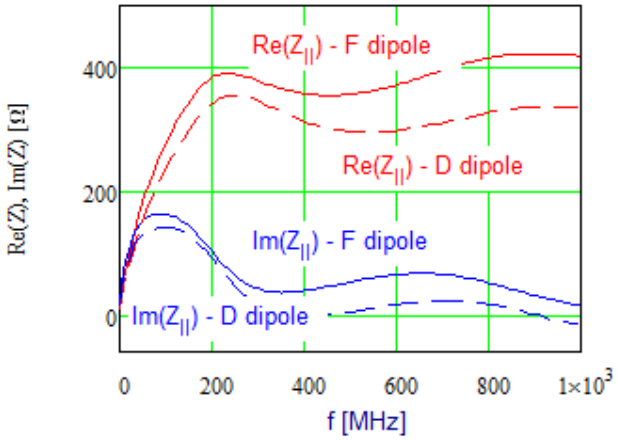

Figure 2.67: The dependences of longitudinal impedance on frequency computed with Eq. (2.10) for the Booster F and D dipoles for parameters presented in Table 2.18.

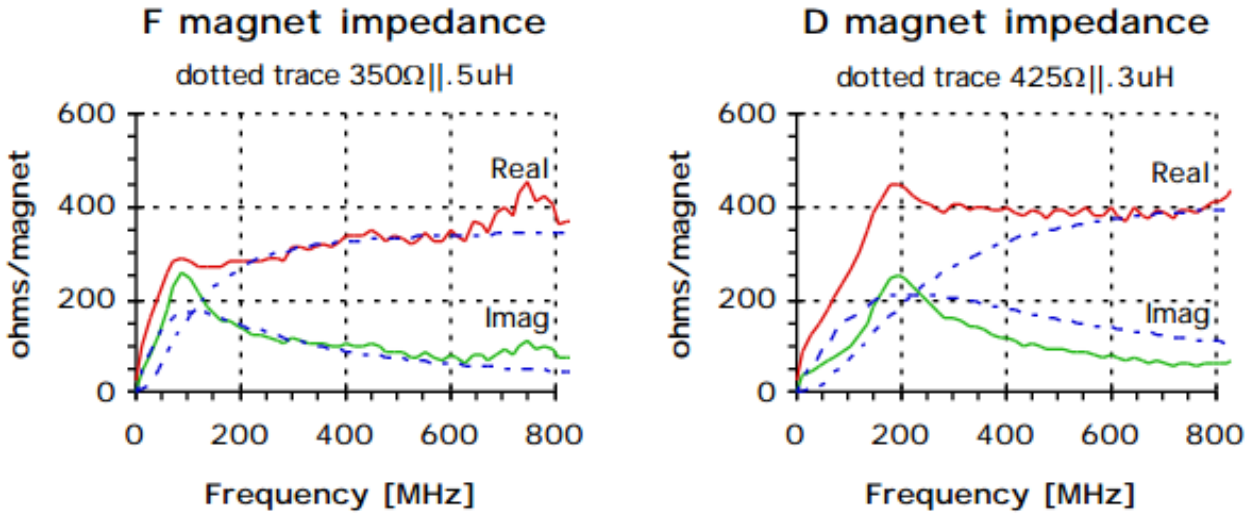

Figure 2.68: Dependence of longitudinal impedance of Booster dipole on the frequency measured with the stretched wire method for F and D dipoles [34].

The beam-based measurements of the effective Booster impedance have been based on the measurements of the accelerating phase shift with beam current [35]. To achieve this we acquired row analog signals coming from the resistive wall monitor (measuring the beam current), the RF sum and the horizontal BPM used in the LLRF for measurements of momentum offset. The sampling rate required to digitize the longitudinal density distribution for each bunch is quite high ($\geq 2 \cdot 10^{10}$ s^{-1}). If the measurements of the entire accelerating cycle would be carried out it would result in $\sim 6.6 \cdot 10^{8}$ samples per channel. This volume of data significantly exceeds memory of the scope used for measurements. Therefore, the data was acquired near injection and around transition crossing. This data was sufficient to reconstruct the beam dynamics for the entire accelerating cycle. The data

analysis allowed us to perform calibration for the amplitude of RF voltage near transition to better than 1% and relative timing between RF and beam signals to better than 1 deg. [36]. The measured shift of accelerating phase with beam intensity is presented in Figure 2.69. Together with the RF voltage calibration it was employed to finalize the Booster impedance value used in the beam acceleration simulations described in the following section.

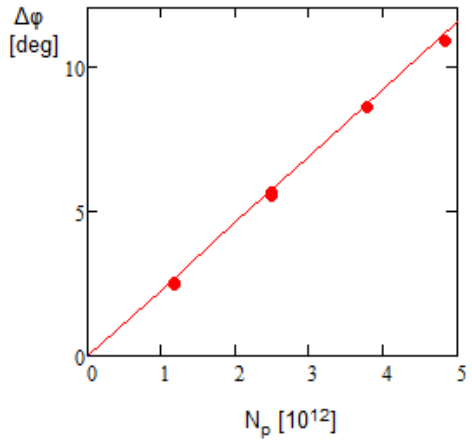

Figure 2.69: The dependence of accelerating phase on the number of particles in the beam shortly before transition; 82 bunches fill 84 RF buckets; the RF voltage is 800 kV and the accelerating phase for zero current is about 50 deg.

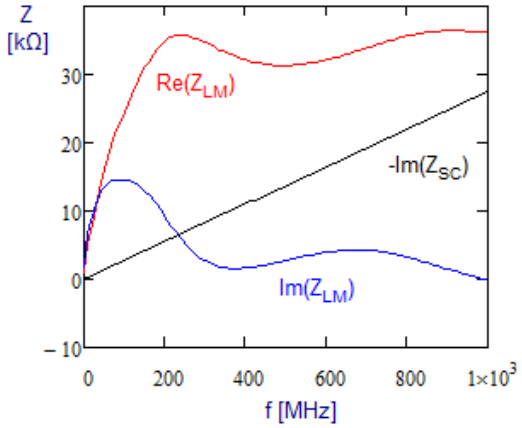

Figure 2.70: The longitudinal impedances of beam space charge, Z_{SC}, and all Booster dipoles, Z_{LM}, used in simulations of the beam acceleration.

The longitudinal impedance due to bunch space charge is:

$$Z_{\|_{SC}}(\omega) \approx -iZ_0 \frac{\omega}{\beta\gamma^2\omega_0} \ln\left(\frac{r_c}{1.06\,\sigma_{tr}}\right), \quad \frac{r_c}{\sigma_\perp} \geq 2\,, \tag{2.13}$$

where β and γ are the beam relativistic factors, ω_0 is the revolution frequency, r_c is the vacuum chamber radius and $\sigma_\perp$ is the rms transverse beam size. The space charge impedance diminishes fast with beam acceleration. However its contribution is still essential at the transition crossing. Figure 2.70 compares the space charge impedance and the total resistive wall impedance of all Booster dipoles. Other sources of the impedance are small and can be safely omitted in the described below simulations of beam acceleration.

2.3.5. Transition Crossing

The software used for simulation was benchmarked on the measurements of beam acceleration in the Booster [36, 37]. The measurements resulted in dependences on time for the RF voltage, the accelerating phase, the momentum offset and rms bunch length near transition crossing. The actual transition crossing time and the second order slip-factor[7] were not known to sufficient accuracy and were used as free parameters. An adjustment of these two parameters yielded good agreement between simulations and measurements. Similar to the actual accelerator the dipole and quadrupole dampers were used in simulations to stabilize the beam.

The simulation for PIP-II were based on the same software, which was developed for analysis of beam acceleration in the present Booster. However, there are a few differences, which have to be taken into account:

- The injection energy is increased from 400 to 800 MeV
- The beam injection is much longer and it includes the longitudinal painting as was described in Section 2.3.2.3
- The repetition rate is increased from 15 to 20 Hz and
- The beam intensity is increased to $6.5 \cdot 10^{12}$.

In addition, a small Q-jump was used in simulations to reduce the emittance growth related to the transition crossing. The jump is supported by existing trim quadrupoles which currents are switched from positive to negative at the maximum rate supported by present power supplies. The peak power supply voltage of 170 V yields the current rate of 63.7 A/ms and the quad strength rate of 1.58 kG/ms. The simultaneous ramping for all 24 quads located in the short straights with β_x=34 m results in the rate of momentum compaction change of $d\alpha/dn$ =$7.56 \cdot 10^{-6}$ per turn. For a ramp duration of 200 turns it results in the total horizontal tune change of ~0.09 (±0.045).

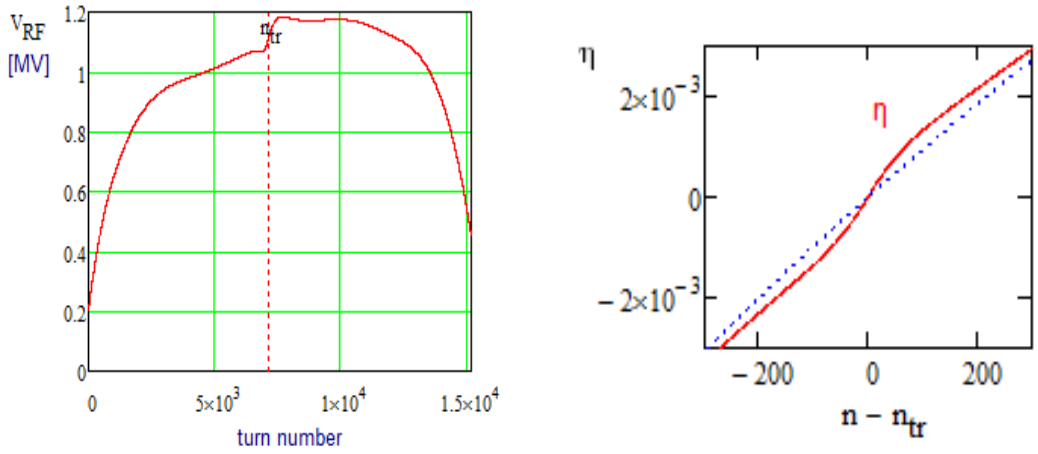

Figure 2.71: Dependence of RF voltage on the turn number (left) and dependance of slip-factor, η, on the turn number counted from transition crossing (right). The red dashed line shows the location of transition crossing. The blue dashed line presents the slip-factor in the absence of Q-jump.

[7] Here we define the 2nd order slip-factor, η', so that the longitudinal relative particle displacement after one revolution is equal to: $\Delta L / L = \left(\alpha - 1/\gamma^2\right)\Delta p/p + \left(\alpha' + 3\beta^2/(2\gamma^2)\right)(\Delta p/p)^2 + \ldots = \eta \Delta p/p + \eta'(\Delta p/p)^2 + \ldots$, $\eta' = \alpha' + 3\beta_{tr}^{\ 2}/(2\gamma_{tr}^{\ 2})$, were β_{tr} and γ_{tr} are relativistic factors at transition, and α and α' are the first and second order momentum compaction factors, respectively.

Figure 2.71 shows the RF voltage and the slip-factor used in the described below simulations. As one can see, the peak RF voltage is significantly higher than the maximum accelerating rate of 738 kV/turn achieved in the middle of accelerating cycle (see Figure 2.61). This large voltage is required for reduction of the longitudinal emittance growth related to the transition crossing. It is more important after transition where it suppresses the growth of tails. Therefore, the RF voltage after transition is close to its maximum of 1.2 MV. Using a Q-jump, as shown in the right pane of Figure 2.71, increases the rate of slip-factor growth by 1.8 times and results in an additional reduction of the emittance growth related to the transition crossing.

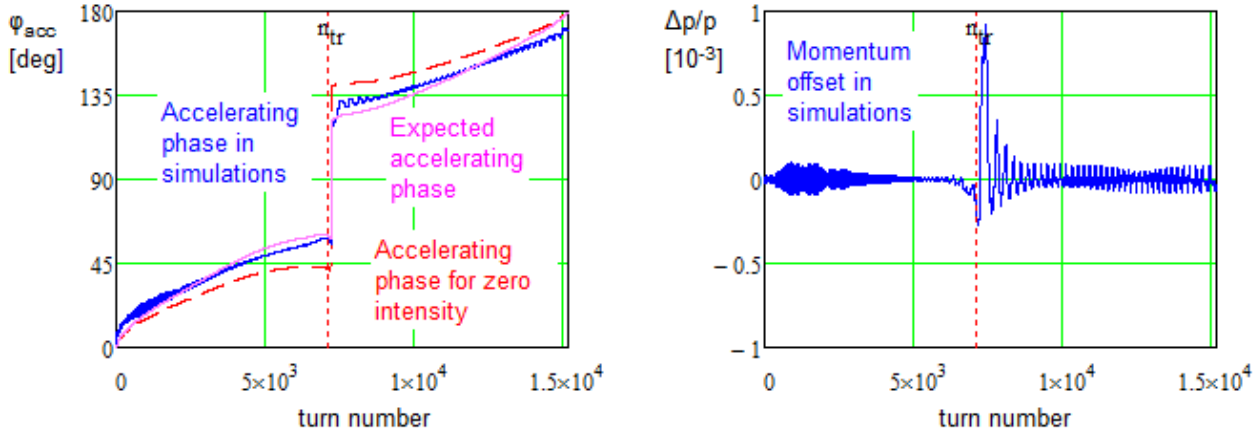

Figure 2.72: Dependence of accelerating phase (left) and the average momentum offset (right) on the turn number.

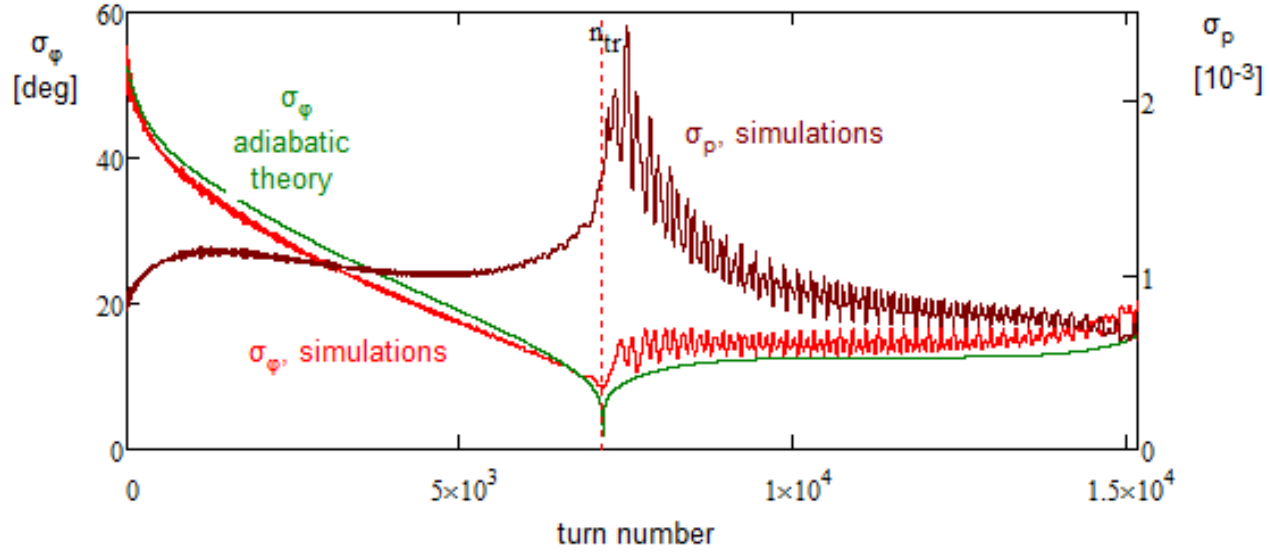

Figure 2.73: Dependence of rms bunch length, σ_ϕ, and rms momentum spread, σ_p, on the turn number.

Figure 2.72 shows the dependence of accelerating phase on the turn number. The red dashed line presents the accelerating phase required for acceleration of a zero intensity beam. An increase of beam intensity results in an impedance-induced beam deceleration. It shifts the accelerating phase before and after transition (see Figure 2.69) and results in a reduction of transition crossing phase jump as shown by magenta line representing the accelerating phase used in the simulations. The

value of the jump was adjusted to minimize oscillations of the average momentum, as presented in the right pane of Figure 2.72. Finally, the blue line in the left pane presents the actual accelerating phase obtained in the simulations. As one can see the transition crossing excites oscillations of the accelerating phase and the beam average momentum. It is related to bunch length oscillations excited by transition crossing (see Figure 2.73), which subsequently introduce oscillations of impedance-induced beam deceleration and the average momentum. These oscillations are suppressed by the feedback system built into the simulations and operating similar to the radial position feedback used in the real Booster. The jump of accelerating phase was delayed by 70 turns. This delay significantly reduces the emittance growth excited by the transition crossing.

Figure 2.73 shows the dependence of rms bunch length on the turn number. A mismatch between the adiabatic theory and simulations in the first half of the cycle (before transition) is mainly related to the focusing force non-linearity due to large bunch length. This non-linearity of focusing strength as well as the impedance-induced voltage are not accounted in adiabatic theory. However, as one can see the bunch length is smoothly changed before transition and there is no longitudinal emittance growth. Transition crossing results in almost instantaneous emittance growth. The bunch becomes quite short near transition and generates enormous voltage, which greatly distorts the bunch phase space in just few tens of turns. This effect is greatly amplified by the absence of synchrotron motion near transition. Figure 2.74 presents the bunch distributions shortly before and after transition and the corresponding impedance-induced voltage. The peak of this voltage is about 250 kV. It causes a sag of the beam energy in the bunch center yielding an unrecoverable growth of the effective emittance. The quadrupole damper used in simulations operates similarly to the quadrupole damper in the actual Booster. It prevents uncontrolled emittance growth after transition crossing.

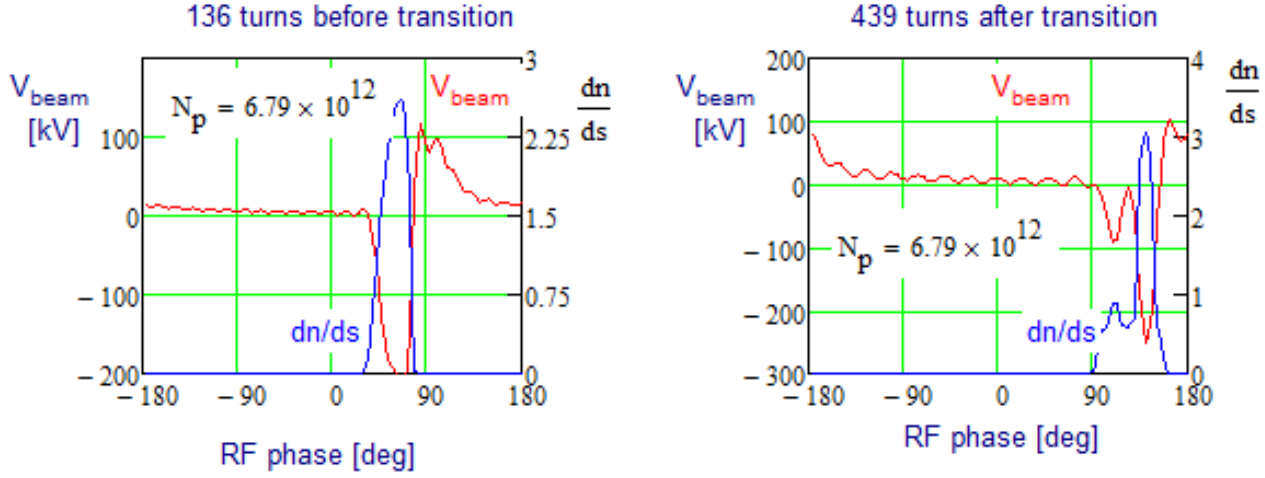

Figure 2.74: Dependences of beam distribution (blue lines) and beam indfuced voltage (red lines) on the RF phase shortly before and after transition. The phase of 90 deg. corresponds to on-crest acceleration.

The Booster simulations showed a strong effect of the second order slip-factor on the transition crossing. The second order slip-factor was adjusted to minimize the emittance growth. The optimal value for the second order momentum compaction is equal to $\alpha_p = -0.09$ ($\eta_p = -0.041$). The value of the second order slip-factor depends on the tune chromaticity; and its value at transition is controlled by the timing of the sextupole polarity flip required to support transverse beam stability before and after transition. Figure 2.75 presents dependence of the second order momentum compaction on the tune chromaticity computed for present Booster optics near transition. One can see that the second order slip-factor can be varied in the required range. It depends linearly on the horizontal

chromaticity and is weakly affected by the vertical one.

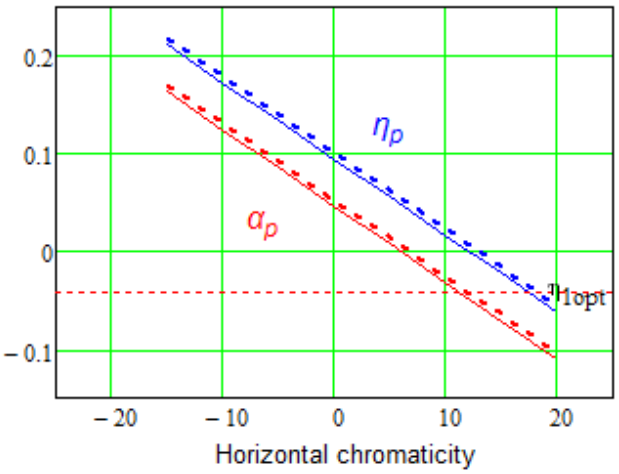

Figure 2.75: Dependance of the second order momentum compaction, α_p, and slip-factor, η_p, on tune chromaticity computed for present Booster optics near transition; solid lines – ξ_v=0, dashed lines – ξ_v=4. Dashed horizontal line shows the optimal slip-factor, η_{1opt}=–0.041.

An increase of particle intensity greatly amplifies the Booster sensitivity to errors. In particular, the required accuracy for the second order slip-factor should be within ±0.02, and the accuracy for timing of the accelerating phase jump needs to be within ±5 turns. The already achieved accuracies of these parameters are close to the above requirements, and their achievement for PIP-II should not present an outstanding problem. Note that presently there is no reliable procedure to determine the transition crossing time and the second order slip-factor at the transition with the required accuracy. Therefore, detailed optics simulations are expected to be helpful in resolving this issue. As presently, the final word will be with empirical adjustments. Note that in the above simulations we did not account for the voltage induced by the beam in the accelerating cavities. Presently, it results in significant variations of accelerating voltage near transition. However, the simulations for the existing Booster show that these details do not play a significant role in the emittance growth and therefore these voltage variations were not accounted. The PIP-II beam intensity increase will result in larger beam induced voltage and, consequently, some improvements in the local cavity feedbacks will be required to suppress these voltage variations. A usage of adaptive feedforward system could greatly simplify requirements to these feedbacks.

Figure 2.76 presents the dependence of effective beam emittance on the turn number. The emittance is defined as $\varepsilon_{L95\%} = 6\pi\sigma_p\sigma_x$, which corresponds to the definition of 95% emittance for a Gaussian beam. Here σ_p is the rms momentum spread and σ_x is the rms bunch length. One can see almost instant emittance growth after transition crossing. Some slow reduction of the emittance after the jump is related to the imperfection of this definition. However, the emittance growth at the cycle end is real and it is increased if the RF voltage in the second half of the accelerating cycle is reduced. The left pane in Figure 2.77 shows the particle phase space at the end of acceleration. As one can see, the majority of particles are located inside the required phase space ellipse with 0.1 eV·s area. Note that this ellipse is shifted from the coordinate's origin. It is related to the impedance-induced beam deceleration and residual synchrotron oscillations. The ellipse parameters are shown in the figure. The right pane shows the corresponding particle distribution over single particle emittance (ascribed phase space) and its integral showing the percentage of particles located in a given phase space. As one can see about 98% of particles are located in the target phase space of 0.1 eV·s.

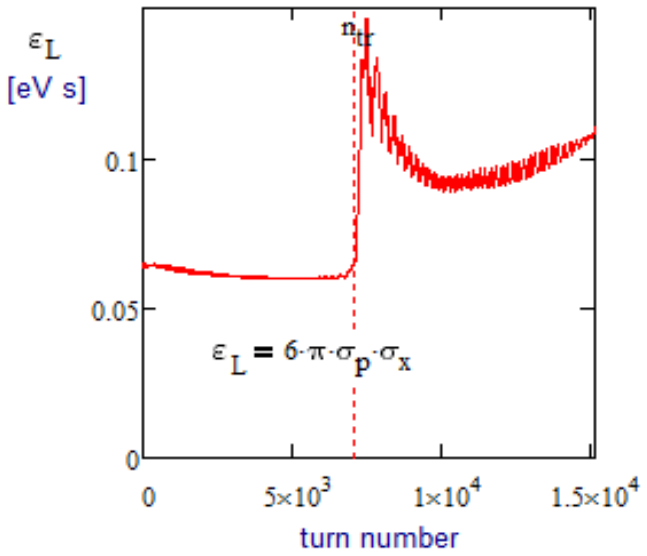

Figure 2.76: Dependence of effective longitudinal emittance on the turn number.

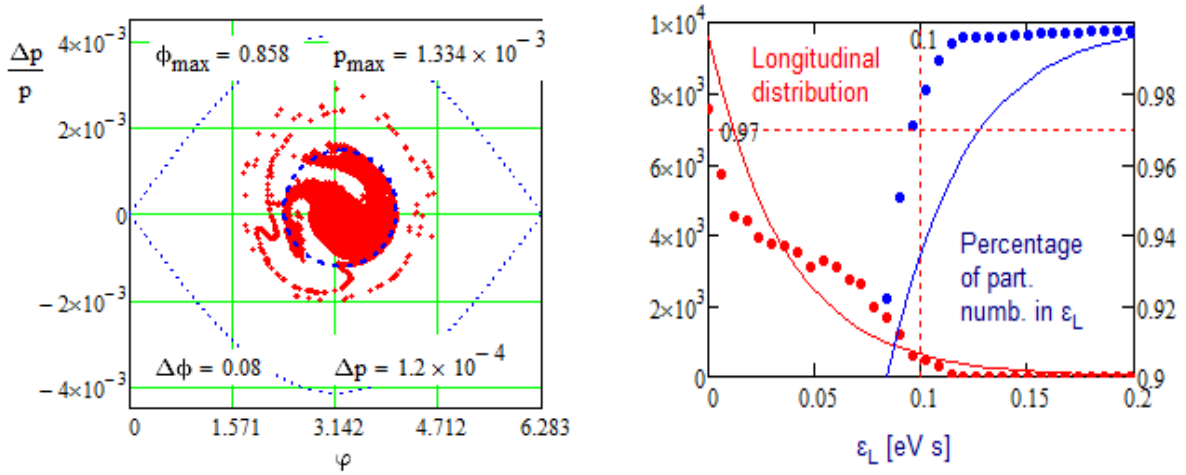

Figure 2.77: The phase space of at the acceleration end (left) and corresponding longitudinal distribution over the single particle emittance and its integral. 50,000 particles were used in this simulation. Dashed lines in the left pane show the boundaries of RF bucket and the target emittance of 0.1 eV·s.

2.3.6. Modifications to the Booster Magnet System Required for 20 Hz Operation

The present system has 96 magnets in a 24 cell arrangement (see Figure 2.78). These are driven by four power supplies that are the MR (Main Ring) style, 720 Hz update rate SCRs (Silicon-Controlled Rectifier). Their regulation is based on magnetic field measurements in a reference magnet with B-dot coil and transductor electronics. A sinusoidal drive signal excites the resonant system with a quality factor of about 40 for 15 Hz operation. Corrections for losses and line voltage variations are done by a card in a VXI crate. Regulation is good to about a part in 4000.

The conversion of GMPS (Gradient Magnet Power Supply) controls from 15 to 20 Hz does not look difficult. The system was designed to run at 10 GeV and therefore it is capable to operate at

higher voltage and power compared to the present 8 GeV, 15 Hz operation.

To verify that the Booster dipoles can operate at 20 Hz an experimental test was carried out [38]. Measurements were performed on both a Booster gradient magnet and a Booster choke with the intent to compare the 15 Hz losses with the 20 Hz losses for the proposed Booster upgrade. The analysis carried out after the measurements suggests that running the Booster at 20 Hz with magnet current ramping in the same range as for the present operation will require about 3.9% more power. To increase the resonant frequency the resonant capacitor at each "Girder" must decrease from ~8.33 mF to ~4.69 mF. As result, the capacitor voltage will increase by about 32% with a subsequent slight increase in the rms current for the choke, magnets and capacitors. This also implies that the rms current per μF will increase as well. The girder drive voltage will increase by about 9.2 V (p-p). The present magnet power system runs on 4 power supplies but can operate with only 3 supplies. Booster at 20 Hz would require all 4 power supplies to operate.

To support effective longitudinal painting the pulse-to-pulse relative stability of injection magnetic field has to be better or about 10^{-4}. It is almost an order of magnitude better than the present stability. Such stabilization can be achieved by direct stabilization of magnetic field ramp or using field correction with dipole correctors, which are controlled by field measurement in a reference dipole.

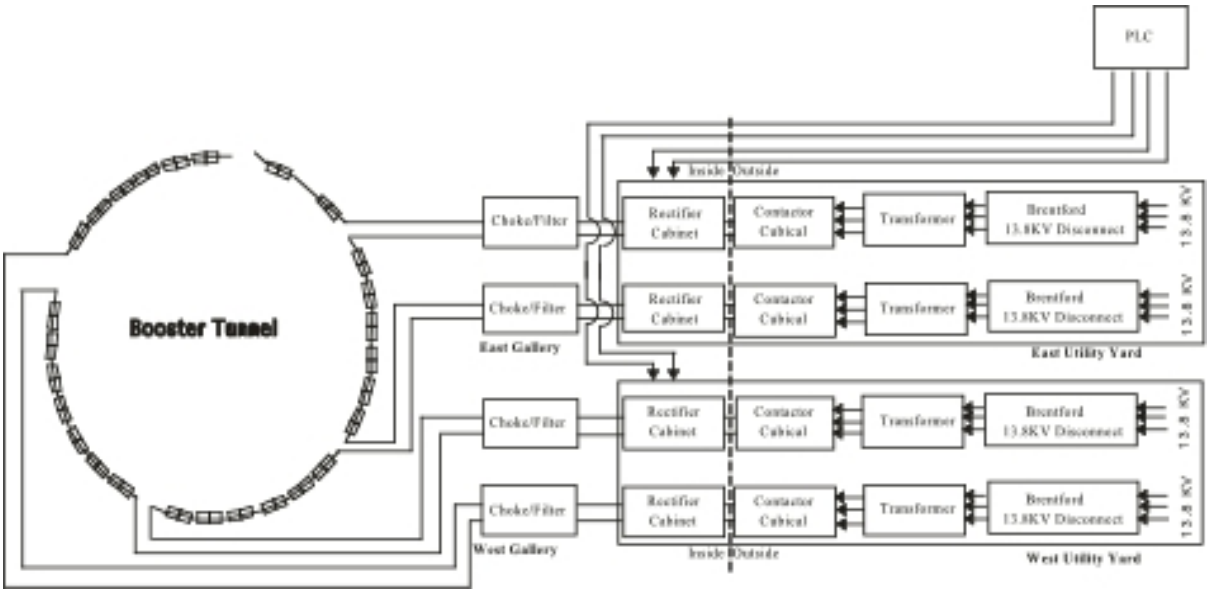

Figure 2.78: Schematic of the Booster magnets power system.

2.3.7. Transverse Beam Instabilities

The main challenges for beam stability in the Booster are associated with instabilities at injection and transition. The longitudinal instability at transition is considered elsewhere [39] and is not discussed below. Table 2.19 provides the main beam parameters used in the instability studies presented below.

The Booster impedances are dominated by the impedances of the laminated magnets. The analytical model for these impedances is developed in Ref. [32, 40, 41] and corresponding parameters required to compute them are presented in Table 2.18.

The transverse impedances of the focusing and defocusing magnets are shown in Figures 2.79 and 2.80. The horizontal and vertical impedances of the entire Booster and the corresponding wakes are averaged with beta-functions. The corresponding plots for the specified average beta-functions at

the magnet locations (β_{xF}, β_{yF}, β_{xD}, β_{yD}) = (30m, 7m, 11m, 18m) and the average beta $\bar{\beta}$ =11m are shown in Figures 2.81 and 2.82.

Table 2.19: Beam parameters used in estimates of Booster transverse instabilities

	Requirement	
Bunch population, N	$8.3 \cdot 10^{10}$	
Longitudinal emittance, rms, $\varepsilon_{\|}=\sigma_z\sigma_E$	4.8	meV·s
Maximum RF Voltage , V	0.75	MV
Maximum acceleration rate, $\dot{\gamma}$	0.5	ms^{-1}
Transition gamma, γ_t	5.47	

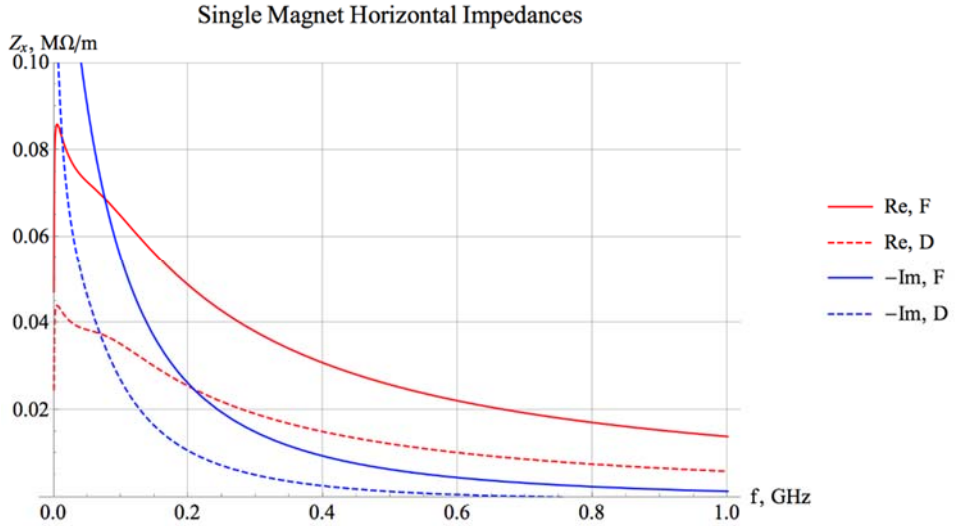

Figure 2.79: Horizontal impedances of the focusing and defocusing magnets.

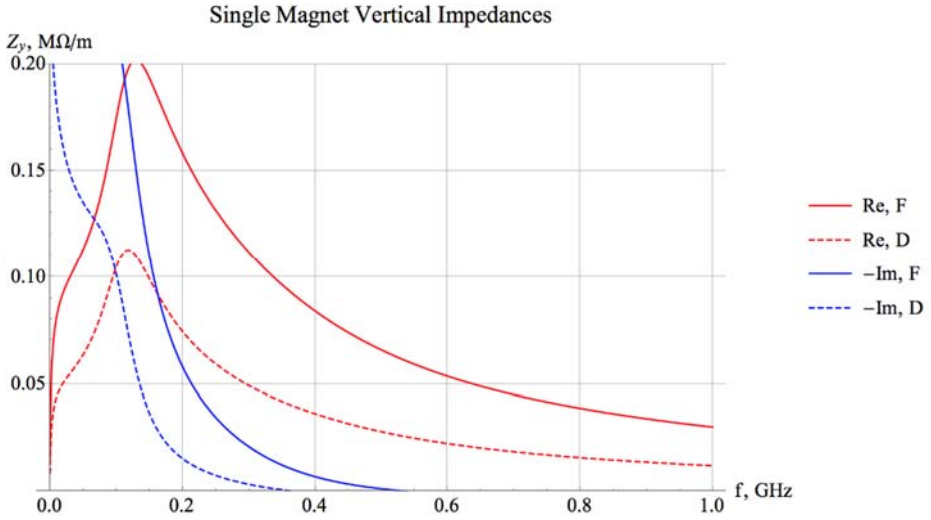

Figure 2.80: Vertical impedances of the focusing and defocusing magnets.

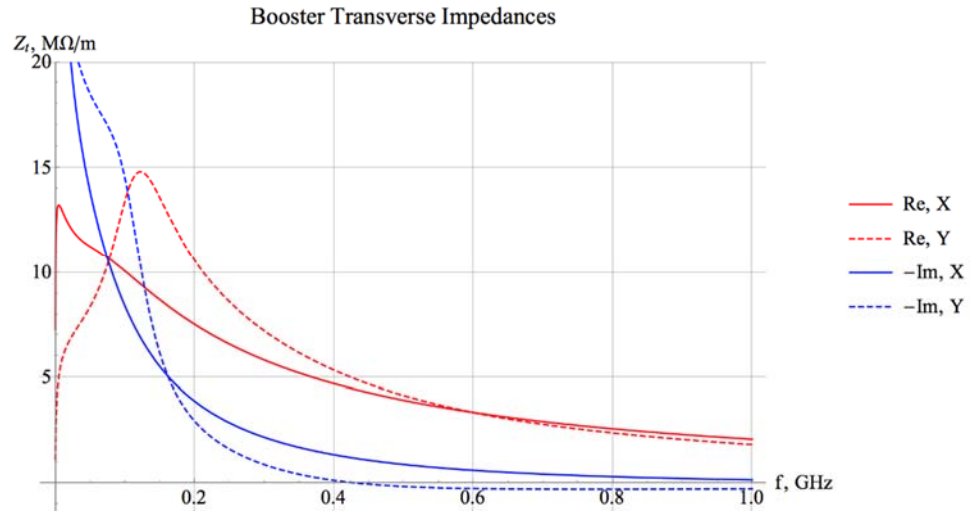

Figure 2.81: Transverse impedances of the Booster.

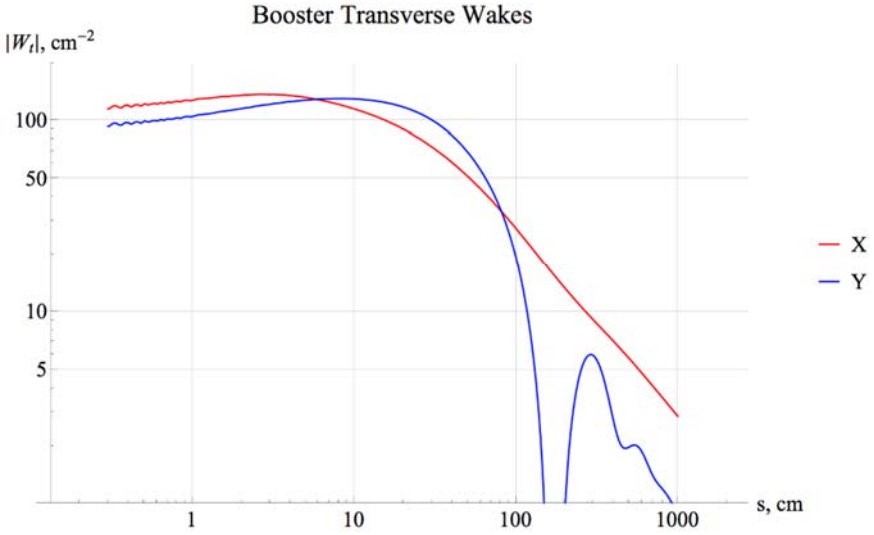

Figure 2.82: Horizontal and vertical wakes of the Booster.

For multi-bunch beams with strong space charge [42], the modes are characterized by two indexes: the single-bunch (head-tail, or intra-bunch) index n, and the coupled–bunch (inter-bunch) index μ. At the first order of the perturbation theory over the wake function, the coherent tune shift $\Delta\nu_{n\mu}$ of the mode $|n,\mu\rangle$ is proportional to the sum of single- and coupled-bunch diagonal matrix elements of the wake function [42,43]:

$$
\begin{aligned}
&\Delta\nu_{n\mu} = -\frac{Nr_p\bar{\beta}\left(\hat{W}_n^{\mathrm{SB}} + \hat{W}_{n\mu}^{\mathrm{CB}}\right)}{4\pi\beta^2\gamma} \equiv \Delta\nu_{n\mu}^{\mathrm{SB}} + \Delta\nu_{n\mu}^{\mathrm{CB}};\\
&\hat{W}_n^{\mathrm{SB}} = \iint ds ds' \bar{W}(s-s')\exp(i\zeta(s-s'))\rho(s)\rho(s')y_n(s)y_n(s');\\
&\hat{W}_{n\mu}^{\mathrm{CB}} = W_\mu^{\mathrm{CB}}\left|I_n(\chi)\right|^2;\ \ I_n(\chi) = \int ds \exp(i\chi s/\sigma_s)\rho(s)y_n(s);\\
&W_\mu^{\mathrm{CB}} = \sum_{k=1}^{\infty}\bar{W}(kC/M)\exp(ik\psi_\mu);\quad \psi_\mu = 2\pi\left(\{Q_b\}+\mu\right)/M;\quad \mu = 0,1,\ldots,M-1.
\end{aligned}
\tag{2.14}
$$

Here N is the number of particles per bunch, r_p is the proton classical radius, β and γ are the relativistic factors, $\chi = \xi\sigma_s / (R\eta) \equiv \omega_\xi \sigma_\tau$ is the head-tail phase (see Eq. (6.187) in Ref. [44]), ξ is the chromaticity, η is the slip-factor, $\rho(s)$ is the normalized line density, $y_n(s)$ is the n-th head-tail eigen-function, M is the number of bunches, and $\{Q_b\}$ is a fractional part of the betatron tune. At sufficiently small head-tail phase, the single-bunch growth rate can be neglected below the transverse mode coupling instability (TMCI) threshold, while the coupled-bunch growth time is calculated as $[\omega_0 \,\mathrm{Im}(\Delta\nu_{00}^{CB})]^{-1} = 80$ μs for the horizontal direction, in agreement with Ref. [45]. A feedback can be taken into account similarly to the coupled-bunch wake [43]; for a bunch-by-bunch damper with a gain g that yields the damping rate:

$$\mathrm{Im}(\Delta\nu_{n\mu}) = -g\left|I_n(\chi)\right|^2 . \tag{2.15}$$

To make the description complete, the Landau damping has to be taken into account. To do that, the estimations of Landau damping suggested in Ref. [42] have to be compared with dedicated tracking simulations, *e.g.* with the Synergia [46]. When this is done and the full simulation scheme made complete, predictions and recommendations for various operation scenarios could be derived. An application of the bunch-by-bunch damper is known to be able to reduce the growth rate several times [47].

At transition, the strong head-tail instability is suppressed by the chromaticity, which threshold is proportional to the bunch population. Thus, an increase of the beam intensity by a factor of 1.5 compared with the current value would require similar growth of the chromaticity.

2.4. Recycler and Main Injector Modifications

2.4.1. Technical Requirements and Scope

The performance requirements of the Main Injector/Recycler complex are summarized in Table 2.20. The Recycler has recently been reconfigured as a proton accumulation ring in support of the NOvA experiment. For PIP-II an increase in beam intensity of 50% over current operations is required. It will be accompanied by a modest (10%) decrease in the Main Injector cycle time for 120 GeV operation. The primary requirement on the Recycler is to slip-stack twelve Booster batches and to deliver this accumulated beam to the Main Injector in a single turn. In order to maintain losses at current levels the efficiency of this operation has to be at least 97%.

Table 2.20: Main Injector/Recycler requirements for 0.9-1.2MW operations at 60-120GeV

Performance Parameter	Requirement	
Particle Species	Protons	
Injection Beam Energy (kinetic)	8.0	GeV
Extracted Beam Energy (kinetic)	60-120*	GeV
Protons per Pulse (injected)	7.72×10^{13}	
Protons per Pulse (extracted)	7.49×10^{13}	
Slip-stacking Efficiency	97	%
Controlled 8 GeV losses to Abort	0.8	%
Controlled 8 GeV losses to Collimators	1.5	%
Uncontrolled 8 GeV losses	0.5	%
Transition Losses	0.2	%
Cycle Time	0.7-1.2	s
Beam Power	1.0-1.2	MW
Beam Emittance (95%, normalized)	20	mm-mrad
Bunching Factor	2	
Peak Laslett Tune Shift in MI acceleration	-0.06	

* The Main Injector is capable of maintaining beam power of 1.2 MW for energy range 80-120 GeV.

In order to provide the RF power required to accelerate 7.5×10^{13} protons three options could be considered:

1. Operate the current RF cavities with two power tubes instead of one in a push-pull configuration. This will require doubling of the number of modulators and solid-state drivers.
2. Use a new more powerful power tube, such as the EIMAC 4CW250,000B. This will require a new mounting configuration (to accommodate the much longer tube), new modulators, and upgraded power amplifier cooling.
3. Replace the entire RF system with a new one (new cavities and PAs). The advantage of this solution is that it can accelerate enough intensity to reach 2.3 MW in the next round of the Accelerator complex upgrade.

Options 1 and 2 will be considered for PIP-II in more detail since they are substantially less expensive

than Option 3.

2.4.2. Slip-stacking in the Recycler

To be ready for the next Booster injection in time, the beam separation for slip-stacking in the Recycler has to be 1680 Hz or 33 MeV (one Booster batch slippage in one Booster tick). The figure of merit in slip-stacking is the parameter alpha that relates the frequency separation in the synchrotron frequency unit (f_s) or the doubled energy separation in the bucket height unit (H_B):

$$\alpha \equiv \frac{\Delta f}{f_s} = 2\frac{\Delta E}{H_B} \quad . \tag{2.16}$$

For α=2, the hypothetical independent buckets overlap 50% in energy, and the single particle motion is chaotic everywhere within them. The case of $\alpha = 4$ gives tangent boundaries for the hypothetical buckets and in the case of $\alpha = 8$ there is space for a complete empty bucket between the upper and lower hypothetical buckets. In practice, we have found that a value of α greater than 5 is adequate. Note that for the given frequency separation further increase of α does not yield larger RF bucket size (area of stable motion). A plot of α as a function of the RF voltage for 1680 Hz separation is shown in Figure 2.83. From that figure we can see that an RF voltage of 140 kV meets our requirements.

The choice of RF voltage determines the area of longitudinal phase space where particles will survive for a sufficiently long time. Figure 2.84 shows the particles in the initial matching beam contours that survive after 300 msec. The largest beam contour with no particle loss corresponds to an emittance of 0.10 eV-sec (±4.2 nsec, ±8.0 MeV). If we want slip-stacking with 97% efficiency then 97% of particles from the Booster should be included in that matching contour.

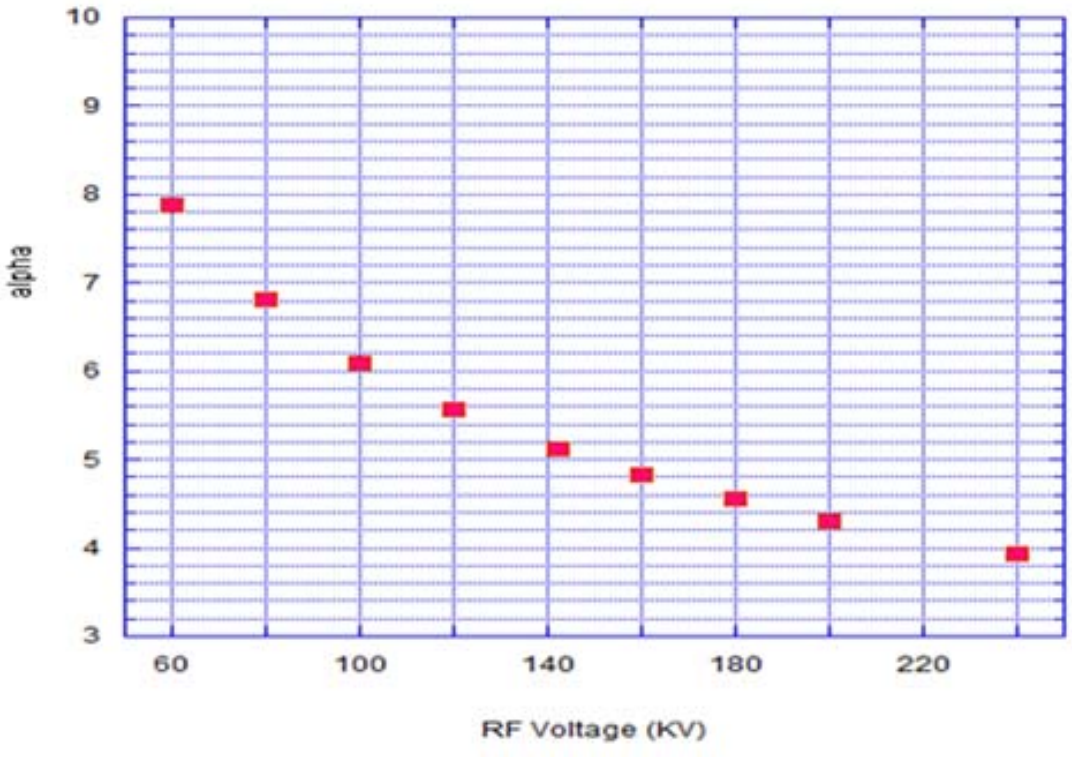

Figure 2.83: α vs. RF voltage for 1680 Hz separation.

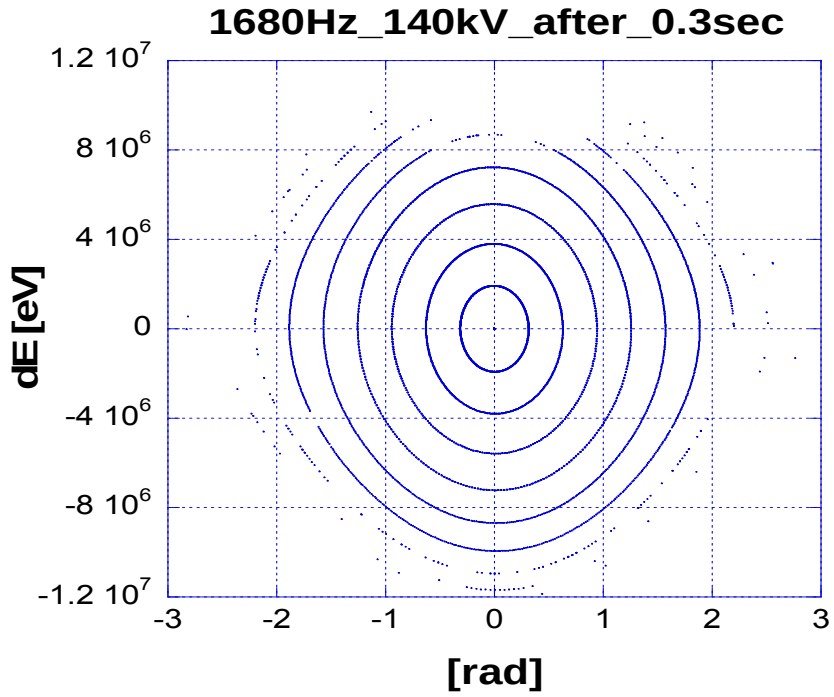

Figure 2.84: Particles on initial matching contours in a 140 KV bucket after 300 ms of slip-stacking with 1680 Hz separation.

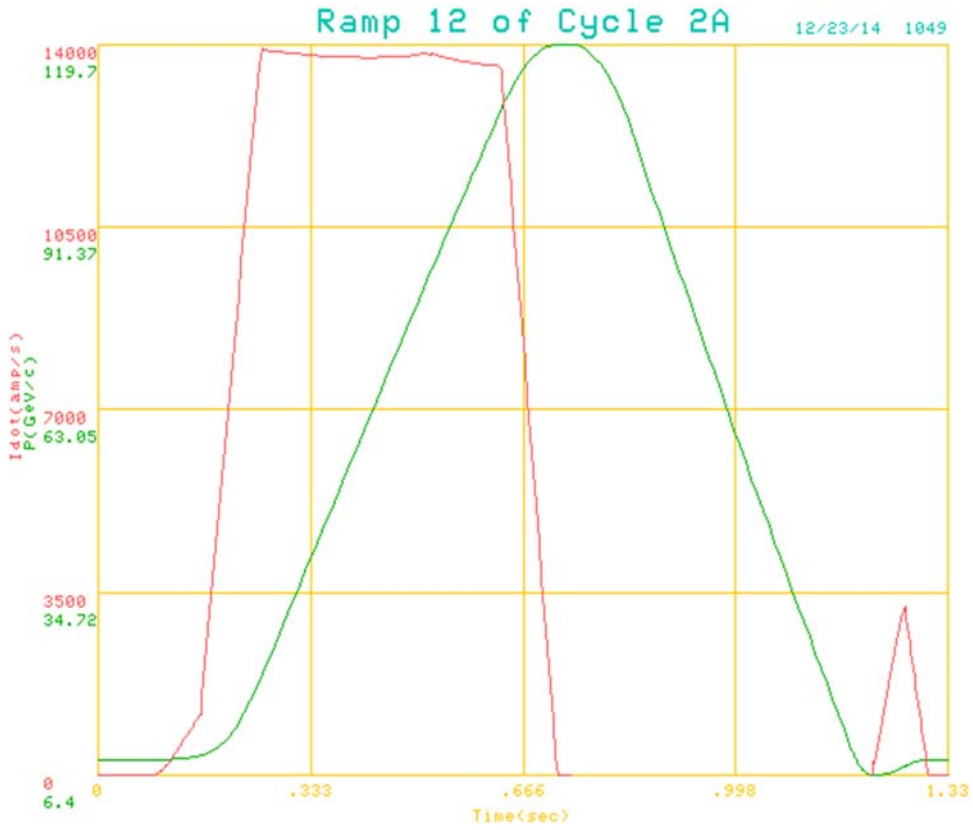

Figure 2.85: The current MI accelerating cycle. The momentum and the rate of dipole current change (acceleration rate) vs time are shown.

2.4.3. Acceleration in the MI

The current (NOvA) MI Acceleration cycle is shown in Figure 2.85. The total cycle duration is 1.33 s. The cycle time can be reduced to 1.2 s by optimizing the 8.9 and 120 GeV dwell times. In the same figure the acceleration rate, Idot, vs time is also plotted. From the conversion coefficient of 57.754 A/GeV we can see that the maximum acceleration rate is 240 GeV/s. The MI RF has to provide enough voltage to support this acceleration rate and also to provide the required bucket area. From operational experience with slip-stacked beam a bucket area of at least 2.0 eV·s is required above transition to contain the beam tails and avoid losses. The total RF voltage of 4.4 MV is needed to accelerate the beam and provide the required bucket area above transition. Since the maximum operational voltage from each RF station is 240 kV, all 18 RF stations originally installed in the MI are required. During the NOvA shutdown two spare MI RF stations were installed giving us some margin and enabling operation with up to 2 RF stations down. The RF voltage and bucket area during the current MI ramp are shown in Figure 2.86.

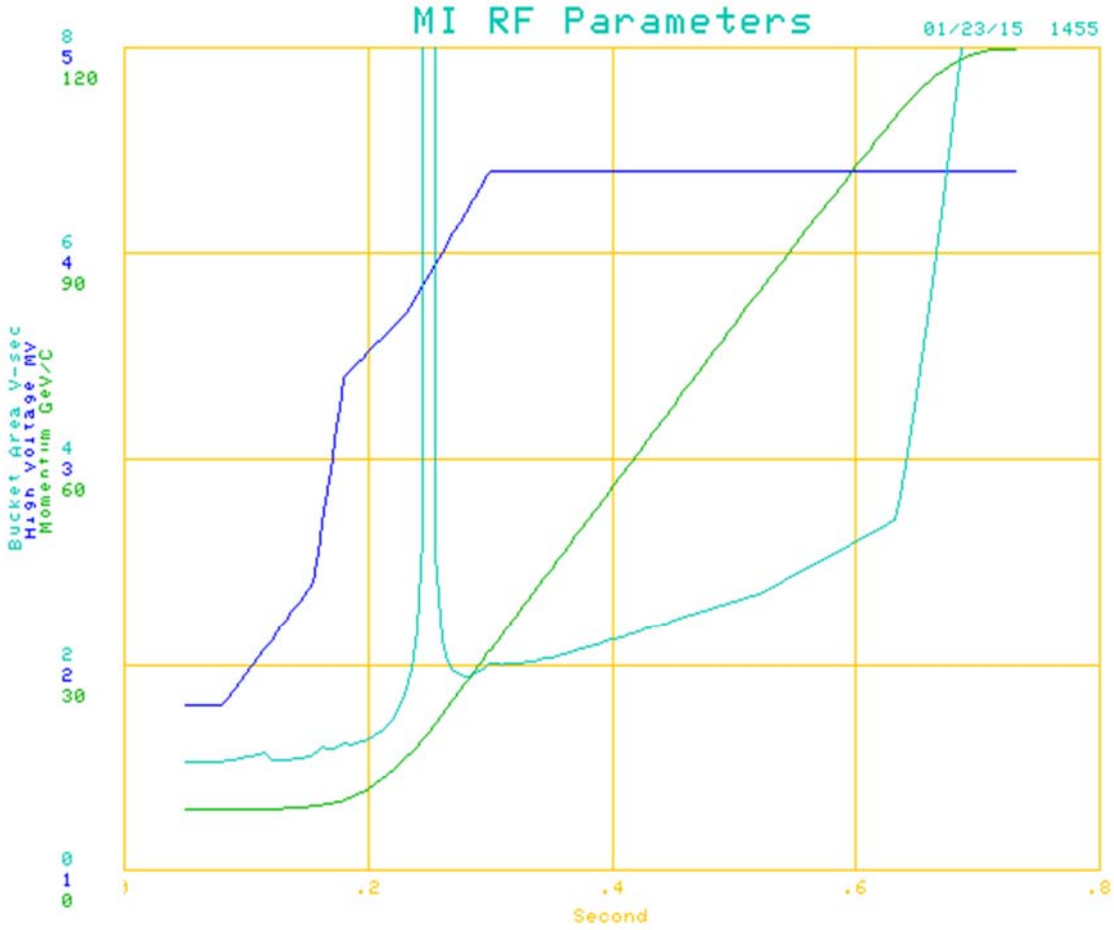

Figure 2.86: RF Voltage and bucket area during the MI acceleration with present cycle.

The MI ramp can be configured for different momenta. Figure 2.87 presents the MI cycle time vs beam momentum for PIP-II operation. The cycle times have been rounded up to the nearest 1/20 s. Based on the cycle times the calculated MI beam power vs beam momenta is shown in Figure 2.88.

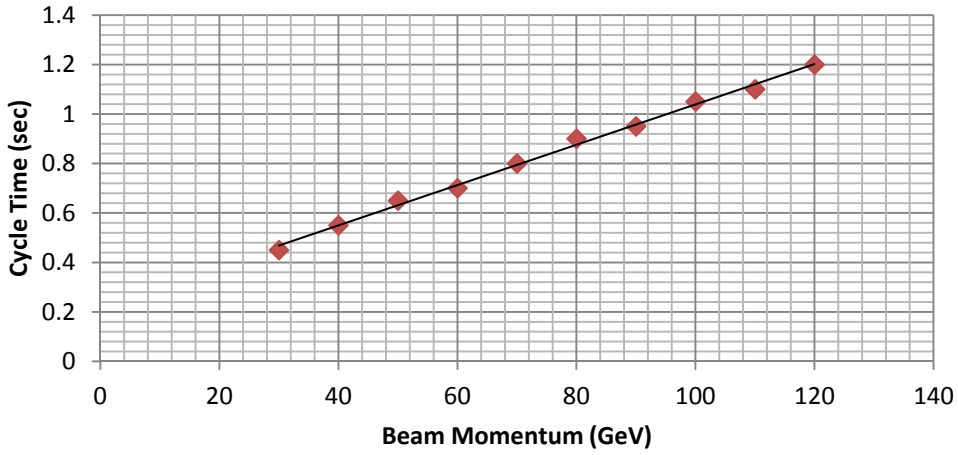

Figure 2.87: MI cycle time vs beam momenta.

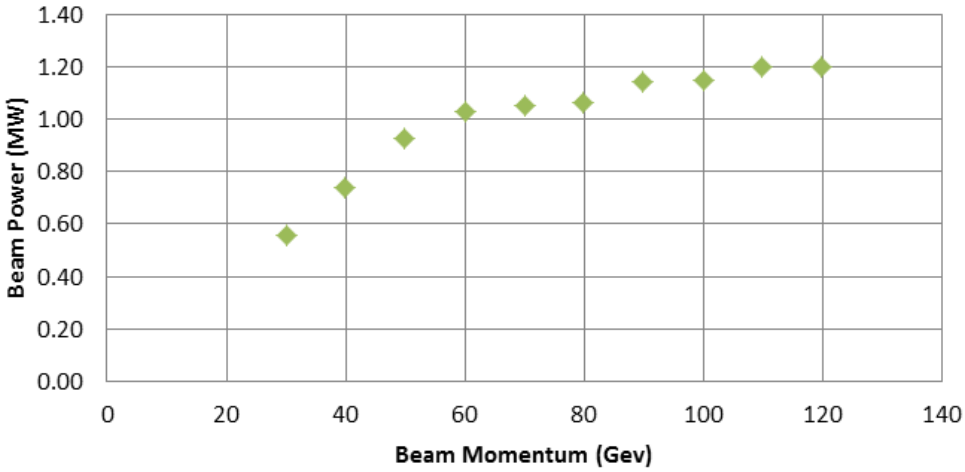

Figure 2.88: MI beam power vs beam momenta.

2.4.4. MI Transition Crossing

MI transition crossing is dominated by non-linear effects because of the large longitudinal emittance. Since the Booster will be upgraded to run at 20 Hz instead of 15 Hz the frequency separation for slip-stacking will be increased to 1680 Hz from present 1260 Hz resulting in larger longitudinal phase space area at injection and, consequently, larger longitudinal emittance after recapture in the MI. To reduce the effects of the transition crossing a first order gamma-t jump has been considered.

For MI the non-adiabatic time T_c which represents the time during which the longitudinal motion of the synchronous particle is not well represented by a slowly varying Hamiltonian, is around 1.5 ms. The nonlinear time T_{nl} which parameterizes the Johnsen effect [48, p. 285], in which particles with different momenta cross the transition at different times, is 2.3 ms. The nominal bipolar jump illustrated in Figure 2.89 maintains a clearance of

$$\left|\gamma-\gamma_t\right| \geq 1 \sim 2\gamma' T_{nl} \tag{2.17}$$

except for about 0.5 ms. Transition is crossed at $d\left(\gamma-\gamma_t\right)/dt = 4000 s^{-1}$ almost sixteen times faster than without the jump.

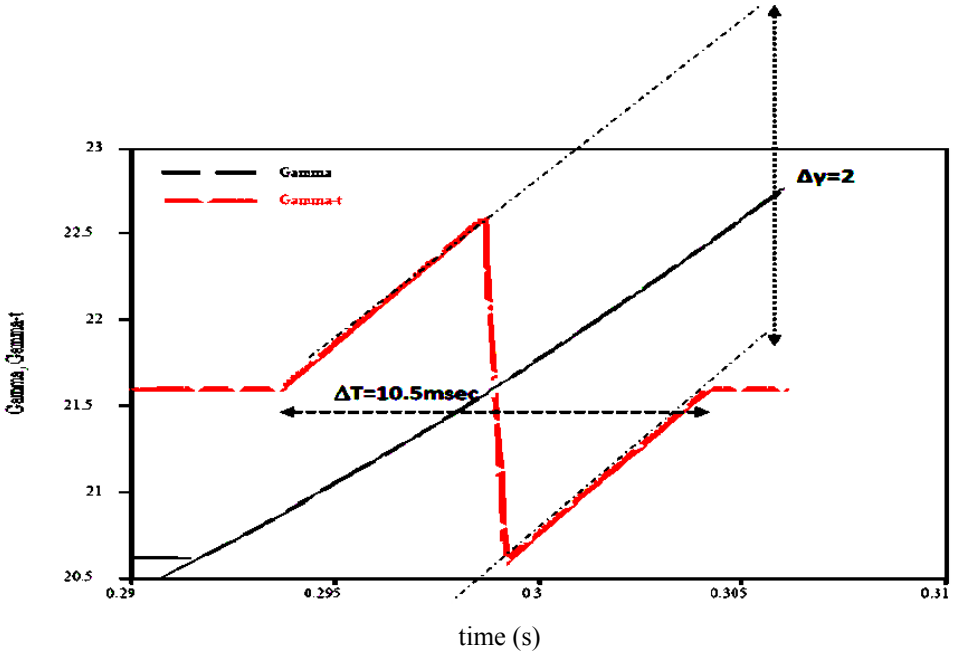

Figure 2.89: MI bipolar gamma-t jump. Transition is crossed 16 times faster with the transition jump than without.

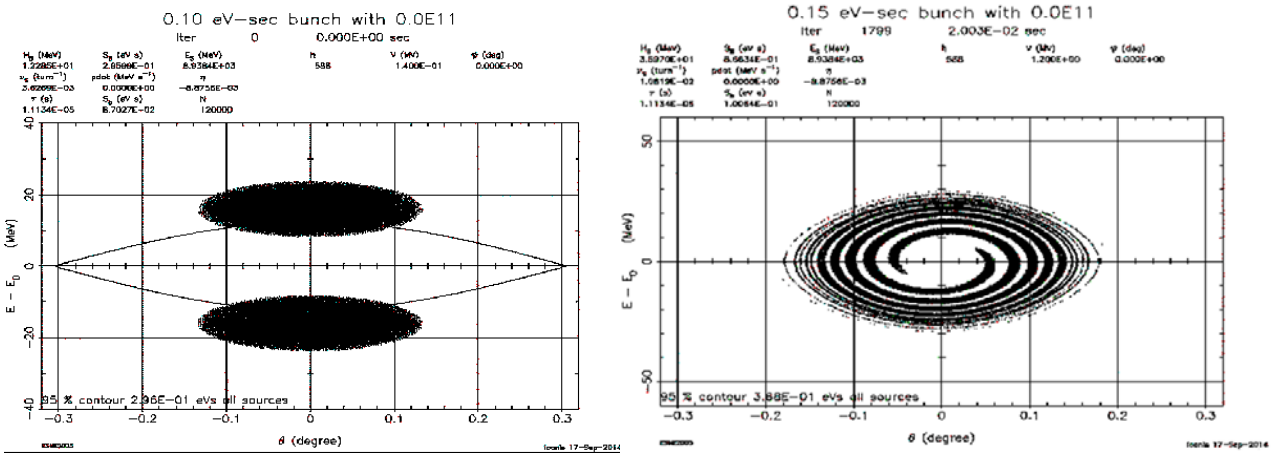

Figure 2.90: Initial condition for the ESME simulation. In the left picture two 0.1 eV-sec bunches captured in 145 kV buckets separated by 1680 Hz are shown. In the right picture the resulting distribution after recapture with 1.2 MV in MI is shown.

A series of ESME simulations were performed. They accounted for the space charge impedance, Z/n and the gamma-t jump. The initial conditions are shown in Figure 2.90. The final bunch distribution after recapture in MI has a bunch area of 0.5 eV-sec (100%). Figure 2.91 presents the pdot and the RF voltage curve used for the MI ramp in the ESME simulations.

The beam distributions after transition with and without gamma-t jump are shown in Figures 2.92 and 2.93. From Figure 2.92 it can be seen that without a gamma-t jump the low energy tail of the bunch that develops after transition is similar in the cases with zero charge and full charge indicating that it is non-linear effects and no space charge that is dominating the transition crossing in MI. The low energy tail exceeds the momentum aperture of MI leading in beam scraping and beam loss. With the full gamma-t jump the low energy tail is eliminated while with half the jump the beam is contained within the MI momentum aperture as presented in Figure 2.93.

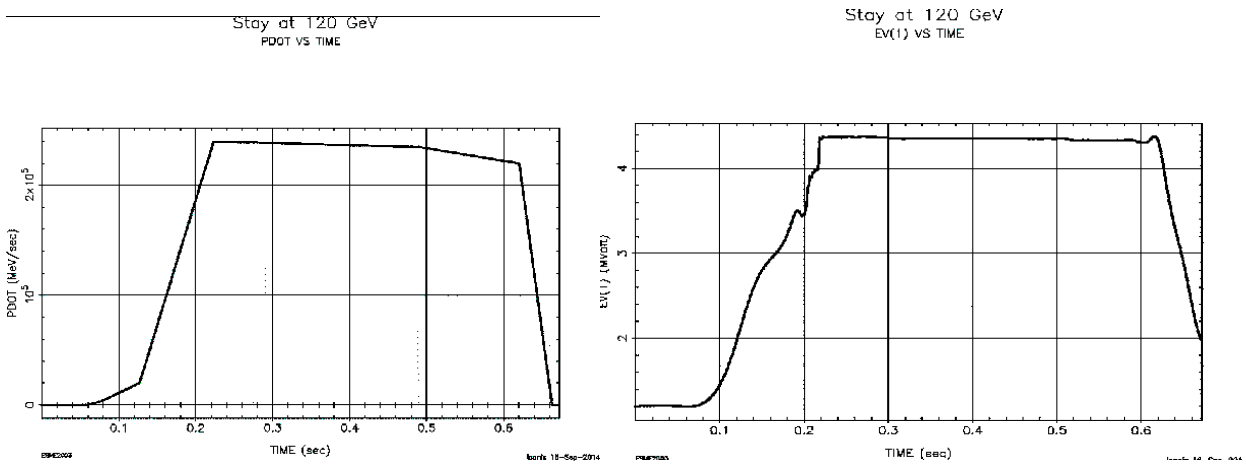

Figure 2.91: Pdot and RF voltage during the MI ramp used in ESME simulations.

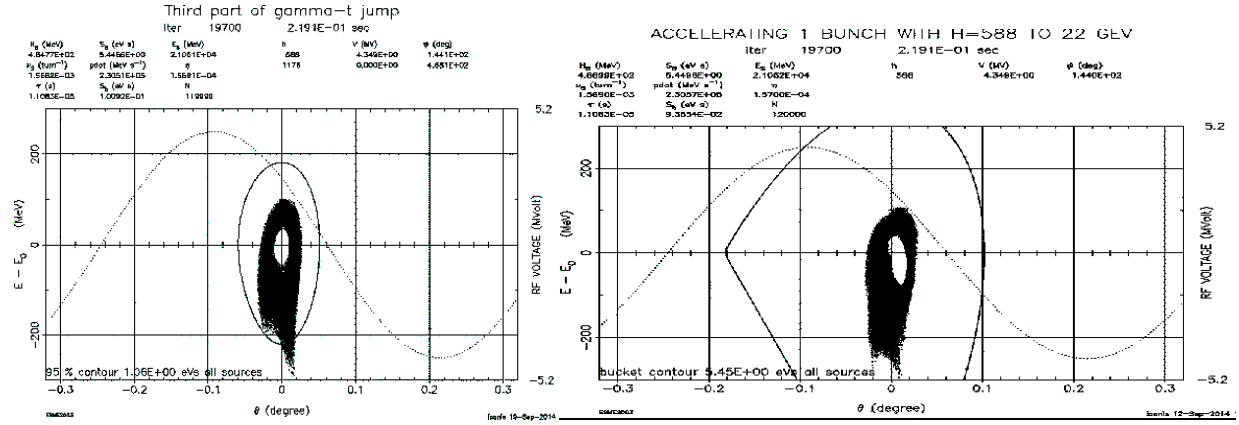

Figure 2.92: Phase space distribution after transition in MI with zero charge (left) and full charge (right).

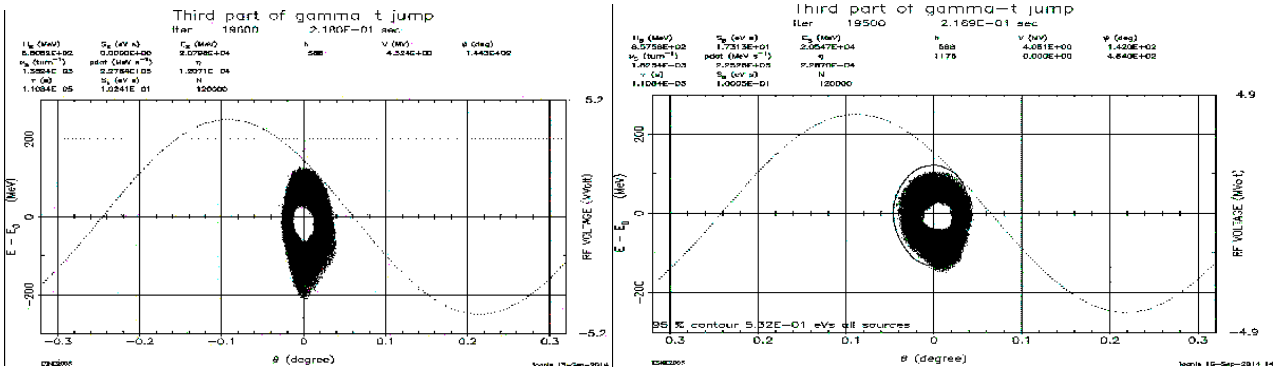

Figure 2.93: Phase space distribution after transition with full charge and two different sizes of the gamma-t jump. Half jump (left) and whole jump (right).

2.4.5. Beam Stability in the Recycler and MI

The main beam parameters used for the Recycler stability estimate are listed in Table 2.21. At injection with $\gamma = 9.5$ the space charge is strong transversely, i.e. its tune shift ΔQ_{sc} is much larger than the synchrotron tune Q_s; the space charge is also important longitudinally, leading to about 20% of the synchrotron tune depression [44], and possibly to a longitudinal instability similar to the

"dancing bunches" [49]. The longitudinal instability can be significantly enhanced by coupled-bunch interaction through high order modes (HOM) in the cavities, leading to the growth rate [50]:

$$\tau_{\|}^{-1} = \frac{MNr_p \eta R_s \omega_r \rho_{\omega_r}^2}{\gamma C Q_s Z_0}; \qquad \rho_{\omega_r}^2 = \exp\left(-\omega_r^2 \sigma_\tau^2\right); \quad Z_0 = 377\,\Omega. \tag{2.18}$$

Here R_s is the shunt impedance, ω_r is the HOM frequency, and σ_τ is the rms bunch length in time units. For R_s=35 kΩ, $\omega_r/(2\pi)$=150 MHz, and σ_τ =1.9 ns this yields a rather high frequency suppression factor $\rho_{\omega_r}^2 = 0.03$, leading to $\tau_{\|} = 30\,\text{ms}, \tau_{\|}^{-1} = 0.02\omega_s$. A narrow-band damper could suppress such slow coupled-bunch motion if it is required.

Table 2.21: Beam parameters in the Recycler used in beam stability estimates

Bunch population, N	$8\cdot10^{10}$	
Number of bunches	81·6·2=972	
Transverse emittance, norm. rms, $\varepsilon_{n\perp}$	2.5	mm mrad
Longitudinal emittance, rms, $\varepsilon_{\|} = \sigma_\tau\sigma_E$	5.5	meV·s
Maximal RF Voltage , V	0.125	MV
Transition gamma, γ_t	21.6	

The transverse single-bunch instability is described by a growth rate [42]

$$\tau_{\perp SB}^{-1} = F_{SB}(\chi)\frac{Nr_p \bar{W}_{SB}\bar{\beta}}{4\pi\gamma} \tag{2.19}$$

where $F_{SB}(\chi) \le 0.1$ is the chromaticity factor determined by the head-tail phase $\chi = \zeta\sigma_s$, $\bar{W}$ is a bunch-averaged wake function, and $\bar{\beta}$ is the average beta-function. For $\chi \ge 1$, the chromaticity factor saturates at its maximum, $F_{SB}(\chi) \simeq 0.1$. For the resistive wall case, with the half-gap b and the conductivity σ, the average wake is estimated to be:

$$\bar{W}_{SB} = \frac{\pi^2}{12}\frac{2C}{\pi b^3\sqrt{\sigma\sigma_\tau}} \tag{2.20}$$

Altogether, this leads to single-bunch instability with a growth time $\tau_{\perp SB} = 20$ ms or in other words $\tau_{\perp SB}^{-1} = 0.03\omega_s$.

The coupled-bunch transverse impedance due to wall resistivity is:

$$Z_{CB} = Z_0 R\frac{\pi^2}{12}\frac{\delta}{b^3} \tag{2.21}$$

where δ is the skin depth at the corresponding coupled-bunch frequency. The corresponding instability growth rate is:

$$\tau_{\perp \mathrm{CB}}^{-1} = \left| I_n(\chi) \right|^2 \frac{MNr_p \bar{\beta}}{\gamma T} \frac{Z_{\mathrm{CB}}}{Z_0 R} \tag{2.22}$$

where the coupled-bunch chromatic form-factor $I_n(\chi)$ is given by Eq. (2.14). For the parameters of Table 2.21, this yields a growth rate close to the synchrotron frequency, $\tau_{\perp \mathrm{CB}}^{-1} = 1.2\,\omega_s = 1.8 \cdot 10^3\ \mathrm{s}^{-1}$. The Recycler bunch-by-bunch transverse dampers have been very effective in damping the wall current instability. During slip-stacking the present dampers are not effective and therefore they are turned off. In order to stabilize the beam the chromaticity is increased by about 11-12 units (to -18 from -6). For PIP-II parameters a suppression of this instability most likely would require both the transverse damper and rather strong octupoles or electron lens. Another possibility – a special damper capable of damping the transverse motion of both beams in the course of slip-stacking - is also being discussed [51].

Space charge effects during slip-stacking in the Recycler with high chromaticity have been simulated with Synergia [46]. The space charge footprint at -18 chromaticity is shown in Figure 2.94.

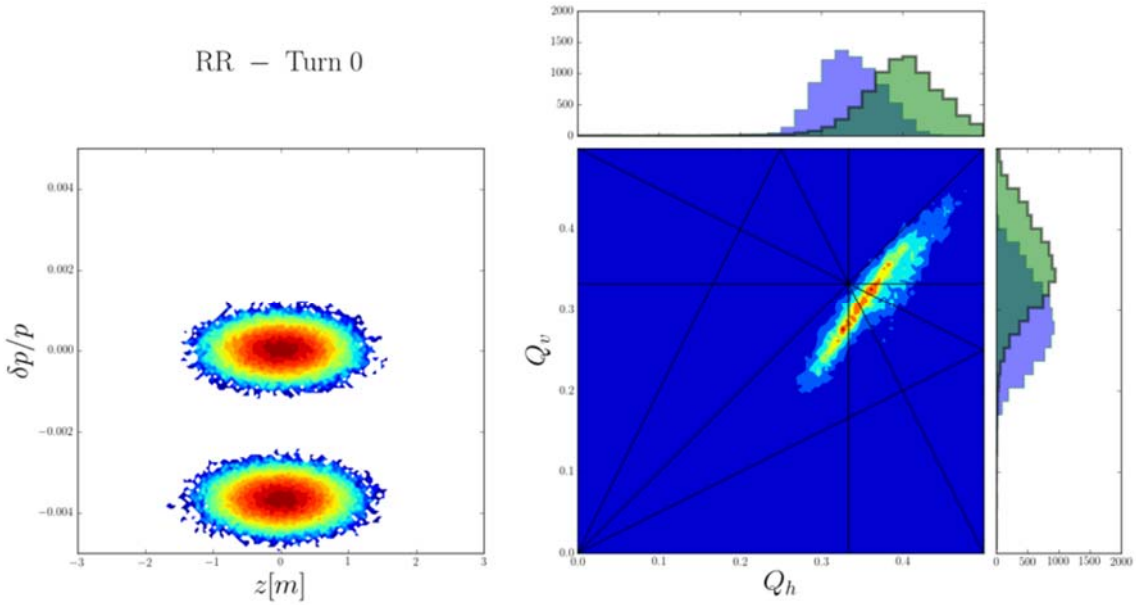

Figure 2.94: The longitudinal phase space (left) and space charge footprint (right) for the PIP-II case.

Currently, the Recycler performance is not limited by the electron cloud instability. A series of beam studies and simulations are underway to evaluate if electron cloud will be an issue in the Recycler and MI with PIP II beam intensities. So far, beam scrubbing has been effective in reducing the SEY value of the SS beam pipe in both Recycler and MI. A beam pipe coating in both Recycler and MI is also an option.

2.4.6. Electron Cloud Mitigation

Electron cloud generation could be a possible instability source for the intensities in the Recycler and Main Injector.

The instability growth rates are so high that the instability hardly can be suppressed with a damper. The best approach is to mitigate the generation of the cloud itself. There have been a series of measurements in the Main Injector, looking at the secondary electron yield and cloud generation. A

dedicated measurement setup now exists at MI-52, with newly developed RFA detectors. Both TiN and C coated beam pipes have been installed and measurements made. Both coatings show significant reductions in secondary electron generation when compared to an uncoated stainless steel pipe. VORPAL simulations are being benchmarked against these measurements. There is a plan to install a SEY (Secondary Emission Yield) stand in the Main Injector in order to measure the effect of scrubbing in situ for different kinds of stainless steel. A picture of the SEY measuring stand is shown in Figure 2.95.

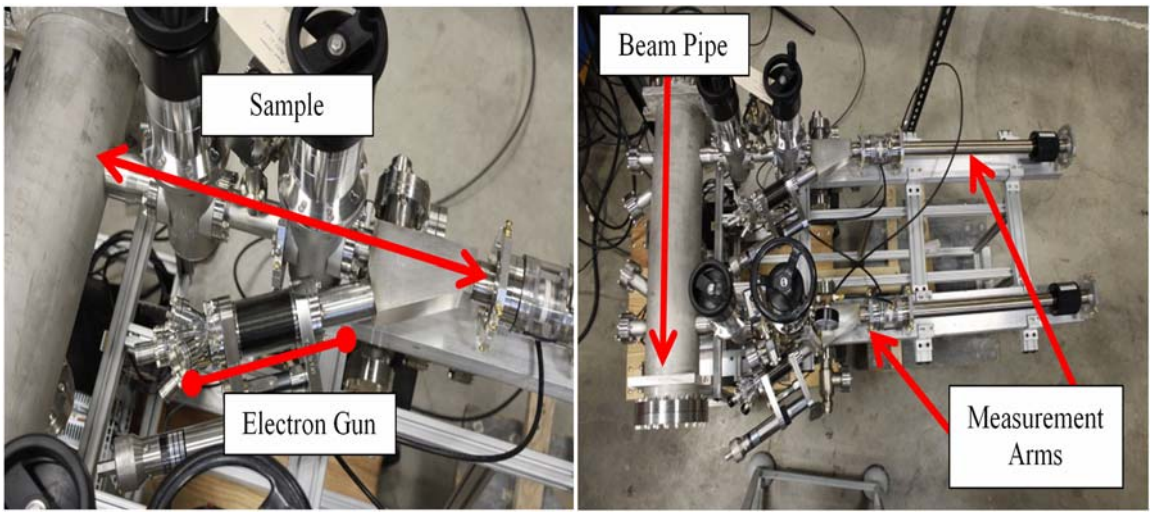

Figure 2.95: SEY Measuring Stand.

Research continues on the coating process. The Main Injector beam pipe is captured in the dipole magnets, so the coating needs to take place in situ. A coating (sputtering) facility is set up in E4R. It has successfully coated a 6 m long piece of round MI pipe with TiN and measured the coating thickness. It will be used to coat test coupons for SEY measurements in the Main Injector. The experience from our coating facility will be used to estimate the effort required to in-situ coat the Main Injector beam pipe with TiN.

3. DESIGN CONCEPTS OF MAJOR SUBSYSTEMS

3.1. SC Linac

3.1.1. Warm Frontend

The PIP-II warm frontend consists of an ion source, Low Energy Beam Transport (LEBT), Radio Frequency Quadrupole (RFQ), and Medium Energy Beam Transport (MEBT). The H^- beam originates from a 5 mA (nominal, 10 mA max) DC ion source and is transported through the LEBT to a CW normal-conducting RFQ, where it is bunched and accelerated to 2.1 MeV. In the MEBT a bunch-by-bunch chopper provides the required bunch patterns, removing 60-80% of bunches according to a pre-programmed timeline. To foresee possible upgrades, all elements of the frontend are designed for beam currents of up to 10 mA. The beam energy of 2.1 MeV is chosen because it is below the neutron production threshold for most materials. A wall shielding the frontend from radiation generated in the main linac is envisioned in the MEBT to allow servicing the ion sources without interrupting the linac beam.

3.1.1.1. Ion Source

The ion source assembly is a DC, H^- source delivering up to 10 mA of beam current at 30keV to the LEBT. The ion source specifications are listed in Ref. [52]. The present scenario assumes using the volume cusp, filament-driven, ion source presently commercially available from D-Pace Inc. ([53], Figure 3.1). This source is capable of delivering up to 15 mA with a satisfactory transverse emittance of < 0.2 μm (rms, normalized), but its mean time between maintenance is relatively short. The main reason is the source filaments, which need to be replaced every 300-500 hours. To maximize the beam uptime, two ion sources are planned to be installed (see Figure 2.2). In principle, each source can be removed for repairs, installed back, and conditioned without interrupting the operation of the other source. However, to be implemented, access to the portion of the beam enclosure where the ion sources reside is needed while the accelerator is running. In turn, radiation shielding is required before the beam is accelerated in the HWR cryomodule.

Figure 3.1: Photograph of the D-Pace ion source (foreground) with a vacuum chamber.

The ion source was purchased from D-Pace Inc. to be used in the PIP2IT. It has been in operation

since 2013. While presently not stated as a requirement for PIP-II, a modulation circuit was built and mounted onto the ion source extraction electrode to provide pulsed operation. This capability brings flexibility to the commissioning of the beam line downstream and an additional level of protection in the Machine Protection System.

It should be noted that alternatives to the D-Pace Inc. ion source may be considered. Several groups around the world have been engaged into R&D that may lead to an ion source with the proper characteristics for PIP-II and a much longer time between maintenance than is currently available.

3.1.1.2. LEBT - Low Energy Beam Transport

The LEBT transports the beam from the exit of the ion source to the RFQ entrance and matches the optical functions to those of the RFQ. In addition, the LEBT forms a low-duty factor beam during commissioning and tuning of the downstream beam line and interrupts the beam as part of the Machine Protection System (MPS). Pulsed beam operation and fast machine protection are achieved via a chopper assembly, which consists of a kicker combined with an absorber. In addition, in the case of severe failures, the beam is disabled by turning off the ion source's extraction and bias voltages, as well as the switching dipole power supply. In some scenarios, the LEBT chopper assembly can also be used as a pre-chopper to assist the MEBT chopping system.

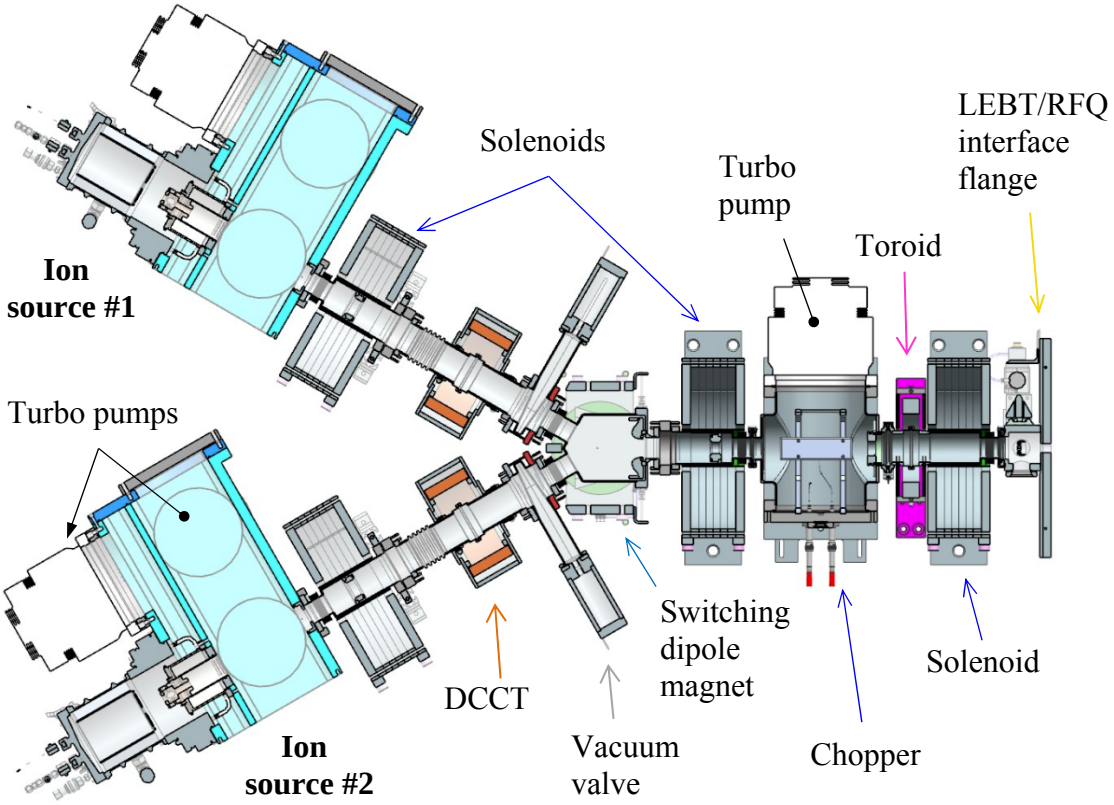

Figure 3 2: Section view of the LEBT with two ion sources.

Layout

The LEBT consists of 3 solenoids (for each leg), a slow switching dipole magnet, a chopping system, water-cooled Electrically Isolated Diaphragms (EID), an electrically-isolated, water-cooled, movable vertical electrode assembly with 3 apertures, and beam current diagnostics – DCCT after solenoid #1 and AC current transformer ("toroid") after the chopping system (Figure 3.2). An

emittance scanner [54] is located at the exit of each ion source. Dipole correctors are mounted inside each solenoid allowing the beam to be steered in any direction. The edge focusing of the switching dipole is adjusted to minimize the asymmetry between horizontal and vertical focusing. As already stated in Section 2.1.2.1, the ~2 m beam line length ensures that the gas migrating from the ion source to the RFQ is kept at a manageable level.

Chopping system

For accelerator front-ends with similar beam parameters as PIP-II, most LEBT's employ a transport scheme that relies on almost complete neutralization of the beam to counteract the effects of space charge during transport. However, neutralization is inevitably broken in the vicinity of a chopper. In order to decrease the distance that the beam travels with full space charge and low energy, the chopping system is often located just upstream of the RFQ. Such location has several features contradicting the principles described in Section 2.1.2.1. First, absorption of the cut-out beam creates a significant gas load into the RFQ. Second, the short distance required between the last solenoid and RFQ limits the possibilities of fitting in a simple and robust chopper. It also makes it difficult to place diagnostics downstream of the chopper, for instance, to measure the beam current entering the RFQ. Following this logic, the chopping system is placed between solenoids #2 and #3.

The chopping system is a simple electrostatic kicker, with the particularity that one of the electrodes is also the absorber. Such a design is inherently robust against un-controlled beam losses, which can quickly become an issue even at the relatively modest maximum beam power of 300 W (DC). In addition, it removes the need for a dedicated absorber electrode downstream, thus making the overall chopping system more compact. The absorber plate is at the ground potential but electrically isolated in order to measure the primary beam current. When the beam is passed through, the design of the chopper electronics allows applying a DC voltage to the kicking plate to clear secondary ions out of the beam path.

Electrically Isolated Diaphragms (EID)

The beam line includes 3 water-cooled, Electrically Isolated Diaphragms (EID), two of which are located within solenoid #1 and #2 and the third just downstream of the electrostatic kicker.

The primary function of these electrodes is to minimize uncontrolled beam losses. They are sized such that if there is some beam loss (*e. g.* before the optics is properly tuned, or during the rise and fall time of the kicker (EID #3)) it would most likely occur at these locations first. The EIDs are electrically isolated to allow the beam loss to be measured.

Second, the EIDs play the role of potential barriers in the transport scheme with an un-neutralized section, confining ions in sub-sections of the beam line.

Finally, they are used to measure the beam size and center the beam. This is achieved by steering the beam with upstream correctors and recording the current drawn by the electrodes.

In addition, there is a so-called scraper assembly just downstream of Solenoid #3, which is an additional movable electrically-isolated and water-cooled electrode with 3 apertures. (2 round apertures and a 'D-shaped' aperture). A small round aperture is used to create a pencil beam. A larger round aperture placed concentrically with the RFQ entrance aperture during normal operation protects the RFQ vanes. The 'D-shaped' aperture is used to measure the beam current density profile by moving its edge across the beam and recording the scraper current as a function of the scraper position. Finally, the scraper can be placed such as to intercept the beam completely. For the larger round aperture, the size of the opening is chosen to scrape the halo particles that otherwise would be lost in the RFQ or MEBT. Also, the variation of beam current intercepted by the scraper while

moving the beam across the opening with upstream dipole correctors gives information about the beam position and core size for both planes.

Emittance growth mitigation

To satisfy both the beam physics requirements and the design choices for PIP2IT, a hybrid transport scheme was devised, where the beam propagates through the first 'high pressure' part of the LEBT being neutralized, but neutralization is prevented in the second part, which starts right upstream of the chopper (see Section 2.1.2.1). For a beam with modest perveance, this transport solution nearly preserves the beam emittance if the transition to the un-neutralized section occurs where the beam current density profile is close to the profile corresponding to uniform distribution [55]. While the ion source may not be optimized to deliver a beam with uniform current density, because of the finite extent of the beam emitter (*e.g.* plasma surface) and the geometry of the extraction system, one would expect the spatial distribution of the beam to have relatively sharp edges. In addition, because of the ion source current overhead, it is possible to implement significant scraping that would result in only keeping the core of the particles' distribution, inherently more uniform than the tails. At the same time, the beam formation out of a plasma in a near thermal equilibrium must result in a Gaussian velocity distribution in transverse momentum at the beam emitter location.

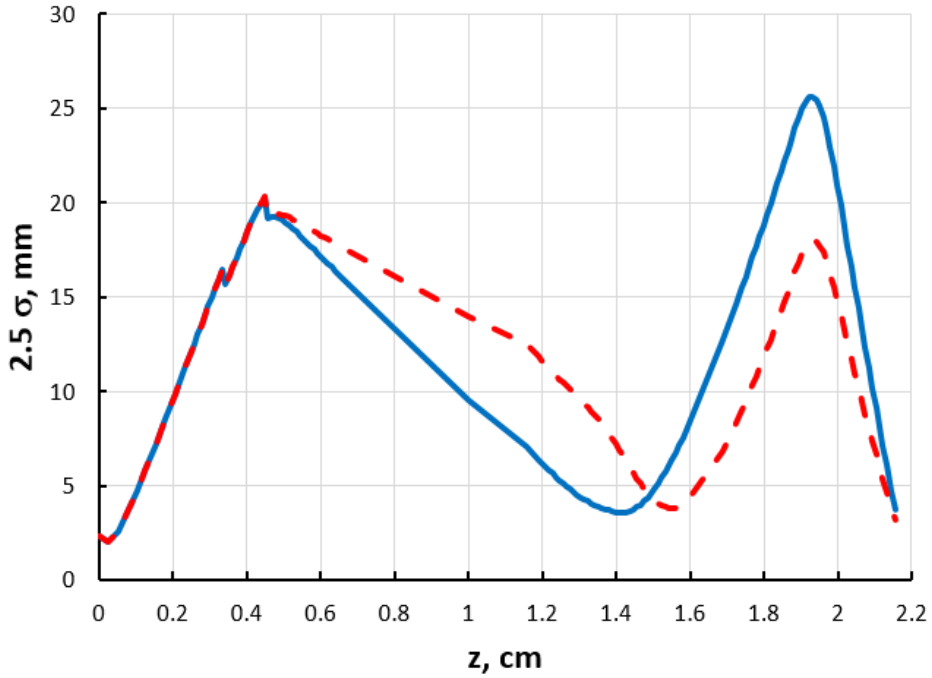

Figure 3.3: Beam envelopes (2.5σ) obtained with TraceWin. Currents in focusing solenoids are 154, 187 and 223.5 A (blue curve) and 143, 158 and 240 A (red dashed curve) for Solenoids #1, #2 and #3, respectively. Input distributions (uniform current density and Gaussian distribution in velocity subspace) are the same for both simulations; I_{beam} = 5 mA (after scraping in the first solenoid).

To illustrate this model, Figures 3.3 to 3.5 show TraceWin simulations, where the initial distribution is uniform in the subspace of transverse coordinates and Gaussian in the velocity subspace. While the final Twiss parameters are nearly equal (Figure 3.3), the solenoids have different current values: in one case (red traces or dots on the plots), the beam is nearly uniform near the chopper, while it is Gaussian for the second case (blue traces or dots on the plots) (Figure 3.4).

Correspondingly, the emittance growth is lower in the first case than in the second one (Figure 3.5). Note that ~20% of the beam is scraped off before the first solenoid.

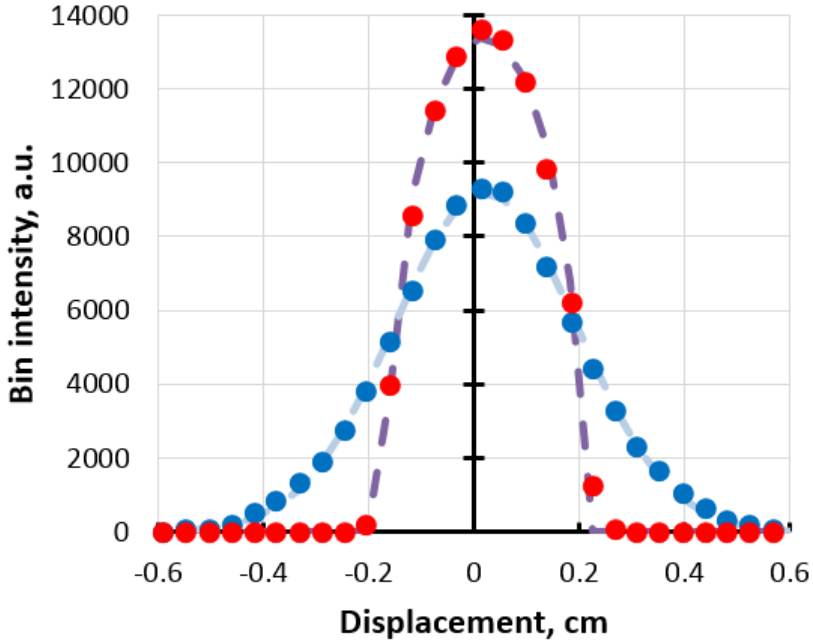

Figure 3.4: 1D beam profiles 20 cm downstream of EID #2 corresponding simulations shown on Figure 3.3. Dashed curves are fits, assuming uniform (purple) or Gaussian (light blue) distributions.

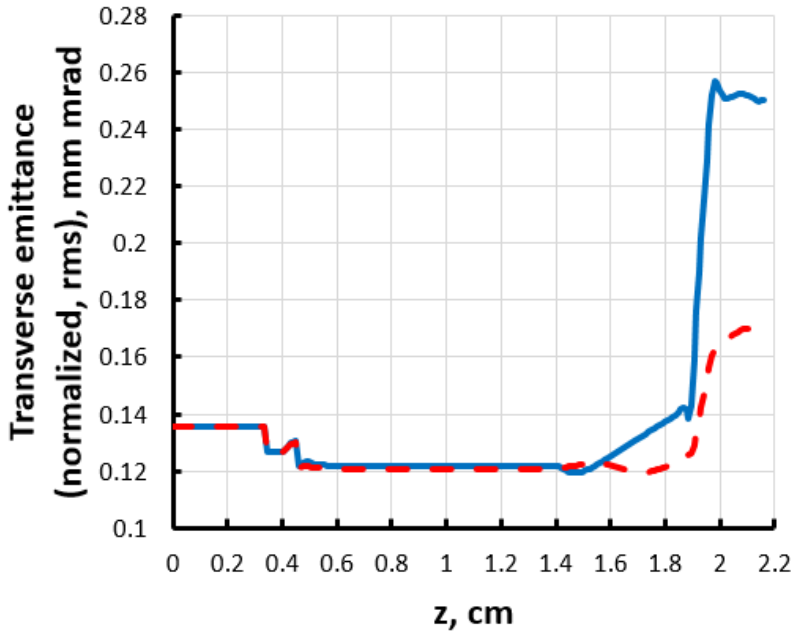

Figure 3.5: Emittance evolution along the beam line corresponding to the simulations shown in Figure 3.3.

Measurements at the PIP2IT were carried out with the transverse emittance station [56] installed in close vicinity of RFQ input flange. They show a behavior similar to the simulations. Namely, starting with the same ion source tune, different solenoid current settings lead to different emittances for the same measured Twiss parameters at the end of the beam line. In addition, profile

measurements carried out between solenoid #1 and #2 show that the beam distribution is indeed uniform-like or Gaussian-like depending only on the value of the solenoid #1 current. Thus, both measurements and simulations indicate that the proposed transport scheme allows one to deliver the beam with the required properties to the RFQ.

3.1.1.3. RFQ - Radio-Frequency Quadrupole Accelerator

The 162.5 MHz CW RFQ will accelerate an H^- ion beam with currents of up to 10 mA from 30 keV to 2.1 MeV (see Ref. [57] for specifications). Presently the PIP-II RFQ is assumed to be identical to the one used for PIP2IT, which was constructed and built by LBNL [58], and which design is based on the experience accumulated the LBNL team earlier and, in particular, on the SNS RFQ [59]. The RFQ is a 4.45-m long, four-vane copper structure composed of four longitudinal modules. The nominal vane-to-vane voltage is 60 kV. A series of 32 water-cooled pi-mode rods provides quadrupole mode stabilization, and a set of 80, evenly spaced, fixed slug tuners is used for the final frequency adjustment and local field perturbation corrections. It was delivered to FNAL in 2015 and has been commissioned and operated at the PIP-II Injector Test (PIP2IT). The PIP2IT RFQ has already proven that it can operate at full, CW power and can accelerate pulsed beam with greater than 95% efficiency. Preliminary measurements verify its good performance. Capture and transmission efficiency has been verified up to 95%, which is the current limit in instrumentation accuracy. Figures 3.6 and 3.7 present RFQ views as a CAD model and as an actual accelerator component installed in the PIP2IT enclosure.

RF matching into the RFQ cavity is done with two 162.5 MHz input couplers designed and verified at FNAL [60]. A CAD illustration of the coupler is shown in Figure 3.8. These couplers were designed to transport up to 75kW of RF power with full reflection, without breakdown. It has two design features that are unique with respect to other RF cavity input couplers: the antenna is forced-air cooled to guard against potential water leaks in the RFQ vacuum chamber, and the antenna is capacitively coupled to the end-wall, allowing DC biasing to reduce multipacting. The couplers have been verified up to 120kW of CW drive into the RFQ, and a bias of 1kV on the antennas is enough to eliminate multipacting around the couplers to support stable operation at full power.

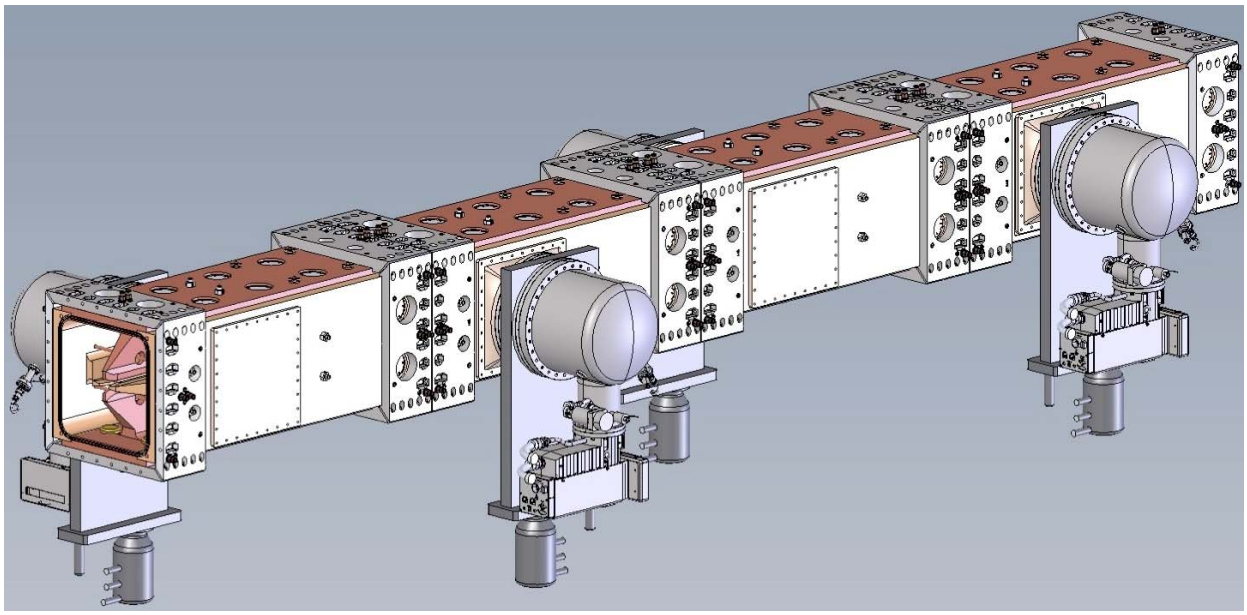

Figure 3.6: CAD model of the full four-module RFQ.

Figure 3.7: RFQ installed in PIP2IT beamline.

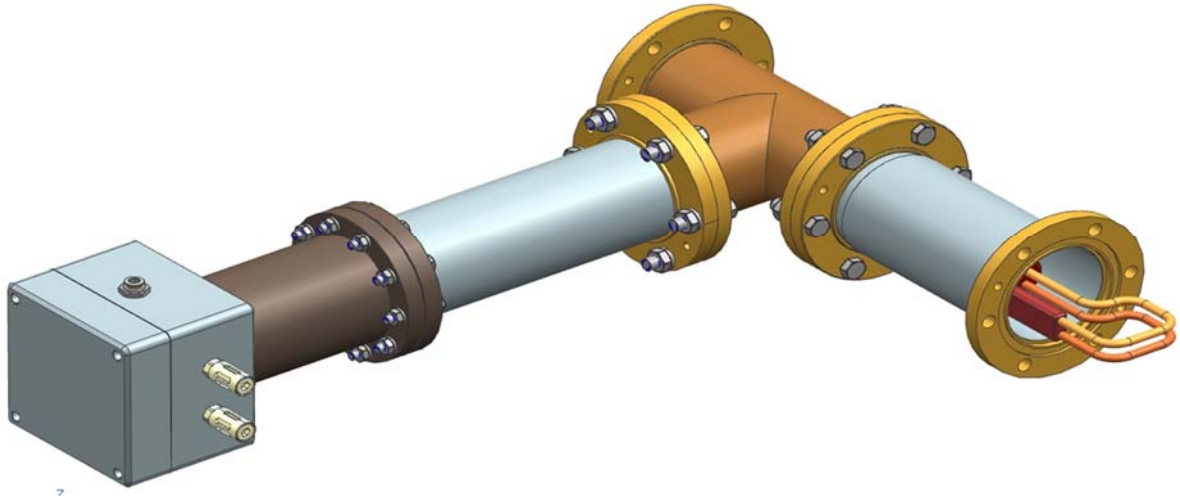

Figure 3.8: Solid model of the RFQ input coupler design.

RF power is provided by two, 75kW 162.5 MHz solid-state power amplifiers from Sigma Phi Inc. Each amplifier is protected from power reflected from the RFQ using 75kW circulators from Ferrite Inc. The added expense of the RF circulators has been justified with the improved stability of RFQ operation. In particular, they allow the RFQ to be operated over a larger range of resonant frequency offsets and to obtain pulsed operation with variable duty factors viable.

The resonant frequency of the RFQ is controlled thermally by adjusting the temperature difference

of water circuits, which cool the vanes and the RFQ walls. The choice of such scheme is supported by much larger sensitivity to the temperature difference than to the average temperature of the circuits. The corresponding frequency response parameters are shown in Table 3.1. The temperature difference is achieved by redistribution of cooling water flow between these two circuits. For pulsed operation, duration of RF duty cycle can also be used for the temperature stabilization. For CW operation, resonant frequency must be maintained with cooling water temperature regulation only. An adaptive control system has been designed that will regulate the steady state temperature of the RFQ cooling system to better than 0.1°C. A simple block diagram description of the system is shown in Figure 3.9. The system is also designed to respond to sudden changes of thermal load due to RF power trips. The goal is a reduction of time necessary for bringing the RFQ resonant frequency to the nominal value after a trip. Consequently, it will decrease the beam downtime.

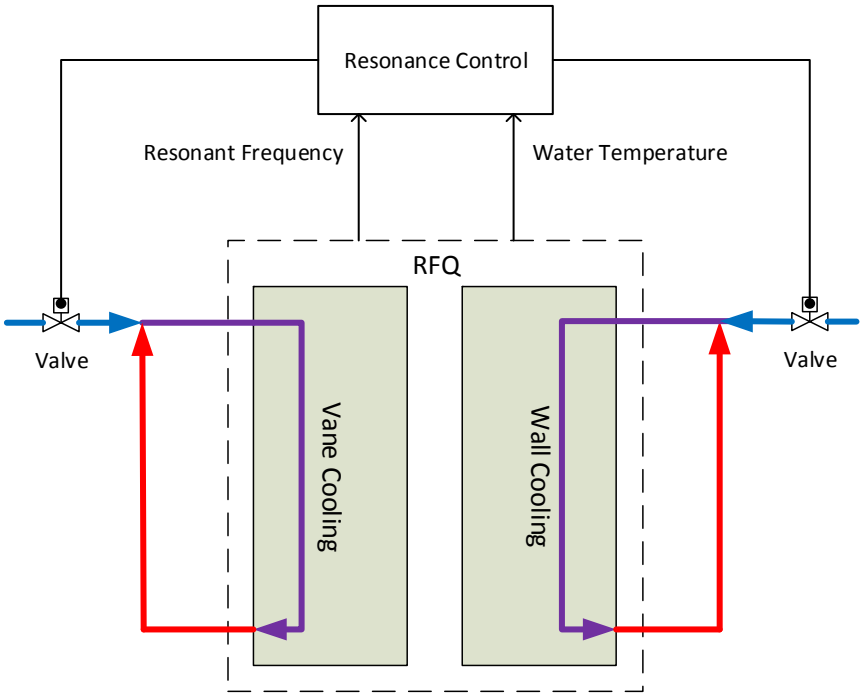

Figure 3.9: Simple block diagram showing resonant control system with RFQ. The system monitors water temperature and RFQ resonant frequency, and adjusts flow rate of cooling water into wall and vane cooling loops.

A series of RF and thermal finite-element models of the RFQ have been developed using ANSYS®. An example of the temperature contour plots for the cavity body and vane cutback region is shown in Figure 3.10. From the RF analysis, the average linear power density was determined to be 137 W/cm with a peak heat flux on the cavity wall of only 0.7 W/cm^2. With 30°C water in the vane and wall cooling passages, the resulting temperature profile in the cavity body ranges between 32 and 37°C at full RF gradient.

Additional modeling has been carried out. It includes stress and displacement analyses, thermal analyses of the tuners, pi-mode rods and vane cutbacks, and prediction of the frequency shift of the RFQ cavity due to thermal loading and changes in the cooling water temperature.

The RF design issues [11] include mode stabilization, field flatness, radial matching, and entrance and exit terminations. Table 3.1 summarizes the RF and thermal design results.

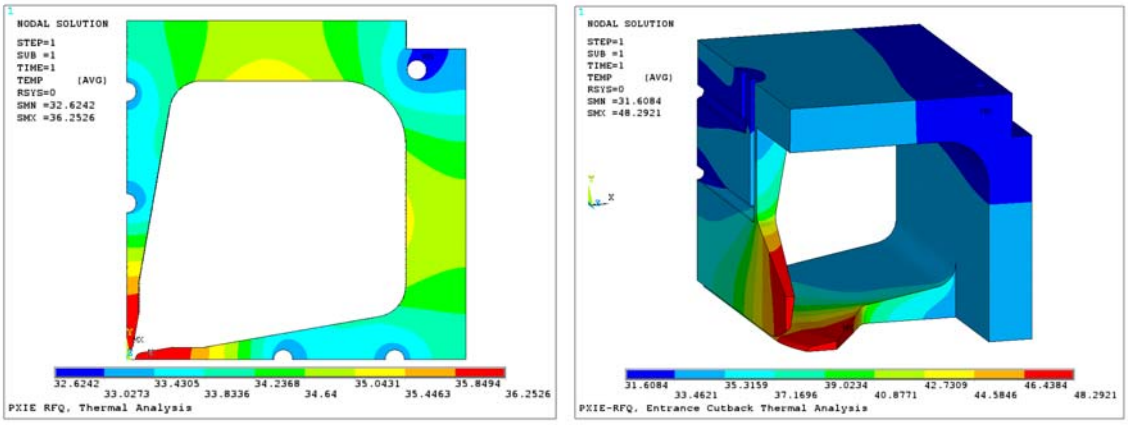

Figure 3.10: Temperature distribution in one RFQ quadrant body (left) and cut-back (right). The color scheme (degrees C) is at the bottom of each plot.

Table 3.1: Main parameters of the PIP-II RFQ electromagnetic design

Parameter	Calculated	Measured
Center Frequency, MHz	162.493	162.445
Frequency of dipole mode, MHz	181.99	180.52
Q_0 factor	14660	13000
Total power loss at 60 kV, kW	74.6	90
Vane cooling resonant frequency parameter, kHz/°C	-16.7	-16.4
Wall cooling resonant frequency parameter, kHz/°C	13.5	13.9

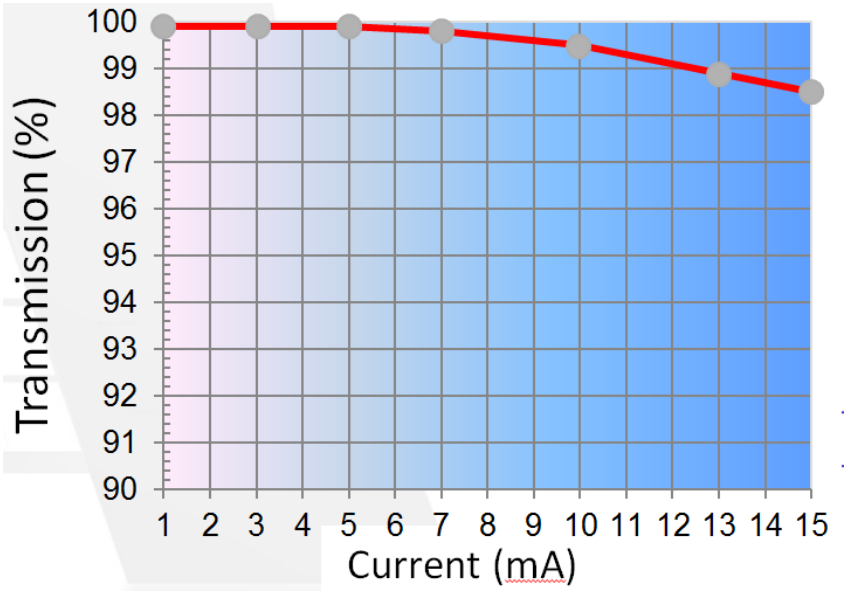

Figure 3.11: Dependence of the calculated RFQ transmission on the beam current.

The beam loss inside RFQ may result in degradation of the RFQ performance [61]. The PIP-II RFQ accelerates is expected to accelerate very large charge and, consequently, minimization of the beam loss has a primary importance. Figure 3.11 presents the dependence of computed RFQ

transmission on the beam current. The design has over 98% transmission for the beam current from 1 to 15 mA. At the nominal current of 5 mA, 99.8% beam capture is achieved in this simulation.

3.1.1.4. MEBT – Medium Energy Beam Transport

The H^- beam accelerated in the RFQ to 2.1 MeV enters the MEBT line, where it is chopped and matched for injection into the HWR cryomodule. The MEBT structure is presented schematically in Figure 2.8, and replicated below for reading convenience as Figure 3.12.

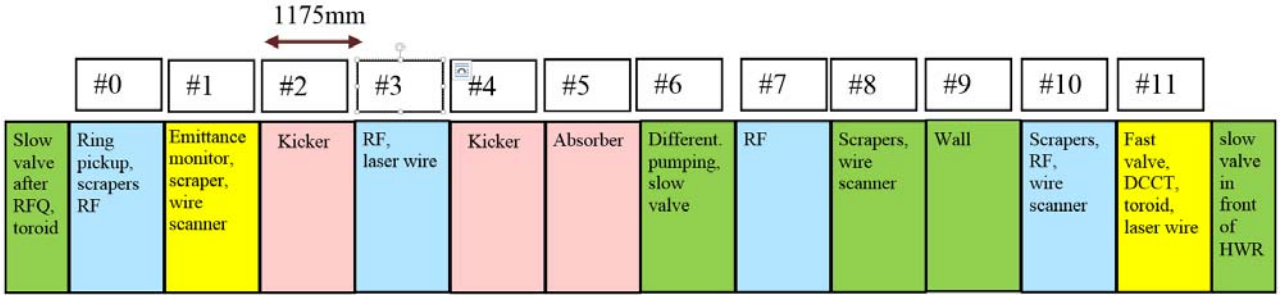

Figure 3.12: The MEBT structure. Sections are color-coded according to their main functions: green- vacuum, blue- RF, yellow- instrumentation, and pink – chopper.

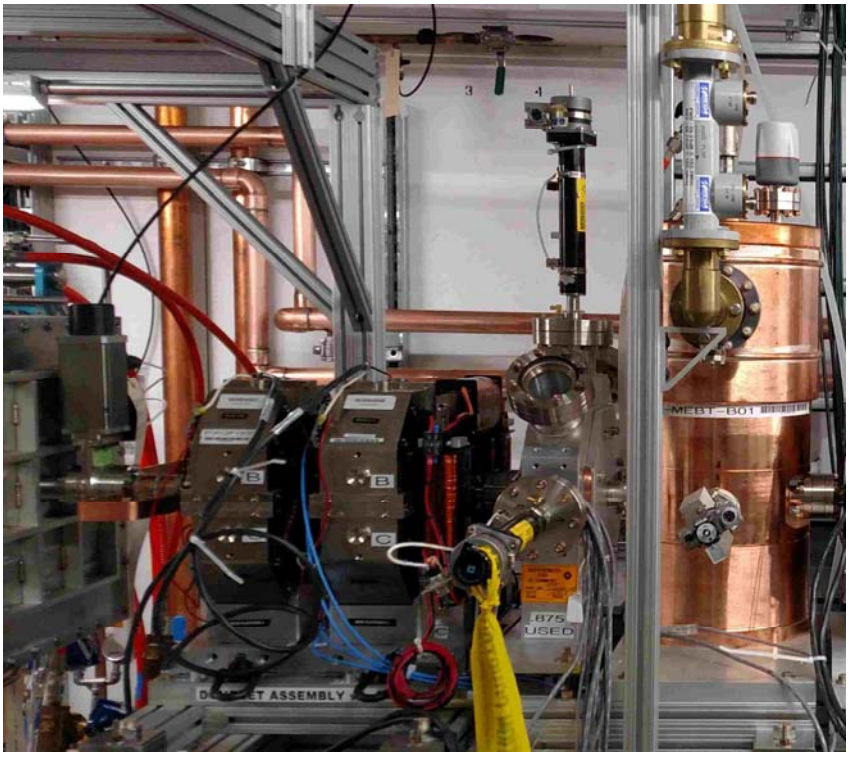

Figure 3.13. The MEBT section #0 as installed at PIP2IT. A quadrupole doublet is followed by a dipole corrector set, a scraper assembly, and a bunching cavity. A BPM is placed between the quadrupoles and is attached to the pole tips of the upstream quadrupole.

In addition to chopping and matching, the MEBT contains tools to measure the beam properties; a scraping system to protect both the SRF cavities and sensitive elements of the MEBT itself; and a vacuum system. In this chapter, the following major MEBT subsystems are discussed:

1. Transverse focusing
2. Longitudinal focusing

3. Chopping (kickers and absorber)
4. Scraping

Note that the vacuum system, instrumentation, MPS, HLRF, LLRF, and controls are described in other sections of this document and are mentioned here only as they are relevant to the overall design.

Transverse focusing

Transverse focusing is provided primarily by equidistantly placed quadrupole triplets; the only exception is two doublets immediately following the RFQ. Each triplet or doublet is followed by a pair of dipole correctors. The design of the central quadrupoles incorporates the BPMs mounted to their pole tips in order to assist with trajectory tuning. The specifications for the quadrupoles and correctors are listed in [62]. Figure 3.13 shows the air–cooled magnets. They were produced by BARC, India, according to these specifications, and are installed at PIP2IT.

The spaces between neighboring triplets or doublets are referred to as MEBT sections. The section separation in the regular part of the MEBT is 1175 mm, which leaves a 650-mm long (flange-to-flange) space for various equipment (only 480 mm in the section between doublets labeled #0 on Figure 3.12).

The 3σ envelopes of the passing-through bunches are presented in Figure 3.14, and corresponding simulated emittances along the MEBT are shown in Figure 3.15.

The envelope is kept varying gently over the MEBT length to avoid an emittance growth and is smaller only at the entrance and exit, where matching to RFQ and HWR occur. The notable exception is Section #8, where the vacuum chamber diameter is reduced to 10 mm over 200 mm. This insert is a part of Differential Pumping Section, which minimizes a flow of the gas released in the absorber to the SRF.

Longitudinal focusing

To keep the beam properly bunched and to match its longitudinal phase space to the first superconducting cryomodule, the MEBT includes four identical room-temperature bunching cavities. The cavities are specified in Ref. [63] and described in [64]. Each cavity is a quarter-wave 162.5 MHz resonator with the nominal accelerating voltage of 70 kV (at β=0.0668). At time of writing this document, one of four cavities is already manufactured and is installed at PIP2IT. Its view is presented in the right-hand side of Figure 3.13.

Chopping system

The chopping system envisioned for the PIP-II MEBT consists of two identical kickers and a beam absorber. The kickers, deflecting the beam in the vertical (Y) direction, are separated by a phase advance of ~180º (Y-direction) and synchronized, allowing the summation of their deflections. The absorber is at an additional ~90º of the phase advance with respect to the last kicker so that the angle introduced to a bunch by the kickers is translated at the absorber location into a 6σ separation in Y plane between the centers of the bunches designated for removal (“chopped-out”) and for acceleration (“passed–through”). In the main scenario of the kicker operation, both the chopped-out and passed-through bunches are deflected but into opposite directions, by applying opposite voltage polarities to the kicker plates. The simulated Y beam envelopes for these two cases are compared in Figure 3.16.

Both the kickers and the absorber require state-of-the-art designs.

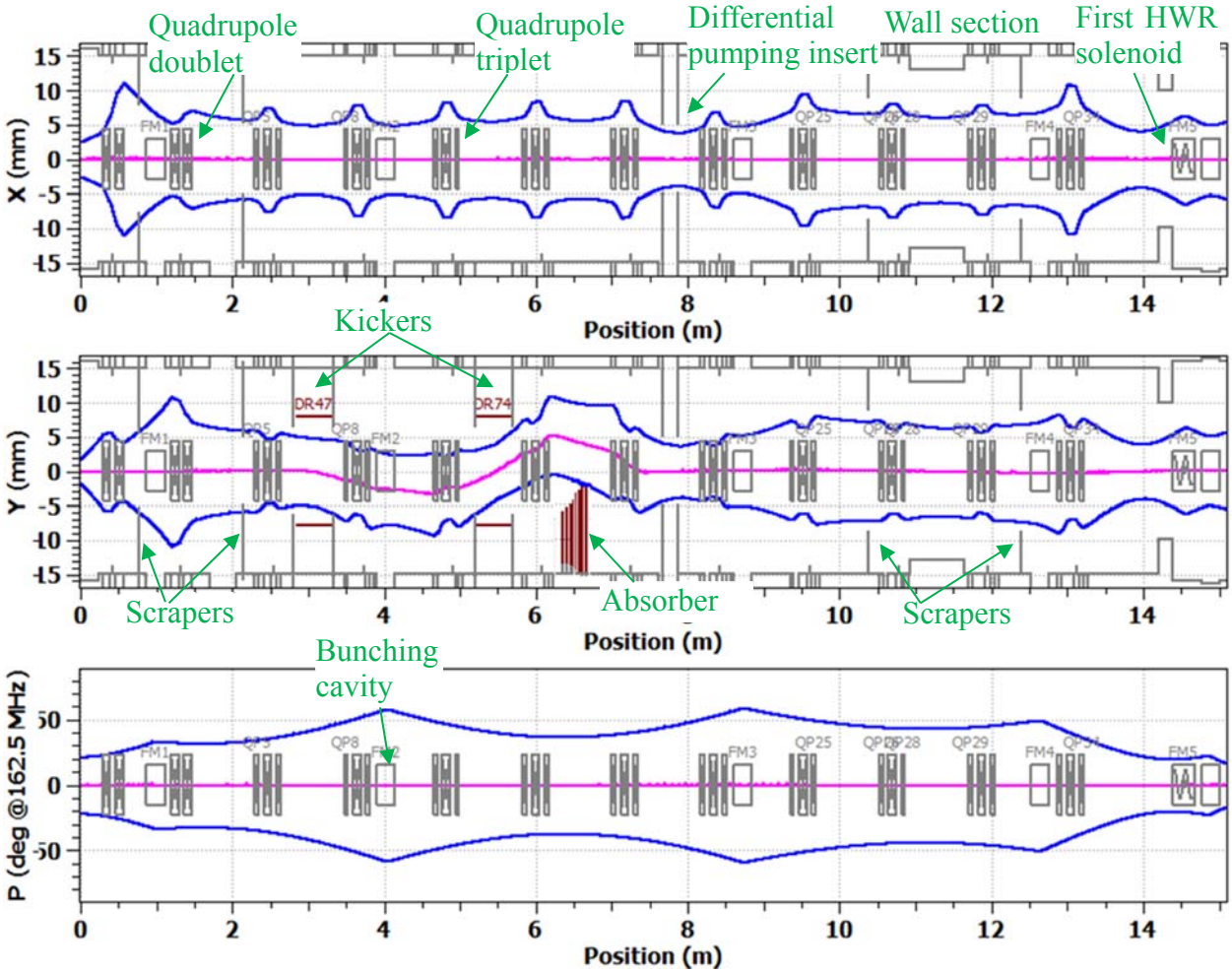

Figure 3.14. 3σ envelopes of the passing-through bunches simulated with the TraceWin code. The average beam current is 5 mA. Zero longitudinal position corresponds to the end of the RFQ vanes. The initial distribution is Gaussian in each of 6 dimensions. The initial transverse emittances are equal, 0.21 μm, and the longitudinal emittance is also 0.28 μm (both rms, normalized).

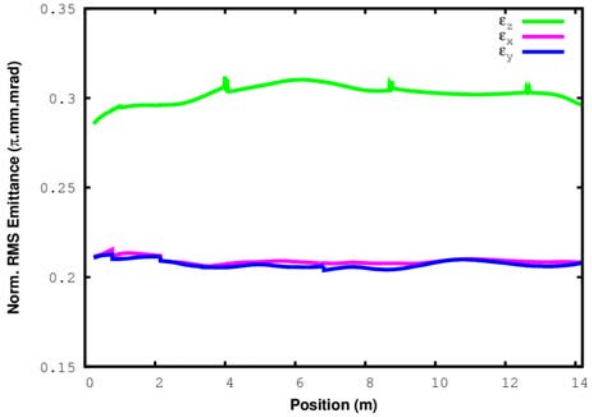

Figure 3.15. Simulated dynamics of the normalized rms beam emittance along the MEBT.

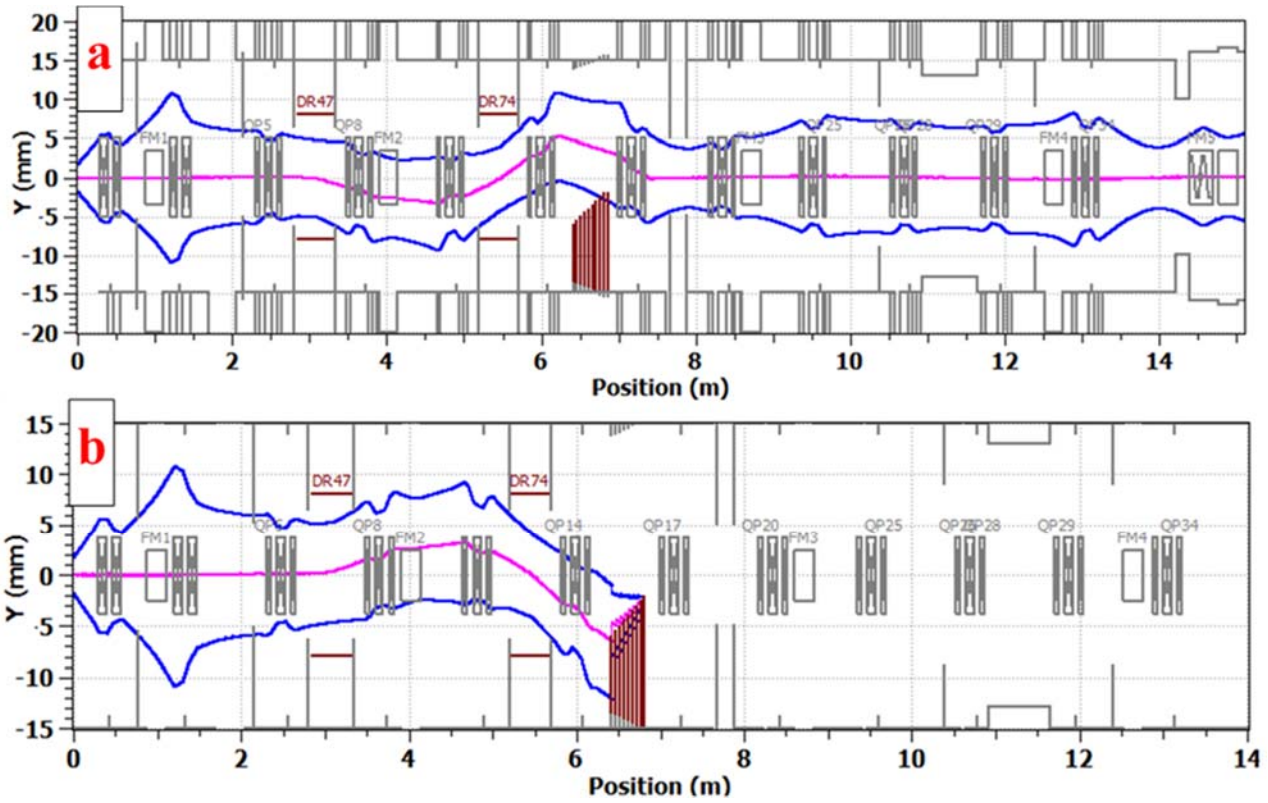

Figure 3.16. 3σ envelopes of the passing- through (a) and chopped-out (b) bunches simulated with TraceWin. The top plot is identical to the middle plot of Figure 3.14 and shown for comparison. For the top picture (a), voltages on the top and bottom plates of the first kicker are -250 V and +250 V, correspondingly, and opposite for the second kicker, (+250V, -250V). For bottom picture (b), all voltage values are inverted, i.e. (+250V, -250V) for the first kicker and (-250V, +250V) for the second.

Kickers

Each kicker is a 50 cm set of electrostatic plates connected by a broadband, travelling-wave structure. In average the transverse electric field of the kicking pulses propagates through the structure with a phase velocity equal to the speed of the H^- ions (20.0 mm/ns, $\beta = 0.0668$). Specifications for the kicker can be found in Ref. [65]. Top and bottom parts of the kicker are powered from pulse generators with voltages of opposite polarity so that to double the kick value. The required voltages is ±250 V. To minimize the emittance growth the electric field, co-propagating with a bunch, has to be uniform within about 10% along the length corresponding to 6 rms bunch lengths (1.3 ns or 26 mm). That requires the voltage for pulses flat-top/bottom to be constant within 25 V. The bunches are separated by the period of the 162.5 MHz RFQ frequency. The corresponding distance, 123 mm, is much larger than the gap between the kicker plates, 16 mm, and, therefore, the electric field deflecting one bunch does not directly affect other bunches.

Based on the experience from other labs (see, for example, [66]), special attention is paid to the survival of the kickers in real operational conditions, where errors are unavoidable. First, the design is specified to withstand a steady-state heating by 20 μA beam loss (0.4% of the nominal 5 mA beam) and an accidental loss of 20 J (2 ms at 5 mA). Second, the kicker aperture of 16 mm is limited to 13 mm by electrically-isolated protection plates installed on both sides of the kicker so that in the case of mismatched transport or steering error, the beam current intercepted on these plates would trigger

the MPS (Machine Protection System) to switch-off the beam.

Presently two versions of the kicker are being investigated [67]. In this document, they are referred by the characteristic impedance of their travelling wave structures: 50 Ohm and 200 Ohm.

The primary candidate is the 50-Ohm version, where the kicker plates are connected in vacuum by cable delay lines (purple loops in Figure 3.17a).

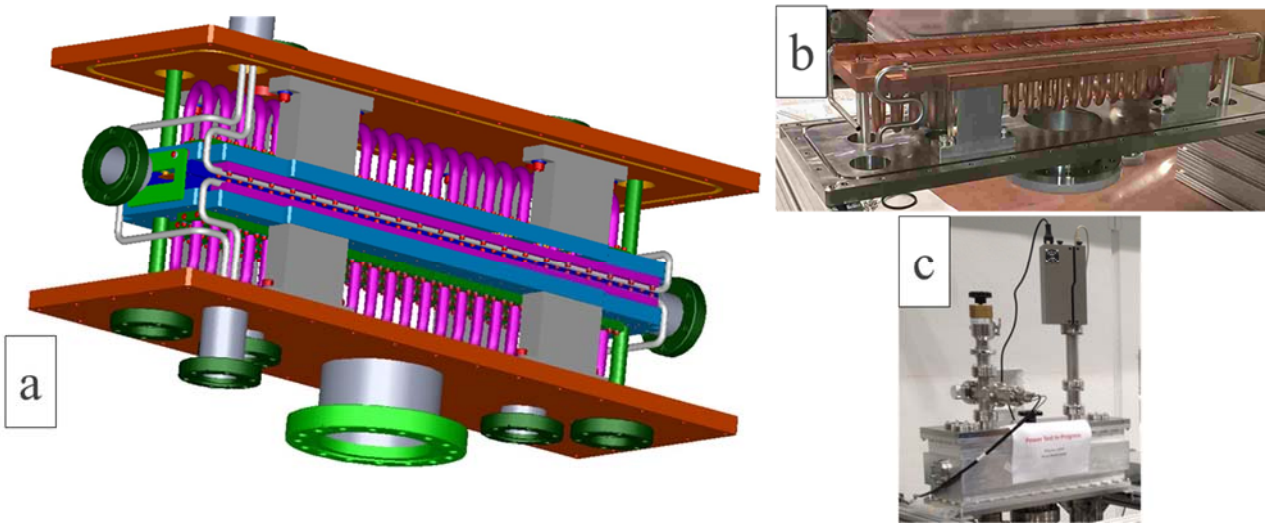

Figure 3.17: (a) 3-D model of the 50-Ohm kicker structure (side walls of the vacuum box are removed for presentation purpose). (b) One plate of the kicker during assembly. (c) Kicker under power testing.

Each kicker is driven by two commercially available linear amplifiers. Because these amplifiers are AC–coupled, the voltage applied to each plate is bipolar with zero average over a 162.5 MHz period. Signal distortion caused by the imperfections of the amplifier characteristics, cabling, and dispersion in the kicker structure are corrected by a corresponding pre-distortion of the amplifier's input signal. The scheme was successfully tested with a similar amplifier of a lower power as shown in Figure 3.18 from Ref. [67].

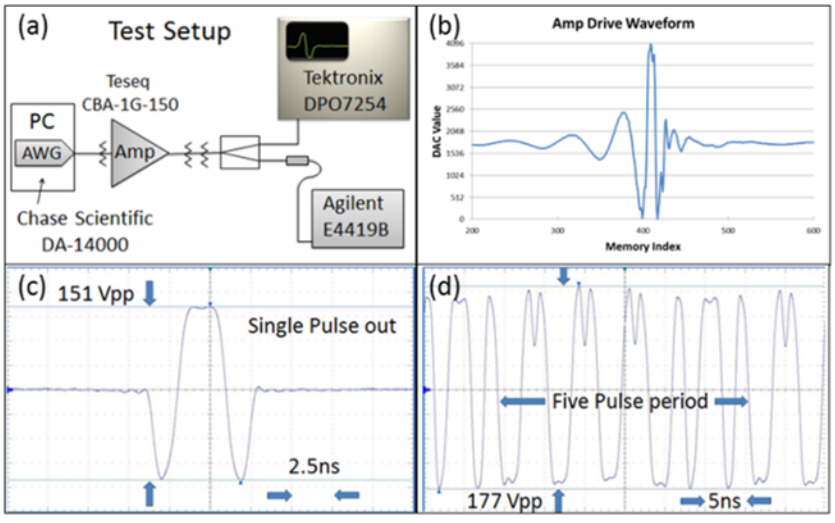

Figure 3.18: Test of the CBA 1G-150 amplifier with pre-distortion. (a) scheme of the test; (b) pre-distorted input signal and (c) corresponding output signal for a single pulse; (d) output for a CW pattern, corresponding to removal of four consecutive bunches followed by a one-bunch passage.

The 200-Ohm travelling-wave structure is a helical winding around a grounded cylinder with plates attached to the windings (Figure 3.18).

The main idea for this scheme is that the high impedance decreases the power requirement for the driver to the level where a state-of-the-art fast switch can be developed to drive the kicker. Since such driver is DC-coupled, the pulse can remain unipolar during each 162.5 MHz period. Consequently, the 500-V transitions between chopped-out and pass-through states do not require the second part of the pulse with other polarity, thus reducing requirements to duration of the rise and fall times. It also significantly simplifies the requirements to the dispersion of the travelling-wave structure (*e.g.* non-linearity of phase response with frequency). An example of an output pulse of a prototype driver is shown in Figure 3.20. Note that because of the non-standard impedance, custom-made feedthroughs, transmission lines, and current loads had to be developed for this scheme.

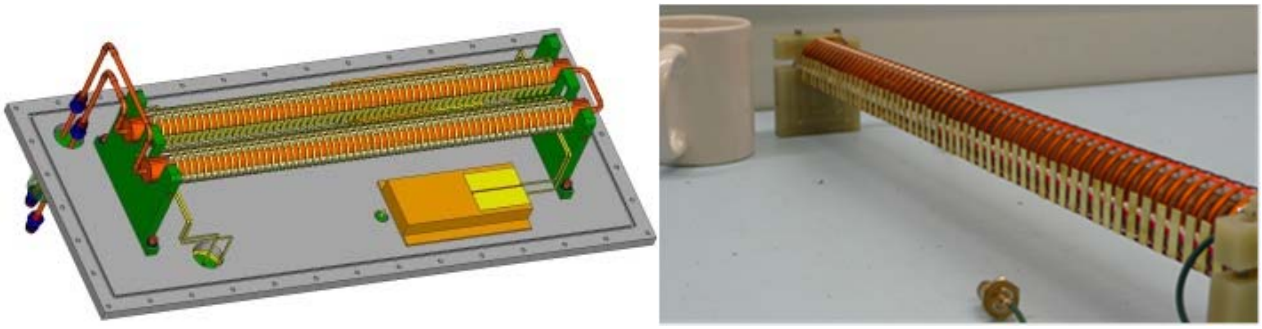

Figure 3.19: Conceptual design (left) and photograph (right) of a single-helix model of the 200-Ohm dual-helix kicker.

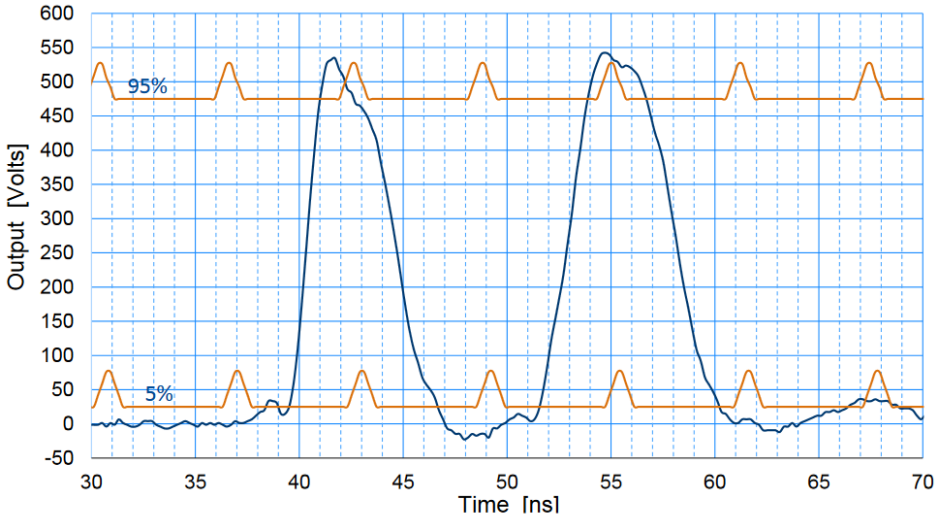

Figure 3.20: Example of an output pulse of a prototype driver being developed at Fermilab. The blue curve is the measured output voltage of the fast switch shaped to remove two bunches out of a CW sequence. The orange lines indicate the ±5% tolerance boundary for the voltage stability and mark the assumed position of the bunches and their 6σ length.

Development of both versions has not found any showstoppers yet. Prototypes of each kicker went successfully through high-power (thermal) tests and low-power RF measurements. The 50-Ohm kicker development advanced further, and the amplifiers are available for purchase. The 200-Ohm kicker scenario is potentially cheaper, though the driver is still in the R&D phase, and its CW

performance has not been demonstrated. Decision of which version to choose for the final implementation at PIP-II will be based on the results of tests at PIP2IT.

Absorber

The undesired bunches are directed onto an absorber that is displaced vertically from the beam line axis. To accommodate the entire beam the RFQ can deliver, the absorber is specified in Ref. [68] for the maximum beam power of 21 kW (a 10-mA CW beam completely diverted to the absorber). The power density in the beam with a ~2 mm rms radius exceeds by an order of magnitude what is technically possible to intercept at normal angle of incidence without melting the surface. To decrease the surface power density, the absorber is positioned at a small angle (29 mrad) with respect to the beam (Figure 3.21).

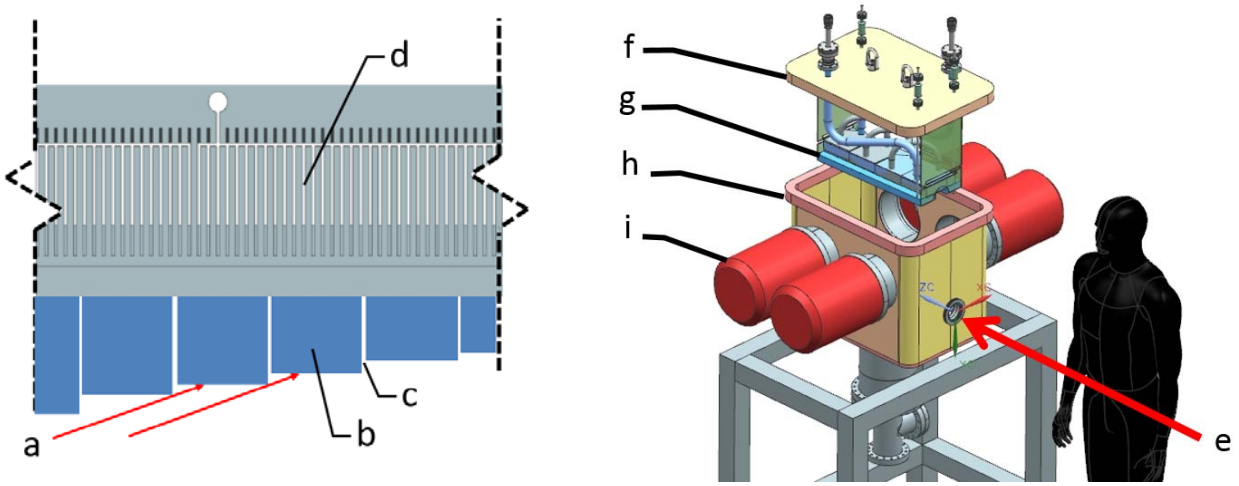

Figure 3.21: A conceptual design of the MEBT absorber. Left: a side-view cross section of the absorber showing (a) the beam incident on the surface, (b) the segmented absorber blocks, (c) the shadowing step increment (magnitude exaggerated), (d) the 300μm wide water cooling channels with 1mm pitch. Right: an exploded view of the absorber assembly showing (e) the incoming beam, (f) the flange-mounted absorber subassembly (g) the absorber blocks, (h) the enclosure with provisions for secondary particle absorption, (i) the turbo pumps.

Challenges in the absorber design include spreading the energy deposition, managing surface effects (sputtering and blistering), containing secondary and reflected particles, accommodating radiation effects, maintaining vacuum quality, and survival at high temperatures with temperature-induced mechanical stresses. Presently the design choice is an absorber with an absorbing surface composed of multiple absorber blocks made of the molybdenum alloy TZM and preloaded against a water-cooled aluminum strongback [69]. In comparison with an initially considered monolithic design, this solution slightly increases the thermal conductance from the absorber surface to water channels but dramatically decreases the chance for catastrophic failure if a crack developed at the absorbing surface propagates all the way to the water channels. Power management in a ¼-size prototype of such design was successfully tested on an electron-beam test stand [69].

In CW mode, the beam stopped at the absorber delivers quite large volume of hydrogen as well as results in additional degassing from the receiving surface of the absorber. If not addressed, it can spoil the vacuum in the MEBT. To suppress H^- stripping and to reduce the gas load to the downstream cryomodule the vacuum in vicinity of absorber should be better or about $2 \cdot 10^{-7}$ Torr. It is supported

by four turbo-pumps installed at the absorber enclosure and the differential pumping pipe installed in the section #6.

Scraping system

Each of the sections #0, 1, 8, and 10 in Figure 3.12 contains a set of 4 scrapers (Left, Right, Top, and Bottom), totaling 16 plates. A scraper is an electrically-insulated, 75W-rated TZM plate movable across the 30-mm MEBT aperture [70]. The scrapers will be used for several purposes: (1) for beam halo measurements and removal, (2) protection of downstream equipment from a beam loss caused by beam envelope and trajectory mismatches, (3) as auxiliary beam density distribution diagnostics, and (4) formation of a pencil H^- beam for measurements downstream. The last two items are related to the short-pulse mode of operation. The scraper sets in each of the upstream and downstream pairs are separated by a phase advance of ~90° to ensure removing effectively particles with large transverse actions.

A simulated example of the protection the scrapers provide is shown in Figure 3.22. The simulation considers a mis-phase of the kickers, so that the voltages on all kicker plates are half of the nominal value required for chopping bunches out. In this scenario a significant portion of the beam misses the absorber but is intercepted by a scraper downstream. Consequently, in the case high power operation, it will result in a beam trip by the MPS.

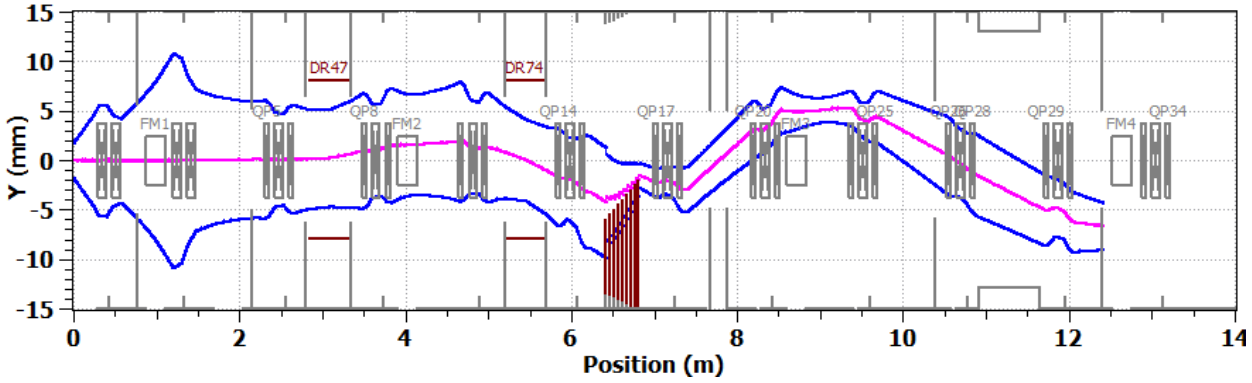

Figure 3.22: Beam Y 3σ envelope with voltages on all kicker plates equal to half of the nominal value required for chopping bunches out.

Similar to the absorber, in CW mode, the beam stopped at the scrapers delivers hydrogen and results in degaussing from their surfaces. The scraper irradiation also can generate dust particles due to blistering and sputtering. Considering this, the design assumes that steady-state scraping removes ~1% of every bunch with the first two scraper sets and ~0.1% with the third and fourth.

3.1.2. Superconducting Accelerating Structures

The parameters and requirements associated with all of the accelerating structures and cryomodules within the linac have been summarized in Tables 2.3, 2.4 and 2.5. This section describes design concepts for the cavity types required in the linac, and the associated cryomodules.

3.1.2.1. Half-Way Resonator (HWR) Cryomodule

The initial proposal included 325 MHz Single Spoke Cavities of type 0 (SSR0), to accelerate the H^- beam from 2.1 to 10 MeV. To maintain high beam quality, an adiabatic increase of the accelerating gradient in the SSR0 cavities was necessary, and satisfying the adiabaticity condition required 3 cryomodules comprising 24 SSR0 cavities. After careful consideration, a design based on 162.5-MHz Half-Wave Resonator (HWR) cavities was selected instead. This design has several substantial advantages if compared to the 325 MHz SSR0 option:

- Only 8 HWRs are required to accelerate the beam to ~10 MeV while maintaining high beam quality.
- Reduced RF defocusing due to both the lower frequency and the lower synchronous phase angle results in a much faster energy gain without emittance growth.
- It opens the possibility to use 162.5 MHz rebunchers in the MEBT to allow for longer drift spaces for the fast beam choppers.
- Significant cost reduction due to the reduced component count.

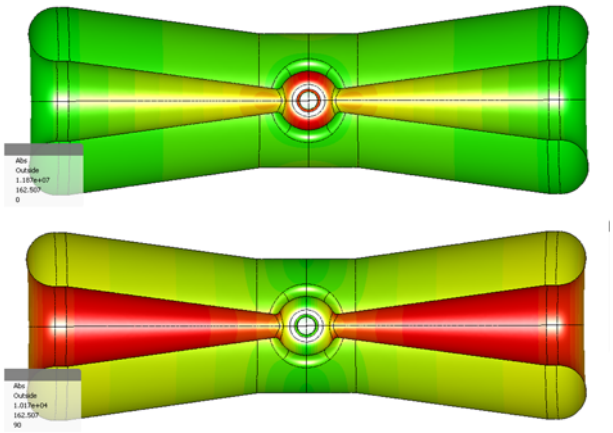

Figure 3.8: Left - Half-wave resonator model in Microwave Studio (MWS). The picture shows electric (top) and magnetic field (bottom) distributions on the surface. Red is high intensity and green is zero.

The beam dynamics optimization determines that a cavity beta of β_{OPT}=0.112 is optimal. The cavity design is based on recent advances in SRF technology for TEM-class structures being developed at ANL. Highly optimized EM parameters which maximize the real-estate gradient while maintaining low dynamic cryogenic loads and peak surface fields were achieved using a conical shape for both the inner and outer conductors. A "donut" shaped drift tube in the center conductor (see Figure 3.8) has been developed to minimize the undesirable quadrupole component of the electric field as is shown in Figure 2.28. Utilization of the HWR requires two major sub-systems: a 10 kW RF coupler and a slow tuner. A capacitive adjustable 10 kW RF coupler prototype has been designed, constructed, and successfully tested in 2014. It will provide RF power through the port which is perpendicular to the beam axis in the center of the cavity (Figure 3.9). A pneumatically actuated mechanical slow tuner which compresses the cavity along the beam axis is located outside

of the helium vessel and will be attached to the SS beam port flanges shown in Figure 3.9. A fast tuner is not required for CW operation anticipated for the HWR. The power margin (see Table 2.11) was chosen to be sufficient to suppress microphonics (mainly related to helium pressure fluctuations) without fast tuner. The required cavity bandwidth (loaded) is 60 Hz. The main parameters of the HWR are shown in Tables 2.3 - 2.5.

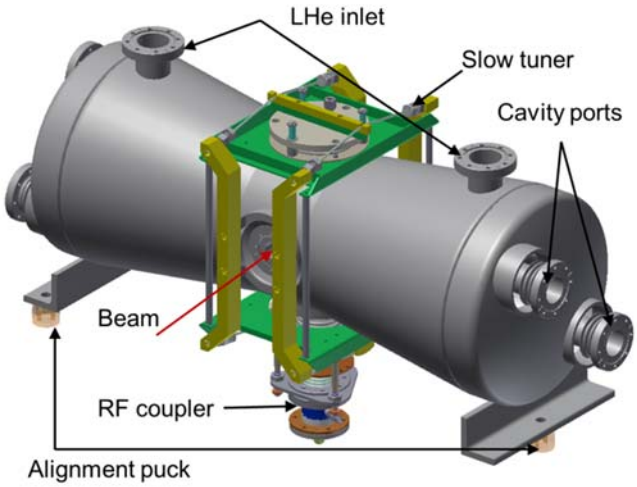

Figure 3.9: HWR cavity 3D model in INVENTOR

Extensive finite element analysis of the cavity included simulations to evaluate the integrity of the cavity per the Fermilab ES&H manual. The simulations include protection against plastic collapse, local failure, buckling, ratcheting and fatigue failure to ensure that the operating loads are below the maximum allowable limits. The maximum structural load is determined by the pressure set by the operation of the cryogenic system and the safety pressure relief valve. The evaluation was performed for 30 psig at room temperature and 60 psig at 2 K^0 in the helium space of the cavity in compliance with the Fermilab requirements. In general, the over pressure condition could occur during the initial cryogenic cooling with the cavity structure at or near room temperature. Since the room temperature strength limits (*i.e.*, yield and ultimate stress) are lower than for cryogenic temperatures and the operating margin is smaller here, the room temperature limits were studied in more detail. The stress analysis was performed in the presence of the slow tuner and other appurtenance loads. The final design exceeds all evaluation criteria for the niobium and the stainless steel (SS) parts, respectively. Two methods have been studied for minimization of the cavity frequency sensitivity to fluctuations of the helium pressure: (1) adding gusseting to reduce the cavity deflections in the high magnetic and electric field regions, and (2) varying the depth of the flat dish located opposite to the RF coupler port. The results of these studies showed that no gusseting is required; a minimal value of 1.4 kHz/atm was achieved by optimizing the dimensions of the flat dish penetration. Simulations of the slow tuner were performed by applying a force to the SS flanges of the helium jacket. For example, a 10 kN force results in a frequency shift of -120 kHz.

The primary operational parameters for the HWR presented in Tables 2.3 – 2.5 are based on experience with the ATLAS energy upgrade cryomodule and its long term operation [72], and recent tests of the first undressed HWR cavities. As shown in Figure 3.10, the tests of ATLAS 72 MHz Quarter Wave resonators (QWR) show ~2 nΩ residual surface resistance at 48 mT, which readily supports design parameters of the HWRs. Recent measurements of the two first HWR cavities showed Q_0 equal to $1.7 \cdot 10^{10}$ at the operating gradient which corresponds to a surface resistance of 2.8 nΩ. Although this value is slightly larger it actually is a more optimistic value for the surface

resistance if one takes into account the 2.2 times increase in the operating frequency. Thus measured Q_0 value provides a margin of more than 3 times relative to a conservative value of Q_0 presented in Table 2.6. Note that the ATLAS cavities were measured in a real cryomodule while the HWR cavities in the test-stand. However, experience accumulated in recent years assures us that there is no significant Q_0 increase when cavity is moved to a cryomodule.

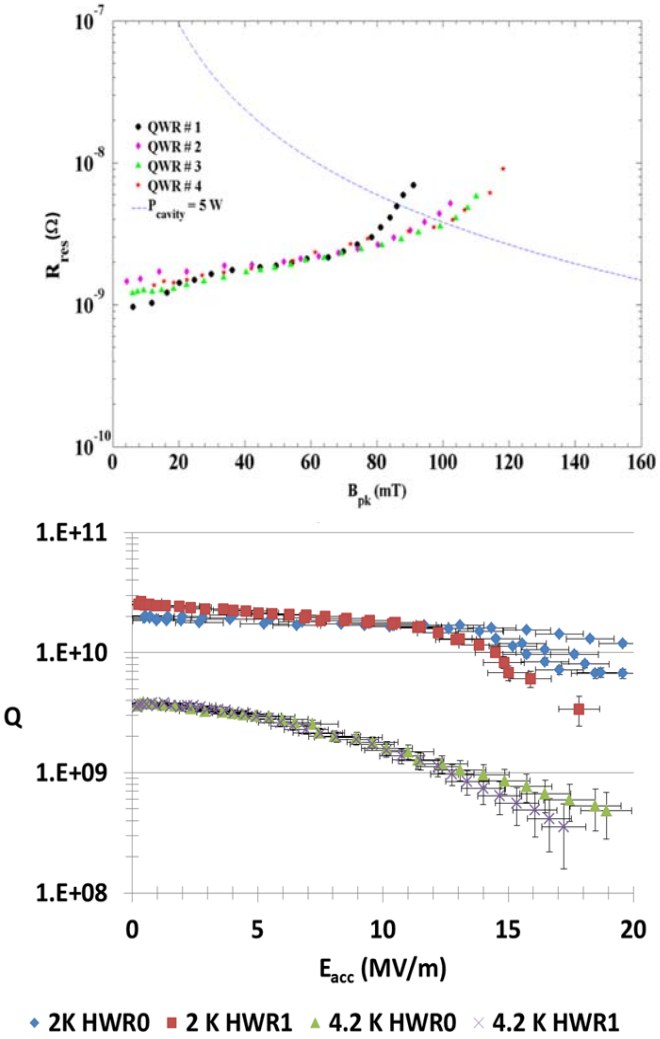

Figure 3.10: Cavity residual resistance measured in the ANL Intensity Upgrade QWR (left) and recent measurements of Q_0 dependence on the accelerating gradient for the first two HWR cavities (right); operating accelerating gradient is 9.7 MV/m, and corresponding peak magnetic field – 48 mT.

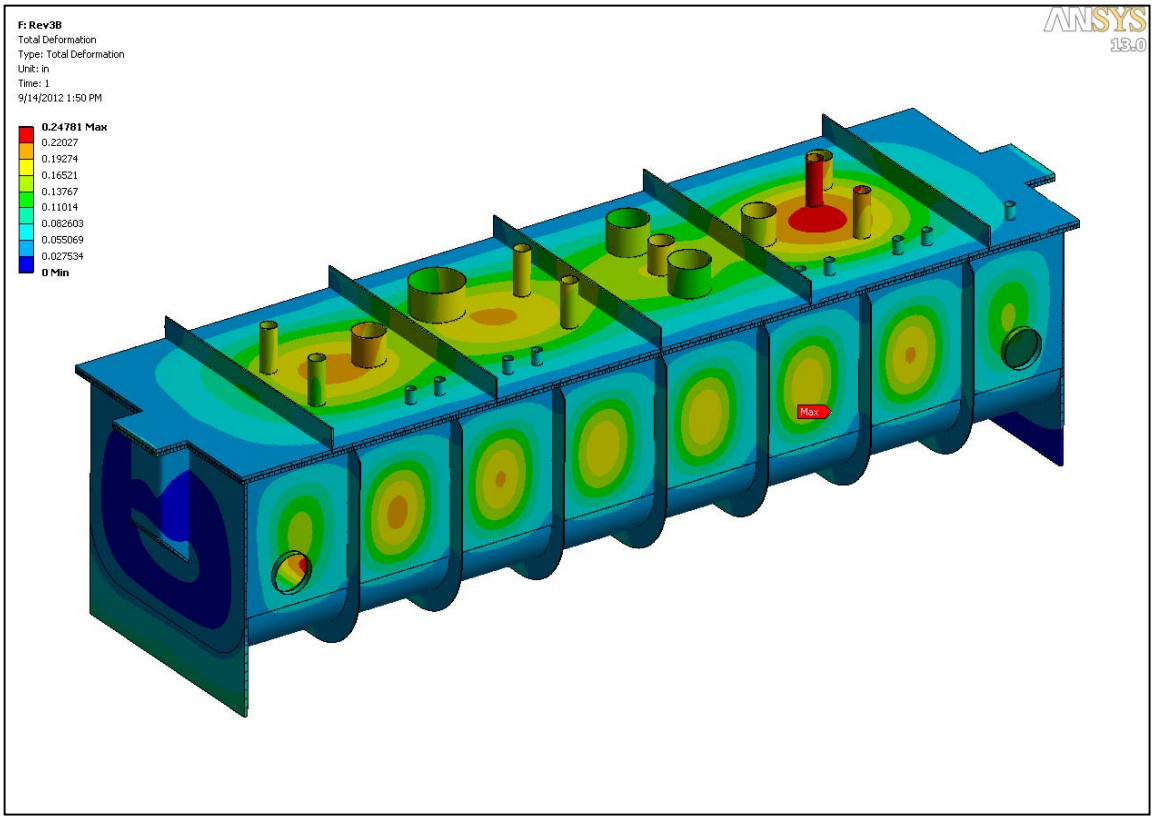

Figure 3.11: ANSYS results of the vacuum vessel deformation due to a 14.7 psi static pressure gradient across the walls. The red color corresponds to displacements greater than 0.6 inches with the maximum being 0.67 inches.

The cryomodule designs all build upon past ANL experience with box cryomodules. In the HWR case the cryomodule is much wider due to the half-wave cavities being mounted on their sides. To keep a half-cylinder bottom would make the vacuum vessels unacceptably tall. We have arrived at making the vacuum vessel a box which appears to be a good compromise between fabrication cost, structural integrity and minimizing cryostat height. The radii of the rounded corners were chosen to fit the contents of the box minimizing the overall height including the depth of the required gussets. Figure 3.11 shows the results of ANSYS calculations of the structural deformations due to vacuum resulting in walls being pulled to the inside. Notice that the structure pulls in about 0.25" on average due to evacuation, the maxima are between 0.5" and 0.67". Motion of the vacuum vessel wall moves the internal magnetic shielding and stresses the baton points which may degrade performance. Reducing the maximum displacement to less than 0.25" will avoid this but it adds the cost of additional gusseting. Future tests are planned to evaluate the magnetic shielding.

The cryomodule houses 8 sets of identical components. Each set forms a focusing period and includes a resonator, a SC solenoid with 4 dipole coils and a Beam Position Monitor (BPM). Beam dynamics requires the solenoids to be aligned to better than ±0.5 mm peak transversely with $\pm 0.1^0$ for all of the rotation angles with similar constraints on the cavities. The beam-line string length is 6 meters and will be supported and aligned on a cryomodule spanning titanium rail system, called the strong-back as shown in Figure 3.12. The strong-back is composed of 2 inch × 8 inch grade 2 titanium plates formed into a box and supported by titanium hangers. Each component is mounted on top of the strong back with its own independent kinematic-alignment hardware.

Table 3.2 summarizes the estimated static and dynamic heat loads at each temperature level in the

cryomodule assembly (Figure 3.13) from all sources. The following sources were included in the calculation of 2K heat load: cavities, RF couplers, helium manifold, radiation from 70K to 2K, instrumentation, high current leads, strongback hangers, cavity and solenoid cooldown lines, vacuum manifold, slow tuners, and gate valves. Changing the operating voltages by + and -20% will result to 28W and 21 W total 2K heat load respectively. Currently two HWR prototypes are being fabricated. In addition, a high-power RF coupler, a BPM and SC solenoid were built and cold tested.

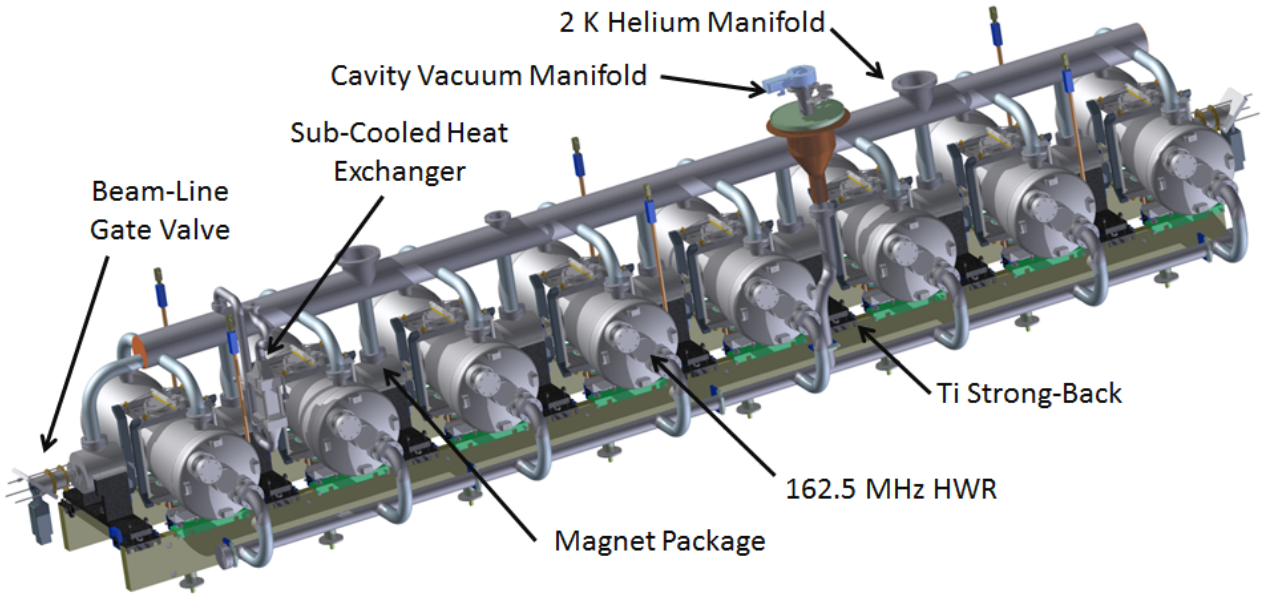

Figure 3.12: HWR Cavity String Assembly.

Table 3.2: HWR Cryomodule Heat Load Estimate

Temperature	Load, W
2 K, static	14
2 K, dynamic	12*
5 K	60
70 K	250

*This value takes into account actual voltage distribution on the HWR cavities

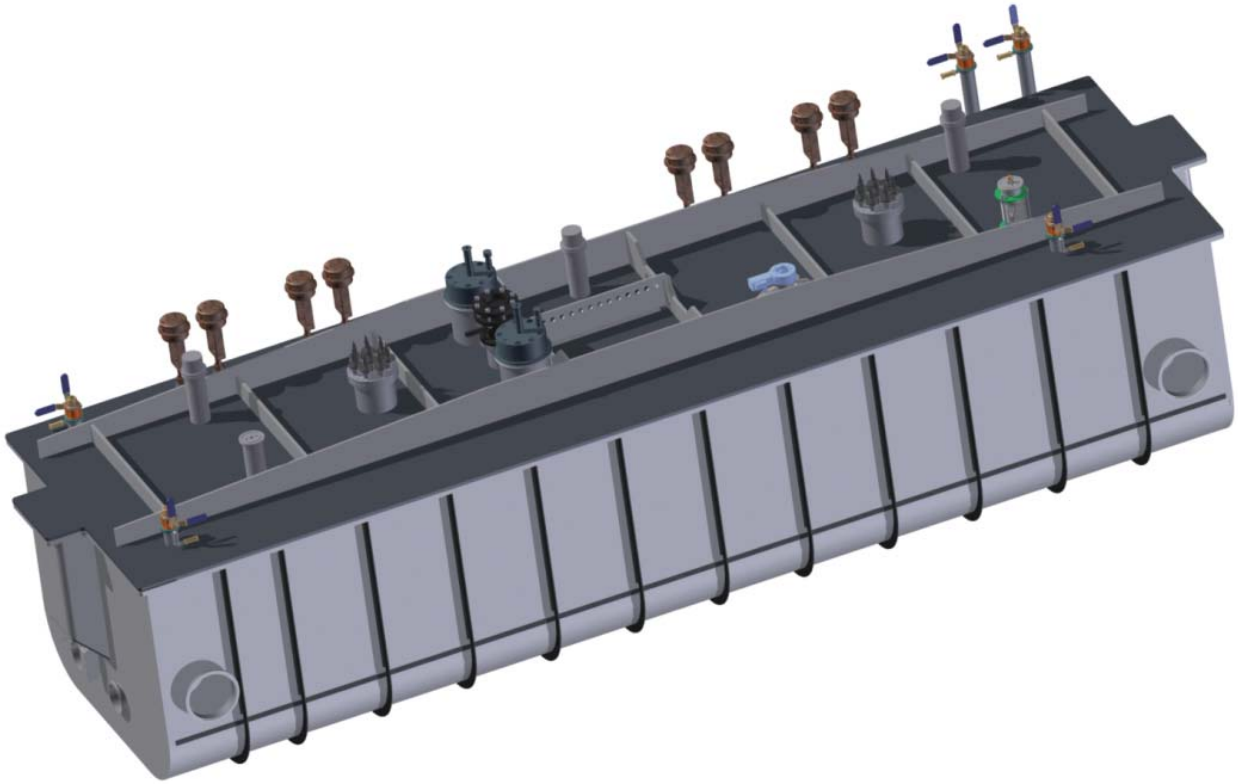

Figure 3.13: HWR cryomodule assembly.

3.1.2.2. Single Spoke Resonator I (SSR1) Cavities and Cryomodules

Two 325 MHz cavity types are required to accelerate beam from 10 to 185 MeV (β=0.15 to 0.63). They are named SSR1 and SSR2. The general requirements on their parameters are listed in Tables 2.3 – 2.5.

SSR1 Cryomodule

Acceleration from 10 to 35 MeV utilizes superconducting SSR cavities with $\beta_{opt} = 0.222$ (SSR1). The cavity has geometrical and electro-magnetic parameters shown in Tables 2.3 – 2.5. A SSR1 cavity matching these requirements has been designed, fabricated, and tested with RF power as part of the HINS program. The mechanical design, including focusing elements, is displayed in Figure 3.14.

Figure 3.15 shows the first (SSR1-02) cavity fabricated as part of the HINS program. The left photograph shows the bare cavity, the right a "dressed" cavity encased in its He jacket with ancillary slow and fast (piezo) tuners. To date an additional ten bare cavities were fabricated and delivered to Fermilab, (SSR1-05 – SSR1-14). All of them have been tested and showed parameters suitable for operation in PIP-II. The measured performance at 2K of the bare cavity in a vertical test is displayed in Figure 3.16. Note that the cavities are made from niobium, which is not certified for high-gradient ILC operation due to demonstrated higher losses than material from certified vendors. However, all the cavities show a $Q_0 > 7\times10^9$ at the 2K at the operating gradient of 10 MeV/m, which is well above the required value $Q_0 > 6\times10^9$. Note that the cavity SSR1-02 made of certified material demonstrated a $Q_0 = 1.1\times10^{10}$ at 2K at the operating gradient. The measured surface resistance of this cavity as a function of temperature is shown in Figure 3.16. The cavity operational and test requirements are summarized in Table 3.3.

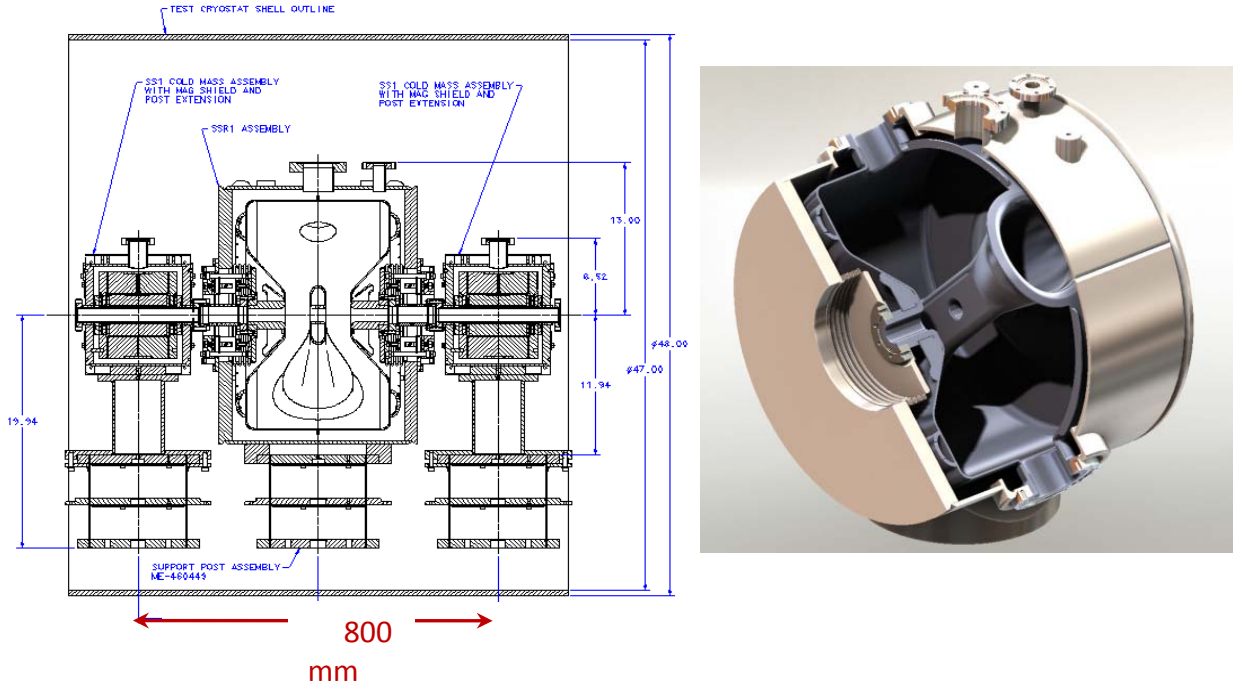

Figure 3.14: SSR1 cavity mechanical design and cutaway view.

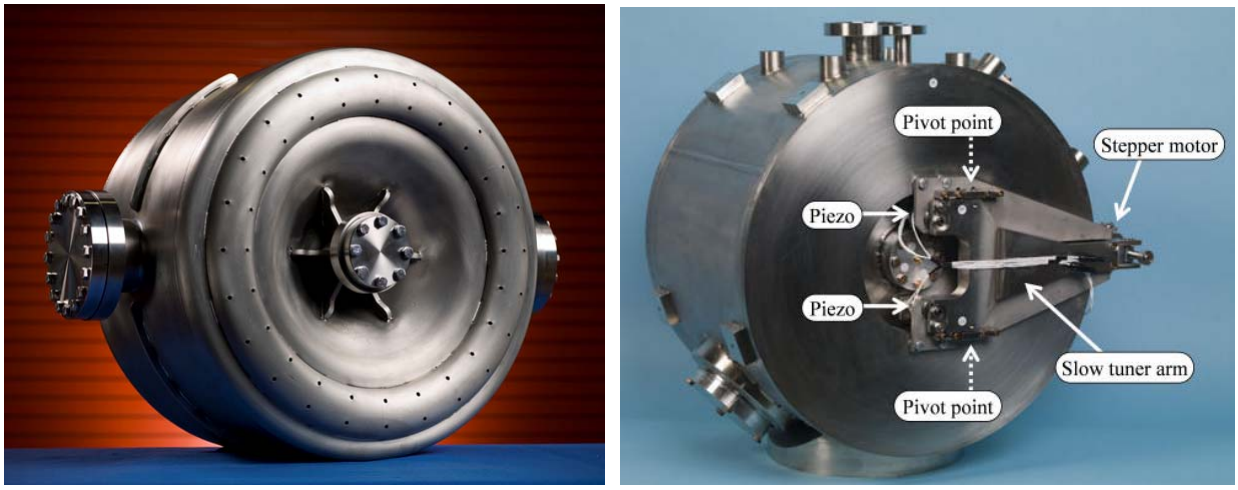

Figure 3.15: Photographs of the bare and dressed prototype SSR1 cavity

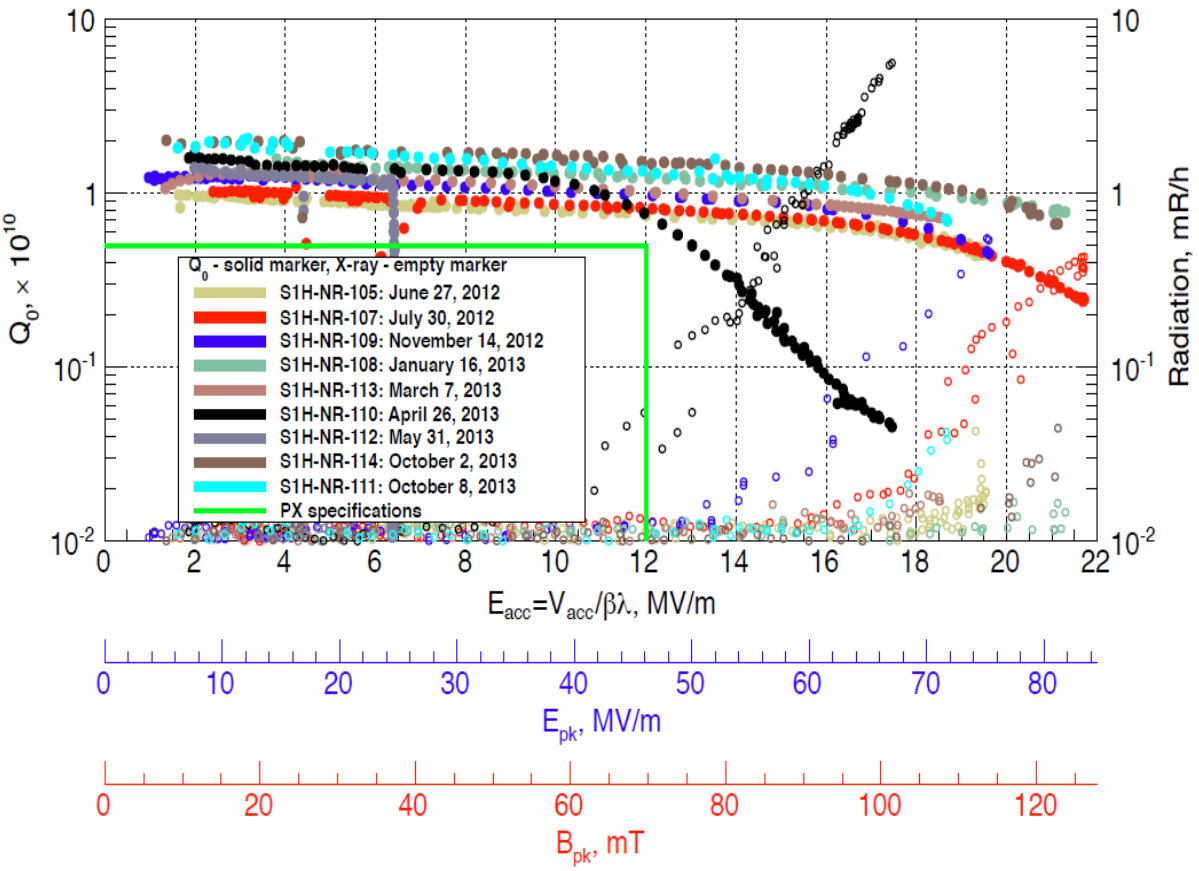

Figure 3.16: Q_0 vs. acceleration gradient from the cold test of the nine SSR1 cavities (β = 0.222). Operating voltage of 2.05 MeV corresponds to B_{peak} = 58.1 mT.

A spoke cavity has no axial symmetry. Therefore its quadrupole component cannot be compensated over the entire range of cavity operation. Figure 2.28 presents the dependence of the quadrupole effect on the beam velocity. Due to engineering limitations, mainly related to the RF couplers, the cavities are rolled by 45°; consequently, their quadrupole field is also rolled and is equivalent to a skew-quadrupole field. The cavity skew-quadrupole fields will be compensated by correction coils located inside nearby focusing solenoids and capable to create dipole and skew-quadrupole fields.

In order to attain the requirements for frequency range and resolution (Table 3.4), the tuning systems for cavities of narrow bandwidths such as SSR1 typically integrate coarse and a fine mechanisms engaged in series. The first normally utilizes a stepper motor with large stroke capability and limited resolution, the latter usually contains piezo-electric actuators with limited stroke but virtually infinite resolution.

The coarse tuner is predominantly used to achieve consistently the resonant frequency during the cool-down operations. The range necessary to compensate for cool-down uncertainties is estimated to be 50 kHz. In the event that a cavity must be detuned as a result of a malfunction, the coarse tuning system must be able to shift the frequency away from resonance by at least 100 bandwidths, which equals to ≈10 kHz, so that the beam is not disturbed. The requirement on the range was set arbitrarily considering a safety margin of 2.7. The requirement on the resolution of the coarse tuning system is set to a value that would allow operation in the event of a failure of the fine-tuning system. Based on other applications, it is believed that such resolution can be achieved with a coarse tuning system.

Table 3.3: SSR1 cavity operational and test requirements.

Parameter	Requirement
Max leak rate (room temp)	$< 10^{-10}$ atm-cc/sec
Operating gain per cavity	2.0 MeV
Maximum gain per cavity	2.4 MeV
Max. power dissipation per cavity at 2 K	5 W
Sensitivity to He pressure fluctuations *df/dP*	< 25 Hz/Torr
Field flatness	Within ±10%
Multipacting	None within ±10% of operating grad.
Operating temperature	1.8-2.1 K
Operating pressure	16-41 mbar differential
MAWP	2 bar (RT), 4 bar (2K)
RF power input per cavity	6 kW (CW, operating)

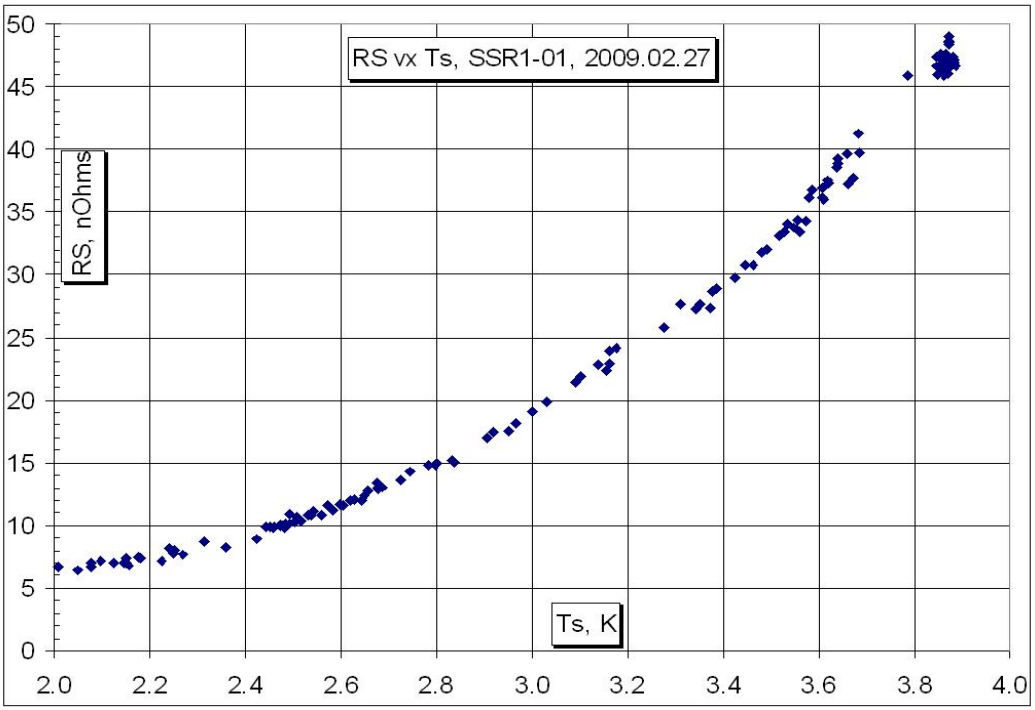

Figure 3.17: Temperature dependence of the surface resistance for SSR1 cavity.

Table 3.4: SSR1 tuning system requirements

	Requirement
Coarse frequency range	135 kHz
Coarse frequency resolution	20 Hz
Fine frequency range	1 kHz
Fine frequency resolution	≤2 Hz

It is conservatively assumed that the coarse system cannot be operated during beam acceleration; it is thought that the vibration of a stepper motor may induce vibrations in the cavity severe enough to disrupt the operation. Thus, fine tuners shall be designed to compensate, at a minimum, the frequency shifts of the cavity induced by fluctuations of the helium bath pressure. The use of fine tuners will reduce considerably the hysteresis of the system by limiting the elements in motion during the tracking of the frequency. A particular design effort shall be dedicated to facilitate access to all actuating devices of the tuning system from access ports on the vacuum vessel. All actuating devices must be replaceable from the ports, either individually or as a whole cartridge.

Figure 3.18: SSR1 cavity, helium vessel, and tuner.

The Helium vessel is fabricated from a non-magnetic stainless steel (e.g. 316L) designed to house a 2 K helium bath sufficient to remove up to 5 watts average dissipated power, with appropriately sized supply and return piping. It meets the requirements of the Fermilab ES&H Manual for cryogenic pressure vessels and is rated at an MAWP (Maximum Allowable Working Pressure) of no less than 2 bar at room temperature and 4 bar at 2 K. The cavity vessel with tuner system is shown in Figure 3.18.

SSR1 Current Leads

Each focusing element package contains five coils: the main solenoid, operating up to 100 A, and four coils which can be combined to serve as both *x* and *y* steering and skew-quadrupole correctors. Each coil can operate up to 50 A. A conduction cooled current lead design modeled after similar leads installed in the LHC at CERN is being developed for use in the SSR1 cryomodule. Thermal

intercepts at 70 K and at 5 K help reduce the heat load to 2 K, nonetheless, these current leads represent a significant source of heat at the low temperature end. There will be one lead assembly for each magnetic element.

SSR1 Solenoid and Beam Position Monitor

The four magnet packages in the cryomodule each contain a focusing solenoid (lens) and four corrector coils all operating in a helium bath at 2 K. The general design requirements for the lenses in the SSR1 cryomodule are summarized below.

Requirements essential for the beam dynamics in the linac:

- The integrated focusing strength of the lens must be not less than 4 T^2m;
- Each lens must contain 4 coils which can be combined into two dipole correctors; bending strength of each corrector must be not less than 0.0025 T-m;
- The clear aperture in the lens must be not less than 30 mm;
- The uncertainty in the location of the effective magnetic axis in the focusing solenoid of the lens relative to reference points on the outer surface of the device must be better than 0.1 mm rms.

Requirements essential for proper functioning of the cryomodule:

- Maximum current in the solenoid must be less than 100 A;
- Maximum current in the dipole correctors must be less than 50 A;
- A LHe vessel must be used for cooling the windings down to 2 K;
- The lenses must be quench-protected; the energy deposited in the lenses after quenching must be as low as reasonably achievable;
- The LHe vessel must meet the requirements of the Fermilab's ES&H manual chapters for pressure vessel;
- The design of the LHe vessel must ensure reliable and reproducible mechanical connection to the alignment fixture of the cryomodule;
- The maximum magnetic field generated by lenses in the cryomodule in the area near the surface of the SSR1 superconducting cavities must not exceed the level that would result in more than two-fold reduction of the intrinsic quality factor after quench event at any point on the surface of the cavity.

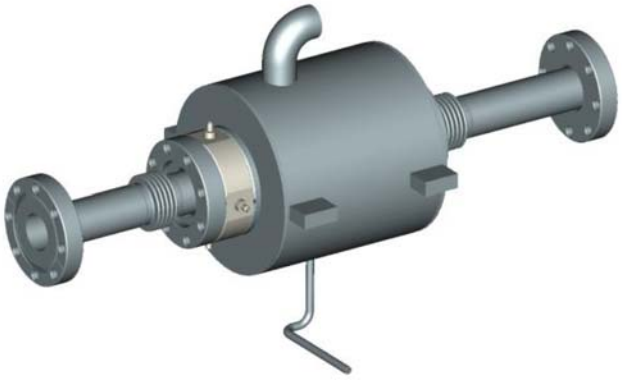

Figure 3.19: Solenoid and BPM assembly.

The linac lattice, especially the low-beta section, provides limited space along the beamline for beam diagnostics either inside individual cryomodules or between adjacent modules. In order to conserve axial space along the beamline a button-type beam position monitor (BPM) has been chosen for installation in the SSR cryomodules. For a non-relativistic beam they also generate larger signal than strip-line BPMs. A total of four BPMs will be installed in the cryomodule, one near each magnetic element. These devices are compact and lend themselves well to incorporation into the solenoid magnet package as shown in Figure 3.19. The bellows at either end of the beam tube allow independent alignment of each magnet.

Final Assembly

The final assembly of the SSR1 cryomodule for SSR1 is shown in Figures 3.20 and 3.21. Figure 3.20 shows the cavity string consisting of the cavities, solenoids, beam position monitors, and internal piping mounted on support posts that are in turn mounted to the strongback. Figure 3.21 shows the entire cryomodule assembly.

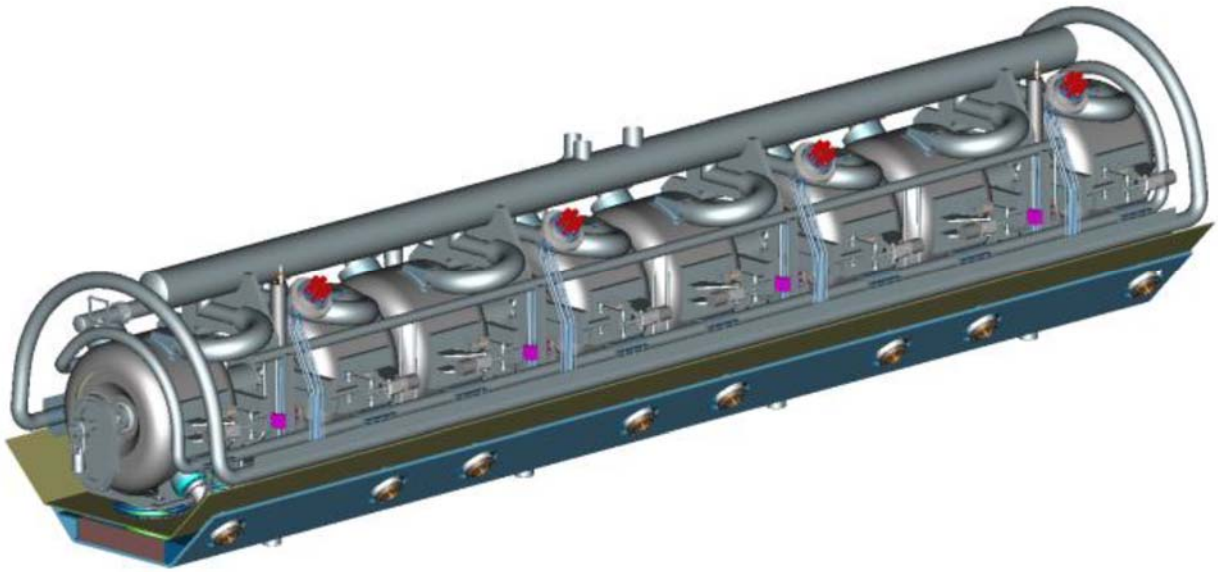

Figure 3.20: SSR1 cavity string assembly.

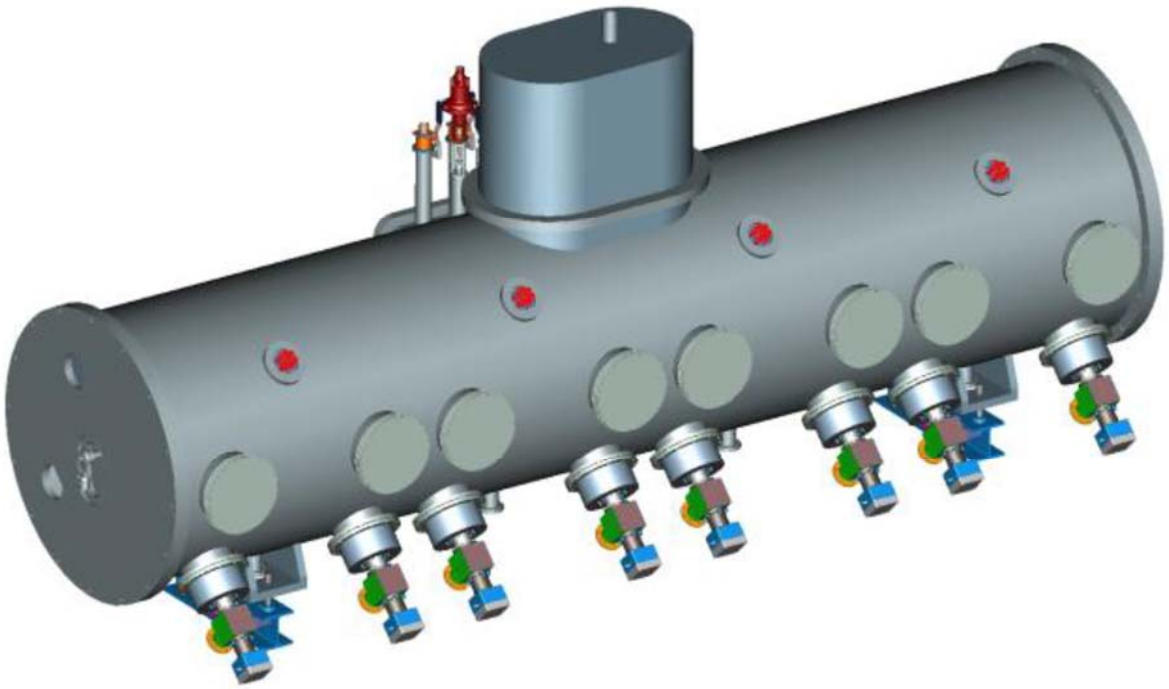

Figure 3.21: SSR1 cryomodule assembly

SSR1 Heat Load Estimate

Table 3.5 summarizes the estimated static and dynamic heat loads at each temperature level in the cryomodule assembly from the primary sources. As mentioned earlier, the nominal 70 K thermal shield and intercepts may operate anywhere between 45 and 80 K.

Table 3.5: SSR1 Cryomodule Heat Load Estimates

	Per Unit (W)			Units	Total (W)		
	70 K	5 K	2 K		70 K	5 K	2 K
Input coupler, static	5.4	2.8	0.5	8	43	23	4
Input coupler, dynamic	0	0	0.25	8	0	0	2
Cavity, dynamic	0	0	1.8	8	0	0	14
Support post	2.8	0.4	0.05	12	33	4	0.6
Conductor Lead Assembly	36.8	13.2	1.2	4	147	53	5
MLI*	30.5	0	1.4	1	31	0	1
Cold-warm transition	0.7	0.1	0.01	2	1	0.2	0.02
TOTAL					255	80	27

* MLI stands for multi-layer thermal insulation.

3.1.2.3. Single Spoke Resonator II (SSR2) Cavities and Cryomodules

Acceleration from 35 to 185 MeV utilizes superconducting SSR cavities with $\beta_{opt} = 0.51$ (SSR2). The cavity geometrical and electro-dynamic and mechanical design parameters are listed in Tables 2.3-2.5. The cavity layout is shown in Figure 3.22.

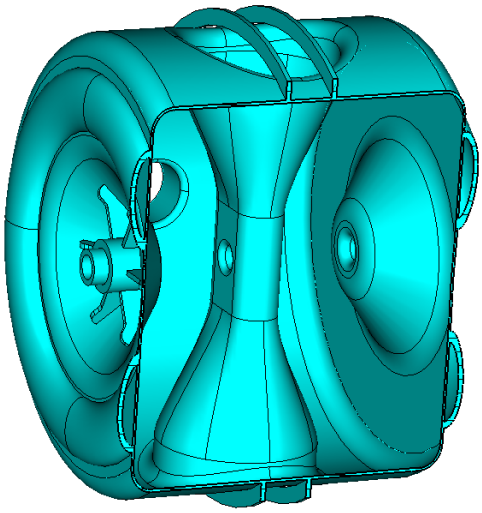

Figure 3.22: SSR2 cavity layout.

Similar to the SSR1 cryomodule, the quadrupole field is compensated by corrector coils which have independent leads. The helium vessel of SSR2 cavity has a design similar to the SSR1 cavity helium vessel. The input coupler and the fine and coarse tuners are the same as for SSR1 cavity.

Mechanical parameters of the SSR2 cavities are presented in Table 3.6. The SSR2 cryomodule design contains eight identical slots. Each of them can accommodate either an SSR2 dressed cavity or a focusing solenoid with a corrector package and BPM. The SSR2 cryomodule comprises 5 dressed cavities and 3 solenoids. The overall cryomodule length will be approximately 6.5 m. The vacuum vessel diameter will be 1.22 m (48 inches). Each cryomodule will be configured as a stand-alone unit, *i.e.* the vacuum vessel ends will be closed and cryogenic connections will be made at each module. Connections for cryogens and cryogenic control valves will be located in a mid-span vacuum vessel extension. The only module-to-module connection will be the beam line. The only beam instrumentation internal to the cryomodule assembly will be BPMs.

Table 3.6: Mechanical parameters of the SSR2 cavities

	Requirements	
Mechanical	Radius, Length	280 mm, 540 mm
	He Vessel Material	Stainless Steel
	Maximum Allowable Pressure, MAWP	2 bar RT, 4 bar CT
	df/dp	≤ 25 Hz/mbar
Coupler	Max. design forward power	30 kW
Tuning	Coarse tuning range	135 kHz
	Fine tuning range	1000 Hz

3.1.2.4. Medium-beta Section (LB650 and HB650)

Acceleration from 185 MeV to 800 MeV will be provided by two families of 5-cell elliptical cavities operating at 650 MHz and designed to β_G =0.61 and β_G =0.92. The cavity shape is optimized to decrease the field enhancement factors (magnetic and electric) in order to improve the interaction between the beam and the cavities. In order to do this, the cavity aperture should be as small as possible subject to the following considerations:

- field flatness,
- beam losses,
- mechanical stability,
- reliable surface processing.

The working gradient is chosen to provide a peak surface magnetic field that allows operation below high-field Q-slope, see Figure 2.16. For a frequency of 650 MHz the peak magnetic field should be not greater than ~70 mT. In addition we require that the peak surface electric field be lower than 40 MV/m in order to avoid the risk of strong field emission.

Linear perturbation theory indicates that for given relative errors in the frequencies of cavity cells the field flatness, $\delta E/E$, is determined mainly by the distance, δf, between the operating frequency and the frequency of the neighboring mode, $\pi(n\text{-}1)/n$. Expressing the result in terms of the coupling parameter, k, between cells and the number of cells one obtains:

$$\frac{\delta E}{E} \approx \frac{f_\pi}{\left| f_\pi - f_{\pi(n-1)/n} \right|} \equiv \frac{f_\pi}{\delta f} \approx \frac{(n-1)^2}{k} \quad . \tag{3.1}$$

Thus, a cavity with fewer cells allows a smaller coupling coefficient, k, for a given field flatness. For example, the 9-cell ILC cavity has $\delta f/f_\pi$ of 6×10^{-4} (k = 1.87%) and for the 5-cell 650 MHz cavity one can take the same $\delta f/f_\pi$ at least, yielding $k > 0.5\%$.

The apertures selected for the cavities represents a trade-off between requirements related to the cell-to-cell coupling and beam loss. The 805 MHz superconducting section of the SNS proton linac, which is close to the PIP-II linac in average current, operates with cavities that have an aperture of 83 mm for the low-beta part and 100 mm for the high-beta part. Their experience is that these cavities operate with tolerable beam loss at these apertures. Thus, we have adopted similar dimensions for the 650 MHz cavities of PIP-II. In addition, it appears that these apertures will also be adequate to facilitate the required surface processing.

The 650 MHz cavities require sufficient wall thickness to minimize sagging caused by the overall weight. Figure 3.23 shows results of a simulation of the cavity sag caused by its weight as a function of wall thickness for the 650 MHz cavities and the ILC (1300 MHz) cavity. Note that stiffening rings are used for both the ILC and 650 MHz cavities to increase the rigidity of cavities. A requirement of limiting the maximum cavity sag to 120 μm (the same as ILC) results in a 4 mm wall thickness. A small cavity wall slope (designated by α in Figure 3.24) gives more freedom to decrease the field enhancement factors. However, the slope is limited by surface processing and mechanical stability requirements. The chosen slope of about 2° results in an acceptable value for the field enhancement.

Optimization of the two 650 MHz cavity shapes was based on the constraints discussed above. The cavity performance parameters are summarized in Table 2.5. The physical description of the cavity shapes is displayed in Figure 3.24 and Table 3.7. Requirements for maximum cavity detuning amplitude and cavity sensitivity versus helium pressure fluctuations were discussed in Section 2 (see also Ref. [31]). Note that the 650 MHz cavities have small beam loading, and thus microphonics

mitigation is essential. Therefore the cavities are over-coupled; both active and passive means for microphonics compensation are planned to be used [74]. The preliminary mechanical design of the HB650 cavity is shown in Figure 3.25.

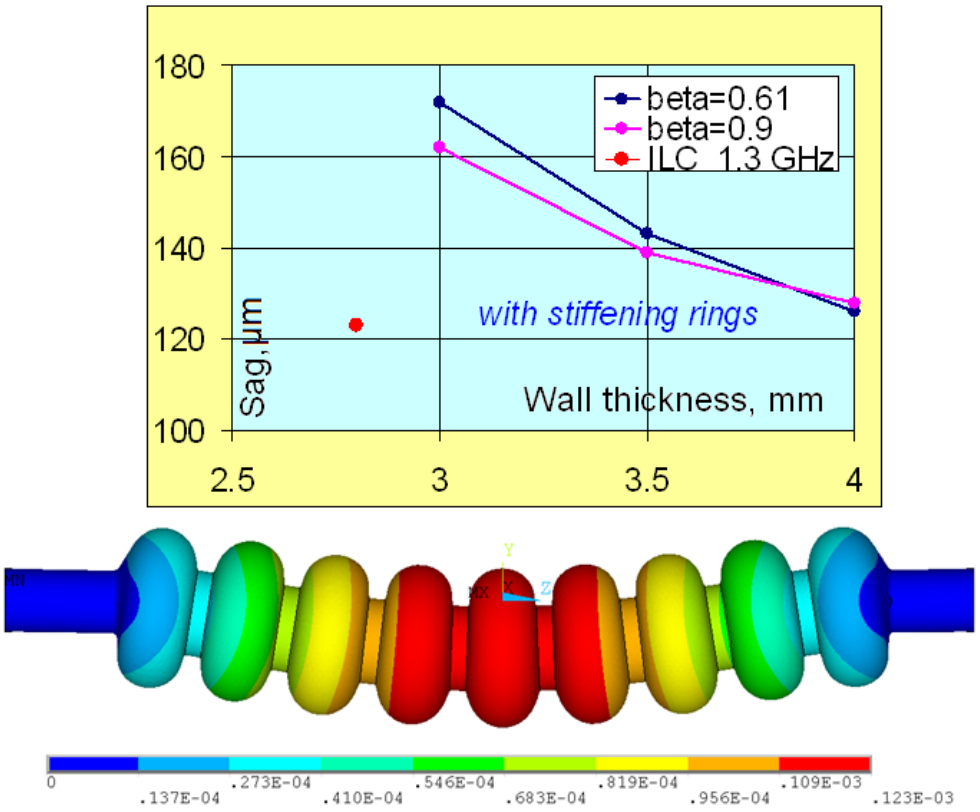

Figure 3.23: The cavity sag versus the wall thickness.

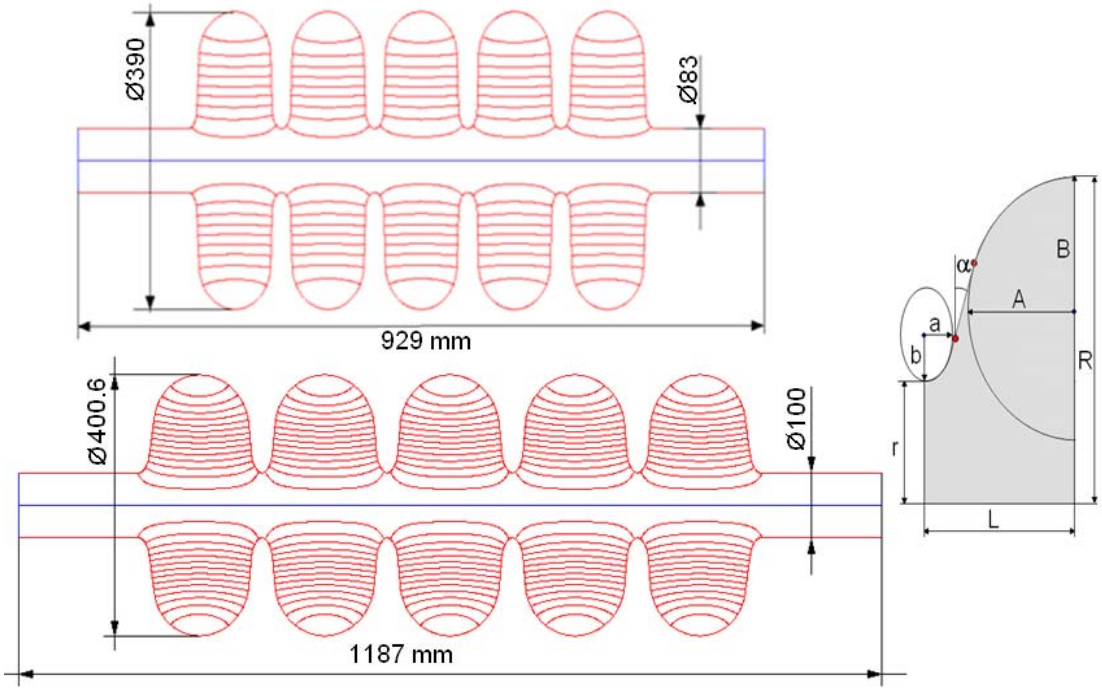

Figure 3.24: Layout of 650 MHz cavities: LB650 - top and HB650 - bottom.

Table 3.7: Dimensions of 650 MHz cavities

Dimension*	LB650		HB650	
	Regular cell	End cell	Regular cell	End cell
r, mm	41.5	41.5	59	59
R, mm	195	195	200.05	200.05
L, mm	70.3	71.4	106.1	97.6
A, mm	54	54	85	84
B, mm	58	58	78	90
a, mm	14	14	20	13
b, mm	25	25	33	28
α,°	2	2.7	1.9	1.3

* See Figure 3.24 for definition of dimensions.

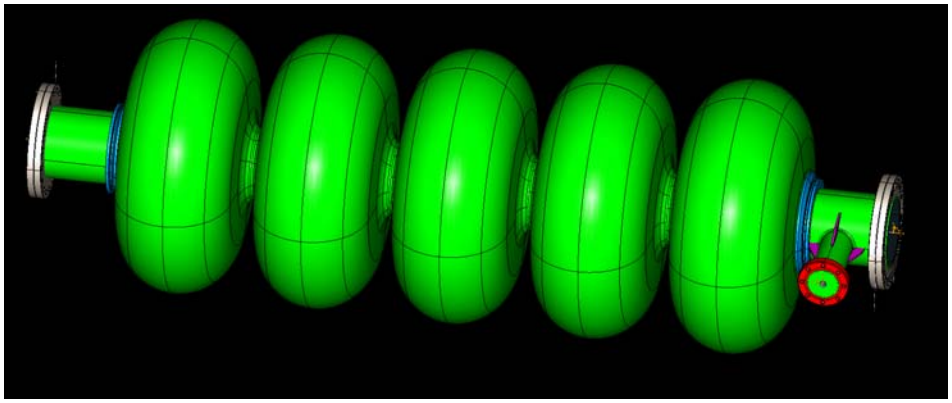

Figure 3.25: Preliminary mechanical design of the HB650 cavity.

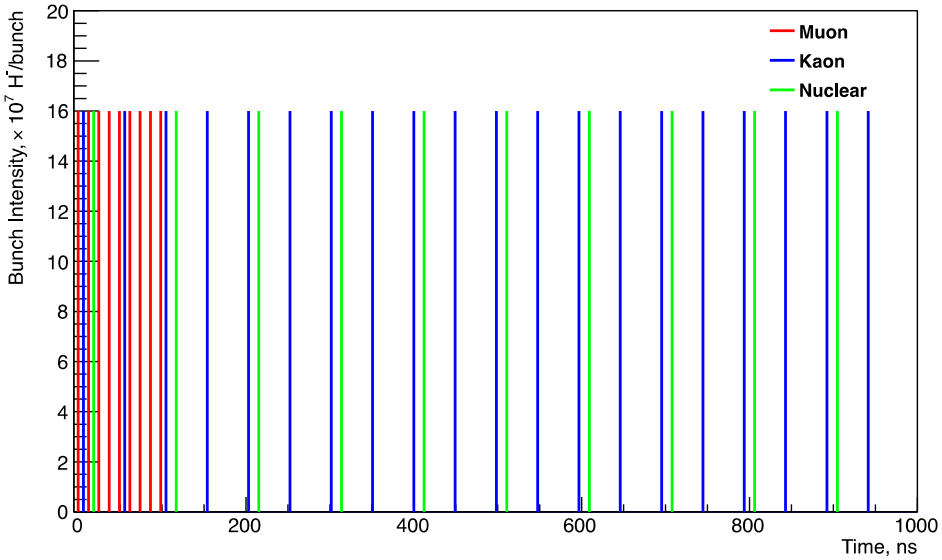

Figure 3.26: Beam structure for 3 GeV program.

Neither HB650 nor LB650 cavities contain HOM dampers – they are not necessary for the required beam current [75]. This choice is also supported by experience accumulated in the SNS [76]. An absence of HOM dampers is more problematic for future PIP-II upgrades. Here we consider the Project X parameters as an example. Figure 3.26 presents a possible bunch structure considered in Ref. [4] for CW linac operating with 1 mA average beam current and beam delivery to three experiments running in parallel (muon, kaon, and nuclear experiments) with different beam structure for each experiment. Figure 3.27 shows the corresponding spectrum, assuming very short bunches of equal charge and an absence of timing jitter. The spectrum and *(R/Q)* values of HB650 cavity are shown in Figure 3.28.

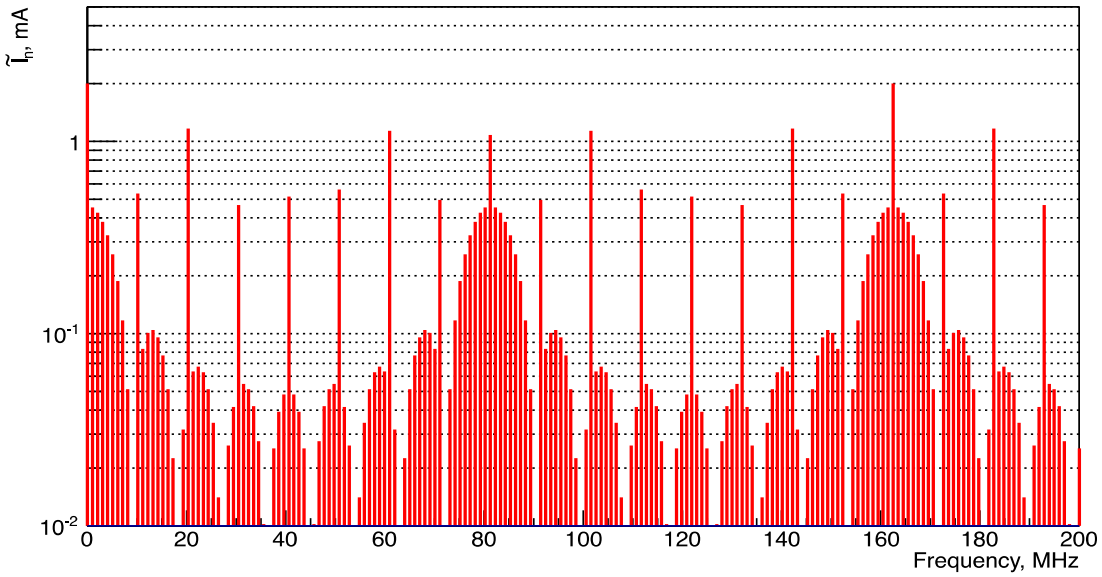

Figure 3.27: Beam spectrum of 3 GeV program.

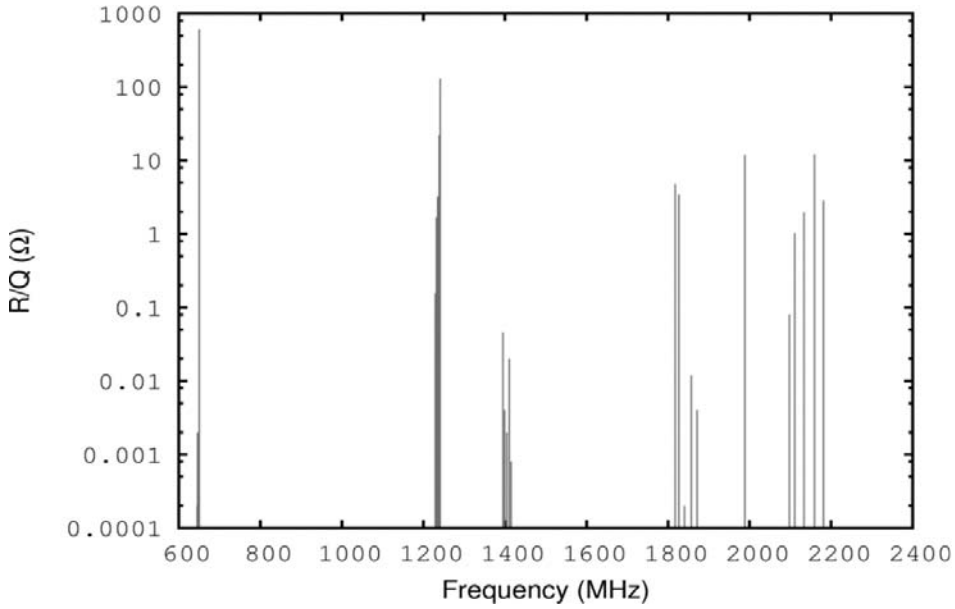

Figure 3.28: (R/Q) of the monopole HOMs in the HB650 cavities.

The amplitude of an excited monopole HOM, U_{HOM}, depends on the amplitude of the nearest beam spectrum line, I, the detuning δf, and the distance between the HOM frequency f and the beam spectrum line frequency. It can be estimated for a high Q resonance (assuming $\delta f / f \ll 1/Q$) by the following:

$$U_{HOM} \approx \frac{I(R/Q)}{4\sqrt{2}\delta f / f} \tag{3.2}$$

If the high order mode is exactly at resonance, then

$$U_{HOM} = \frac{1}{2} I(R/Q) Q_L \tag{3.3}$$

where Q_L is the loaded quality factor of the mode. The cryogenic losses depend on the square of the HOM amplitude:

$$P_{loss} \approx \frac{U_{HOM}^2}{(R/Q)Q_0} \tag{3.4}$$

Requiring P_{loss} to be much smaller than the sum of the static heat load and the cryogenic losses due to the accelerating mode (20 W), and assuming the intrinsic quality factor is $Q_0 = 5 \times 10^9$ one obtains the maximum allowable value of the monopole HOM loaded quality factor to be: $Q_L \ll 6 \times 10^7$.

Similarly, requiring that excitation of a monopole mode does not increase longitudinal emittance, $\varepsilon_z \gg U_{HOM}\sigma_z / c$, an estimation of the safe frequency detuning yields:

$$\delta f \gg f \frac{I(R/Q)\sigma_z}{4\sqrt{2}\varepsilon_z c} \tag{3.5}$$

Here σ_z is the bunch length, and c is the speed of light. The worst case is at the beginning of $\beta_G = 0.92$ section, where the bunch length is maximum ($\sigma_z/c = 7.7 \times 10^{-3}$ ns). Assuming that the second pass-band monopole HOM (1241 MHz and R/Q = 130 Ohm) is the nearest beam spectrum line (I = 1 mA), and an emittance of $\varepsilon_z = 1.5$ keV ns, one obtains the following estimate for frequency detuning: $\delta f \gg 140$ Hz.

A more accurate estimate of coherent HOM excitation in the Project X linac is performed using statistical analysis based on the expected spread of data for the HOM parameters (frequency, impedance and quality factor). Errors of cavity shape introduced in manufacturing are taken into account by allowing random variations of the cavity profile within 0.2 mm of ideal shape. In order to estimate the probability of cryogenic losses, and relative change of longitudinal emittance, 10^5 random linacs were generated using predicted deviations of frequency, loaded quality factors and impedances of monopole HOMs. It was found that the probability to have losses above 0.1 W per cryomodule is extremely small: 10^{-4} for an average beam current of 1 mA.

The beam structure, shown in Figure 3.26 consists of three main sub-components (1 MHz, 10 MHz and 20 MHz). The phase of the voltage of an HOM excited by the resonance with one of the beam components is random with respect to two other components of the beam. In case of a high-Q resonance such a HOM may introduce a significant energy variation and longitudinal emittance growth along the beam train. Results of statistical analysis show, that the probability of the emittance to double is 10^{-3} for the beam current of 1 mA. Based on this analysis the conclusion is made that HOM couplers are not needed in 650 MHz cavities. More details can be found in Ref. [75].

3.1.2.5. The 325 MHz and 650 MHz Main Couplers.

Main RF power couplers have to provide reliable operation of accelerator cavities at the following power levels: 17 kW at 325MHz and 64 kW at 650 MHz.

Criteria for coupler design are: reliability, minimizing production and operating costs. The coupler parameters chosen on the base of these requirements are presented in Table 3.8. The views of the couplers are presented in Figure 3.29.

Table 3.8: Parameters of 325 the MHz and 650 MHz Main Couplers.

Operating Frequency	325 MHz	650 MHz
Output diameter	3", SS, not coated	3'', SS, copper coated
Antenna diameter	0.5'', copper	0.5", copper
Antenna cooling	Air	Air
Window	Single, Al_2O_3, 6mm	Single, Al_2O_3, 6mm
Input	3-1/8'' coaxial	Rectangular waveguide
Multipactor suppression	HV bias	HV bias
Cryo-load, 2K, 0kW/P_{max} *	0.06W / 0.5W	0.24W / 0.45W
Cryo-load, 5K, 0kW/P_{max} *	0.58W / 2.8W	1.8W / 2.7W
Cryo-load, 70K, 0kW/P_{max} *	2.0W / 5.4W	4.4W / 6.0W

*Pmax = 30 kW traveling wave for 325MHz, P =120 kW traveling wave for 650MW

To make coupler production more effective, an approach of maximum unification of parts was chosen during electromechanical design. Couplers for both frequencies should contain maximum number of common (shared) parts.

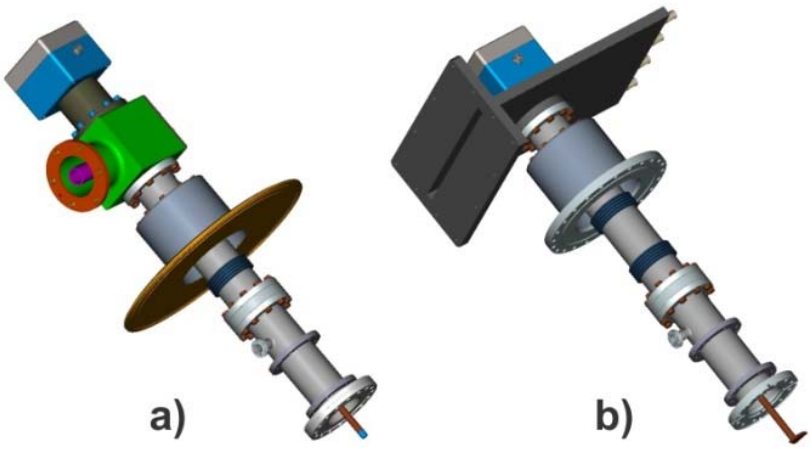

Figure 3.29: General views of a) 325MHz and b) 650 MHz couplers.

Table 3.9: Design parameters of the SSR1 main coupler.

	Requirement
CW Power	30 kW
Multipactor threshold	25 kW (Trav. Wave)
Passband	50 MHz

Input impedance	50 Ω
Output	3’’× 0.5’’ coaxial
Output impedance	105 Ω

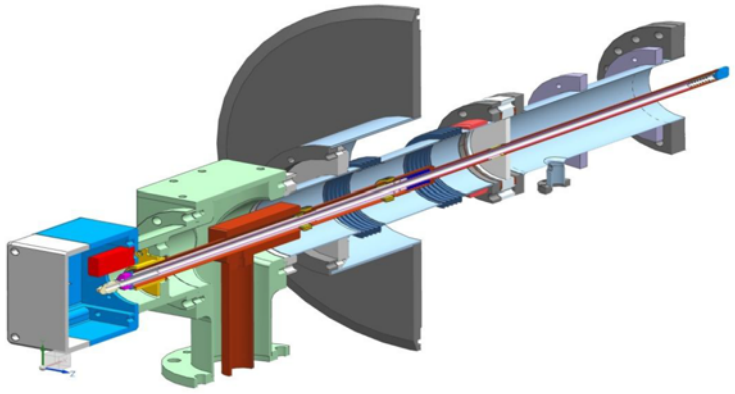

Figure 3.30: View of the SSR1 input coupler.

The coupler for 325 MHz was designed, built and successfully tested. Its design is based on a 105 Ω coaxial line. The coupler will be used for both SSR1 and SSR2 cryomodules. Its maximum power of 30 kW CW is determined by requirements for an eventual upgrade of PIP-II to 5 mA average beam current [73]. The coupler contains a single warm ceramic window that provides separation of the warm and cold coupler sections. During cryomodule fabrication, the cold section can be installed on the cavity in the cleanroom prior to assembly of the string. The warm section can then be installed from outside the vacuum vessel during final assembly. The inner conductor is solid copper with phosphor bronze bellows to accommodate motion due to misalignment and thermal contraction. The cold end of the outer conductor is 316L-stainless steel. The warm end is copper with phosphor bronze bellows. Heat load estimates don’t suggest a significant penalty for not copper plating the outer conductor. A forced-air cooling tube is inserted into the inner conductor after assembly that supplies air to cool the coupler tip. The coupler parameters are shown in Table 3.9. Figure 3.30 shows details on the coupler design.

3.1.2.6. Measures Aimed at Reduction of RF Loss in Walls of SC Cavities

Cryogenic loss in a cavity is determined by the R/Q value, G-factor and surface resistance. The surface resistance in its turn is a sum of the residual resistance and the BCS resistance.

Through other sections of this document we use a conservative approach based on the Q-values already achieved in operating cryomodules. In this case, the BCS resistance as a function of the frequency and temperature may be estimated using the following formula,

$$R_{BCS} \approx 2\cdot 10^{-4}\,\frac{1}{T}\left(\frac{f}{1.5\cdot 10^{9}}\right)^{2} e^{-17.67/T}\quad , \tag{3.6}$$

where the frequency, f, is measured in Hz, and the temperature, T, in K. For 650 MHz and 2 K one obtains RBCS~2.7 nΩ. Modern surface processing technology provides a residual resistance of ~5 nΩ [27] resulting in the total resistance of ~8 nΩ. Assuming a medium field Q-slope at the peak field of 70 mT of about 30%, this yields a target for Q_0 value of the 650 MHz cavity of ~2×10^{10}. This value was used above in Section 2.1.3.2.

However, there has been recent significant progress in improvement of quality factors of SRF

cavities via two breakthroughs: cavity surface doping with nitrogen [77] and manipulation of trapped magnetic flux via cooling [78].

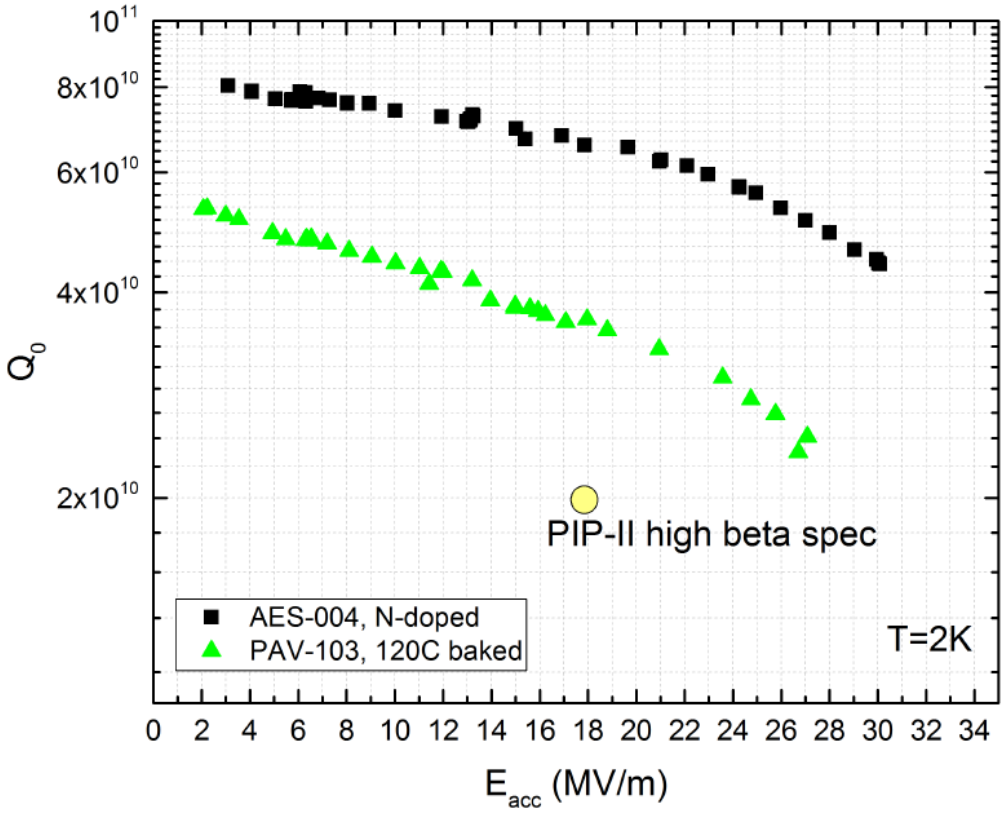

Figure 3.31: The dependence of Q_0 on the accelerating voltage for the 650 MHz, 120C baked cavity and the N doped cavity. The first one was manufactured by AES and another one by PAVAC. The measurements were carried out at 2K.

The first finding has enabled lowering both BCS and residual resistance components for 1.3 GHz cavities systematically by a factor of more than two. More than twenty 1.3 GHz cell cavities have been treated with N doping at Fermilab, Jlab and Cornell, achieving an average Q ~ $3.5 \cdot 10^{10}$ at 16 MV/m and 2K, which is three times higher than with standard 120C bake processing (ILC/XFEL recipe). Recently also several 650 MHz cavities have been treated with standard 120C bake processing and N doping, showing outstanding results far exceeding the current specifications for PIP-2 of $2 \cdot 10^{10}$ at 2K and 17 MV/m, as shown in Figure 3.31. For the 120C bake cavities the Q_0 is $3.5 \cdot 10^{10}$ at 2K and 16 MV/m. For the N doped ones Q_0 have reached $7 \cdot 10^{10}$ at 2K and 17 MV/m, exceeding by a factor of more than three the current PIP-2 specifications. With such quality factors and the cryo-plant capacity considered in Sections 2.1.3.2 and 3.4 the cryo duty-factor could be increased by about three times from ~5% to ~15%. That corresponds to an order of magnitude increase of the beam duty-factor from ~1% to ~11%. That enables experiments with high duty factors even with the present cryo-plant capacity.

Slow versus fast cooling has been demonstrated to significantly deteriorate performance of 1.3 GHz cavities due to poor flux expulsion efficiency. Recently the same experiment has been performed for 650 MHz cavities and results showed very little degradation with slow cooling versus fast cooling, as shown in Figure 3.32, hinting to a likely weaker losses dependence of trapped flux due to the lower RF frequency. This is promising for full realization of these high quality factors in cryomodule, where magnetic flux manipulation becomes more challenging.

Further studies are aimed to assure that the results achieved in a vertical test can be obtained in an operating cryomodules.

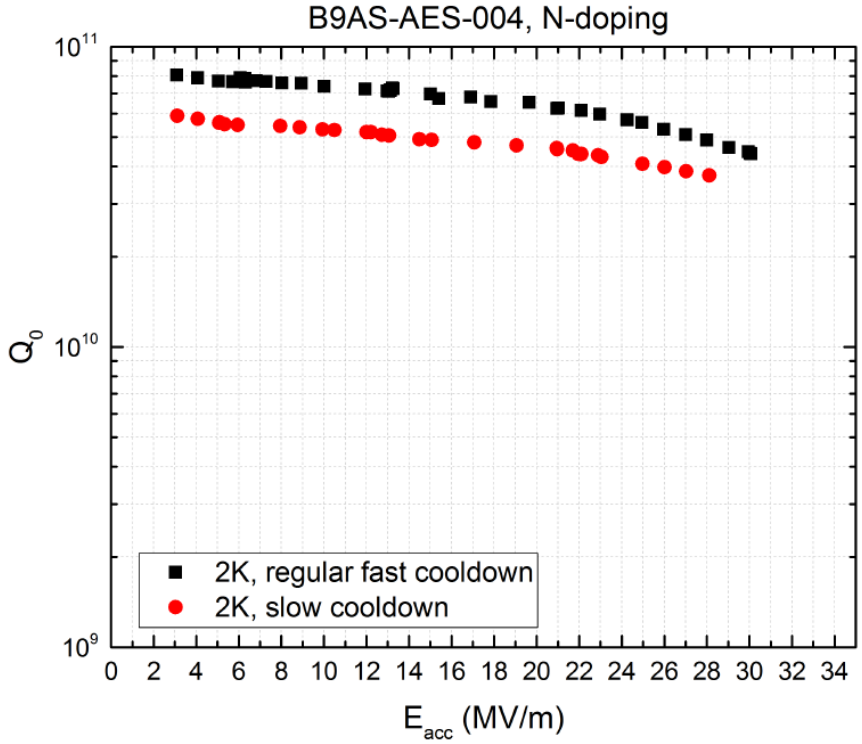

Figure 3.32: The dependence of Q_0 on the accelerating voltage for the N doped 650 MHz cavity for the fast and slow cool downs.

3.1.3. RF Power and Low Level RF

3.1.3.1. RF Power

There are 120 RF systems included in the linac. With the exception of the RFQ they are deployed as one amplifier per cavity. Parameters of the RF amplifiers are presented in Table 3.10. In comparison to the power requirements presented in Table 2.11 the RF amplifier powers were rounded to about ~10% larger values to get an allowance for operation with some cavities operating at reduced accelerating gradient. All RF systems will utilize continuous wave (CW) amplifiers, although SSR1, SSR2, LB650 and HB650 will operate in the pulsed regime to reduce RF cryogenic power. They will be used in CW mode later when the SC Linac will be upgraded to run for muon experiments.

Table 3.10. Parameters of RF amplifiers

	Frequency (MHz)	Number of RF cavities	Number of RF amplifiers per cavity	Regime of operation	RF amplifier power (kW)
RFQ	162.5	1	2	CW	75
MEBT Bunching cavities	162.5	3	1	CW	3
First HWR cavity	162.5	1	1	CW	3
Other HWR cavities	162.5	7	1	CW	7
SSR1	325	16	1	Pulsed	7
SSR2	325	35	1	Pulsed	20
LB650	650	33	1	Pulsed	40
HB650	650	24	1	Pulsed	70

The RFQ has two input ports and is driven by two 75 kW CW solid-state amplifiers. Three room temperature buncher cavities and one cryomodule containing eight superconducting HWRs operate at 162.5 MHz. They will have one solid-state amplifier each operating at power levels of 3 to 7 kW. The first HWR cavity operates at about half of the accelerating voltage and therefore uses smaller power. Two SSR1 cryomodules operating at 325 MHz will be populated with eight cavities each and powered by 7 kW solid-state amplifiers. Seven SSR2 cryomodules with 5 cavities each will be powered by 20 kW solid-state amplifiers. Eleven LB650 cryomodules with 33 cavities and four HB650 cryomodules with 24 cavities will each be powered by IOT amplifiers. It is possible that a solid-state or injection locked magnetron will be used at 650 MHz as R&D for those technologies mature.

The RF distribution system for the CW linac will utilize rigid coax commensurate with system power levels, 6-1/8", 3-1/8", or 1-5/8" EIA flanged sections. The final connection to the cryomodules will utilize a section of flexible transmission line to minimize connector location tolerances. Each RF system will have a circulator and a load to isolate the cavity from the power amplifier. This level of protection is essential in SRF systems due to the full power reflection from the cavity in the absence of beam. Cavity and drive sample signals will be provided to the LLRF for vector regulation and frequency control of the cavities. All of the RF amplifiers will be water cooled to minimize the heat load to the building HVAC system.

While each amplifier has built in protection which includes, water flow, water temperature, pressure differential, and reflected power monitoring; a global interlock and hardware protection system must be designed for all RF systems. This will include water flow to loads and circulators, spark detection on cavity couplers, and RF leakage detection.

The low level RF (LLRF) system will provide a drive signal on the order of 0 to +10 dBm for each RF power source. The amplifier(s) will provide sample signals of the pre-driver and final outputs. All amplifiers will be self-contained units complete with integral power supplies, protection circuits, and control interface.

3.1.3.2. Active Suppression of Microphonics and Lorentz Force Detuning

High accelerating gradient and comparatively small beam current result in high values of loaded

quality factors, and, consequently, narrow bandwidth and high sensitivity to microphonics (see Chapter 2.1.33). It is difficult to accurately predict uncompensated detuning levels because detuning can be driven by such a variety of different factors. Crude estimates of the range of expected levels can be made by examining the pressure regulation, cavity sensitivity and vibration levels measured in existing machines.

Pressures in large cryogenic systems can be easily regulated to 1% or better [31]. SNS and JLab are able to maintain steady state pressures to within 100 uBar and 25 uBar respectively but both can experience occasional much larger transients. With careful design cavity pressure sensitivity (df/dP) can be reduced to a few Hz/Torr. The sensitivity of the Quarter Wave Resonator and Half Wave Resonators of ISAC-II machine at TRIMF was ~3 Hz/torr and <1Hz/Torr respectively. The sensitivity of the most recent SSR1 prototype developed at Fermilab is 4 Hz/Torr. This prototype was specifically designed to minimize df/dP. An earlier prototype which was not designed with the explicit goal of minimizing df/dP exhibited a sensitivity of 150 Hz/Torr.

Estimates for the expected range of detuning levels due to mechanical vibrations can be extracted from measurements of rms pulse-to-pulse variations in the resonance frequencies of the 1.3 GHz elliptical cavities in the two cryomodules, CM1 and CM2, tested in NML in at Fermilab. Detuning levels ranged between 8 Hz for cavities at either end of the cryomodules to 2 Hz for cavities at the center of the cryomodules. The larger values measured for the end cavities were attributed to vibrations caused by nearby vacuum pumps. The levels measured in the NML cryomodules represent only detuning due to mechanical vibrations. The CM1 and CM2 cavities have pressure sensitivities of approximately 50 Hz/Torr, but the NML detuning control system adjusts the piezo bias voltage on a pulse-by-pulse basis to compensate for variations in the helium bath pressure.

Detuning due to the Lorentz force may vary between cavity types depending on the design. The resonance frequency of the SSR1 prototype varies by about 0.5 kHz as the cavity is ramped to full gradient. Table 3.11 collects the ranges of detuning expected from each individual source and gives a range of peak uncompensated detuning expected from all sources combined, while Table 2.12 lists the parameters relevant to detuning compensation for each PIP-II cavity type.

A comparison of the narrow matched bandwidths planned for the PIP-II cavities to the expected range of uncompensated detuning emphasizes the importance of exploiting all possible passive compensation measures. Cavities must be designed to minimize sensitivity to pressure; the cryogenic system must be designed to minimize pressure variations; and the cryomodule and other systems of the SC Linac must be designed to minimize vibrations transmitted to the cavities.

Even if all passive measures are fully exploited some form of active detuning compensation will almost certainly be required even for future CW operation of SC Linac. It is absolutely required for the pulsed operation of PIP-II.

Table 3.11: Expected ranges of uncompensated detuning from random sources for the PIP-II cavities

Pressure Related Detuning			
Source	Units	Lower	Upper
Peak pressure variation	mbar	0.02	0.3
Mean pressure sensitivity	Hz/mbar	5	150
Peak pressure sensitivity variation	Hz/mBar	5	5
Peak pressure related detuning	Hz	0.2	45

Vibration Related Detuning			
Source	Units	Lower	Upper
RMS detuning due to mechanical vibrations	Hz	2	8
Peak (6 Sigma) detuning due to mechanical vibrations	Hz	12	48

Lorentz Force Related Detuning			
Source	Units	Lower	Upper
Peak detuning due to the Lorentz Force	Hz	1	50

Total Uncompensated Detuning			
Source	Units	Lower	Upper
Peak uncompensated detuning (Hz)	Hz	13	143

Detuning Compensation for PIP-II

Minimizing detuning in the PIP-II cavities will require a three-pronged approach:

- Fully exploiting all passive compensation measures during cavity and cryomodule design,
- Development and validation of active detuning compensation algorithms, and
- Detuning Control System engineering.

All of the PIP-II cavities types will be designed to minimize *df*/*dP*. The pressure sensitivity of the second SSR1 prototype was designed to minimize *df*/*dP* at 5 Hz/Torr compared to 150 Hz/Torr for the first prototype. Prototypes of the other four PIP-II cavity types have not yet been constructed or tested. Steps that may be taken to minimize Lorentz force detuning and mechanical vibrations are under investigation but no design goals have been set as yet.

The first step towards implementing an active detuning compensation system for the PIP-II cavities is the development, demonstration and validation of an appropriate set of algorithms using single cavities and prototype cryomodules. Once the performance of these algorithms has been satisfactorily demonstrated, they can be integrated into the Low Level RF control system.

While considerable progress has been made in the active stabilization of SRF cavity resonance frequencies using piezo actuator over the last decade, the field is still in its infancy. DESY pioneered the use of piezo actuators to compensate for Lorentz force induced detuning of the SRF cavities. Studies in the HoBiCaT test stand at BESSY, Berlin, showed that the resonance frequency of 1.3

GHz elliptical CW cavities could be actively stabilized to better than 1 Hz rms. An adaptive feed-forward algorithm developed at Fermilab has been used to successfully stabilize the resonance for both CW and pulsed SRF cavities. While these techniques were able to control detuning in individual cavities over the duration of each respective test, it has yet to be demonstrated that any of those techniques can routinely stabilize the resonance frequency for every cavity in a CW or pulsed machine with narrow-bandwidth SRF cavities to the required level over the entire planned machine lifetime. The factors that drive the performance of active stabilization are still not well understood. Until they are, it will be difficult if not impossible to engineer a system capable of meeting the detuning control requirements for such a linac.

Optimal Control and System Engineering

In sharp contrast to the ad-hoc techniques employed to date, optimal control offers a well-defined systematic approach to the problem of combined electro-mechanical control of SRF cavities. The Lorentz force couples the electromagnetic and mechanical states of the cavities. Knowledge of one should aid in the compensation of the other but the techniques employed to date treat resonance stabilization independently of the control of the cavity gradient and phase. Optimal control techniques were pioneered by Richard Kalman of Stanford in the 1950s. Since then they have found wide use in a variety of areas of biology, economics, ecology, engineering, finance, management, and medicine but only limited use in accelerator control systems despite the performance improvements they could bring.

The first step in implementing an optimal SRF cavity control system involves characterizing the electro-mechanical response of each individual cavity via a series of stimulus-response measurements including detuning due to piezo response and detuning response to reactive power modulation. Models of the response suitable for use in subsequent steps can be extracted using the minimal state-space realization (MSSR) system-identification algorithm of Kalman and Ho.

The second step involves estimating the cavity electromechanical state at each point in time from real-time measurements of the cavity base-band RF signals. At each time step the Kalman filter determines optimal estimates of the cavity electro-mechanical state by minimizing a quadratic cost function that depends on the measured values of the cavity RF baseband signals, piezo actuator voltage and current, the previous state estimate, the covariance of the signal noise, the covariance of the previous state estimate, and the a-priori cavity response model determined in the first step.

In the final step a Linear Quadratic Gaussian Regulator (LQGR) minimizes at each point in time a cost function similar to that used by the Kalman filter to determine the combination RF and piezo drive signals most likely to keep the cavity gradient, phase and detuning at their target values.

These steps provide a well-grounded chain of deterministic algorithms that can be used to automatically characterize, model and optimally control detuning and field stability of any superconducting cavity or chain of cavities. Steady-state versions of the Kalman filter and LQGR can be implemented in real-time using commercially available FPGA signal processing boards.

The two SSR1 prototype cavities have been used to study microphonics compensation during tests in the STC test stand in the Meson Detector Building (MDB). Tests in 2011 using the first SSR1 prototype showed it was possible to stabilize the resonance frequency to less than 0.5 Hz over a period of 20 minutes with a quite simple algorithm. Further studies, following quality factor measurements for the second prototype, showed that it was possible to stabilize the resonance frequency of even very narrow band-width cavities for extended periods. Studies in the STC continue with the aim of developing and demonstrating the performance of a set of algorithms appropriate for active compensation of the PIP-II cavities.

Once a well-defined set of detuning compensation algorithms have been developed and their performance has been satisfactorily demonstrated using single cavities and the prototype cryomodules, the algorithms will be integrated into the Low Level RF control system. While the development stage will focus on meeting the required performance goals, the system engineering stage will focus on the large scale deployment of those algorithms. Reliable operation of the PIP-II machine will require an efficient and robust implementation capable of compensating detuning for every cavity for the lifetime of the accelerator.

3.1.3.3. Low Level RF

The Low Level RF system encompasses the programming and regulation of the cavity field amplitude and phase as required by the longitudinal beam dynamics in the machine. It also controls or interfaces to the ancillary equipment that is involved in the generation of RF. Hardware and software modules include Cavity Field Controller, Resonance Frequency Controller, Master Oscillator, Phase Reference Line, LO distribution, Transfer Synchronization to Booster, Beam Chopper Waveform Generator, and the interface to interlocks, timing systems and the control system (see Figure 3.33). The LLRF will also be involved in longitudinal phase space painting into the Booster.

The Linac is constructed with accelerator sections with the following frequencies; 162.5 MHz, 325 MHz and 650 MHz. Additionally 1300 MHz is provided for instrumentation and local clock generation. The basic configuration is that one RF amplifier will drive one cavity with the exception that two amplifiers will drive the RFQ. There is a mixture of warm copper cavities (the RFQ and buncher cavities) and 5 types of SRF cavities. There is also a mixture of CW systems with the HWR and SSR1 cavities and pulsed systems for the rest of the linac.

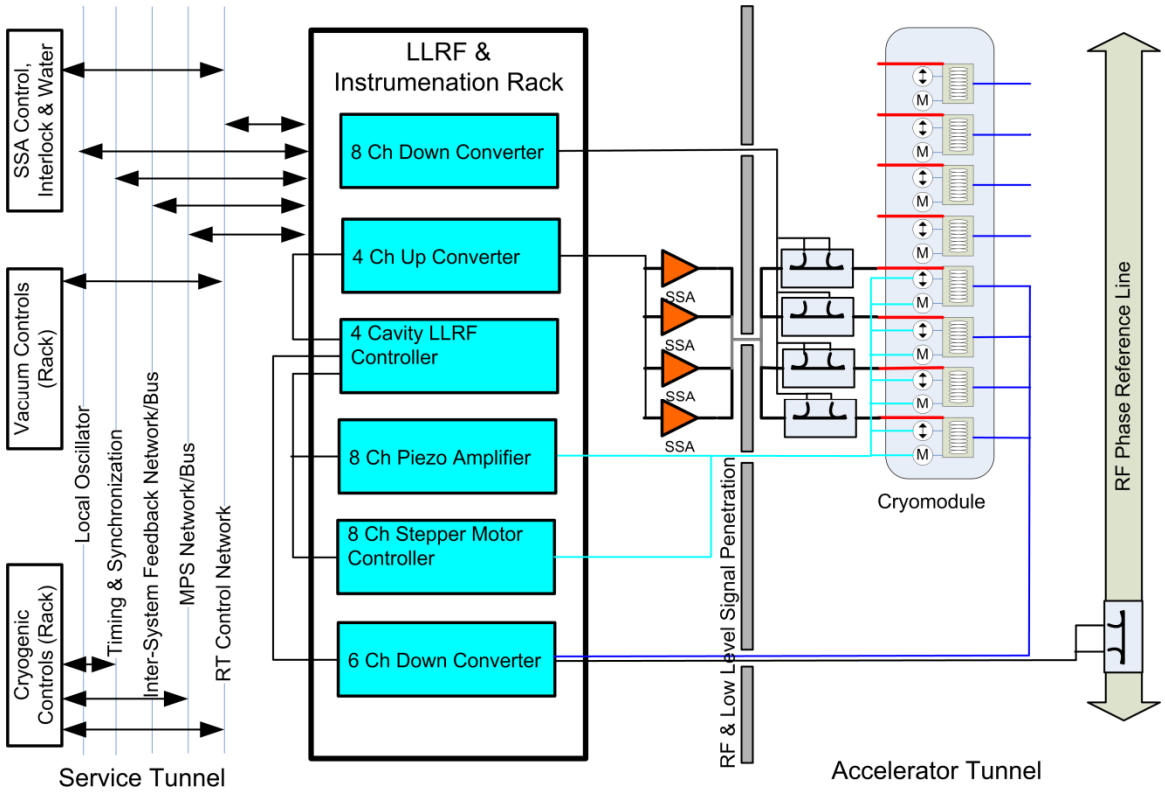

Figure 3.33: Four cavity RF system including LLRF rack.

LLRF Regulation Strategy

The requirements for the linac beam energy stabilization are determined by the Booster RF bucket height and, requirements related to the static longitudinal painting in the course of multi-turn beam injection (see Section 2.3.2.3) which result in the linac rms energy stability being better or about 0.01%. The strategy to reach this extremely tight goal is based on a two-step energy stabilization. First, the voltage of each individual cavity is stabilized to 0.1 % and 0.1 degree. Second, the beam based feedback, which uses a few last linac cavities, stabilizes the linac energy to 0.01%. To achieve that, the beam-based energy feedback has to be sufficiently fast. For given cavity bandwidths it requires that the correcting signal has to be back to the linac cavities with less than 4 microsecond delay. The beam energy and phase measurements are used in two ways, first to make real time corrections using select cavities and, secondly, to provide input to the learning feed-forward system. The learning feed-forward system greatly reduces the RF stability requirements for time periods greater than 1 s by correcting for cable delays and electronic system drifts.

The same regulation accuracy of about 0.01% rms is required for the Booster magnetic field at the injection. It can be achieved with the scope extension of the new Booster cogging system which is presently under commissioning. In particular, the feedback system can be based on the magnetic field measurement in the Booster reference magnet with subsequent average magnetic field correction by Booster dipole correctors – similar to the new cogging system.

The beam current, cavity field gradients, Lorentz Force Detuning (LFD) and worst-case microphonics determine the loaded cavity Qs, bandwidths and RF power requirements (see Section 2.1.3.3). Precision corrections of the LFD and microphonic disturbances through Resonance Frequency Control, are required for gradient regulation without exceeding the available RF power overhead. Resonance control to meet these requirements requires a large coordinated engineering effort including both mechanical and electrical designs. Resonance control is covered below in more detail.

Phase Reference Generation and Distribution

The phase reference system starts at the Linac frontend with a 162.5 MHz Master Oscillator (see Figure 3.34). The 162.5 MHz Master Oscillator is inside a temperature controller chassis and generates the 182.8 MHz local oscillator signals for the LLRF up-converters and down-converters for the 162.5 MHz linac section. The 162.5 MHz is driven into a closed loop phase averaging reference line that is located alongside the accelerating structure. The reference line is tapped providing signal to cables run alongside the cavity probe cables providing first order cable temperature compensation. This first reference line provides signal for the main timing system, instrumentation and the beam chopper controller.

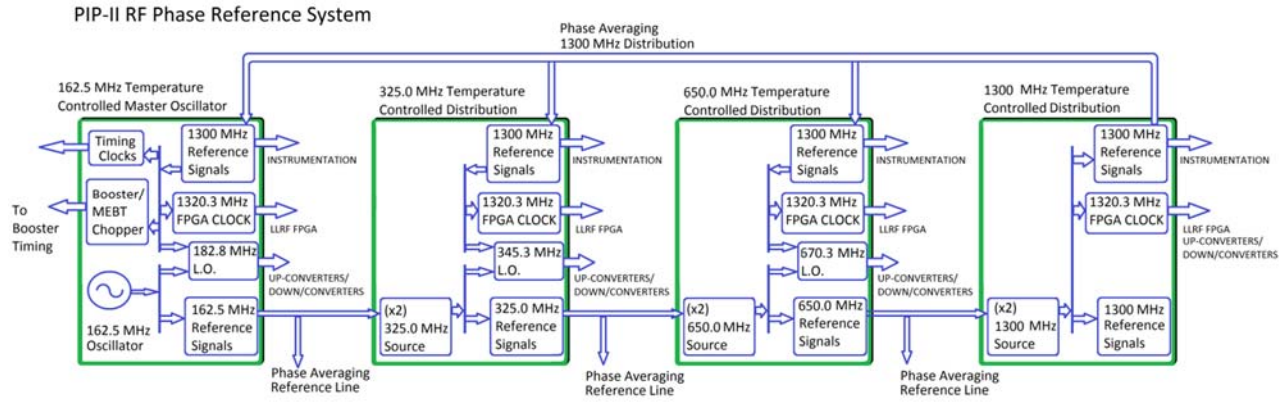

Figure 3.34: Master Oscillator and Multi-frequency Phase Reference Lines

The 162.5 MHz phase reference line also provides signal to the 325 MHz Slave Oscillator that tightly tracks the 162.5 MHz phase. The 325 MHz oscillator generates the 345.3 MHz local oscillator signals in the same fashion as is done in the 162.5 MHz master oscillator. A 325 MHz phase averaging reference line is setup in the same fashion as the 162.5 MHz reference scheme. This chain of frequency multiplication is repeated for the 650 MHz sector and finally the 1300 MHz sector. The 1300 MHz master oscillator also serves as the source for a phase averaging reference line that travels back down to the lower frequency sectors, providing 1300 MHz taps for instrumentation, and it will provide for a single 1320.3 MHz clock for LLRF digital systems distributed through the Linac.

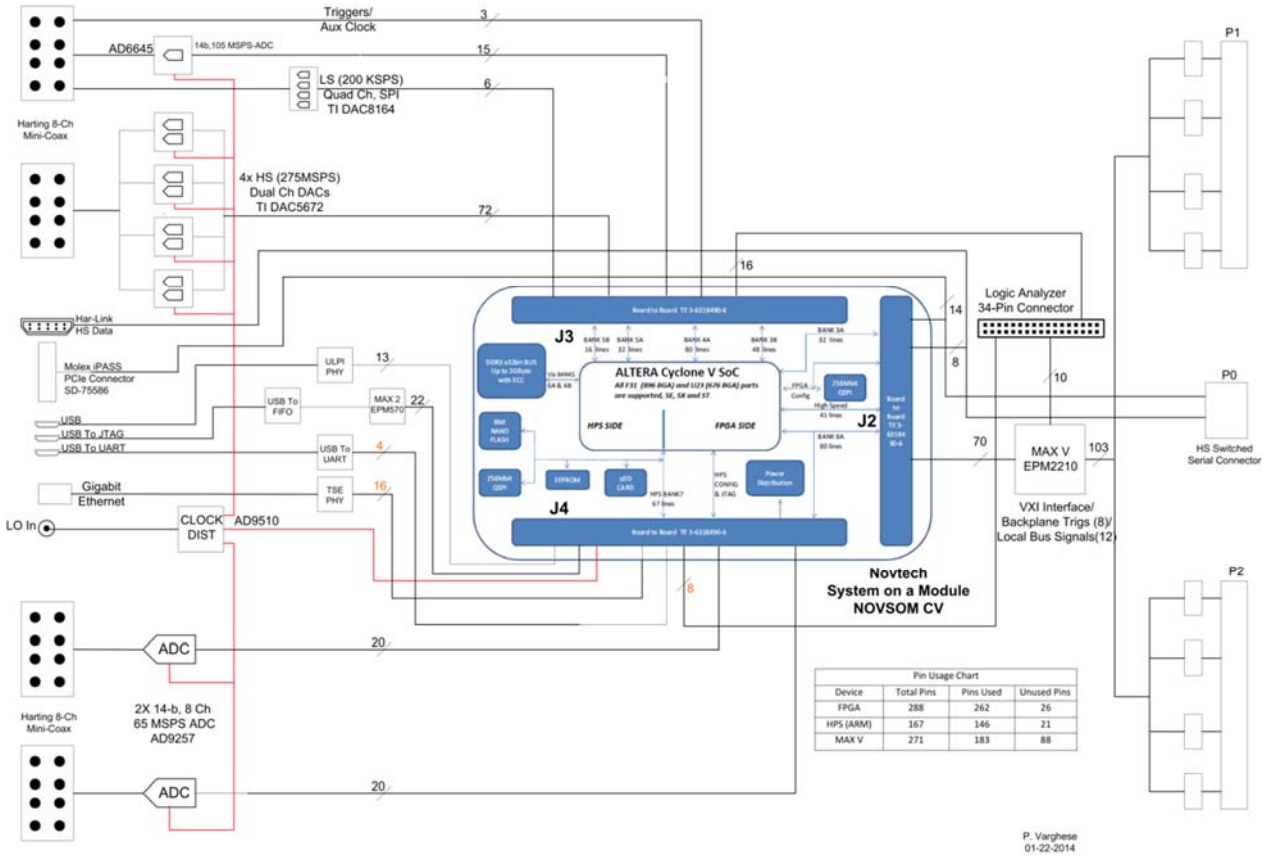

Figure 3.35: LLRF 4 Station Field Controller Module

LLRF Control Rack

The LLRF is organized in a group of up to four cavities serviced by one rack of electronics as shown in Figure 3.35. It includes control of the cavity voltage and cavity resonance and has the interface to the computer controls, timing and fast feedback systems. The group of four cavities allows for an economy of scale in the hardware design while keeping cable runs as short as possible. The signal path is kept as direct as possible with cables from the accelerator tunnel brought directly to precision receivers that down-convert the RF signals to a standard intermediate frequency (IF) that is common to all RF systems. The IF is digitized and then digitally processed for all control algorithms within Field Programmable Gate Arrays (FPGA). These algorithms generate the RF drive provided to the power amplifiers and the piezo actuator drive for cavity resonance control. Noise levels of lower than -150 dBc/Hz and closed loop bandwidths of ~50 kHz are required for precision regulation. The controller is designed to support both CW and pulsed operation. It is expected that

each cavity will be operated CW during some part of commissioning and tests. CW operation with low cavity bandwidths requires startup in a self-excited loop with a transition to a generator driven loop to align with the beam phase. Pure pulsed operation requires a complex phase trajectory program to fill the cavity with energy. A prototype system is under development for PIXIE. It includes the LLRF four Station Field Controller Module shown in Figure 3.35. The FPGA, CPU, memory and other interface components are located on a replaceable System on Module (SOM) allowing an easy upgrade path in the future of these rapidly advancing components. The LLRF system provides both RF waveforms and sampled values to the control system that are calibrated and highly linear. These best represent the cavity field and directional RF signals and will be used for all data analysis.

Beam Chopper Waveform Generator and Booster Injection

LLRF will also generate the waveforms needed for the beam chopper[8] and the 44.705 MHz RF signal for the Booster to lock to during the 4 millisecond injection period. The waveforms require complex pre-distortion for the chopper amplifiers which is better implemented with the entire waveforms calculated and played out from tables. There are several advantages to waveform tables: repeatability from pulse to pulse, local storage of beam waveforms in LLRF and instrumentation systems, and learning in the generator and LLRF based on beam loss patterns. A multi-channel 4 GSPS arbitrary waveform generator is specified for this purpose.

[8] The beam chopper removes bunches on the boundary of RF buckets and forms a 3 bunch long extraction gap.

3.2. Booster

3.2.1. Radiation Shielding of the Booster Injection Absorber

The geometry model used for the shielding calculations with the MARS15 code [79-81] for the injection absorber in the tunnel is shown in Figures. 3.36 and 3.37. The absorber consists of a 2″x2″x12″ tungsten core surrounded with 6″ of iron located on a concrete pedestal.

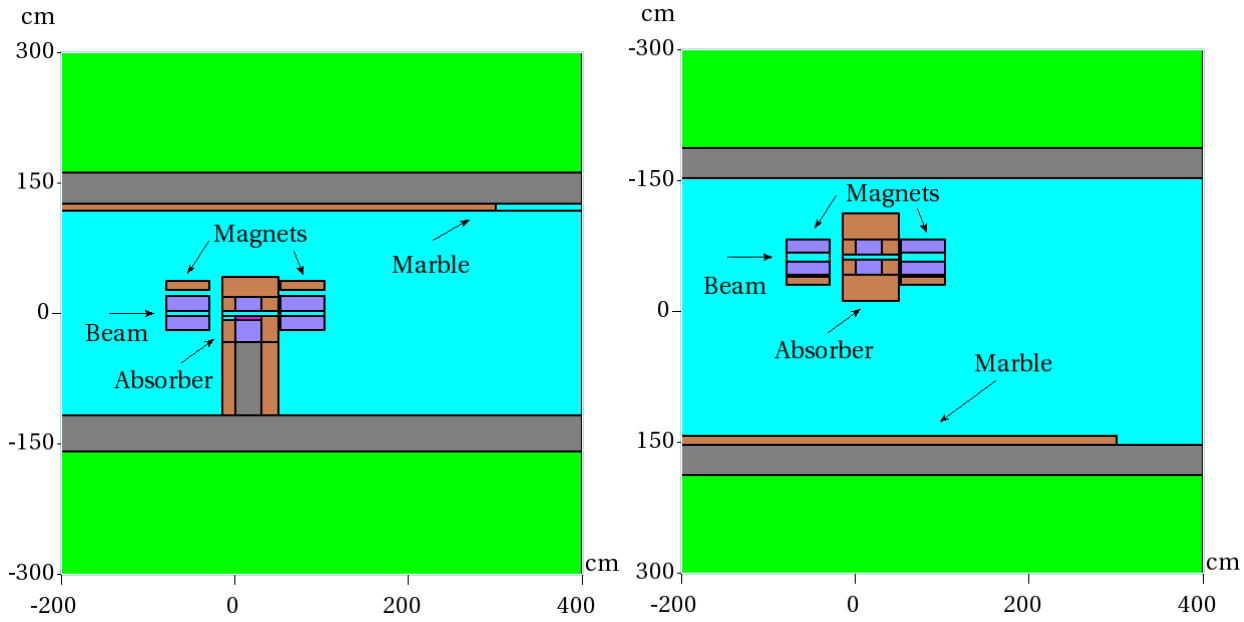

Figure 3.36: Elevation and plan view (left and right, respectively) of the MARS15 model of the absorber.

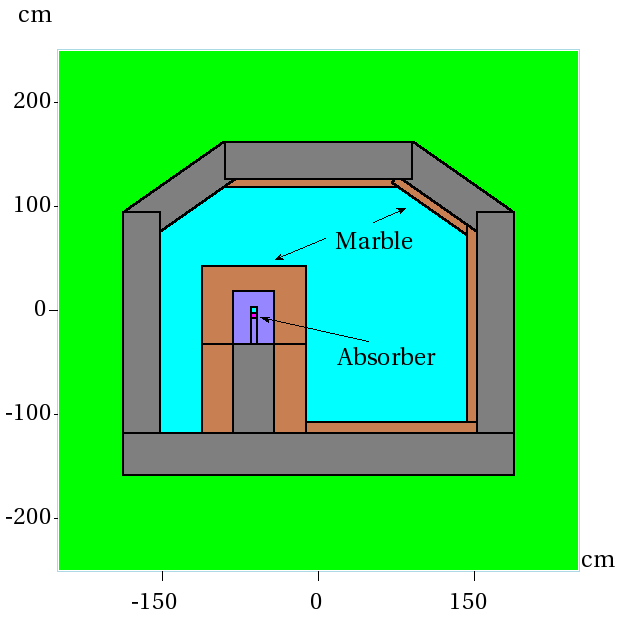

Figure 3.37. Cross section of the MARS15 model of the absorber in the tunnel.

In order to reduce residual activation of the absorber, the absorber core is surrounded with several thick layers of marble. The model also includes magnets upstream and downstream of the absorber as well as layers of marble (4″ thick and 200″ in length) on the tunnel floor, walls and ceiling mostly

on the aisle side where the residual dose should be as low as possible. At the same time, comparison of the calculated residual dose on the wall side and aisle side reveals the high efficiency of the marble in terms of residual dose reduction. This model is a result of several iterations performed in order to reach acceptably low levels of surface water activation, residual activation of the absorber itself, tunnel, and magnets both upstream and downstream, as well as absorbed dose in the magnets. A comparison of the calculated residual dose on the wall side and isle side shown below reveals high efficiency of marble in terms of residual dose reduction.

The calculated star density distribution around the absorber has the peak value of about 7.66×10^{-9} $cm^{-3}p^{-1}$ and is shown in Figure 3.38. According to the Fermilab concentration model, it means that the activated surface water should be removed with sump pumps approximately once a year.

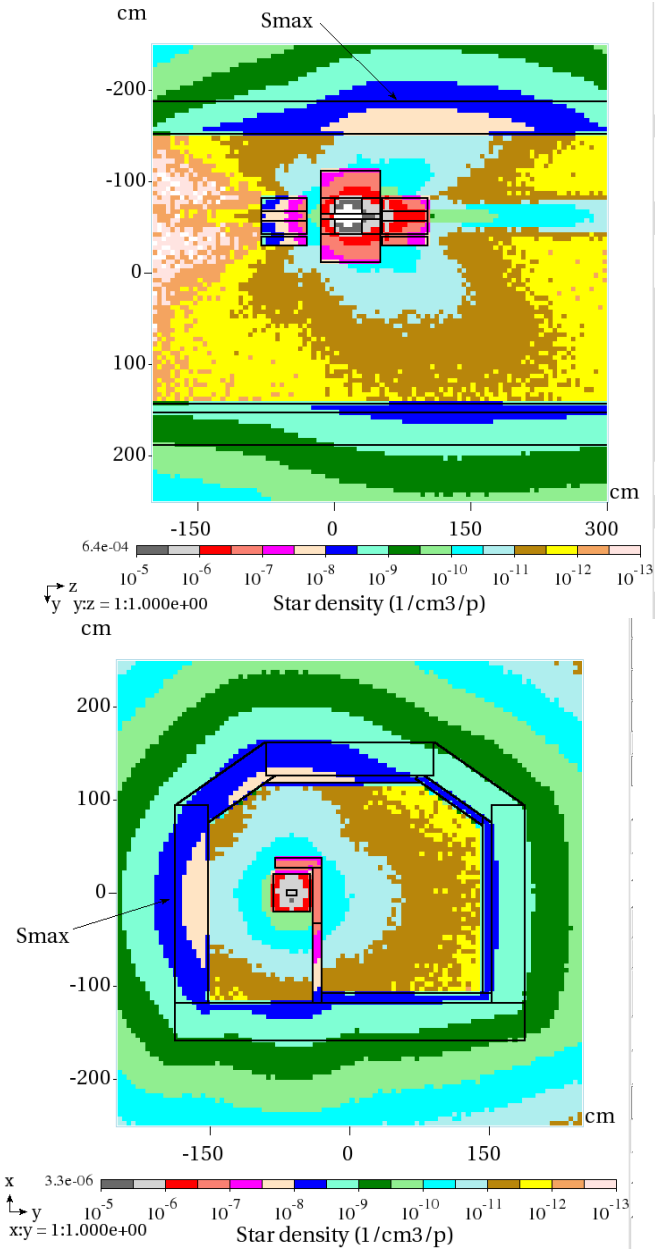

Figure 3.38: Calculated star density distribution around the absorber: plan view (left) and cross section (right).

The calculated distribution of the residual dose is shown in Figure 3.39. One can see that the maximum contact residual dose is below 1 mSv/hr on surfaces that can be easily or accidentally reached by personnel during routine maintenance procedures. Without the 4″ thick marble layers above and on the isle side of the upstream and downstream magnets, the contact residual dose could be well above 1 mSv/hr. The maximum residual dose on the tunnel wall on the left side of the absorber is about 15 mSv/hr, while on the right of the absorber the dose on the tunnel wall and floor does not exceed 0.3 mSv/hr. The latter allows us to further optimize the shielding, if necessary, and reduce the amount of marble on the tunnel walls and floor as well as around the absorber and magnets upstream and downstream.

The calculated peak absorber dose in the magnet downstream of the absorber is about 4 MGy/yr (see Figure 3.40) while the expected lifetime of magnet components such as kapton, insulation (G10) and epoxy is 20-30 MGy. In other words, according to the current design the expected lifetime of the first magnet downstream is about 5-7 years. Shielding optimization in order to significantly increase the lifetime looks questionable because this magnet is practically in contact with the absorber.

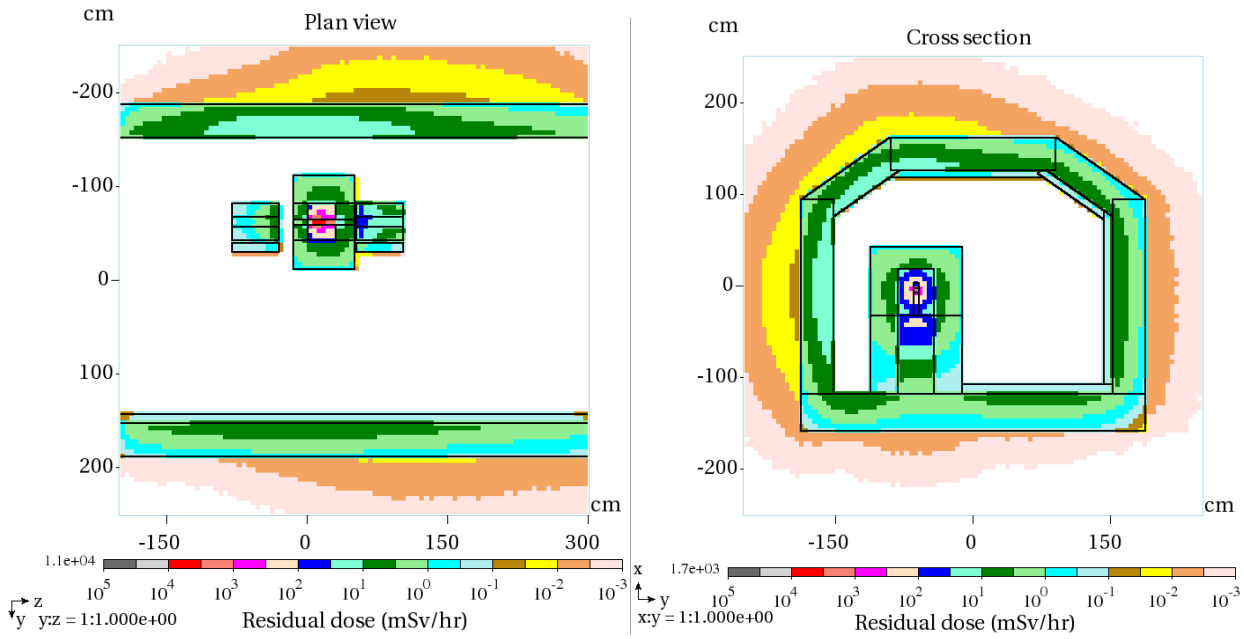

Figure 3.39: Calculated residual dose around the absorber for 30-day irradiation and 1-day cooling.

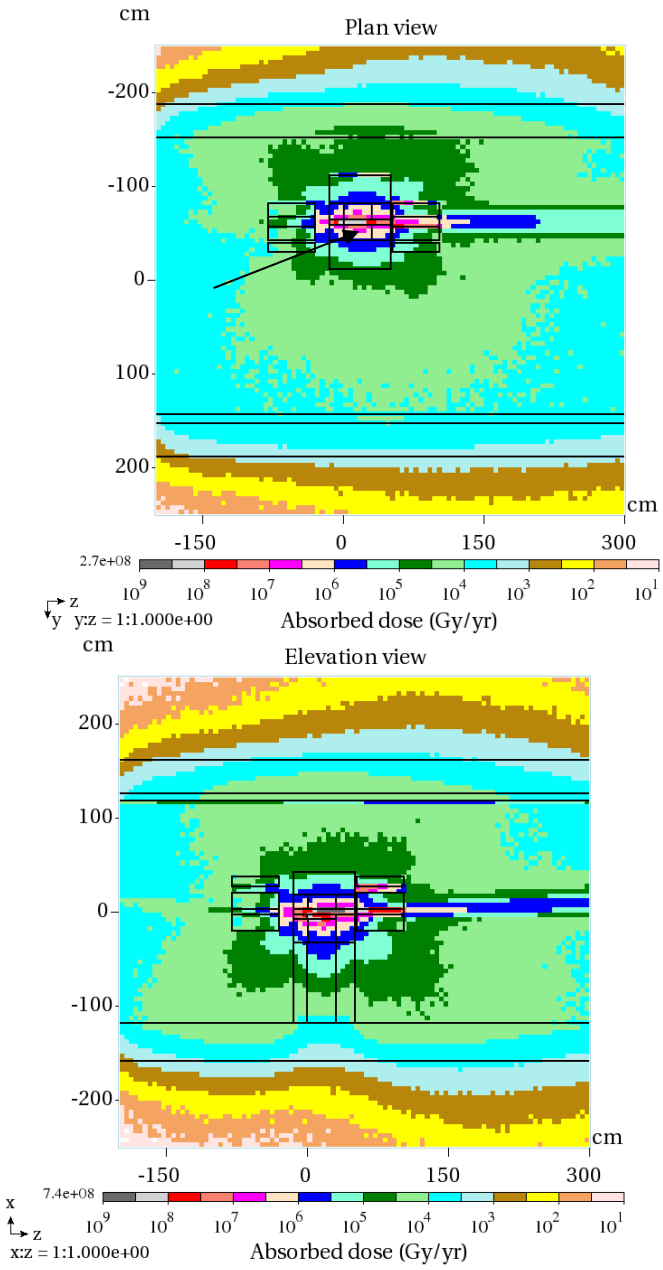

Figure 3.40: The calculated distribution of absorbed dose around the absorber. The peak absorbed dose in the magnet downstream is shown with arrows.

3.3. Main Injector and Recycler

3.3.1. Hardware for Main Injector Transition Crossing

Designs for a γ_t-jump in the Main Injector have been studied for the last 15 years. Details can be found in the Proton Driver Design Report [82]; a brief summary is included here. The system consists of 8 sets of pulsed quadrupole triplets. Each triplet has two quads in the arc and one of twice the integrated strength in the straight section, with a phase advance of π between each quadrupole. The perturbation to the original lattice is localized. In particular, the dispersion increase during the jump is small ($\Delta D_{max} \approx \pm 1$ m), which is the main advantage of a first-order jump system. Each triplet is optically independent from the others and provides roughly 1/8 of the total required jump amplitude (*i.e.*, $\Delta\gamma_t \approx \pm 0.25$ per triplet). The power supply uses a GTO (gate turn-off thyristor) as the fast switch and a resonant circuit with a 1 kHz resonant frequency. The beam pipe is elliptical and made of Inconel 718. It has low electrical conductivity σ and high mechanical strength so eddy current effects are relatively small. The eddy current effects scale as σd, where d is the pipe wall thickness. The σd value of Inconel 718 is about four times lower than that of stainless steel.

The 8 pulsed triplet locations are summarized in Table 3.12. Since the original study was done, there have been changes to the Main Injector and these locations need to be revisited. A set of magnet design parameters has been developed and modeled (see Table 3.13).

Table 3.12: Candidate γ_t quad triplet locations

Pulsed Triplet	Quad Locations
1	104, 108, 112
2	226, 230, 302
3	322, 326, 330
4	334, 338, 400
5	404, 408, 412
6	526, 530, 602
7	622, 626, 630
8	634, 638, 100

Table 3.13: Pulsed quadrupole magnet parameters

	Requirement
Integrated Gradient	0.85 T
Vacuum pipe cross section (elliptical)	2.4 x 1.125 in
Field Quality, 1 inch radius	2%
Maximum length	17 in
Maximum Current	200 A
Maximum Voltage	As low as possible

3.3.2. RF System Modifications

The Recycler and Main Injector need new 1st and 2nd harmonic RF cavities. The same cavities

will be used in both machines. A cavity design has been developed, with perpendicular biased tuners and R/Q ≈ 30 Ω. A mechanical drawing of the cavity is shown in Figure 3.41. The cavity parameters are shown in Table 3.14. Higher Order Mode (HOM) Coaxial dampers for the 53 MHz cavities have been designed. The effect of the HOM dampers on the first 2 monopole cavity modes is shown in Figure 3.42. A mock-up of the first harmonic cavity has been constructed and a set of low level RF measurements were taken. A preliminary design of the second harmonic cavity that is a scaled down version of the first harmonic has been completed.

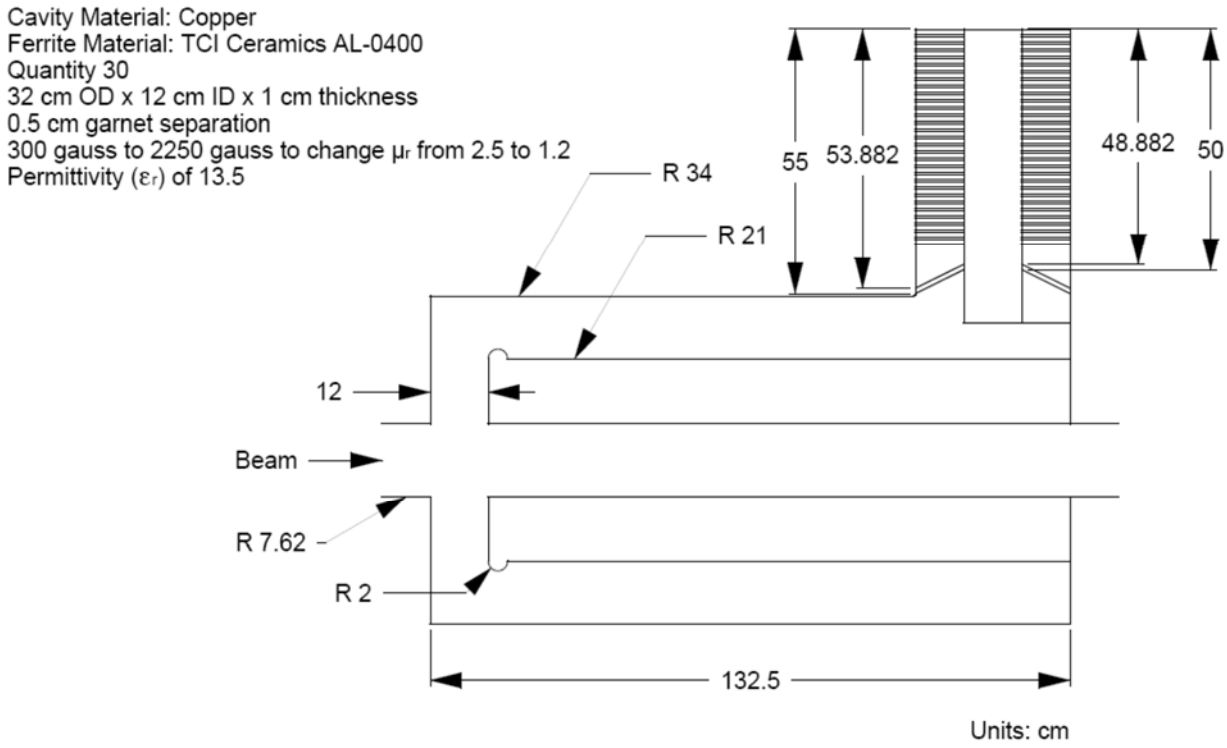

Figure 3.41: Mechanical dimensions of the 53 MHz cavity.

Table 3.14: Parameters of the new 53 MHz cavity as a function of ferrite permeability

Tuner Intrusion 75 mm @ V_{pk}=240 kV	μ_r =1.2	μ_r =2.5	
R/Q	36.4	31.5	Ω
Q_0	12244	12023	
f	53.3047	52.6152	MHz
P_{wall}	64	76	kW
$P_{ferrite}$	6	42	kW
$P_{ceramic}$	0.2	0.6	kW

The power source needs to provide greater than 550 kVA of total power and 4.65 A of current. To simplify operation and maintenance, the source should have enough bandwidth to power both the 1st and 2nd harmonic cavities. The EIMAC 8973 power tetrode amplifier has a maximum operating frequency of 110 MHz, output power capabilities greater than 1 MW, and plate dissipation of 1 MW. An 8973 tube has been purchased and a power test stand is being developed.

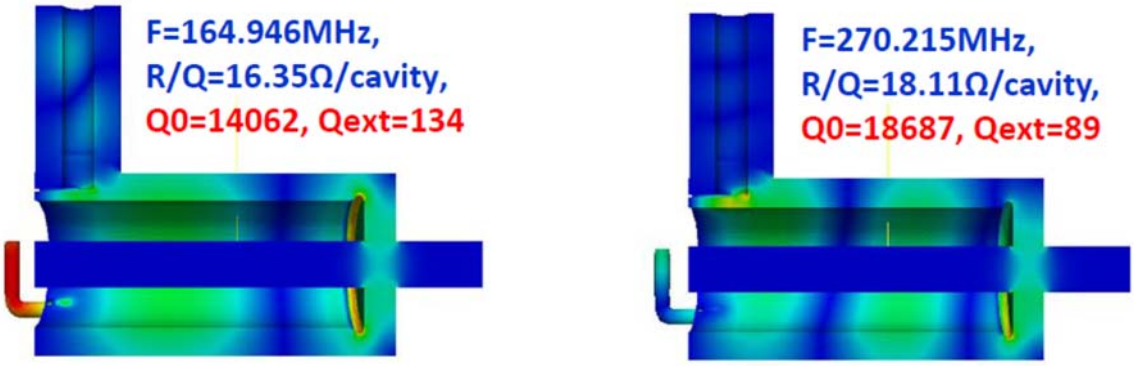

Figure 3.42: Effect of the 53 MHz cavity HOM dampers on the first two monopole modes.

3.4. Cryogenics

3.4.1. Cryogenic System Configuration

The Linac cryogenic system (see Figure 3.43) consists of three major subsystems: the Superfluid Helium Cryogenic Plant (SHCP) that produces the refrigeration, the Cryogenic Distribution System (CDS) that delivers the refrigeration from the SHCP to the SRF Linac, and the associated auxiliary systems. The cryogenic system is expected to operate for 20 years, with an estimated continuous operation of two to five years without a scheduled shutdown. The expected availability of the SHCP is 98%, which would define the availability of the entire system. The cryogenic system as a whole is required to perform the following functions:

- Provide sufficient cooling at appropriate temperature levels to enable operation of the SRF cavities and other cryogenic components within their respective operational conditions.
- Ensure that the system shall support controlled cool-down and warm-up of cryomodules.
- Ensure that the system and its components comply with the Fermilab ES&H manual.
- Provide for proper protection of process fluids from contamination.

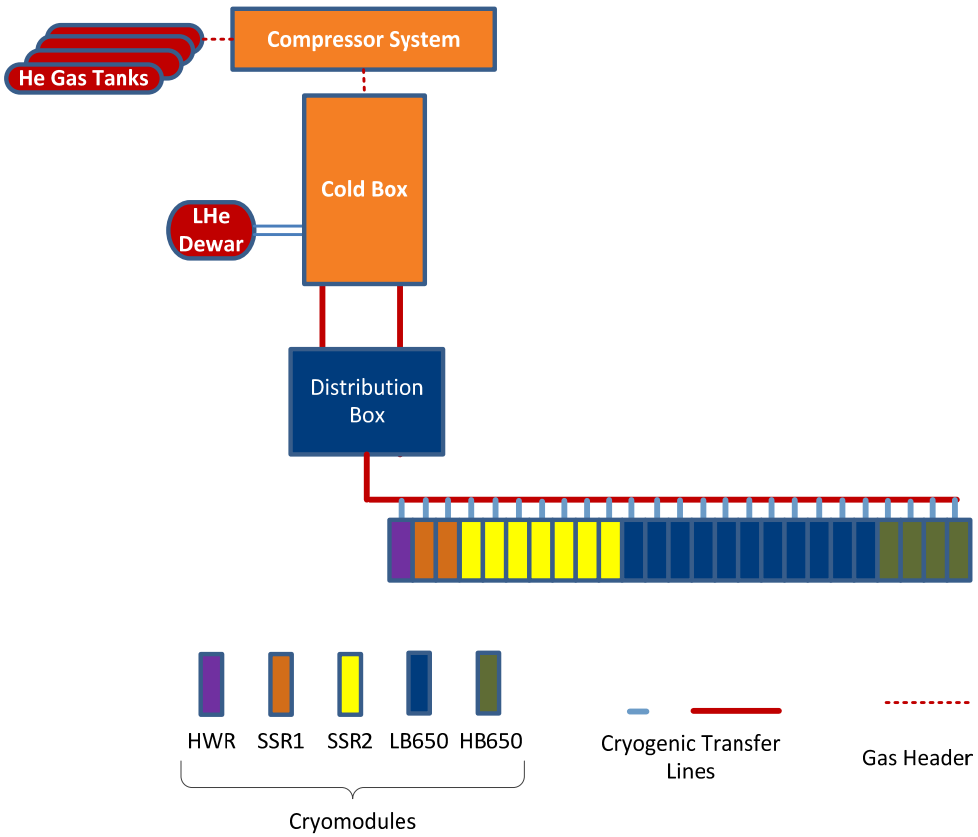

Figure 3.43: Layout of PIP-II cryogenic system.

The cryogenic system will be designed to operate as efficiently as is practical over a wide range of operating requirements [83]. Efficiency will be important for the operating modes that are expected to last for extended periods of time, such as normal Linac operation at 2 K, 2 K standby (RF off) and 4.5 K standby. Operating procedures for the cryogenic system include:

- Controlled linac cool down and warm up.
  The cryogenic system must be able to reliably cool down and warm up the cryomodule string within the cool down rate and temperature difference constraints imposed by the cryomodule design.
- Linac liquid helium fill
  This represents the 4.5K liquefaction capacity of the cryogenic system and determines the time required to fill the cryomodule string with 4.5K liquid helium.
- 4.5 K standby
  During extended shutdown periods, it is desirable to keep the cryomodule string cold and all circuits at positive pressure, thus minimizing the operating cost as well as the risks of contaminating the cold circuits.
- 2 K standby
  During shorter shutdown periods, it is desirable to keep the cryomodule string at 2K. With the RF off, the heat load to the cryogenic system at 2K will be about 50% of the nominal load in the pulsed regime of linac operation.
- 2 K operation in the pulsed mode
  This represents the normal operation of the Linac in the pulsed mode at the estimated heat loads.
- 2 K operation in the CW mode
  This represents the normal CW operation of the Linac at the estimated heat loads.

3.4.2. Superfluid Helium Cryogenic Plant (SHCP)

The SHCP will utilize a mixed compression cycle, as opposed to the all cold compression cycle. The mixed cycle has been successfully used in many superfluid helium cryogenic plants including LHC (CERN) and CMTF (Fermilab). The cycle was also recently chosen by XFEL (DESY) and European Spallation Source (ESS) after independent review of an industrial studies conducted by the helium cryogenic plant manufacturers [83a]. Simplified cycle diagram is presented in Figure 3.44. The cycle utilizes a combination of three stages of cold compressors and a sub atmospheric warm compressor operating in series. The major advantage of this cycle is the wide range of efficient capacity modulation.

Table 3.15: Cryogenic load requirements for the SHCP

	High Temperature Thermal Shield (HTTS) 35 – 80 K	Low Temperature Thermal Shield (LTTS) 4.5 – 9 K	2 K
Maximum cooling power[W]	≥9,100	≥1,500	≥1,900

The PIP–II SHCP design will incorporate the components to accommodate all required operating modes of the PIP-II Linac as well as devices necessary for its function verification. The cryogenic load requirements for the SHCP operation in the CW mode are presented in Table 3.15. The "Maximum cooling power" accounts for all the dynamic and static heat loads in cryomodules, loss in the cryogenic distribution system and required safety factors in the heat loads. The SHCP shall be designed for stable operation for any external load between zero and the maximum values specified.

The SHCP shall have a provision to simulate the heat loads for performance tests. The detailed specifications for the SHCP are developed jointly by Fermilab, USA and DAE, India as a part of the ongoing IIFC collaborative efforts. The SHCP shall be procured from industry by DAE and supplied as an in-kind contribution to Fermilab. The major components of the SHCP are the helium warm compression system (WCS) and the cold box (CB), both of which, along with SHCP process control system and instrumentation, are part of the procurement.

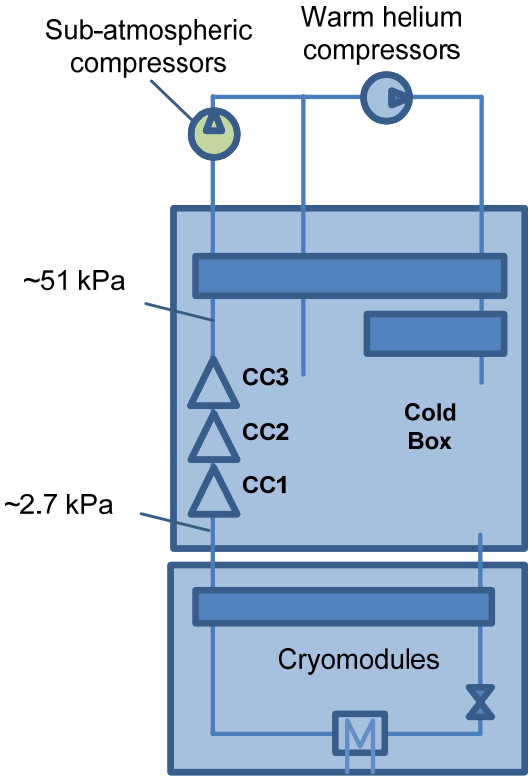

Figure 3.44: Simplified Schematic of a Mixed Compression Cycle.

The WCS consists of the group of equipment needed to compress the required mass flow of pure helium gas for both the atmospheric and the sub-atmospheric pressure circuits. The WCS cools gas after compression to ambient temperature and restores its original purity. The performance of the WCS should satisfy the cryogenic load requirements (Table 3.15). The major components of WCS are as follows:

- Compressor skids;
- Bulk oil removal, cooling and circulation equipment;
- Final oil removal system;
- Charcoal adsorbers;
- Dryer;
- Oil and Gas Filters;
- Gas management panel;
- Helium guard for sub-atmospheric circuits;
- Pump and purge system;
- Gas analysis equipment;
- Safety devices;
- Electrical systems and controls;

- Valves;
- Interfaces for connecting to the CB and helium buffer vessels.

The CB of the SHCP is a vacuum vessel with clean inner surfaces, covered by multi-layer insulation and housing all the equipment and piping used in the refrigeration process. The CB package also includes instrument panel with transmitters, switches, process and utility instrumentation, instrument air and cooling water connections and distribution, purge connection, electrical cabinet for terminals, transmitters and other hardware. The major components of the CB are as follows:

- Aluminum plate-fin process heat exchangers;
- Cryogenic turbo-expanders (TEX);
- Cryogenic cold compressors (CC);
- Valves at cryogenic temperature with manual or pneumatic actuators;
- Valves at ambient temperature operating at sub-atmospheric pressure;
- Safety valves and other safety devices;
- Dual bed 80K adsorbers and single bed full flow 20K adsorber;
- Filters;
- Phase separator and sub-cooler;
- Vacuum insulation system;
- Heaters;
- Temperature sensors and pressure sensing taps;
- Interfaces for connecting to the WCS, liquid helium Dewar and Cryogenic Distribution System (CDS).

SHCP control system will be equipped with all instrumentation necessary for safe and reliable operation. The instrumentation will allow for flow and pressure measurements, temperature, speed controls and impurity monitoring. The control system will consist of a main process control programmable logic controller (PLC), remote input/output modules at equipment positions and Human-Machine-Interface displays. It will include all software required for safe and reliable operation of the system.

Most of the auxiliary equipment, including warm helium storage tanks, liquid helium Dewars, etc., will be reused from the Tevatron. Chillers for turbines and cold compressors, insulation vacuum pumping system (roughing and diffusion pumps), and associated instrumentation will be procured from industry.

3.4.3. The Cryogenic Distribution System (CDS)

The CDS consists of the equipment required to feed and return the cold helium via vacuum insulated pipelines to the SRF Linac components. The equipment includes distribution boxes (DB), cryogenic transfer lines, bayonets and turnaround boxes. The major features of the CDS may be described as following:

- A multi-circuit transfer line will run from the SHCP CB (Figure 3.45) into the PIP-II tunnel and along the length of the SRF Linac. The design of this transfer line will be consistent with CW operation.
- In steady state operation, the CB will supply supercritical helium at around 4.5K and a maximum supply pressure of 4 bar to the CDS.
- The supercritical helium line is divided into two streams inside the cryomodules, one of which is directed to the sub-atmospheric heat exchanger and subsequent JT valve, while the

other is directed to the Low Temperature Thermal Shield (LTTS). This LTTS return line enters the CDS at a temperature of about 9K in normal operation.

- The sub-atmospheric return stream from the CDS to the CB has a temperature of about 3.8K in normal operation.
- The CB will supply to the CDS the high-pressure helium gas at 35-40 K for the High Temperature Thermal Shield (HTTS). This shield flow is returned from the CDS to the CB at about 80K.
- The CDS will have a separate cooldown (return) line, which will return helium gas to the CB at different temperatures during the cooldown operation of the CDS and cryomodules.
- The CDS transfer line would make use of 25 inline bayonet cans (one for each cryomodule) and a turnaround box at the end. In parallel, in the vertical plane, there will be a warm helium vent header.
- Connections between the distribution boxes and the cold box are accomplished via removable vacuum insulated cryogenic transfer tubes ("U-tubes"), while the connection to the tunnel transfer line is welded. This architecture provides flexibility for positive isolation of tunnel components and strings of cryomodules from the SHCP during installation, commissioning, operation and maintenance, including repairs.
- Each cryomodule is connected to the transfer line via U-tubes. It provides for maximum segmentation of the Linac.
- The estimated pressure drop for the transfer line elements along the CDS and the cryomodules are presented in Table 3.16.

Table 3.16: Estimated pressure drop along the CDS and cryomodules

Circuit	Operating Pressure	Estimated pressure drop
	[MPa]	[kPa]
2K return	3.13e-3	0.4
4.5K supply	$0.22 \leq P \leq 0.4$	25
LTTS return	$0.22 \leq P \leq 0.4$	3
HTTS supply	$0.3 \leq P \leq 1.8$	5
HTTS return	$0.3 \leq P \leq 1.8$	7

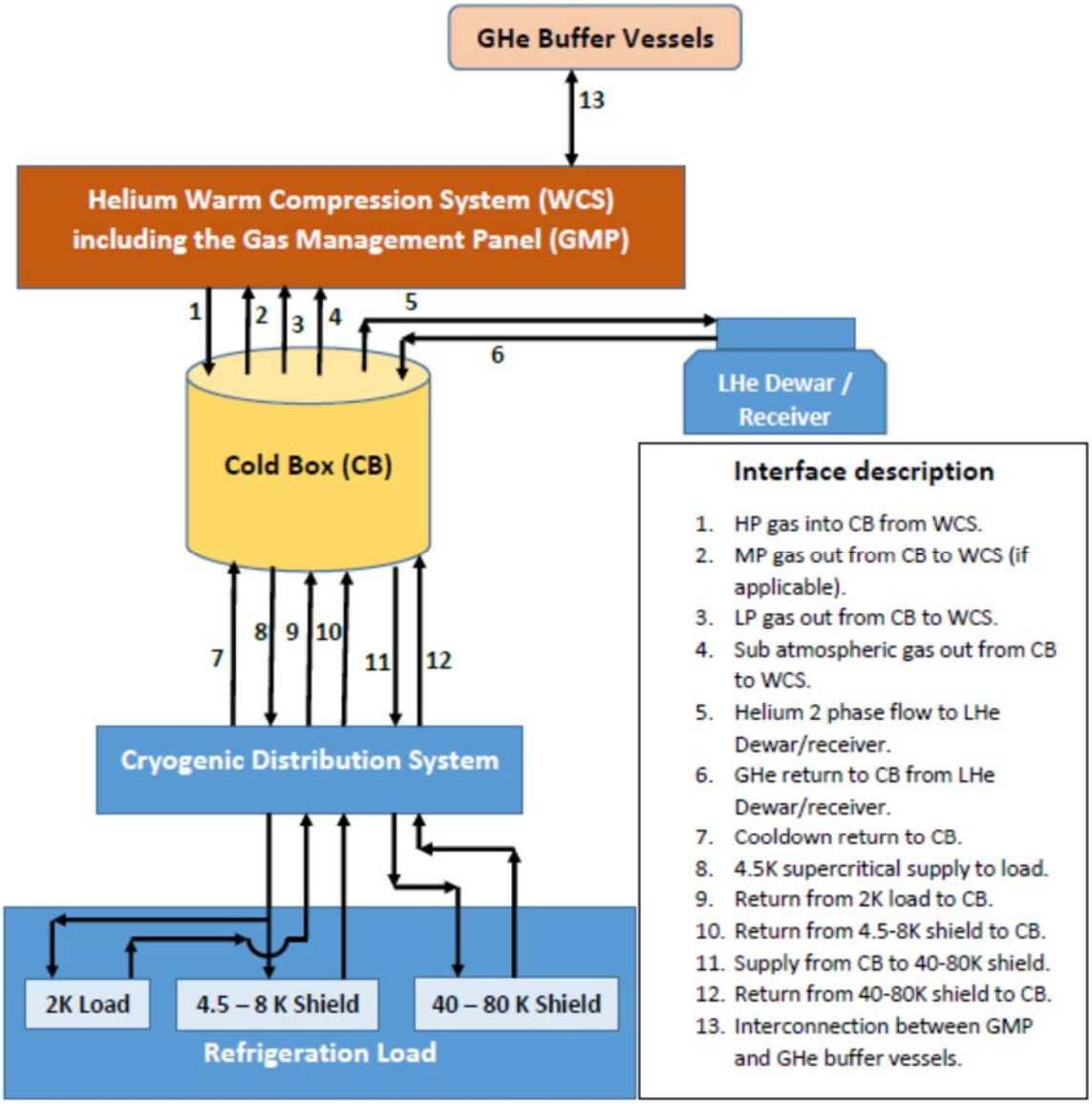

Figure 3.45: Simplified Schematic showing the SHCP, the CDS and the distribution of cryogenic refrigeration to load (cryomodules).

3.4.4. Steady State Operation of the SHCP

The different steady state operation modes of the proposed SHCP are listed in Table 3.17. The major features of the steady state operation are:

- Ability to cope with the cooling loads for each of the steady state operation modes listed in Table 3.17.
- In the "4.5K stand by" mode, the only heat load applicable is the static heat load (heat in leak) of cryogenic distribution system and testing components.
- In the "Maximum capacity" mode, along with the static heat load, the dynamic heat load due to magnet current and RF power being turned on, also comes into the picture. This mode represents the maximum SHCP refrigeration capacity at 2K to deal with the maximum heat load considering all the safety factors.

- The “Pulsed operation” and “CW operation” modes represent the design condition of the SHCP to take care of all the dynamic and static heat loads but without considering the safety factors and loss in the cryogenic distribution system.
- Apart from these refrigeration modes, there exists a provision of a helium liquefaction mode at 4.5K.
- Complete exclusion of liquid nitrogen pre-cooling in the SHCP design.
- Capability of transition from one operation mode to another with minimal manual intervention.
- Automatic reaction to changes in heat load by reducing or increasing SHCP performance without active participation of an operator.

Table 3.17: Steady State Modes of operation of the SHCP

Circuit	LHe [g/s]	4.5K Standby [W]	Pulsed operation [W] *	CW operation [W] *	Maximum Capacity [W]
2K	N.A.	N.A.	≥ 320	≥ 1,680	≥ 1,900
4.5K?	TBD*?	_	_	_	_
LTTS	_	≥ 800	≥ 800	≥ 800	≥ 1,500
HTTS	≥ 7,000?	≥ 3,000	≥ 3,000	≥ 3,000	≥ 9,100

* The load does not account loss in the cryogenic distribution system and technical margin

3.4.5. Transient Operation of the SHCP

The transient operation modes of the SHCP involves the cool down, warm up and responses to fault conditions and normal shut down. The magor features of the cool down mode are:

- Capability of cooling down the SHCP CB either alone or together with the Linac cryomodules (CM).
- CB to operate in a mode of liquefaction at rising level once the Linac CM cold masses reach a temperature below 5 K.
- Capability of supporting cool down of LTTS and/or HTTS circuits prior to, or simultaneously with, the cooling of the 2K circuit.
- Pump down to achieve 2K by switching on the CC train to start only when the 4.5K circuit is in normal operation, the Linac CMs are filled with 4.5K liquid helium (LHe) and when the cool down of the sub-atmospheric circuits including the header is completed.
- Capability to cope with different pump down volumes right from one CM to the entire Linac CM set.
- Capability to re-start pump down after a scheduled or un-scheduled stoppage of the CC train.
- Capability of pumping down a single CM in case of its replacement/maintenance.
- Capability of pumping down both with or without the sub-atmospheric header.

The major features of the warm up mode are:

- Capability of warming up the CB either alone or together with the Linac cryomodules (CM).
- Capability of warming up together with any number of CMs, ranging from one to the entire set.

The major features of the SHCP responses to fault conditions are:

- Capability of withstanding heat load variation, without a trip or significant excursion of operating parameters.
- Provision of protection of plant components in the event of beam line vacuum loss and insulation vacuum loss in CMs.
- Support (without damage to plant components) of abnormal shutdown modes such as those due to component trip, failure of compressor system, utilities interruption and other emergency trips.
- Capability to cope with unexpected controls or communication interruption or failure without damage to plant components.
- Capability of plant restart without warm-up or purge of its circuits after incidents such as power glitch, cooling water outage, etc.
- Capability of TEX and CC restart without warm-up or purge of cold circuits.
- Capability of plant restart without warm-up or purge of its circuits after reset of an interlock that caused a component or element false trip.

The major features of the SHCP normal shut down mode are:

- Capability of plant shutdown via either local or remote command without damage to components.
- Normal shutdown mode sequence to bring about pressurizing of all circuits (including the normally sub-atmospheric circuits) to above atmospheric pressure to protect these from possible contamination.

3.4.6. Interfaces of the SHCP

The major interfaces of the SHCP includes that between the CB and WCS, CDS and LHe Dewar. The CB will be connected to the WCS by at maximum four main helium lines (HP delivery, LP return, sub-atmospheric return and MP return) without counting auxiliary lines for bearing gas, purging requirements, etc. The physical interface between the SHCP CB and the SRF Linac CDS will be one single transfer line port incorporating six lines (Figure 3.45, Table 3.18). The port would contain a vacuum barrier to separate the insulation vacuum of the transfer line from that of the CB.

Table 3.18: CDS Transfer line sizes

Line description	Line size (NPS)
4.5K Supercritical helium (supply)	2” Schedule 10
Sub – atmospheric helium (2K return)	10” Schedule 5
LTTS return	2” Schedule 10
HTTS supply	2” Schedule 10
HTTS return	2” Schedule 10
Cool down (return)	3” Schedule 10

Table 3.19: SHCP interface with the CDS/LHe Dewar

	Supply		Return	
	P	T	P	T
Circuit	[MPa]	[K]	[MPa]	[K]
2K	_	_	2.7e-3	≤ 3.8
4.5K supercritical	0.22 ≤ P ≤ 0.4	≤ 4.5	_	_
LHe	0.12	Sat. Temperature	LHe Dewar pressure – ΔP_1*	Sat. Temperature
LTTS	_	_	0.22 ≤ P ≤ 0.4	≤ 9
HTTS	0.3 ≤ P ≤ 1.8	35 – 40	P – ΔP_2#	≤ 80

* ΔP_1 is the pressure drop in LP return of the transfer line (about 5 kPa)

ΔP_2 is the pressure drop in the HTTS line as provided in Table 1.2.

The LHe Dewar, apart from providing a buffer supply of liquid helium during regular operation, will be used during the acceptance of the SHCP. The physical interface between the CB and the transfer lines leading up to the LHe Dewar will be bayonet couplings. The requirements to process parameters at the interface between the SHCP and the CDS as well as the LHe Dewar for each of the steady state operation modes are presented in Table 3.19.

3.4.7. Infrastructure and Utilities Requirements

The major PIP-II cryogenic infrastructure consists of the Warm Compression System (WCS) building, the Cold Box (CB) building and the interconnection between the CB building and the PIP-II tunnel, housing the Cryogenic Distribution System (CDS). The design of the cryogenic infrastructure will include adequate provisions to minimize transmission of vibration to the PIP-II tunnel in order to prevent excitation of microphonics in the SC cavities.

The major requirements to the WCS building are:

- High bay area: 60’ x 200’ (Floor) with a 25 metric ton EOT crane.
- Electrical power: 3 phase, 4.16 kVAC, 60 Hz with minimum power requirement of about 3.5 MW; 3 phase, 480 VAC, 60 Hz with minimum power requirement of about 200 kW for auxiliary equipment; 1 phase, 120 VAC, 60 Hz incidental requirements (20 kW). Class 2 (AC power from UPS) for operating the control panels.
- Cooling water: About 1500 gpm with a supply temperature of about 85 – 95 ^{o}F and allowable rise in temperature of about 18 ^{o}F.
- Ventilation blower: 300 kW approx.
- Instrument air: 500 gpm approx.

The major requirements to the CB building are:

- High bay area: 50’ x 125’ (Floor) with a 15 metric ton EOT crane and a side bay area.
- Electrical power: 3 phase, 480 VAC, 60 Hz with minimum power requirement of about 100 kW for auxiliary equipment; 1 phase, 120 VAC, 60 Hz incidental requirements (30 kW).

Class 2 (AC power from UPS) for operating the control panels.

- Cooling water: About 200 gpm with a supply temperature of about 50 – 60 ^{o}F and allowable rise in temperature of about 9 ^{o}F.
- Instrument air: 500 gpm approx.

3.5. Instrumentation

Various beam instrumentation and diagnostics systems are necessary to characterize the beam parameters and the performance in all PIP-II sub-accelerators. For startup and initial beam commissioning, we need to provide, at a minimum, beam instruments in order to observe:

- Beam intensity,
- Beam position / orbit,
- Transverse beam profiles,
- Beam phase / timing.

The high beam intensity / power and the presence of superconducting technologies also require a reliable, fail safe machine protection system (MPS) to prevent quenches in cryogenic elements or damage due to an uncontrolled loss of the high power beam. This system will be based on beam loss monitors (BLM) and other beam intensity monitors (*e.g.* toroids).

Beside these core beam instrumentation systems, more specialized beam diagnostics need to be provided, e.g. to characterize the longitudinal bunch profile and tails, transverse beam halo, bunch-by-bunch chopping efficiency and more advanced beam emittance measures. Many types of beam monitors (*e.g.* BPMs, toroids, *etc*.) can be standardized. However some areas in PIP-II, such as the frontend (H^- source, RFQ and MEBT) will demand dedicated beam diagnostics (Allison scanner, fast Faraday cup, e-beam scanner, vibrating-wire, etc.).

For the linac the beam monitoring within the cryogenic environment is limited to beam orbit monitoring with BPMs. Most other beam diagnostics will be located at warm sections between cryomodules. In addition, if the space is available, we will also investigate the possibility of incorporating laser profile monitors between cryo-modules.

In order to develop this beam instrumentation, a complete set of "beam measurement requirements" has to be established. Each sub-accelerator (linac, transport lines, Booster, MI, Recycler) needs to address the operating modes with the nominal, as well as non-standard beam parameters, and all requirements for the different beam measurements (resolution, precision, dynamic range, etc.). We foresee the following general detectors and systems for beam instrumentation and diagnostics.

Beam Position Monitors

The beam orbit monitoring is the most fundamental measurement and the most powerful diagnostics tool in an accelerator. PIP-II requires a large number (~100) of new warm and cold beam position monitors (BPM), thus making it a complex and expensive measurement system. 37 BPM pickups will be located inside HWR, SSR1 and SSR2 cryo-modules. Their design has to be done to meet UHV, cryogenic and clean room requirements simultaneously. Recently the prototype of the HWR and SSR1 BPM pickups was successfully tested in the Argonne National Laboratory. All linac BPMs are based on four electrode pickups and have to be capable to measure all 3 coordinates, horizontal, vertical and RF phase, as well as a measure of the beam intensity. BPMs in the linac-to-Booster line are single coordinate pickups: horizontal or vertical depending on their location (horizontal near F quad, vertical near D quad).

The spectrum of BPM signals is concentrated in high frequency (up to a few GHz). It requires high quality RF cables to transmit their low-power high frequency signals to the read-out hardware

outside the accelerator tunnel. This requirement may impact the arrangement or layout of some conventional facilities.

The major requirements on BPM accuracy come from optics measurements based on the differential orbits. It requires the relative position measurements better than 30 μm, the relative RF phase measurements better than 0.1 deg. and relative beam intensity under 1%,

Beam Profile Monitors

Profile monitors are required at a few locations in the MEBT, the SC Linac and the Linac-to-Booster transfer line for measuring the beam emittances and phase space to match the beam to the Booster injection. Options for transverse profile monitors in the H^- sections of PIP-II are the standard multi-wire monitor and the newer laser profile monitor. Laser-based profile monitors are intended as the primary technology choice with standard multi-wires as a fallback technology. Laser profile monitors also allow measurements of the longitudinal beam profile. In addition, profile measurements in the rings will be made using ionization profile monitors and electron wire profile monitors.

Beam Loss Monitors

Typical fast ionization chambers with a large dynamic range will be utilized for most loss measurements. However, there may be instances where measurements of thermal neutrons or machine activation are desired. The loss monitors will be incorporated in the machine protection system (MPS). Beam loss monitoring with ionization chambers in the low-energy section of the linac are not possible. We intend to measure beam loss, in the linac frontend, through precision beam current measurements as well as by measuring beam current on electrically-isolated scrapper plates.

Beam Current Monitors

To determine the beam current and the beam loss (in absolute units) a combination of DCCTs and beam toroids will be used. They have to allow the high precision beam current measurements for both pulsed and CW operation of the linac. In addition, we estimate that, in the linac, we can obtain beam current measurements to better than 1% through the BPM system.

Special Monitors

Several types of special beam monitors and diagnostic tools are required to verify the beam quality and minimize beam losses. These include monitoring of the transverse beam halo (*e. g.* vibrating wires, laser wires and scrappers), the measurement of bunch-by-bunch chopping efficiency (*e. g.* high bandwidth wall current monitors and deflecting cavities) and the detection of longitudinal tails (*e. g.* laser wires and high bandwidth wall current monitors). A list of special beam monitors and diagnostic tools is not complete but design of generic instrumentation ports in diagnostic sections will allow future instruments to be installed. Development and test of such monitors will be carried out in PIP2IT.

Data Acquisition and Timing

Most beam monitoring systems will use frontend digital signal conditioning and processing methods to extract the wanted beam parameter(s). The generated output data needs to be “time stamped” with respect to the beam event, so beam and other recorded data can be cross-correlated throughout the entire PIP-II complex. This cross correlation will simplify diagnostics and trouble-shooting on the day-to-day operation.

Instrument Physical Space Issues

Sufficient physical space is allocated in the linac optics design to accommodate the required beam detection elements. At some critical, real-estate limited locations, e.g. LEBT, MEBT, injection / extraction, and SRF areas, a compromise must be worked out, which enables an acceptable way to sense the beam without compromising its quality in the diagnostic sections.

3.6. Controls

The control system is responsible for control and monitoring of accelerator equipment, machine configuration, timing and synchronization, diagnostics, data archiving, and alarms. PIP-II will use an evolution of the Fermilab control system ACNET [84], this is the system that is used in the main accelerator complex and also at the NML/ASTA and PIP2IT test facilities [85]. ACNET (Figure 3.45) is fundamentally a three tiered system with frontend, central service, and user console layers. Front-end computers directly communicate with hardware over a wide variety of field buses. User console computers provide the human interface to the system. Central service computers provide general services such as a database, alarms, application management, and frontend support. Communication between the various computers is carried out using a connectionless protocol over UDP. Subsystems developed by collaborators based on the EPICS control system can be integrated into the main system.

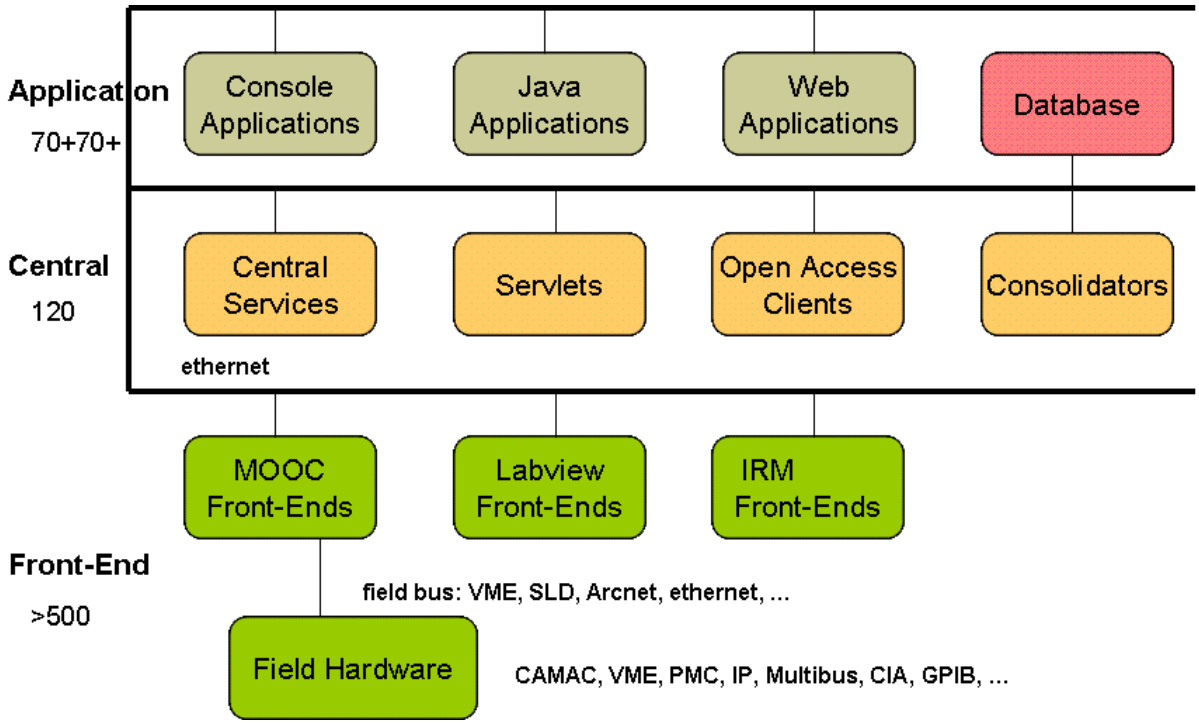

Figure 3.45: PIP-II Controls System architecture.

The scale of the control system is expected to be similar to that of the complex when the Tevatron was operating. The system should support up to 1M device properties. Time stamping must be provided so that all data from the SC Linac can be properly correlated with that from the existing complex. The control system should contribute less than 1% to operational unavailability. The high beam power implies the need for a sophisticated machine protection system to avoid damage to the accelerator due to errant beam pulses.

The Fermilab Accelerator Control System makes use of a 2 tiered timing system for the accelerators. The top level is a 10 MHz based clock system (TCLK) that provides basic system co-ordination and data acquisition timing. The second level clock system is specific to each accelerator and is synchronous to beam in that machine. The beam sync clocks have base frequencies that are derived from the machine's RF to provide bunch level timing for devices such as intensity monitors, BPMs and kickers. Relevant clock events are reflected from one level of clock system to the other as needed to support operations. A new upper level timing system will be developed that is a major

enhancement over the TCLK and MDAT links in the main complex. A prototype has been developed based on a 1 Gbps data link that adds a data payload and cycle stamp to each clock event transmission. The latter will allow reliable correlation of data across different frontends. The prototype design will be updated based on requirements for the SC Linac to serve as its beam synchronous clock.

It is highly desirable to have a single control system operating the entire complex rather than separate systems for the new linac and older parts of the system. There should only be a single copy of core services such as alarms and data archiving. Software applications should be able to access any device in the system. This model simplifies development and operation, and reduces long term maintenance costs of the complex. The current control system covering the Booster, Main Injector and Recycler represents a large investment in both software and hardware and it is not practical to completely replace it by the start of PIP-II operations. The strategy will be to gradually update parts of the system before and during PIP-II construction, and in support of the NML and PIP2IT test facilities. This upgrade will include modernizing the application software environment as well as replacing obsolete hardware. Upgraded timing and machine protection systems will be developed for the PIP-II linac that will accommodate the legacy hardware in the existing parts of the complex. These systems as well as the linac control software will be prototyped at NML and PIP2IT

It is recognized that some equipment will be developed outside of Fermilab by institutions with expertise in the EPICS control system. Also it may be appropriate in some cases to use commercial hardware that comes with embedded EPICS software. It is planned to support integration of EPICS frontends and some core applications in the Fermilab control system. This has been demonstrated in several different ways at different levels of the control system at the HINS and NML test facilities. The control system will specify standard interfaces between its internal components as well as with technical equipment. This will make integration, testing, and software development easier and more reliable and reduce the long term maintenance load. Also standard interfaces allow parts of the system to be more easily upgraded if required for either improved performance or to replace obsolete technologies. Only portions of the system need be changed while the core architecture of the control system remains the same.

Operation at 20 Hz

Increasing the Booster repetition rate from 15 to 20 Hz will be a significant change in the control system. The current timing system is based on a 15 Hz signal derived from the 60 Hz line voltage along with a 15 Hz signal generated by the booster GMPS. These are transmitted out to the rest of the complex as TCLK events generated via the Timeline Generator (TLG). These events will have to be changed to 20 Hz events. The shorter time between events and beam pulses will have to be accounted for by software changes to the TLG which generates the main timing signals for the various accelerators. A variety of systems perform software tasks on each 15 Hz pulse and each will have to be examined to ensure there is sufficient time to complete their task when the timing moves to 20 Hz. Though this is a major change that impacts many parts of the control system, it is currently believed that both PIP-II and the remaining parts of the existing complex should be able to adapt.

3.7. Radiation Safety and Radiation Shielding Design

Design requirements and radiation limits for accelerators and beam transport lines are provided by the Fermilab Radiological Controls Manual (FRCM). The manual requires well-engineered designs that maintain occupational and environmental radiation exposures as low as reasonably achievable (ALARA) and that are compliant with applicable regulations and DOE Orders. The first choice for accelerator shielding designs is to have passive shielding elements designed to enable areas external to shielding to be classified as minimal occupancy. Minimal occupancy is defined to mean any area which is not normally occupied by people more than 1 hour in 8 consecutive hours. Dose rates for potential exposure to radiological workers in areas without continuous occupancy are to be ALARA and such that individuals do not receive more than 20% of the applicable limits. The design goal for dose rates in areas of continuous occupancy is to be less than an average of 0.05 mrem/hr and as far below this and ALARA. Reliance on active systems such as radiation safety interlocks and/or beam line instrumentation to achieve radiation safety goals should be chosen only if passive elements cannot, in view of planned accelerator operations, reasonably achieve the level of protection required by the FRCM. Discharges of radioactive liquid to the environment should be kept ALARA. Materials and components should be selected to minimize the radiological concerns, both occupational and environmental. Where removable contamination might be associated with accelerator operations, provisions should be made in facility designs for the containment of such material. Internal radiation exposure is to be minimized in accordance with ALARA principles by the inclusion of engineered controls such as ventilation, containment, filtration systems, where practicable and with appropriate administrative procedures. Efficiency of maintenance, decontamination, operations, and decommissioning should be maximized.

The FRCM specifies the manner in which radiological posting requirements are to be determined. The maximum dose is that which can be delivered under the worst credible accident in that area, taking into consideration circumstances and controls, which serve to limit the intensity of the maximum beam loss and/or its duration. Some examples of accident scenarios are (1) beam intensity significantly greater than the nominal beam intensity; (2) unanticipated beam losses; and (3) single pulse full machine loss on an element. The maximum dose is to be determined through the Safety Analysis, which shall document calculations and measurements of possible radiation exposures, radiation shielding, beam optics and other relevant information. The Safety Analysis must be reviewed and approved by the SRSO prior to construction and/or operation of the beam.

The FRCM specifies requirements for entry controls. Accelerator/beam line areas are to be posted and controlled for the normal operating conditions when the Safety Analysis documents that delivering the maximum dose to an individual is unlikely. Accelerator/beam line areas are to be posted and controlled for accident conditions when the Safety Analysis documents a scenario in which it is likely that the maximum dose may be delivered to an individual.

A Safety Analysis for PIP-II beam operation and the application of the FRCM design requirements to PIP-II are described in the remainder of this section.

3.7.1. Radiation Limits

Safety Analysis

A PIP-II upgrade will change the operation of SC Linac from the pulsed to CW regime. That will enable linac operation with megawatt scale beam power. To determine the range of normal and accident beam loss conditions this Safety Analysis considers both the machine operation in the pulsed and CW regimes as described in Section 1.

Accelerator components such as cryomodules and beam pipes can be damaged or destroyed very quickly by beam power even at the levels envisioned for PIP-II. It becomes much more challenging for the PIP-II upgrade. The PIP-II SC Linac and associated beam lines require unprecedented control of beam orbit, beam optics, and beam losses in order to provide decades of safe operation for experimental programs. Consequently, the control of beam loss through a machine protection system is a primary design consideration for PIP-II.

The principal design features required for the control of beam loss in the SC Linac and Linac to Booster Beam Transport include precision alignment of all accelerator components, precise control of beam focusing, elimination of RF jitter, and precision control of beam orbit. Operation of PIP-II accelerators and beam lines without precision controls could easily result in beam losses exceeding 100 W/m. Machine protection systems are required to ensure that all beam control features are functional and operating as intended. The loss of any precision control feature will cause the machine protection system to inhibit beam acceleration at the ion source and LEBT. The machine protection systems will be capable of limiting or stopping machine operation within a few microseconds of sensing an abnormal condition.

PIP-II accelerators and beam lines accelerate and transport H^- beams. The principal beam loss mechanisms are related to stripping electrons from H^- ions; the causes of stripping include H^- ion collisions with residual gas, blackbody photon interactions, Lorentz force (magnetic stripping), and intrabeam stripping. The major contribution to beam loss comes from intrabeam stripping and this has been determined to be below 0.1 W/m (see Section 2.1.4). Losses from the remaining mechanisms are significantly smaller.

The beam power delivered by the Booster Accelerator has risen significantly over the lifetime of this accelerator, while the radiation shielding available over the Booster beam enclosure has remained fixed. Improvements resulting from PIP and other machine upgrades have led to increasing beam power while controlling and reducing beam losses. An interlocked radiation detector array has been necessary protective measure at the Booster accelerator to compensate for the fixed shielding inventory. Some remaining PIP upgrades are yet to be implemented which will raise the Booster beam power to 80 kW while keeping the beam losses at a fixed or reduced levels. Since it is not practicable to increase Booster radiation shielding, it is necessary to continue with reliance upon an interlocked radiation detector system to limit the severity and duration of beam loss conditions. Reliance upon an interlocked radiation detector system makes it implicit that radiation levels are controlled at defined, normal loss conditions. That is, the normal loss condition is the de facto maximum beam loss condition. The maximum normal loss condition, is limited by the FRCM, while the nominal upper limit is set at some lower level by the laboratory's well established shielding review process.

The MI8 line and the Main Injector accelerator are heavily shielded with 24.5 feet of earth equivalent shielding. The addition of radiation shielding to the MI8 line and the Main Injector accelerator would be both costly and of limited utility. For example, at a beam energy of 8 GeV, a 22.5 kW beam loss is required to exceed the 1 mrem/hr on the surface of the shielding berm. Various machine protection features inhibit the continuous loss of beam power at this level. As is the case for the Booster accelerator, the shielding assessment process is employed to ensure the limits of the FRCM are observed for the MI8 line and the Main Injector. If found to be necessary, a comprehensive, interlocked radiation detection system (TLM) described below can be employed to ensure compliance with all requirements of the FRCM.

The shielding prescription required by this Safety Analysis for the SC Linac and the SC Linac to Booster Transfer Line is discussed below.

Facility Design Beam Loss Level

The conclusion of the above Safety Analysis is that the average beam loss for the SC Linac and the Linac to Booster Beam Transport Line under normal conditions will be of the order of 0.1 W/m. Machine protection systems will monitor the performance of beam focusing, beam orbit, RF stability, and machine alignment. Machine protection systems will reduce accelerator beam power or inhibit accelerator operation in the event the precision control of the accelerator is lost. The reaction time of the machine protection systems under consideration is on the order of a few microseconds. Therefore, only operation under normal conditions should be possible. For the purposes of the facility shielding design, it is assumed that the peak average beam loss will be 1 W/m, a factor of 10 higher than what is expected during nominal beam operating conditions.

Facility radiological design goals

The design goals for the PIP-II SC Linac and the SC Linac to Booster Beam Transport Line meet or exceed the minimum requirements of the FRCM stated above. The design goals are:

1. Permit unlimited occupancy for all service buildings, shielding berms, parking lots, control rooms, and associated areas. By design, radiation levels are to be kept below 0.05 mrem/hr in all accessible locations outside of the beam enclosures for normal operating conditions, based upon an assumed continuous beam loss of 1 W/m. The actual nominal beam loss condition described in the Safety Analysis is expected to be about 0.1 W/m.
2. Permit inspection and maintenance activities within tunnel enclosures while maintaining personnel radiation exposure due to residual activation of accelerator components and beam enclosures at levels as low as reasonably achievable. At 0.1 W/m, the residual dose rates should not exceed about 15 mrem/hr.
3. Limit radiation exposure due to air activation both within the beam enclosure during inspection and maintenance activities and at the site boundary.
4. Limit ground water and surface water activation to levels well below regulatory standards.
5. Prevent the activation of beam component surfaces to avoid the generation of removable radioactivity.
6. Minimize the activation of accelerator components which can impact their useful service life.

3.7.2. Radiological Design Requirements

Nominal beam loss throughout the PIP-II accelerator and beam lines is expected to be about 0.1 W/m. Machine Protection Systems will limit or inhibit beam operations within microseconds of sensing a machine fault. The design requirements for radiation shielding discussed below are based upon an assumed continuous beam loss of 1 W/m. The consequences of the activation of accelerator components, enclosure structures, air, water, and removable contamination are discussed in terms of the expected nominal beam loss of 0.1 W/m as defined in the Safety Analysis.

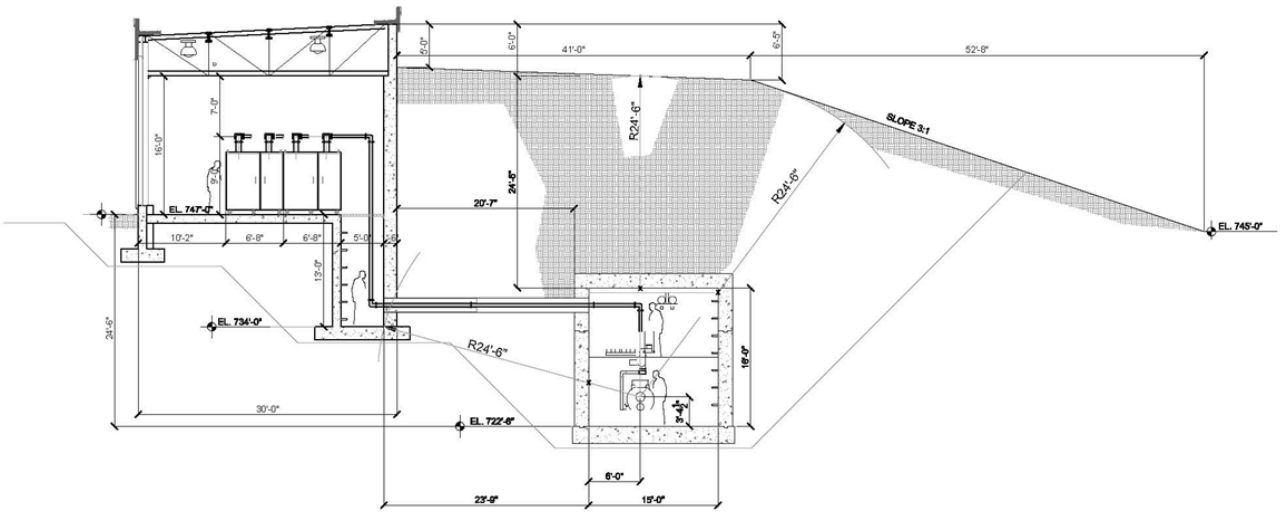

Figure 3.46: An early concept for the cross section of PIP-II linear accelerator enclosure

Radiation Shielding

An early conceptual design of a PIP-II accelerator enclosure is shown in Figure 3.46. An enclosure height of 16 feet is indicated along with passive shielding of 24.5 feet. An option to transport 0.8 GeV beam to the Booster is shown in Figure 3.47. The transport line will be crossing the beam line delivering the 120 GeV MI beam to the experimental areas (former Tevatron/Main Ring tunnel). The tunnel height is 8 feet and the shield is approximately 20 feet. At this time, details of the PIP-II layout and facility design have not been finalized. It is necessary that the accelerator design precede the shield design, but some shielding design concepts for PIP-II are considered here.

An established parameterization [86] is used to determine the radiation dose equivalent rate as a function of energy (GeV), distance (feet), and angle with respect to incident beam direction (degrees) from a low energy proton beam (<1 GeV) incident upon a target:

$$(E, r, \theta_s) = 2\times10^{-5}\left(1+ \mathrm{E}^{0.6}\right)\left(\frac{1-e^{-3.6E^{1.6}}}{\left(0.3048r\left(\theta_s+\frac{40}{\sqrt{E}}\right)\right)^2}\right) \tag{3.7}$$

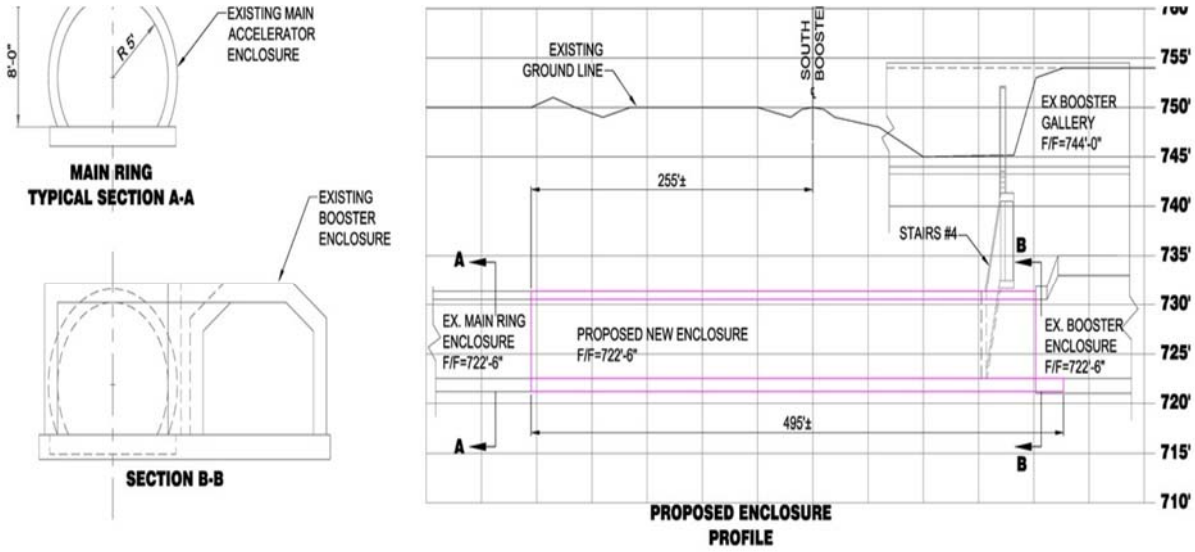

Figure 3.47: 1 GeV transport line to the Booster accelerator

For neutron energies below 100 MeV, the attenuation length in concrete is significantly shorter than that for the neutrons considered in higher beam energy based assessments. For example, for high energy shielding problems, 3 feet of concrete provides a reduction factor of 10 in radiation dose rate. The mean free path of low energy neutrons relative to the high energy asymptote has been parameterized [86]:

$$\frac{\lambda_{LE}}{\lambda_{HE}} = 1 - 0.8e^{-5*E} \quad . \tag{3.8}$$

The reduction in radiation dose rate as a function of energy (GeV and concrete shield thickness (feet) is:

$$A\left(E, T_{conc}\right) = 10^{\frac{-T_{conc.}}{3}/\left(1-0.8e^{-5E}\right)} \tag{3.9}$$

In the dose rate calculations the peak neutron energy, E (GeV), is taken to be equal to the beam energy. This simplification is conservative in that the actual neutron energies are necessarily lower and hence lead to better attenuation provided by the concrete shielding than indicated by Eq. [1]. In addition, the dose equivalent per neutron conversion factor is taken as a constant value of 40 fSv/n over the full range of the neutron spectrum. Thus the resulting shielding calculations are implicitly conservative.

Radiation shielding required to limit radiation dose rates to 0.05 mrem/hr for a 1 GeV linac and beam transport line assuming various beam levels of beam loss is shown in Figure 3.48. The shielding requirement varies with beam energy with the assumed maximum beam power loss for normal and accident conditions. The choice of shielding thickness will take into account a number of factors including the confidence level given to the Safety Analysis including consideration of the projected loss mechanisms and the machine protection system.

An active protection system, the Total Loss Monitor (TLM), currently under development, could be used to guarantee the limitation of any given beam power loss. The use of a TLM system could help to fix the level of beam power loss, and as a consequence, fix the amount of radiation shielding required.

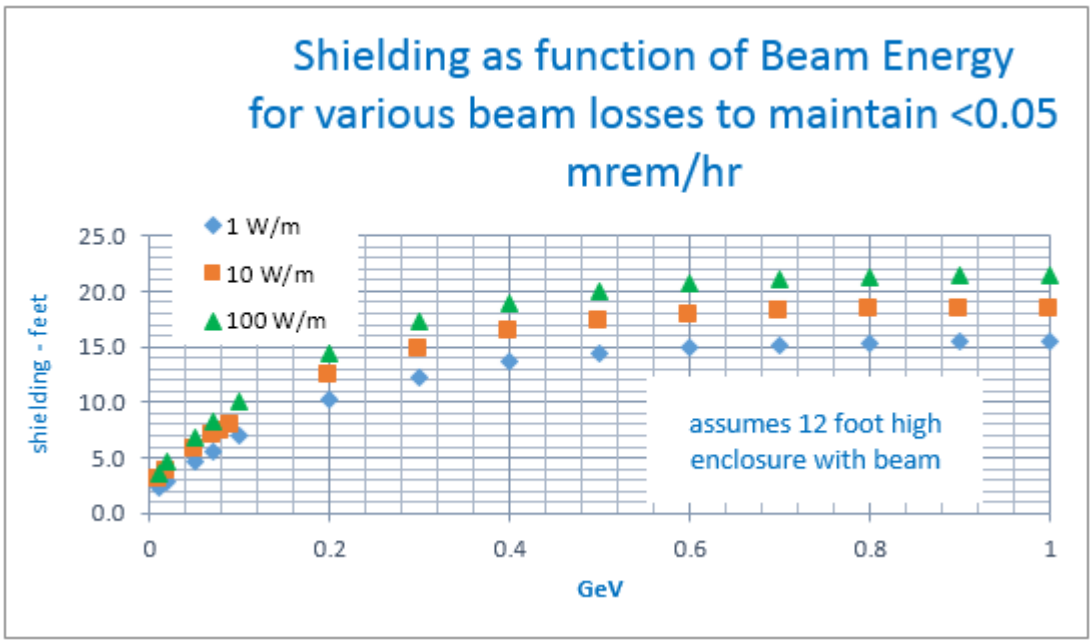

Figure 3.48: Radiation shielding requirements as a function of beam energy and beam power loss for a PIP-II beam enclosure

The TLM is an argon/CO_2 (80%/20%) gas filled ion chamber of variable length with an applied bias voltage. Beam loss in the vicinity of the ion chamber produces a charge whose magnitude is proportional to the amount of beam loss. The TLM response to an 8 GeV proton beam loss made under controlled conditions measured over a wide range of bias voltage and over two decades of beam intensity has been determined as shown in Figure 3.49. The response has been shown to be independent of the TLM length. At the nominal bias of 800 volts, the TLM response to 8 GeV proton beam loss is about 3 nC/E10 protons. Preliminary scaling laws, to be verified in further TLM development work, can be used to predict TLM response at other energies.

The response can be scaled to beam energy down to 1 GeV by the relationship:

$$\frac{3\,\text{nC}}{10^{10}\,\text{protons}} \times \left(\frac{E}{8\ \text{GeV}}\right)^{0.8}$$

The response to beam energy below 1 GeV remains to be determined.

A feature of the TLM system is that an interlock trip level can be established to limit beam loss to 1 W/m or virtually any beam power loss. A TLM, as presently conceived, does not distinguish between distributed losses and single point beam losses. The process to set TLM trip levels consists of two steps: (1) establish the total charge to be collected for a distributed loss, *e.g.*, 1 W/m, (2) evaluate the shielding considering that the total charge is deposited at any single location. If the shielding is sufficient for the maximum charge collection rate at any location, then the TLM can effectively limit both the distributed beam loss and worst case single point beam loss.

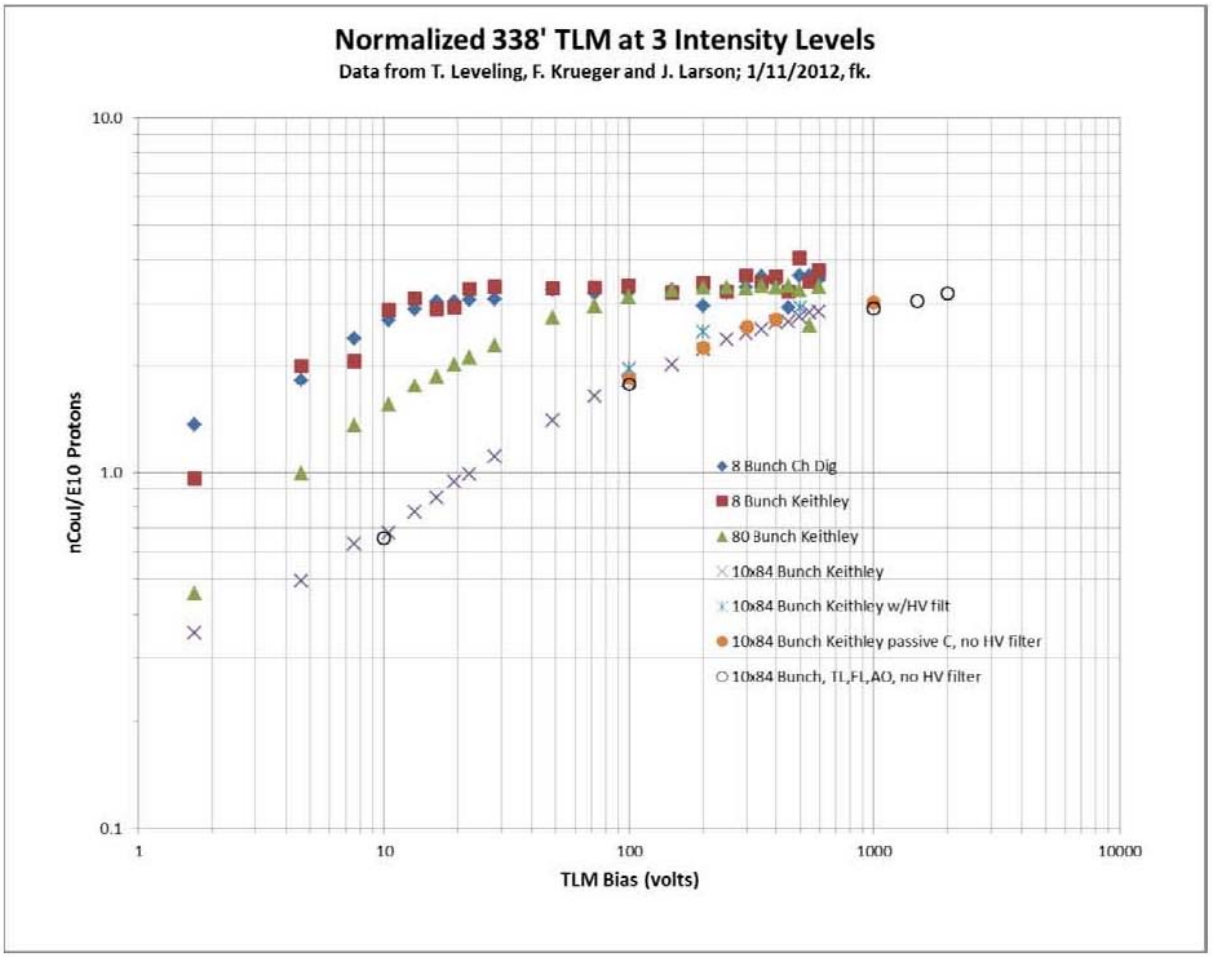

Figure 3.49: Response of 338 foot (103 meter) TLM as a function of applied bias voltage over 2 decades of beam intensity

Based upon preliminary TLM work, it should be possible to limit PIP-II beam loss with a TLM system beginning at the HWR cryomodule and continuing through the entire accelerator and the beam transport chain.

Residual Activation of accelerator components and structures

Residual radiation levels in beam transport lines and accelerators due to operational beam losses must be controlled in order to conduct maintenance activities while keeping personnel radiation exposure as low as reasonably achievable (ALARA). For 1.6-3 MW beam power, small fractions of 1% loss would result in very high residual radiation levels which would render beam enclosure access difficult and maintenance at loss points extraordinarily difficult. A sensitive machine protection system, which inhibits the beam operation when significant losses are present, is required to allow access and maintenance activities as historically enjoyed at Fermilab.

For design purposes, a loss rate of 3 to 10 W/m results in a dose rate of about 100 mR/hr at one foot from beam line components such as magnets and accelerating cavities following a 30 day irradiation period and 1 day of cool down. A loss of 0.25 watts/meter results in a dose rate of about 100 mR/hr at one foot from low mass components such as beam pipes for the same irradiation/cooling period. Radiation levels considered acceptable are typically at least a factor of 5 less than these levels. For example, for a typical magnet beam loss location at 2 W/m, the fractional

beam power loss is 1 ppm. A sensitive machine protection system will be required to quickly identify and suspend operation in the event such losses occur.

In the Safety Analysis, projected normal losses due to intrabeam scattering and other loss mechanisms are below 0.1 W/m. The machine protection system as presently conceived should limit beam loss to < 1 W/m. Consequently, residual activation of the accelerator, beam line components, and tunnel structures should be comparable to or less than levels tolerated in existing and previous machines. While the machine protection system would serve to protect the accelerator and beam line components, the TLM system would serve in a parallel role as a personnel safety system to limit residual activation of accelerator components.

Air activation

Air activation must also be characterized for the projected PIP-II operations. Based upon the anticipated losses described in the safety analysis, the combination of anticipated normal beam loss and the machine protection system should serve to limit the total beam loss levels at or below those produced at existing facilities. Based upon projected losses from the Safety Analysis, no significant air activation is anticipated. While the machine protection system would serve to protect the accelerator and beam line components, the TLM system would serve in a parallel role as a personnel safety system to limit air activation within accelerator enclosures.

Water activation

The site chosen for the new PIP-II accelerator and beam line enclosures is inside the former Tevatron ring. In order to evaluate surface and ground water activation, a geological survey (core borings) will be required to understand ground water migration rates at this site since no data presently exists. An estimate of surface and ground water activation is necessary in order to ensure compliance with regulatory requirements for surface and ground water. However, based upon losses projected by the Safety Analysis, no significant surface water or ground water activation is anticipated. The machine protection system would serve to limit the total beam loss that would also determine the level of surface water and ground water activation. The TLM system would serve a parallel, redundant role to also limit surface and ground water activation.

Radioactive surface contamination

Radioactive surface contamination results coincidentally with the activation of accelerator and beam line components. Maintenance activities are rendered more complicated when radioactive surface contamination is present due to prescriptions for the use of personnel protective equipment including coveralls, gloves, shoe covers, and other protective measures. It is possible in megawatt beam power machines to produce very significant levels radioactive surface contamination at beam loss locations. However, as indicated in the Safety Analysis, the nominal beam power losses are expected to be approximately 0.1 W/m, about a factor of 100 below the beam power loss required to produce the onset of measurable radioactive surface contamination. Consequently, radioactive surface contamination on accelerator, beam line components, and tunnel structures should be comparable to or less than levels tolerated in the existing and previous machines.

Lifetime of machine components

Based upon the level of beam loss projected by the Safety Analysis and also upon experience with existing accelerator and beam line facilities, machine component lifetimes should, in general, be on the order of many decades.

3.8. Machine Protection System

The PIP-II linac will accelerate 2 mA beam current with 1.1% duty factor which results in an average beam current of 22 μA. After a planned upgrade to CW operation, the total beam current will be greater than in any, present HEP hadron linac. A robust Machine Protection System (MPS) will protect the linac components from direct beam induced damage and excessive radiation damage. The main goals of this MPS are as follows:

- Protect the accelerator from beam induced damage,
- Manage and monitor the beam intensity,
- Safely switch the beam off in the case of failures,
- Determine the operational readiness of the machine,
- Manage and display MPS alarms,
- Provide a comprehensive overview of the machine status,
- Provide high availability,
- Provide fail safe operation where possible,
- Provide post mortem analysis.

Several signals from devices or systems will be monitored and utilized as actuators to inhibit the beam at various stages of the accelerator. The main actuator for the beam is the ion source power supply itself. In addition, the LEBT/MEBT choppers' power supplies, the Radio Frequency Quadrupole (RFQ) amplifier, cavity power amplifiers, beam stops, and gate valves will act as additional control devices. A comprehensive overview of the entire machine will be obtained by careful monitoring all relevant inputs from machine diagnostics and critical systems affecting safe or fail safe operation.

The protection system model is based on experience gained from commissioning and operating the SNS accelerator. Its peak current specifications are about 20 times higher than the PIP-II peak beam current specification, and its copper to SC cavity transition occurs at 187 MeV. Above 200 MeV the PIP-II MPS hardware design and placement can be modeled after the SNS system. The PIP-II MPS system will not need response times as stringent as the SNS because of lower peak currents. The challenge for the PIP-II MPS comes from the low energy cryomodule protection (2.1 MeV – 150 MeV) where beam losses have difficulty penetrating the cryomodule and beam pipe.

3.8.1. MPS Configuration

The MPS will be considered to be the collection of all subsystems involved in the monitoring and safe delivery of beam to the dump and not limited to any particular subsystem or diagnostic device. It has connections to several external devices and sub-systems. Figure 3.50 shows a conceptual overview diagram of the MPS. The top layer comprises signal providers such as beam loss monitors, beam position monitors, magnet power supplies etc. Systems at this level send alarms or status information to the MPS logic subsystems (permit system) which issues a permit based on the comprehensive overview of all inputs and requests. Only simple digital signals (*e.g.* on-off, OK-alarm) are transmitted. All devices or subsystems that are determined to be pertinent to protecting the machine or necessary for machine configuration are included. The permit system layer of the MPS will be FPGA based and is thus fully programmable and handles complex logic tasks. The logic here will be designed to ensure safe operating conditions by monitoring operational input, chopper performance, the status of critical devices and by imposing limits on the beam power. The final layer

of the system shows the main actuators. This will comprise all points where the MPS logic may act on the operation of the machine to prevent beam from being produced or transported.

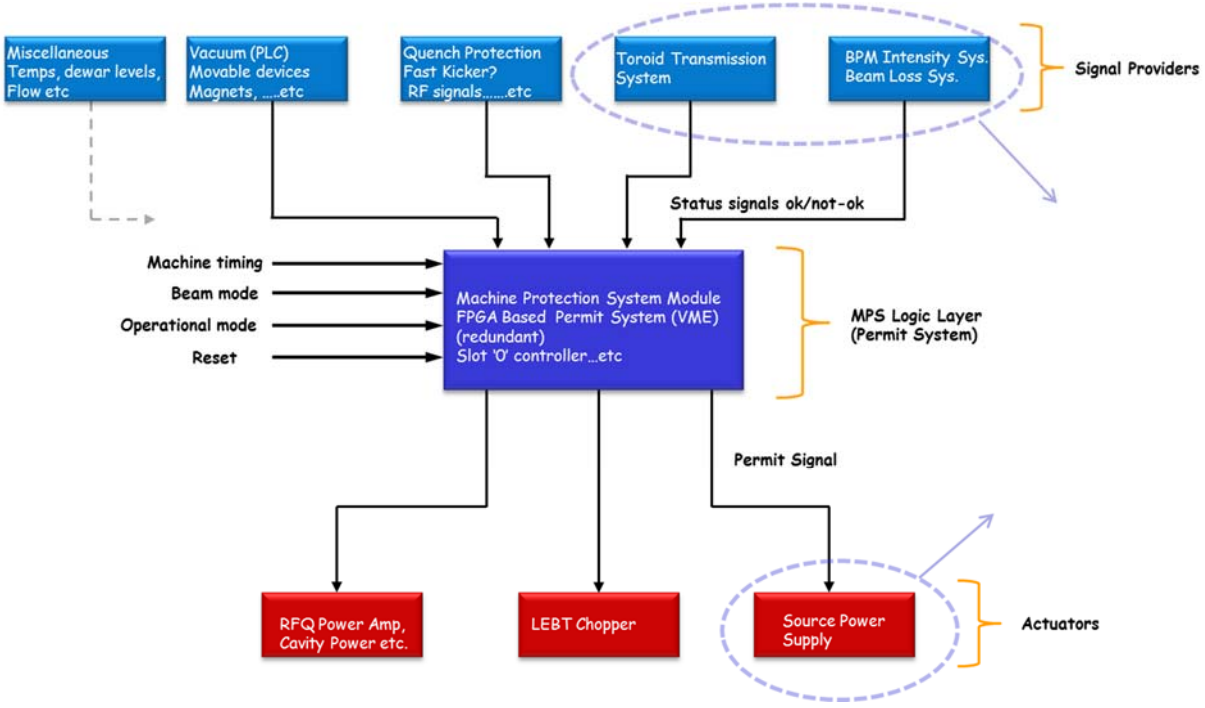

Figure 3.50: MPS Conceptual Layout

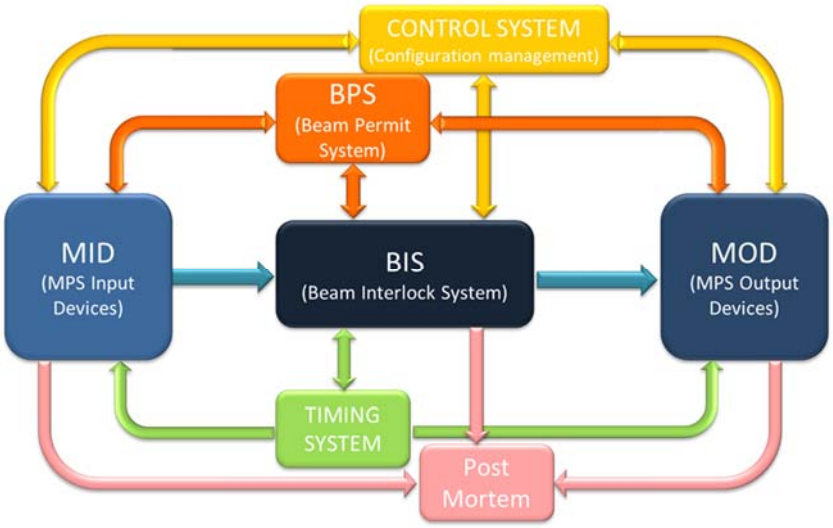

Figure 3.51: Conceptual MPS layout integrated with control system

The entire protection system interfaces with the accelerator control system and machine timing system for configuration management, timing and post mortem analysis as shown in Figure 3.51. The operational modes, operational logic, reaction time and complexity of inputs will differ based on the machine configuration and damage potential at various stages of the accelerator complex.

3.8.2. Protection System R&D

Protecting the superconducting cavities from low energy protons losses where the particle energies are too low to produce significant detectable radiation will be a major part of the

developmental work needed to effectively inject beam without quenches. To achieve this we will need to research sensitive means for measuring these losses and develop an effective feedback for machine protection. In addition we plan to achieve the following goals as a result of designing, constructing and operating the PIP2IT MPS:

- Understand and verify acceptable loss rates in the room temperature sections,
- Develop a strategy to monitor chopped beam from the MEBT,
- Estimate particle shielding effect of superconducting cavities and cryomodules,
- Develop effective algorithms for the FPGA based logic system,
- Demonstrate effective integration with controls/instrumentation and all subsystems,
- Understand dark current effects as it relates to protection issues.

In order to protect the accelerator from damage as the beam transitions from the room temperature sections of the machine to the superconducting sections, some specialized instrumentation may be developed at PIP2IT. Developing an effective algorithm to monitor the beam position as a feedback to machine protection will be of interest for both PIP2IT as well as PIP-II.

4. Siting and Conventional Facilities

4.1. Introduction

The PIP-II conventional facilities will house the accelerator components and support equipment required to install and operate the PIP-II linac and transfer line. The Conventional Facilities portion of the project includes the management, planning, design and construction of new structures, buildings and utilities as well as modifications to existing structures required to install and operate the PIP-II accelerator.

The PIP-II conventional facilities scope includes the elements of work normally included in conventional construction such as earthwork, utilities, structural concrete, structural steel, architectural cladding, finishes, roofing, plumbing, process piping, heating ventilation and air conditioning (HVAC) , fire protection, fire detection, lighting and electrical. This also includes the work required to extend the utilities to the project site, excavation associated with the below grade cast-in-place concrete enclosures, creation of a shielding berm and site restoration.

The PIP-II conventional facilities will consist of the following five (5) functional areas:

1. Site Work
   The Site Work consists of the extension of existing utilities to the PIP-II site, wetland mitigation, roadwork and parking area, hardstands, storage tank foundations and related work to provide the supporting infrastructure.
2. Linac
   The Linac functional area consists of the below grade Front End and Linac Enclosure and the associated above grade Linac Support Building. The Linac Enclosure will house the PIP-II accelerator components as well as provide space for support functions. The Linac Support building will run parallel to the below grade Linac Enclosure and house the components required to operate the PIP-II accelerator. The Linac Support Building includes a high bay service building with a loading dock and related services to accommodate the installation and servicing of beamline components. The Linac Support building will be designed to accommodate visitor tours as part of the Fermilab outreach program.
3. Transport Line
   The Transport Line functional area includes the below grade enclosures to house the beamline components required to transport the proton beam from the new Linac Enclosure to the existing Booster Enclosure and includes the conventional construction work required to cross the existing Main Ring tunnel as well as the work required to transport the beam into the existing Booster accelerator enclosure. This functional area also includes the space and equipment to house the Beam Absorber.
4. Cryogenics Plant
   This functional area consists of the conventional construction required to install, house and operate the cryogenic plant to support PIP-II accelerator operations.
5. Mechanical Plant
   This functional area consists of the conventional construction required to install, house and operate the cooling systems to support PIP-II accelerator operations.

The scope of the conventional facilities portion of the PIP-II project will be realized through

several design and construction packages. This is intended to provide a logical and constructible sequence to reduce the construction period to a minimum. Further design iterations will be required to optimize the construction packaging based on programmatic and funding limitations. The design methodology and construction means and methods for the conventional facilities work are expected to be similar to that which has been employed on the Fermilab site for decades.

4.2. Siting

The location of the PIP-II facility is driven primarily by the physics requirement for close proximity to the existing Booster accelerator (see figure XX) and access to existing infrastructure. The location in the Main Ring infield, adjacent to the Footprint area of the Fermilab campus, allows direct access to existing electrical, water, and cryogenic infrastructure currently located in the vicinity. In addition, the Main Ring infield location is well suited to extensions of chilled water service from the existing Central Utility Building (CUB). At the same time, the Main Ring infield location provides space for future expansion opportunities.

The siting of PIP-II facility was chosen to minimize the impact to existing known wetlands within the Main Ring infield as well as conform to the 2015 Fermilab Campus Master Plan [1] which has designated the area east of Wilson Hall as the Superconducting Linac Complex.

Surface construction for the PIP-II facility includes new buildings, site improvements, roadwork and parking to allow access from the Fermilab Central Campus.

Underground construction includes the Linac Enclosure, the Transfer Line enclosure, and Beam Absorber enclosure. The Linac enclosure is sited at the same elevation as the Booster and the Main Ring tunnel. The Transfer Line enclosure crosses the Main Ring tunnel which holds the existing 120 GeV transfer line to the Fixed Target Area Switchyard. The Fixed Target program is assumed to continue, the PIP-II Transfer Line will rise up and over the existing 120 GeV line as it crosses the Main Ring tunnel on the way to the Booster.

4.1. Requirements

The requirements for the PIP-II conventional facilities scope of work were developed from stakeholder input, organization processes and enterprise assets. The main sources of stakeholder inputs are the other subproject managers gathered from regularly scheduled meetings. The requirements employed in the design and construction of the PIP-II conventional facilities documented in the PIP-II document database **Error! Reference source not found.**.

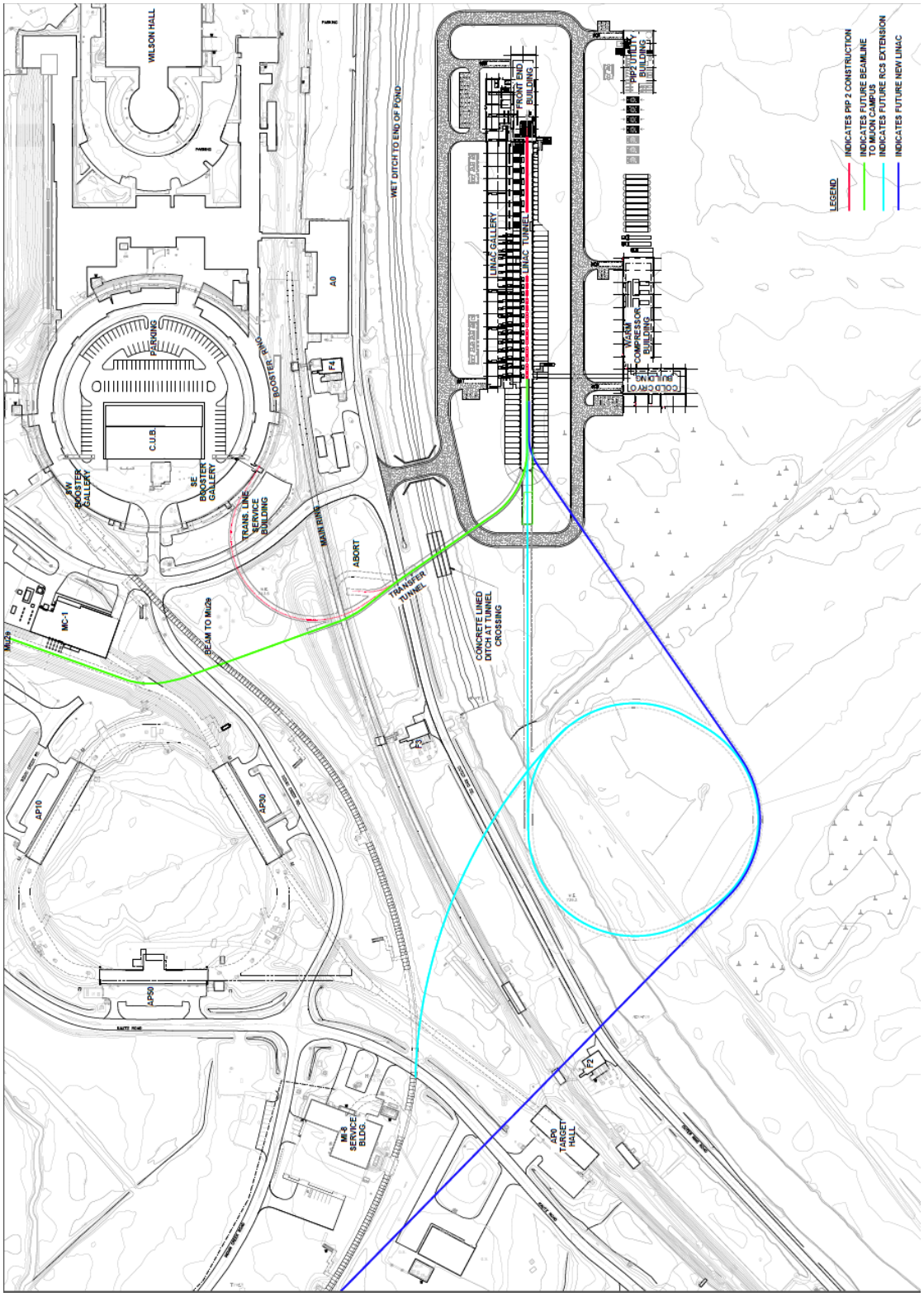

Figure 4.1.

4.1.1. Organizational Processes

Organizational Processes provide institutional requirements for the design, construction and

operations of all projects built and operated at Fermilab. For the PIP-II conventional facilities these requirements are derived from the Policies and Procedures of the Fermilab Directorate, Accelerator Division (AD), and the PIP-II project. All applicable DOE orders and standards are included in these requirements. A selection of applicable standards is listed below:

- DOE Order 151.1C – Comprehensive Emergency Management System
- DOE Order 413.3B – Program and Project Management for the Acquisition of Capital Assets, Change 1 issued 11/29/10
- DOE Order 414.1C – Quality Assurance
- DOE Order 420.1B – Facility Safety
- DOE Order 430.1B – Real Property Asset Management (2/8/08)
- DOE Order 430.2B – Departmental Energy, Renewable Energy and Transportation Management
- DOE Order 450.1A – Environmental Protection Program (6/4/08)
- DOE STD-1066-99 – Fire Protection Design Criteria
- DOE STD-1073-2003 – Configuration Management
- DOE Guide 420.1-2 – Guide for the Mitigation of Natural Phenomena Hazards for DOE Nuclear Facilities and Non-Nuclear Facilities
- 10 CFR 835 – Radiological Protection Program
- 10 CFR 851 – Worker Safety and Health Program
- 10 CRF 851.23 – Safety and Health Standards
- Internal Fermilab permits and work notifications as described in the Fermilab ES&H Manual (FESHM)
- Fermilab Director's Policy Manual (http://www.fnal.gov/directorate/Policy_Manual.html)
- Fermilab Engineering Manual (http://www.fnal.gov/directorate/documents/FNAL_Engineering_Manual.pdf)

4.1.2. Enterprise Standards

Enterprise standards from regulatory agencies, code bodies and trade organizations also provide requirements for the design and construction of the PIP-II conventional facilities. The Fermilab Engineering Standards Manual provides a comprehensive listing of applicable and adopted building codes and design standards. The applicable standards are listed below:

- Codes, Standards, and Guidelines
- International Building Code (IBC) – 2009 Edition
- International Energy Conservation Code – 2009 Edition
- International Fire Code – 2009 Edition
- International Mechanical Code – 2009 Edition
- Minimum Design Loads for Buildings and Other Structures – ASCE 7-05
- Building Code Requirements for Structural Concrete – ACI 318-05
- Specification for Structural Steel Buildings – AISC 360-05
- Building Code Requirements for Structural Concrete and Commentary – ACI 318-08
- Building Code Requirements for Masonry – ACI 530-05
- Illinois Plumbing Code – 2004
- Illinois Department of Public Health Codes
- Illinois IEPA

- NFPA 101 Life Safety Code – 2009 Edition
- NFPA 13 – Standard for the Installation of Sprinkler Systems – 2010 Edition
- NFPA 24 – Standard for the Installation of Private Fire Service Mains and Their Appurtenances – 2010 Edition
- NFPA 30 – Flammable and Combustible Liquids Code – 2008 Edition
- NFPA 55 – Compressed Gases and Cryogenic Fluids Code – 2010 Edition
- NFPA 70 – National Electrical Code – 2008 Edition
- NFPA 70E – Standard for Electrical Safety in the Workplace – 2009 Edition
- NFPA 72 – National Fire Alarm Code – 2010 Edition
- NFPA 80 – Fire Doors and Fire Windows – 2010 Edition
- NFPA 90A – Standard for the Installation of Air-Conditioning and Ventilating Systems – 2009 Edition
- NFPA 90B – Standard for the Installation of Warm Air Heating and Air Conditioning Systems – 2009 Edition
- NFPA 92A – Standard for Smoke-Control Systems utilizing Barriers and Pressure Differences – 2009 Edition
- NFPA 92B – Standard for Smoke Management Systems in Malls, Atria, and Large Spaces – 2009 Edition
- NFPA 110 – Emergency and Standby Power Systems – 2010 Edition
- NFPA 115 – Standard for Laser Fire Protection – 2008 Edition
- NFPA 780 – Standard for the Installation of Lightning Protection Systems (and UL 96A) – 2008 Edition
- ASHRAE Standard 90.1-2004 Energy Standard for Buildings Except Low-Rise Residential Buildings
- ANSI/HFES 100-2007 – Human Factors Engineering of Computer Workstations
- ANSI 17.1 Safety Code for Elevators and Escalators
- ANSI/ASHRAE Standard 62.1-2004 Ventilation for Acceptable Indoor Air Quality
- ANSI/AIHA Z9.5-2003 Standards for Laboratory Ventilation
- ANSI/ASME B31.3 – Process Piping (2002)
- ANSI 31.9 – Building Services Piping (1996)
- Occupational Safety and Health Administration (OSHA)
- Underwriters Laboratory
- ICC/ANSI A117.1 – 2003 Standard for Accessible and Usable Buildings and Facilities Illinois Accessibility Code
- ADA Accessibility Guidelines for Buildings and Facilities (ADAAG) – 2004 will be used for those areas of facility not exempted by Fermilab policy
- Illinois Accessibility Code

4.1.3. Performance Requirements

The performance requirements listed below describe the project specific requirements that exceed or are not addressed in the applicable building codes and standards requirements contained in

Organizational Process or Enterprise Standards listed above.

4.1.3.1. Architectural Considerations

The design of the above grade buildings will be developed based on the 2015 Fermilab Campus Master Plan [2] including the desire that "New buildings and structures should be designed to be fresh, inviting, innovative, dynamic and forward-looking." To this end, the buildings will incorporate the appropriate portions of the design guidelines including:

- Entrances and ground floors that are welcoming;
- Entrances that are evident in the daytime and at night;
- The ground floor will emphasize transparency;
- Service and utilities areas will be located so as to not negatively affect pedestrian paths or building entrances;

The architectural finishes inside the buildings will generally be exposed construction suitable for equipment installation and operation.

Floor surfaces in the Linac Enclosure and lower level of the Linac Support Building will receive an epoxy finish.

4.1.3.2. Underground Enclosures

Open cut excavation techniques are anticipated for the construction of the below grade enclosures. After the concrete enclosure is constructed and damp proofed the enclosures will be backfilled using stone around the enclosure, followed by suitable clays and silts, covered with topsoil and seeded. Shielding berms will be constructed using maintainable 3:H to 1:V slopes.

4.1.3.3. Structural Systems

The structural systems for the PIP-II conventional facilities are expected to be constructed utilizing conventional methods similar to systems utilized at Fermilab over the past 40 years.

Below grade enclosures will be constructed of a cast-in-place concrete, including base, wall and roof slabs. An alternate construction method utilizing precast concrete sections will be investigated during subsequent design phases. These enclosures will be designed to support the shielding loads.

The above grade buildings will be a braced steel frame with pre-finished metal siding with structural steel and where applicable designed to accommodate overhead bridge cranes.

The structural systems for the Warm Compressor Station of the Cryogenics Plant will require vibration isolation in order to avoid impacting the operation of the Linac. An Engineering Note from the LCLS-II project (LCLSII-4.8-EN-0326-R0) titled "Vibration Measurements at the JLAB Cryoplant and Linac [3] noted that compressors at Jefferson Laboratory generated ground motion that resulted in cavity detuning and adversely affected superconducting linac operations. It was also noted that the level of motion decreased rapidly with distance from the cryo compressors with a finding that compressors located 30m (98.5 feet from the Linac is possible without impacting operations. In addition, the engineering note included a recommendation to mount the compressors on an isolated foundation. For PIP-II, the cryogenic compressors will be located approximately 61m (200 feet) away from the Linac and be mounted on isolated foundations.

The flatness and levelness of the new floor slabs built as part of the conventional facilities will be designed for normal construction tolerances and a ASTM E1155 floor flatness value of F(F) 25 and a floor levelness F(L) of 20.

4.1.3.4. Mechanical Systems

The HVAC systems for the PIP-II surface building will conform to ASHRAE 90.1, ASHRAE 62, applicable NFPA requirements and applicable sections of the Fermilab Engineering Standards Manual

Mechanical systems and building automation systems controls will be designed based on Fermilab standards and in accordance with ASHRAE 90.1.

All plumbing work to be designed in accordance with Illinois Plumbing Code and Standard Specifications for Water & Sewer Main Construction in Illinois.

Heating, Ventilation and Air Conditioning Design Parameters

Linac Support Building - High Bay:

- Temperature: winter - 68 degrees F (+/- 5 F) / summer - 78 degrees F (+/- 5 F)
- Humidity: 55% maximum relative humidity, no minimum

Linac Support Building – Gallery Space:

- Temperature: winter - 68 degrees F (+/- 5 F) / summer - 78 degrees F (+/- 5 F)
- Humidity: 55% maximum relative humidity, no minimum

Linac Enclosure:

- Temperature: winter - 68 degrees F (+/- 5 F) / summer - 80 degrees F (+/- 5 F)
- Humidity: 55% maximum relative humidity, no minimum

Transport Line Enclosure:

- Temperature: winter - 68 degrees F (+/- 5 F) / summer - 80 degrees F (+/- 5 F)
- Humidity: 55% maximum relative humidity, no minimum

Cryogenics Plant – Warm Compressor Station:

- Temperature: winter - 68 degrees F (+/- 5 F) / summer - 90 degrees F (+/- 5 F)
- Humidity: 55% maximum relative humidity, no minimum

Cryogenics Plant – Cold Box Station:

- Temperature: winter - 68 degrees F (+/- 5 F) / summer - 90 degrees F (+/- 5 F)
- Humidity: 55% maximum relative humidity, no minimum

Cryogenics Plant – Control Room:

- Temperature: winter - 68 degrees F (+/- 5 F) / summer - 78 degrees F (+/- 5 F)
- Humidity: 55% maximum relative humidity, no minimum

Chilled Water (CHW) will be used to provide a cooling medium for the mechanical equipment used to cool the heat load rejected to air in Pulsed Mode housed in the gallery of the Linac Support Building under pulsed mode linac operations. This system will condition the Linac Service Building utilizing ducted air handling units and be fed from above the space. The source of the CHW will be the existing chillers in Central Utility Building (CUB) which will be extended to the PIP-II project site. Currently, the CHW system has limited capacity to accommodate PIP-II. However, design changes and other uses of CHW from CUB could reduce the capacity which would require the installation of additional chillers.

In order to provide cooling under continuous wave linac operations, a supplemental system based on refrigerant cooling medium will be used to supplement the CHW system used under pulsed mode linac operations. This refrigerant system is based on a modular design that will supply cold air via a

bottom discharge air system.

Industrial Cooling Water (ICW) will be used to provide a cooling medium for the cryogenic compressors housed in the Warm Compressor Station of the Cryogenics Plant. The existing site wide ICW will be extended to the PIP-II project site where it will be strained/filtered to achieve the PIP-II water quality requirements. The ICW will be discharged into a new return ditch and routed to existing return routes to Casey's Pond.

A series of evaporative fluid coolers will be used to provide a cooling medium for the Low Conductivity Water (LCW) system without the use of chillers. This modular design approach will provide the direct cooling of the LCW system without the need for a heat exchanger or cooling ponds.

The Linac Enclosure will be designated an Oxygen Deficiency Hazard (ODH) location and will require a protection system. The Conventional Facilities design will provide the mechanical equipment including fans, louvers and ductwork for the ODH mitigation system. The sensors, controls and programming of the systems will be the responsibility of the controls department.

4.1.3.5. Electrical Systems

The electrical power for PIP-II facility will be provided by extending the existing site wide medium voltage feeder system to the project site in new concrete encased power duct bank.

The conventional facilities portion of the work will include the medium voltage distribution including ductbank, feeders, switches, transformers and incoming service feeds. The conventional facilities portion of the experiment power will end at the incoming service panel.

The house power including general power, lighting and power for mechanical equipment will be the responsibility of conventional facilities.

Emergency lighting and exit signage will be installed as part of the conventional facilities portion of work in accordance with Fermilab guidelines and requirements.

A UFER style ground will be installed that includes connection of the concrete reinforcing to the building ground system and structural elements of the above grade surface buildings.

Basis networking will be installed as part of the conventional facilities portion of the work. This includes extension of the site wide data/communication network to the PIP-II project site. The surface buildings will be provided with basic networking infrastructure including VOIP phone lines, connections to building automation systems and wireless access points. Extension and improvement of the data/communication system for experimental equipment will be done as part of the equipment installation.

The surface buildings will include electronic access control based on the existing site wide security system. This will include access to main building entrances.

4.1.3.6. Fire Protection Systems

Fire Alarm/Fire Suppression systems will be designed in accordance with the applicable sections of the Fermilab Engineering Standards Manual.

Automatic sprinkler systems will be designed to a minimum of an Ordinary Hazard Group 2 classification, in accordance with National Fire Protection Association (NFPA) latest edition. The most commonly used NFPA standards relative to automatic sprinkler systems are: 13, 20, 25, 318 and 750. Automatic sprinklers will be installed in buildings. Automatic sprinklers are not required in the enclosures or vertical exit passageways, based on the Main Injector Life Safety Fire Protection Analysis. Automatic sprinklers were installed in the Main Injector at enclosure stairs connecting to surface buildings and for 50' on either side of the stair alcove. These assumptions will be validated

during subsequent design phases by life safety consultants.

The below grade enclosures will be designed to allow for safe passage of personnel through the enclosure during operations and installation. Egress shall be spaced so that travel distances are no greater than 300 feet where there are two paths of travel to an exit and no more than 50 feet when sprinklered (25 feet without sprinklers) where there is a single path of travel to a vertical exit. Doors will be located at the enclosure levels at each exit but since the vertical distance to the exit discharge is less than thirty feet double doors are not required. All exits from below grade enclosures will lead to an exit discharge without requiring travel through a building.

Fire alarm systems will be designed with a minimum standby power (battery) capacity. These batteries will be capable of maintaining the entire system in a non-alarm condition for 24 hours, in addition to 15 minutes in full load alarm condition. The most commonly used NFPA standards relative to fire alarm systems are: 70, 72, 90A, and 318. Manual pull stations and alarm notifications will be provided in enclosures and buildings. In addition, fire extinguishers will be provided in accordance with FESHM Chapter series 6000.

The facility will be equipped with a hard-wired, zoned, general evacuation fire alarm system consisting of:

- Manual fire alarm stations at the building exits
- Sprinkler system water flow and valve supervisory devices
- Combination fire alarm horn/strobe located throughout the building
- A 24 volt addressable fire alarm control panel
- Connection to the site wide FIRUS monitoring system
- Smoke detection as required.

4.1.3.7. High Performance Sustainable Buildings

Fermilab is committed to designing, locating, constructing, maintaining and operating its facilities in an energy efficient and sustainable manner that strives to achieve a balance that will realize maximum attainable reuse and recycling of depletable resources, in an economically viable manner and consistent with Fermilab' s mission and goals. To accomplish this end, Fermilab complies with Guiding Principles for the Federal Leadership in High Performance and Sustainable Buildings (Guiding Principles). This direction is taken from the Fermilab Director's Policy 3. The project goal is to comply with the DOE's Guiding Principles for High Performance and Sustainable Buildings.

4.1.3.8. Radiation Safety

The conventional facilities will be designed to incorporate the applicable radiation safety requirements as contained in FESHM Section 1100 to reduce exposure to as low as reasonable achievable (ALARA) levels, including shielding labyrinths, exit passageways and passive shielding. The conceptual design is based on a preliminary review if the expected beam intensities and historic data from similar equipment. A complete radiation assessment will be conducted in subsequent project phases. The results of these assessments will be incorporated into the conventional facilities design.

The conventional facilities portion of the project will incorporate physical space for radiation safety interlock system, but the installation of the equipment, extension of monitoring devices and programming of the system will be the done as part of the equipment installation. These systems will be designed in accordance with the FRCM Chapter 10 Radiation Safety Interlock Systems

In accordance with current FRCM requirements, all sump discharges from the Linac Enclosure

and the Transport Line Enclosure will be discharged to cooling ponds or ditches.

4.2. Conventional Facilities Scope

The description of the scope of work for the PIP-II conventional facilities are listed below by functional area.

4.2.1. Site Work Scope

The site work includes wetland mitigation, roadwork and parking area, hardstands, storage tank foundations and related work to provide the supporting infrastructure for PIP-II.

The Main Ring infield has known wetlands which have influenced the siting of the PIP-II facilities. The wetlands in the vicinity of the proposed PIP-II project site were initially delineated and characterized in 2010. In the spring of 2016, these wetlands were revisited to further refine the location and impact of PIP-II. The 2016 wetland assessment report [4] will be used to as a basis for siting decisions and efforts will be made to avoid the impact on these existing wetlands and minimize unavoidable impacts during both the construction period as well as during operation of the new facility.

Wetland delineation of the project area and project plans will be submitted to the U.S. Army Corps of Engineers to determine if a permit would be required under Section 404 of the Clean Water Act. The mitigation strategy, if needed, is to purchase suitable wetland credits for those areas of unavoidable impact.

The existing South Booster Road will be reconfigured in order to allow for the installation of the Transport Line and associated shielding.

New access roads will provide vehicular access to the PIP-II facility from existing Fermilab roads. These roads will be constructed in a similar manner to existing Fermilab roads and will be suitable for all weather access. The access road will intersect existing the existing Main Ring Road at two (2) locations to prevent dead-ends. Paved parking will be provided for vehicles at major entries to the buildings along with a gravel hardstand that will provide a staging area during installation. A paved approach to the at-grade loading dock with suitable truck maneuvering space will be provided.

The existing AZero cooling pond is currently used for cooling existing beamline components in the Main Ring tunnel as well as a return path for Industrial Cooling Water (ICW) discharge from cryogenic loads in the AZero service building. The existing pond will be reconfigured and upgraded to serve as a return ditch for the ICW system. This will include a modernization of the pond banks and the installation of modern pumping equipment.

The extension of existing Fermilab utilities to the PIP-II site. These utilities include Industrial Cooling Water (ICW), Domestic Water Service (DWS), Natural Gas (Gas), Chilled Water (CHW), Sanitary Sewer (SS), data/communication and electrical power. Figure 2, below indicates the location of existing utilities in the vicinity of the PIP-II site.

The ICW service will be extended from the existing lines located near the intersection of Booster Tower Road and Main Ring Road. The existing site wide ICW service is fed from Casey's Pond at the north end of the Fermilab site where it is filtered and treated as it is pumped into the piping network. This service is anticipated to supply 1,400 gallons per minute of treated ICW to provide fire protection in the sprinkler system and hydrants as well as serve as a cooling medium for the cryogenic compressors. The ICW discharge will be piped west of the Main Ring tunnel so that will flow to Casey's Pond via existing cooling ponds and return ditches.

The existing DWS service will be extended from the intersection of Booster Tower Road near the

Central Utility Building (CUB) to provide potable water uses and make up water for process systems. As part of the subsequent design phases, a looped system connecting to other segments of the site wide DWS system will be investigated and incorporated as required.

PIP-II will connect to the existing SS system at Booster Tower Road near CUB. The PIP-II SS system will accommodate discharges from the toilet facilities as well as backwash from process loads. A new lift station at the PIP-II facility will collect the sanitary discharge locally and pump it via a force main to a new manhole installed in the existing SS system.

The existing natural gas (NG) service will be extended from the existing site wide network at Booster Tower Road near CUB. The NG will provide a fuel source for HVAC heating.

The existing CUB chillers have the capacity to supply 300 tons of CHW to PIP-II for cooling. Connection to the CHW Supply and CHW Return lines will be made near Booster Tower Road near CUB and be routed to PIP-II.

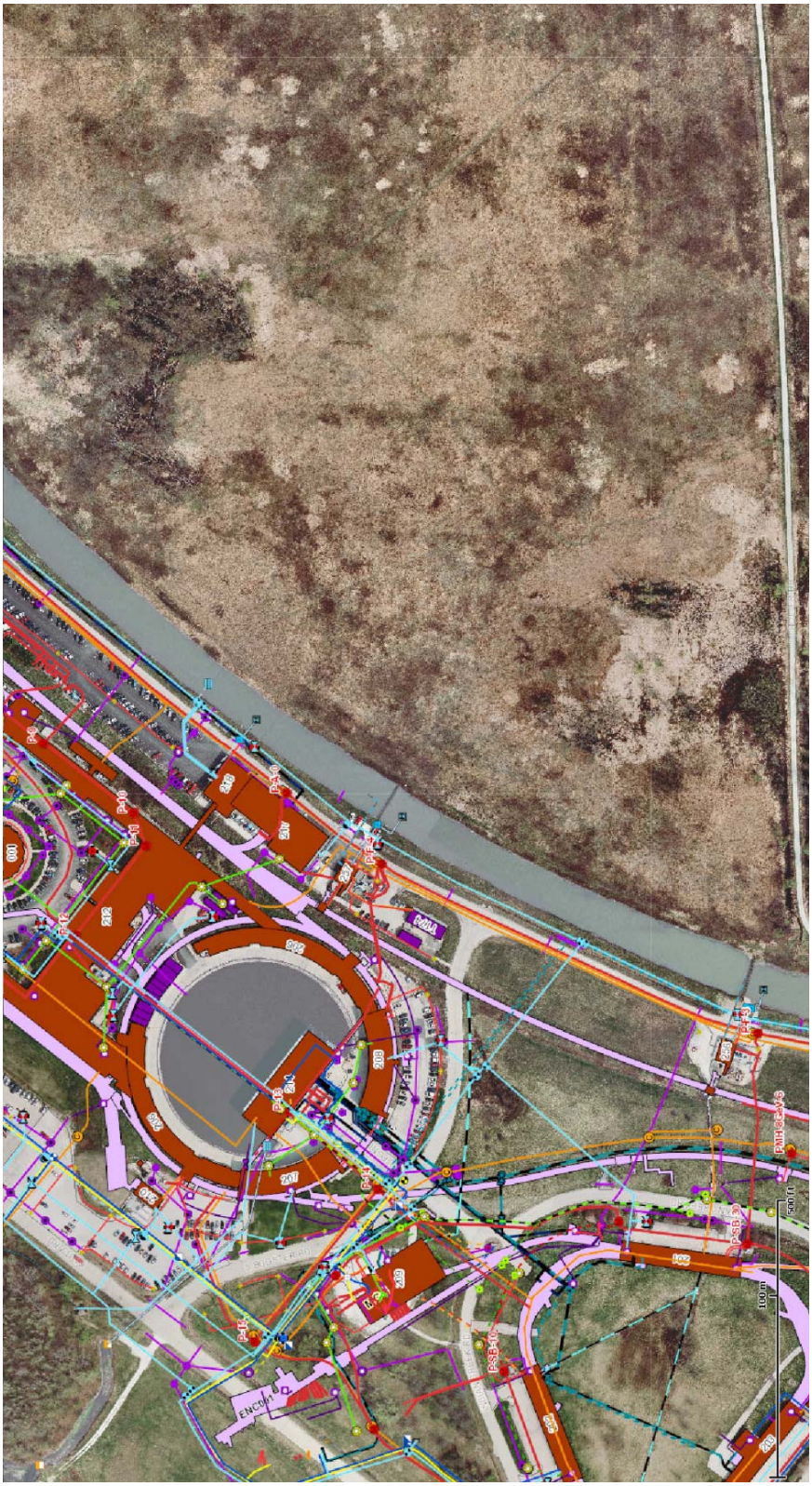

Figure 4.2.

Radioactive Water (RAW) systems will be utilized for the programmatic equipment in the Beam Absorber. The RAW system, based on existing Fermilab system designs, will be double isolated

from surface water and will reject the heat to the LCW system. The design, procurement and installation of the RAW systems are included in the accelerator portion of the project.

The existing 13.8 KV site wide electrical feeder system will be extended to PIP-II to provide a looped feed served primarily from the Master Substation (MSS). A backup up feeder, capable of powering critical portions of PIP-II will be served from the existing Kautz Road Substation (KRS). Connection to the MSS network will be accomplished at manhole P71 in the Main Ring and installed in a new concrete encased ductbank to the PIP-II site. A new substation, consisting of transformers, air switches and related electrical gear will be installed adjacent to the PIP-II Linac Service Building and the Cryogenics Plant.

The existing data and communication system will be extended in new duct banks to PIP-II from existing below grade ductbanks along the Main Ring Road. The connection location is assumed to be the existing communication manhole located adjacent to the Booster Tower.

4.2.2. Linac

The Linac work includes the below grade, cast-in-place concrete Linac Enclosure and the above grade Linac Support Building.

The above grade and below grade portions of the Linac will be designed to include egress, construction type, emergency lighting, exit signage and smoke control ventilation in accordance with the IBC (International Building Code) and NFPA. Automatic sprinkler systems for the Linac Support Building will comply with the standards for an Ordinary Hazard Group 1 classification, in accordance with latest edition of the National Fire Protection Association's (NFPA) Codes and Standards.

The below grade Linac Enclosure is sized to accommodate the length of a 0.8 GeV linac of 203 meter (665 feet) which includes space to accommodate a possible future upgrade of the Linac energy through the installation of four (4) HB650 cryomodules.

The Linac Enclosure will provide space for the linac hardware, penetrations for utilities (power, water, cryogens) and cabling, as well as for equipment installation and maintenance. The Linac Enclosure will also accommodate the logistics of installation, repair and removal of beamline components and related support equipment. Figure 3, below, depicts a typical cross section through the Linac Enclosure showing the space required to accommodate the beamline components as well as the space required for installation.

The depth below grade of the Linac Enclosure is based on the beamline components matching the elevation of the existing Booster component elevation. This places the base slab of the Linac Enclosure at elevation 722' or approximately 25 feet below existing grade.

The below grade enclosure will have code compliance exit stairways provided to conform to the required maximum distance to an exit. These exit stairs will be configured to maintain the radiation safety shielding requirements. Fire detection will be via air sampling and line type sensors.

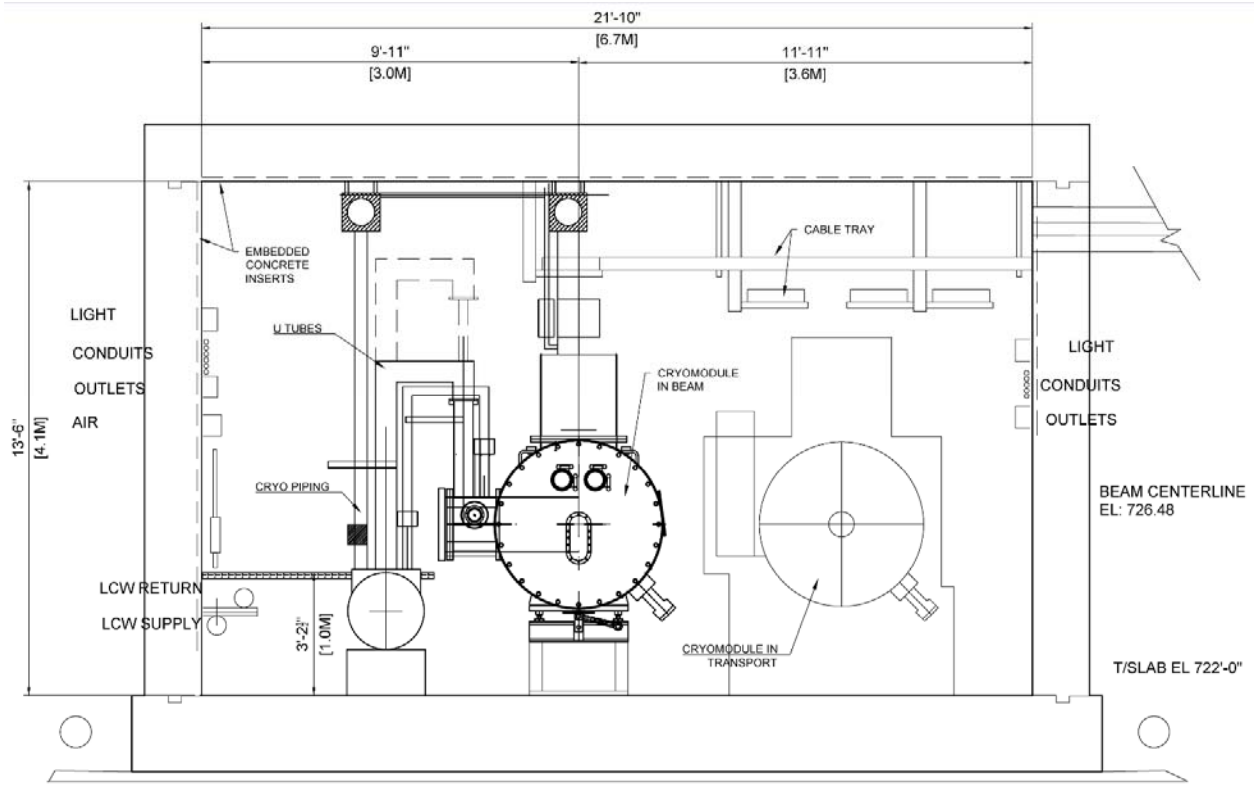

Figure 4.3.

The interior walls and ceiling of the Linac Enclosure will be painted and the exterior will be moisture proofed to provide a safe and dry semi-conditioned space for personnel and equipment. The below grade structures will be flanked with underdrain piping that will negate the hydraulic pressure on the walls and roof of the enclosure. The underdrains will be routed to duplex sumps that will discharge water to existing surface water features and away from the structure.

The walls and ceiling of the Linac Enclosure will be fitted with channel inserts to allow for the support of cable trays, cooling water, electrical conduits and fire detection equipment. Convenience outlets, 120/208VAC, will be provided at least every sixty feet along the walls. 480v/60 amp welding outlets will be provided spaced at 400 feet along the length of the Linac Enclosure.

In addition to required emergency and exit lighting, light fixtures will be provided to supply a minimum of 20 foot-candles. A percentage of these lights will be on uninterruptible power supply (UPS) circuits to provide emergency lighting during power failures.

The Linac Enclosure will be ventilated with neutral, dehumidified air as required by code. The underground air flow will include the provision for Oxygen Deficiency Hazard (ODH) ventilation. The conventional facilities will provide the mechanical equipment and ductwork for ODH ventilation while the controls, sensors, programming and commissioning will be accomplished as part of the equipment installation.

The south (downstream) end of the Linac Enclosure will include an elevator to accommodate the movement of the test carts, diagnostic equipment and related items that are needed for Linac operations and maintenance.

The construction of the below grade structure will utilize traditional “open cut and cover” method. This method has been used successfully at Fermilab for the construction of the majority of shielded enclosures on-site of a similar depth and use.

Based on a preliminary shielding assessment, the design of the Linac Enclosure will accommodate 5.6 meters (18.5 feet) of earth equivalent passive shielding in order to achieve an unlimited occupancy of the Linac Service Building and surrounding spaces. In general this will be accomplished with an earthen berm with maintainable side slopes. For road crossings and areas where berms are not feasible, the design will utilize steel plates to achieve the required equivalent shielding. The 5.6 meters (18.5 feet) of shielding is based on a preliminary assessment which will be finalized during final design. Shielding documentation will be prepared and initial approval for construction obtained prior to the start of construction.

The Linac Support Building will provide space for the support services required to install, operate and maintain the PIP-II beamline components. The Linac Support Building contains three (3) spaces as described below:

High Bay: The high bay portion of the Linac Support Building will provide space for unloading, staging and assembling beamline components. This includes an at-grade loading dock with a 30 ton overhead bridge crane for moving equipment from grade to the below grade portion of the high bay.

The below grade portion of the high will be sized to accommodate the low energy portion of the PIP-II beamline components that do not require radiation shielding as well as space for staging and preparing beamline components for installation. The below grade portion of the high bay will also contain the support equipment and infrastructure required to operate the adjacent beamline components.

Gallery: The gallery space of the Linac Support Building will house the equipment needed to operate the beamline components in the adjacent, below grade Linac Enclosure. The 210 meter (690 foot) gallery will be constructed parallel to the below-grade Linac Enclosure and will provide penetrations for utilities, controls, cooling water, cryogens and related operational services. The south (downstream) end of the gallery will include access to the elevator to Linac Enclosure to accommodate the movement of the test carts, diagnostic equipment and related items that are needed for Linac operations and maintenance.

Support: The support space of the Linac Support Building will house the equipment and services required to support the operation of the building. This includes the following functions:

Process Water Equipment Room to house heat exchangers, pumps, controls and related equipment for the Low Conductivity Water (LCW) system used to cool the beamline components and power amplifiers. Since this space is driven by water containing components, if necessary, this space could be housed in a separate building rather than contained with the Linac Support Building.

Mechanical that supports the operation of the facility.

Electrical equipment that supports the Linac Support Building including the incoming electrical service switchgear, panel boards, and related power supplies. The switchgear will serve conventional facilities equipment, the programmatic equipment and the HVAC systems. This room will house the electrical panels serving the lights, outlets and general building power.

Control Room to house monitoring/control equipment, conference room space for 8-10 people and adjacent workspace;

Visitor's Area suitable for use by outreach programs of up to 15 people;

Building Services including a building manager's office, toilet rooms and janitor's closet;

4.2.3. Transport Line

The Transport Line will house the beamline components required to bring the proton beam from

the downstream end of the Linac Enclosure the existing Booster accelerator. The 225 meter (737 foot) long Transport Line enclosure will generally have a 3 meter (10 foot) wide by 2.45 meters (8 foot) high cross section.

In order to accommodate the crossing of the new PIP-II transport line and the existing Main Ring beamline, the PIP-II beamline will rise up and over the existing Main Ring beamline components. A portion of the existing precast Main Ring tunnel will be removed and replaced with a cast-in-place concrete structure capable of accommodating both beamlines. This portion of the Transport Line enclosure will have a 3.4m (11 foot) high enclosure.

A 9 meter (30 foot) long extraction enclosure stub will be constructed to accommodate possible future beamlines to the Muon Campus region.

The construction of the Transport Line enclosure will utilize traditional "open cut and cover" methods in which earth material is excavated, the concrete beamline enclosure is constructed and the completed enclosure is covered with the excavated material with granular material of the sides of the enclosure to facilitate drainage. This method has been used successfully at Fermilab for the construction of the majority of shielded enclosures on-site.

The interior walls and ceiling of the Transport Line enclosure will be painted and the exterior concrete surface will be moisture proofed to provide a safe, dry semi-conditioned space for personnel and equipment. The enclosure will be flanked with underdrain piping that will negate the hydraulic pressure on the walls and roof of the enclosure. The underdrains will be routed to a duplex sump that will discharge water onto grade and away from the enclosure. The walls and ceiling of the enclosure will be fitted with channel inserts to allow for the support of cable trays, cooling water piping, electrical conduits and fire detection equipment.

Convenience outlets, 120/208VAC, will be provided every sixty (60) feet along the wall on the side of the beamline. Welding outlets, 60 amp / 480V, will be provided at two (2) locations along the length of the enclosure. In addition to required emergency and exit lighting, light fixtures will be provided to supply a minimum of 20 foot-candles. A percentage of these lights will provide emergency lighting during power failures. Lighting will be controlled by the lighting control panel in the Linac Support Building.

The Transport Line enclosure will be separated from the Linac Enclosure by an air barrier to contain the cryogens within the Linac Enclosure. Fire detection will be via air sampling and line type sensors. The fire detection devices will report to the fire panel in MC-1.

A Beam Absorber enclosure will connect to the Transport Line enclosure to house the 20 kW beam absorber, radioactive cooling water (RAW) system and related equipment.

The floor of the Transport Line enclosure will match the elevation of the Linac Enclosure to facilitate the installation of beamline components.

The Transport Line enclosure will be installed beneath the existing Booster Tower East parking lot and building to allow for the PIP-II beam to intercept the existing Booster beamline at the existing Long 11 straight section, which results in minimal displacements of the existing Booster tunnel equipment and reduces the interference with existing support services.

The installation of the Transport Line enclosure will require a partial demolition and temporary support of the existing Booster Tower East building to excavate and install the cast-in-place concrete connection to the existing Booster enclosure.

The Booster Tower Southeast parking lot will be replaced with a shielding berm similar in style and construction to that constructed when the Main Injector 8GeV line was installed at Booster Tower West. Vehicular access to existing electrical equipment in the northeast corner of the parking

lot will be provided for maintenance of the electrical equipment.

The Transport Line will be designed to support up to 5.6 meters (18.5 feet) of earth and concrete shielding in order to provide for "unlimited occupancy" of all above ground areas accessible to the general public. The Transport Line enclosure include code required egress paths. The 5.6 meters (18.5 feet) of shielding is based on a preliminary assessment which will be finalized during final design. Shielding documentation will be prepared and initial approval for construction obtained prior to the start of construction.

Space for beamline power supplies, control equipment and related equipment will be provided in the one bay of the Linac Support Building.

4.2.4. Cryogenics Plant

The PIP-II Cryogenics Plant will provide space for the cryogenics equipment for the PIP-II accelerator components. The Cryogenics Plant will be located at the downstream end of the Linac Enclosure in order to be positioned to allow for future expansion. The Cryogenics Plant contains three (3) primary spaces as described below:

Cold Box Station: The Cold Box Station will contain the equipment to install, operate and maintain the cold box. This includes the following criteria:

- Building Size: 15 m x 40 m (50 feet x 131 feet);
- Overhead crane with a capacity of 15 tons;
- Overhead door 5 m x 5 m (17 feet x 17 feet);
- Maximum floor loading:20,000 kg/square meter (4,096 pounds/square foot);
- Space for five (5) 10,000 liter (2,641 gallons) dewars;
- 565 liters/minute (150 gallons per minute) of chilled water;
- Coordination Center to house 4-8 people;
- Control Room to accommodate equipment, monitors and related control equipment;
- Control Room and Coordination Center should have an isolated HVAC system that is capable of pressuring the room to reduce the oxygen deficiency hazard of the space;

Warm Compressor Station: The Warm Compressor Station will contain the equipment to install, operate and maintain the compressor and related equipment to support the Cold Box Station. This includes the following criteria:

- Building Size: 20 m x 30 m (66 feet x 100 feet)
- Overhead crane with a capacity of 25 tons;
- Overhead door 5 m x 5 m (17 feet x 17 feet);
- Maximum floor loading:20,000 kg/square meter (4,096 pounds/square foot);
- Space for five (5) 10,000 liter (2,641 gallons) dewars;
- The cooling medium for the cryogenics compressors can be industrial cooling water (ICW) if it meets PIP-II quality requirements. A review of the previous tests of the ICW indicate that the water is generally acceptable, but will require additional filtration to meet the solids requirements.

Exterior Space: The exterior space for the Cryogenics Plant will provide for access to the Cold Box Station and Warm Compressor Station. This includes the following criteria:

- Space for ten (10) 113,000 liter (30,000 gallon) storage tanks and related piping;
- Space for one (1) 34,000 liter (9,000 gallon) liquid nitrogen dewar and related piping;
- Space for one (1) truck mounted mobile purifier;

- Space for tanker truck for servicing the storage tanks/dewar;
- Parking for 8-10 vehicles;
- Loading dock access to both the Warm Compressor Station and the Cold Box Station;
- Underground utility tunnel that connects the Cryogenics Plant to the Linac Enclosure.

4.2.5. Utility Building

The PIP-II Utility Building will house the mechanical infrastructure to cool the Cryogenics Plant, LCW systems and HVAC systems. The Utility Building will be located at the upstream end of the Linac Enclosure and will include the following:

- Heat exchangers, pumps, electrical equipment and controls for the LCW and CHW systems;
- Water treatment and filtration systems;
- Electrical equipment;
- Control Room;
- Exterior space for cooling towers.

The Utility Building is sized to accommodate the anticipated equipment for both pulsed mode and continuous wave mode operations.

4.3. Site Power Requirements

An estimate of site power requirements for the linac operating in the pulsed mode and the beam transfer line to the Booster is given in Table 4.1.

The following items were included into the power estimate:

- RFQ and MEBT RF: includes RF sources powering RFQ and MEBT rebunching cavities operating in CW regime.
- SC Linac RF: includes RF sources powering SC cavities to accelerate 2 mA of beam to 0.8 GeV with RF duty factor of 12%. Also included are LLRF, protection circuits and RF controls.
- Magnets: Includes all power supplies for quads, solenoids, dipoles and trim magnets.
- Cryogenic Systems: Based on the CHL upgrade described in Section 3.4.
- LCW (Low Conductivity Water): The primary load is cooling of the RF sources and power supplies for dipoles.
- HVAC (heating, ventilation and air-conditioning): The primary loads are RF power not removed by the LCW system and the removal of heat from equipment galleries.
- Conventional Systems: Power required for other linac/beamline components (vacuum pumps), and for occupied spaces.

The total PIP-II SC linac power is ~6.2 MW. It supports its operation in the pulsed regime.

Table 4.1: Site power estimates.

System	Wall-Plug Power (kW)
RFQ and MEBT RF	320
SC linac RF	1100
Magnets (quads, solenoids,	300
Cryogenic Systems	3250
LCW	200
Chilled water	500
HVAC	200
Conventional Systems	300
Total	6170

References

[1] "Building for Discovery: Strategic Plan for U.S. Particle Physics in the Global Context", Report of the Particle Physics Project Prioritization Panel, May 2014, http://science.energy.gov/~/media/hep/hepap/pdf/May-2014/FINAL_P5_Report_053014.pdf

[2] LBNE Conceptual Design Report Volume 2: The Beamline at the Near Site, October 2012, http://lbne2-docdb.fnal.gov/cgi-bin/RetrieveFile?docid=4317;filename=CDR-beam-volume-101812-reduced.pdf

[3] Proton Improvement Plan website, http://www-ad.fnal.gov/proton/PIP/PIP_index.html

[4] The PIP-II Reference Design Report, V. Lebedev editor, June 2015, http://pip2-docdb.fnal.gov/cgi-bin/RetrieveFile?docid=1&filename=PIP-II_RDR_v0.0.pdf&version=1

[5] G. E. Krafczyk, " Booster 20 Hz tests", Beams-doc-4777, http://beamdocs.fnal.gov/AD-public/DocDB/ShowDocument?docid=4777

[6] M. Plum, et.al., "STATUS OF THE SNS RING POWER RAMP UP", Proceedings of EPAC08, p. 3560-3562.

[7] I. Kourbanis, *et.al*., "Progress Toward Doubling the Beam Power at Fermilab's Accelerator Complex", Proceedings of IPAC 2014 (FERMILAB-CONF-14-187-AD).

[8] "Project X LEBT: Functional Requirement Specifications", TeamCenter Document #ED0001289; uncontrolled copy in Project X Document 912: http://projectx-docdb.fnal.gov/cgi-bin/ShowDocument?docid=912

[9] S. Nagaitsev, *et. al.* "The Project-X Injector Experiment: A Novel High Performance Front-end for a Future High Power Proton Facility at Fermilab", Proceedings of PAC-2013, p. 374.

[10] Ji, Q and Staples, J, Project X Document 897: "Project X H^- Ion Source Acceptance Test and Future Plan", http://projectx-docdb.fnal.gov/cgi-bin/ShowDocument?docid=897

[11] G. Romanov, *et. al.* "Project-X RFQ EM-design", IPAC2012, New Orleans, May 2012; FERMILAB-CONF-128-TD

[12] K.R. Crandall et al. "RFQ Design Codes", Los Alamos Report LA-UR-96-1836 (1996 , Revised, Dec. 7 2005)

[13] "PXIE MEBT Functional Requirements Specification", TeamCenter Document #ED0001303; uncontrolled copy in Project X Document 938: http://projectx-docdb.fnal.gov/cgi-bin/ShowDocument?docid=938

[14] Yakovlev, V, "SRF Linac Technology Development", Proceedings of the XXVI Linac Conference (LINAC12), Tel-Aviv, 2012.

[15] Ciovati, G, "Review of High Field Q Slope, Cavity Measurements", in Proc. SRF2009: 90 (2009).

[16] Project X Document 590: "Assumption about Q values in CW linac", http://projectx-docdb.fnal.gov/cgi-bin/ShowDocument?docid=590

[17] Reschke, D, "Analysis of the RF results of recent 9-cell cavities at DESY", TTC-Report 2009-01, 2009

[18] Brunner, O, et al, "Assessment of the basic parameters of the CERN Superconducting Proton Linac", PRSTAB 12, 070402, 2009

[19] Technical Specifications for High RRR Grade Niobium Sheet for Use in Superconducting Radio Frequency Cavities, Fermilab Specification: 5500.000-ES-371037 Rev B, Fermilab, Technical Division.

[20] Chase, B., Peterson, Th. and Yakovlev, V.,"A Strategy for Cavity Resonance Control in the Project X CW Linac," 02.20.2011, Project X Document 827-v1, ProjectX Database, http://projectx-docdb.fnal.gov/cgi-bin/ShowDocument?docid=827.

[21] Optics files supporting optics for the SC linac and transfer line. PIP-II Document 119; http://pip2-docdb.fnal.gov:8080/cgi-bin/ShowDocument?docid=119

[22] V. Lebedev, et.al. "Intrabeam stripping in H^- linacs", Linac-2010, Tsukuba, Japan, Sep. 12-17, 2010.

[23] A. Shishlo, J., *et.al.* "First Observation of Intrabeam Stripping of Negative Hydrogen in a Superconducting Linear Accelerator" Plum, Phys. Rev. Lett. 108, 114801 (2012).

[24] Krivosheev, O. and Mokhov, N. "Tolerable beam loss at High-Intensity Proton Machines", Fermilab-Conf-00/185, Aug. 2000.

[25] J.-P. Carneiro, "H− Stripping Equations and Application to the High Intensity Neutrino Source", Beams-doc-2740, http://beamdocs.fnal.gov/AD-public/DocDB/DocumentDatabase

[26] G.H. Gillespie, Phys. Rev. A 15, 563 (1977) and 16, 943 (1977), Nucl. Intr. & Meth. B 2, 231 (1984) and B 10/11, 23 (1985).

[27] A. Drozhdin, "H- beam collimation in the transfer line from 8 GeV linac to the Main Injector", Beams-doc-2740, June 2008, https://beamdocs.fnal.gov/AD-private/DocDB/ShowDocument?docid=2201

[28] J. Lackey, et. al., "Operation and Performance of the New Fermilab Booster H^- Injection System", FERMILAB-CONF-07-248-AD.

[29] M. Popovic, et. al., "A Proposed H^- Injection System for the Fermilab Booster", Beams-doc 1784-v1, April 2005.

[30] M.S. Gulley et al., Phys. Rev. A 53, 3201 (1996).

[31] W. Chou, M. Kostin and Z. Tanga, "Stripping Efficiency and Lifetime of Carbon Foils," http://arxiv.org/abs/physics/0611157

[32] V. Lebedev and V. Shiltsev (Eds.), "Accelerator Physics at the Tevatron Collider", Springer, 2014.

[33] Yu. Tokpanov, V. Lebedev, W. Pellico, "MEASUREMENTS OF MAGNETIC PERMEABILITY OF SOFT STEEL AT HIGH FREQUENCIES", Proceedings of IPAC-2012, New Orleans, Louisiana, USA.

[34] James L. Crisp and Brian J. Fellenz, "Measured Longitudinal Beam Impedance of Booster Gradient Magnets", Fermilab-TM-2145, March 22, 2001.

[35] V. Lebedev and C. Bhat, "Booster Transition Crossing," http://pxie.fnal.gov/PIPIImeetings/TransitionCrossing.pdf

[36] V. A. Lebedev, J.-F. Ostiguy and C.M. Bhat, "BEAM ACCELERATION AND TRANSITION CROSSING IN THE FERMILAB BOOSTER", HB-2016.

[37] J.-F. Ostiguy, V. Lebedev and C.M. Bhat, "MODELING LONGITUDINAL DYNAMICS IN THE FERMILAB BOOSTER SYNCHROTRON", IPAC-16.

[38] W. Pellico, "From PIP to PIP-II," https://beamdocs.fnal.gov/AD/DocDB/0047/004700/002/Booster-PIPII-v1.pdf

[39] King-Yuen Ng, "Longitudinal Coupled Bunch Instability in the Fermilab Booster", FERMILAB-FN-0464; KEK-87-17.

[40] A. Burov and V. Lebedev, FERMILAB-TM-2492-AD (2011)
[41] A. Macridin et al., Phys. Rev. ST-AB, 14, 061003 (2011)
[42] A. Burov, Phys. Rev. ST-AB, 12, 044202 (2009)
[43] A. Burov, Phys. Rev. ST-AB, 17, 021007 (2014)
[44] A. Chao, "Physics of Collective Beam Instabilities in High Energy Accelerators", John Wiley & Sons, Inc., Eq. (6.58), (1993)
[45] A. Macridin et al., FERMILAB-CONF-13-431-CD (2013).
[46] Synergia home - https://web.fnal.gov/sites/Synergia/SitePages/Synergia%20Home.aspx
[47] A. Burov, Phys. Rev. Accel. Beams, **19**, 084402 (2016)
[48] J. Wei, "Transition Crossing", in "Handbook of Accelerator Physics and Engineering" (edited by A.W. Chao and M. Tigner), World Scientific, 2nd Printing (2002).
[49] A. Burov, FERMILAB-PUB-11-174-AD (2011)
[50] See Eq. (6.240), p. 360. in Ref. [51]
[51] A. Burov, FERMILAB-PUB-16-279-AD (2016).
[52] "Project X and PXIE Ion Source Functional Requirement Specifications," TeamCenter Document #ED0001288; uncontrolled copy in Project X Document 968:, http://projectx-docdb.fnal.gov/cgi-bin/ShowDocument?docid=968
[53] http://www.d-pace.com/
[54] emittance scanner paper
[55] arXiv paper from Lionel
[56] "PXIE LEBT Beam Transverse Emittance Station FRS", TeamCenter Document #ED0001294; uncontrolled copy in Project X Document 1077: http://projectx-docdb.fnal.gov/cgi-bin/ShowDocument?docid=1077
[57] "Project X RFQ functional physics requirements", TeamCenter Document #ED0001300; uncontrolled copy in Project X Document 894: http://projectx-docdb.fnal.gov/cgi-bin/ShowDocument?docid=894
[58] Virostek, S, et al, "Design and analysis of the PXIE CW Radio-Frequency Quadrupole (RFQ)", in *Proc. of IPAC2012*, New Orleans, Louisiana, USA, 2012, THPPC034.
[59] Ratti, A, et al, "The Design of a High Current, High Duty Factor RFQ for the SNS", in *Proc. of EPAC '00*, Vienna, Austria, 2000, pp. 495-497.
[60] PXIE RFQ coupler
[61] Sang-ho Kim, et.al. "Stabilized operation of the Spallation Neutron Source radio-frequency quadrupole", Phys. Rev. ST Accel. Beams 13, 070101 (2010)
[62] "PXIE MEBT quadrupoles specifications", TeamCenter Document #ED0001312; uncontrolled copy in Project X Document 933: http://projectx-docdb.fnal.gov/cgi-bin/ShowDocument?docid=933
[63] "FRS for Bunching cavity for PXIE MEBT", TeamCenter Document #ED0001307; uncontrolled copy in Project X Document 1071: http://projectx-docdb.fnal.gov/cgi-bin/ShowDocument?docid=1071
[64] Romanov, G, et al, "CW room temperature re-buncher for the Project X front end" in *Proc. of IPAC'12*, New Orleans, USA, 2012, THPPP063
[65] "PXIE MEBT kicker specifications", TeamCenter Document #ED0001305; uncontrolled

cone in Project X Document 977: http://projectx-docdb.fnal.gov/cgi-bin/ShowDocument?docid=977

[66] Diebele, C and Aleksandrov A., "Experimental study of the SNS MEBT chopper performance", in Proc. of IPAC'10, Kyoto, Japan, 2010, MOPD063.

[67] Lebedev, V, et al, "Progress with PXIE MEBT chopper", in Proc. of IPAC'12, New Orleans, USA, 2012, WEPPD078.

[68] "Functional specifications for PXIE MEBT absorber", TeamCenter Document #ED0001304; uncontrolled copy in Project X Document 964: http://projectx-docdb.fnal.gov/cgi-bin/ShowDocument?docid=964

[69] A. Shemyakin and C. Baffes, High power density test of PXIE MEBT absorber prototype, Proc. of LINAC'14, August 31 – September 5, 2014, Geneva, Switzerland, THPP055.

[70] "Functional specifications for PXIE MEBT scrapers", TeamCenter Document #ED0001306; incontrolled copy in Project X Document 1067: http://projectx-docdb.fnal.gov/cgi-bin/ShowDocument?docid=1067

[72] ATLAS 72 MHz energy upgrade cryomodule

[73] Kephart, R (editor), "Project X Functional Requirements Specification," http://projectx-docdb.fnal.gov/cgi-bin/ShowDocument?docid=658

[74] Schappert,W, et al, "Microphonics Control for Project X," PAC2011, New York, March 28, 2011, TUP086.

[75] V.Yakovlev, et al, "HOMs in the Project-X CW Linac," Int. Workshop on Higher–Order Mode Damping in Superconducting RF Cavities, Cornell University, October 11-13, 2010, http://www.lns.cornell.edu/Events/HOM10/rsrc/LEPP/Events/HOM10/Agenda/MA3_Yakovlev.pdf

[76] S.-H. Kim, "HOM Experiences at the SNS SCL," SPL HOM workshop, CERN, June 25-26, 2009. http://indico.cern.ch/event/57247/session/1/contribution/9/material/slides/1.pdf

[77] A. Grassellino, A. Romanenko, O. Melnychuk, Y. Trenikhina, A. Crawford, A. Rowe, M. Wong, D. Sergatskov, T. Khabiboulline, F. Barkov, 2013 Supercond. Sci. Technol. 26 102001 (Rapid Communication).

[78] A. Romanenko, A. Grassellino, A. C. Crawford, D. A. Sergatskov, and O. Melnychuk, Appl. Phys. Lett. 105, 234103 (2014).

[79] N.V. Mokhov, C. James, The MARS Code System User's Guide, http://www-ap.fnal.gov/MARS/

[80] N. V. Mokhov, S.I. Striganov, "MARS15 Overview", in Proc. of Hadronic Shower Simulation Workshop, Fermilab, AIP Conf. Proc. 896 (2007) pp. 50-60.

[81] N. Mokhov, P. Aarnio, Y. Eidelman, K. Gudima, A. Konobeev, V. Pronskikh, I. Rakhno, S. Striganov, I. Tropin, "MARS15 code developments driven by the intensity frontier needs," Progress in Nuclear Science and Technology 4, 496 (2014).

[82] Foster, GW, Chou W, E. Malamud E (ed), "Proton Driver Study II", Chapter 16, Fermilab-TM-2169, (May 2002).

[83] P.Treitea, et al., Design, project execution, and commissioning of the 1.8K superfluid helium refrigeration system for SRF cryomodule testing, ICEC/ICMC 2014 https://indico.cern.ch/event/244641/session/25/contribution/41.pdf

[83a] cryo: independent review of an industrial studies conducted by the helium cryogenic plant manufacturers

[84] Cahill, K, et al, "The Fermilab Accelerator Control System", ICFA Beam Dyn.Newslett.47:106-124, 2008

[85] Patrick, J and Lackey, S, "Control Systems for Linac Test Facilities at Fermilab", Proc. Linac08, Victoria, BC, 2008

[86] Sullivan, AH, "A Guide to Radiation and Radioactivity Levels Near High Energy Particle Accelerators", Nuclear Technology Publishing, (1992).

Appendix A: Beam Transport to the Mu2e upgrade